DISTINCTIVE 2016

2nd Annual Meeting, Bristol, 19th - 20th April

Book of Summaries

DISTINCTIVE
Decommissioning,
Immobilisation and
Storage soluTIons for
NuClear wasTe InVEntories

A university consortium funded
by the Research Councils
UK Energy programme

Research Councils UK Energy For a Low Carbon Future
UNIVERSITY OF LEEDS
UNIVERSITY OF BIRMINGHAM
University of BRISTOL
Imperial College London
Loughborough University
Lancaster University
MANCHESTER 1824 The University of Manchester
The University Of Sheffield.
University of Strathclyde Glasgow
UCL

Master Project List

Theme	Title	Leading Institution	Researcher	Type
1	An Investigation of Wasteform Evolution During Wet-recovery and Drying of SNF	Bristol	Dr. James Edward Darnbrough/Dr. Leila Costelle	PDRA
1	UO_2 Surface Reactivity and Alteration – a Fundamental Study of Photocatalytic and Structural Effects Related to Long Term Storage of SNF	Bristol	Sophie Rennie	PhD
1	Options for Exotic Carbide Fuels	Imperial	Claudia Gasparrini	PhD
1	The Behaviour of Used Nuclear Fuel in Wet Storage	Lancaster	Elizabeth Howett	PhD
1	Determination of Optimum Drying Conditions for AGR fuels	Leeds	James Goode	PhD
1	Use of TRLFS to Investigate Dissolution Rates	Loughborough	Dr. Oliver Preedy	PDRA
1	Characterising the Chemical and Physical Properties of Depleted, Natural and Low-enriched Uranium with Regard to the Suitability of Alternative Disposal Routes	Loughborough	Matthew Druce	PhD
1	Grain Boundary Damage Mechanisms in Strained AGR Cladding Under Irradiation	Manchester	Chiara Barcellini	PhD
1	A Life Cycle Approach as a Decision Tool for Nuclear Waste Management and Decommissioning of Existing and Future Plants	UCL	Andrea Paulillo	PhD
2	Computational Modelling of PuO_2 Ageing and Fuel Residues	Birmingham	Nathan Palmer	PhD
2	In-situ Characterisation of Heavily-Contaminated Plutonium Finishing Environments	Lancaster	-	PhD
2	Real-time Fast Neutron Plutonium Assay for Plutonium Storage and Ageing Applications	Lancaster	Rashed Sarwar	PhD
2	Understanding the Interfacial Interactions of Plutonium Dioxide with Water	Lancaster	Dr. Dominic Laventine	PDRA
2	Investigation of Anomalous Hydrogen Production from Water Adsorbed on Oxides	Manchester	Jamie Southworth	PhD
2	Modelling the Surface Chemistry of PuO_2 at the Molecular Level	Manchester	Dr. Bengt Tegner	PDRA
2	Simulation of Low-energy Electron Radiolysis of Water Adsorbed on Oxides	Manchester	Marisa Smith	PhD
2	Understanding Surface Species and Interactions Between Adsorbed Chloride and Water on Stored PuO_2	Manchester	Sophie Sutherland-Harper	PhD
2	Understanding the Interfacial Interactions of Plutonium Dioxide with Water	Manchester	Dr. Luke Jones	PDRA
2	Ceramic Materials for Actinide Disposition	Sheffield	Dr. Shi-Kuan Sun	PDRA
2	Development of Glass-ceramics for Pu Disposition using Hot Isostatic Pressing	Sheffield	Stephanie Thornber	PhD
2	Understanding Actinide Sorption and Binding to Cement Materials for Radioactive Waste Management	Sheffield	Antonia Yorkshire	PhD
2	The Interaction of Water with PuO_2 Surfaces	UCL	Joseph Wellington	PhD
3	New Ion Exchange Materials For Effluent Clean-up	Birmingham	Ryan George	PhD
3	Novel Ceramic Wasteforms for Cs and Sr Encapsulation	Birmingham	George Day	PhD
3	Novel Ion Exchange Materials	Birmingham	Dr. Evin (Tzu-Yu) Chen	PDRA
3	Corrosion of Uranium in Water and Hydrogen	Bristol	Antonis Banos	PhD
3	Development of Raman Spectroscopy Techniques	Bristol	Kate Wyness	PhD

	for the Remote Analysis of Nuclear Wastes in Storage			
3	The Evolution of Grouted Waste Forms Containing Uranium	Bristol	Haris Paraskevoulakos	PhD
3	Durability of Heterogeneous ILW Glass/Ceramic Wasteforms from Complex Wastestreams	Imperial	Dr. Rama Krishna Chinnam	PDRA
3	Glass Composite Materials for Fukushima ILW Immobilisation	Imperial	Dimitri Pletser	PhD
3	Glass Composite Materials for Sellafield LP&S ILW Immobilisation	Imperial	Charles Hutchison	PhD
3	Magnetic Nanoparticles for Waste Separation or Sequestration	Imperial	Eleonora Cali	PhD
3	Computational Simulations of Storage Pond Sludge Disturbance	Lancaster	Olivia Lynes	PhD
3	Characterisation of Flocculated Waste Suspensions with Acoustic Backscatter	Leeds	Alastair Tonge	PhD
3	Gas Retention and Release from Nuclear Legacy Waste	Leeds	Michael Johnson	PhD
3	Measurement and Modelling of Sludge Mobilisation and Transport	Leeds	Dr. Derrick Njobuenwu/Dr. Hugh Rice	PDRA
3	The Development of Characterisation Techniques for Intermediate Level Waste Sludges	Leeds	Andre Botha	PhD
3	Enhanced Shear Micro- and Ultra-Filtration Without Recycle Pumping	Loughborough	Keith Schou	PhD
3	One Step Extraction and Quantification of Radionuclides Using Superparamagnetic Bead and Nanopore Technologies	Loughborough	Laura Mayne	PhD
3	Autonomous Systems for Nuclear Decommissioning in Extreme Radiation Environments	Manchester	Olusola Ayoola	PhD
3	Irradiated Sludges - Experimental	QUB	Mel O'Leary	PhD
3	Modelling Hydrogen Generation from Radioactive Sludges	QUB	Conrad Johnston	PhD
3	Thermal Treatment of PCM and ILW	Sheffield	Luke Boast	PhD
3	The Interaction of Brucite Surfaces with Uranium and its Fission Products	UCL	Eszter Makkos	PhD
4	Production of Real-time Segmented as-built CAD Models for the Planning and Execution of Remote and Human Intervention Tasks	Birmingham	Henry (Cheng) Zhao	PhD
4	The Impact of Recycled Concrete Fines on the Engineering Performance of Cementitious Infill	Leeds	Toby Lord	PhD
4	Simulating Radiation Damage in Cement	QUB	Ryan Kavanagh	PhD
4	Crack Sealing and Water Transport	Strathclyde	Riccardo Maddalena	PhD
4	Development of Novel, Low Cost Biomineral Permeable Reactive Barriers for Radionuclide Remediation	Strathclyde	Tom Mullan	PhD
4	In-situ Ground Contaminant Containment (Physical barrier)	Strathclyde	Christopher Wong	PhD
4	In-situ Ground Contaminant Containment (Physical barrier)	Strathclyde	Dr. Matteo Pedrotti	PDRA
4	Integrated Sensors for Infrastructure	Strathclyde	-	PhD
4	Nano-cracking of Cement Phases: Reactivity and Dissolution	Strathclyde	Luca Rizzo	PhD

Corrosion at the surface of nuclear materials

J E Darnbrough, S Rennie, I Griffiths, L Costelle, J E Sutcliffe, E Lawrence Bright, T B Scott, R Springell

*Correspondence: j.e.darnbrough@bristol.ac.uk

University of Bristol, Bristol, Uk

Abstract

Uranium based thin films have been created and characterised to aid in the fudamental investigation in to modes of corrosion of nuclear materials for storage and disposal. Two projects have shown that the types of damage that occurs to UO_2 in reactor can be simulated separately through He ion or Xe and Cs ion irradiation. This is observed as either an expansion of the lattice or a removal of crystallitity. The measurement of this damage via the 3 omega method and the effect on thermal conductivity are in early stages.
Work has been undertaken to look at the formation of pyrophoric uranium hydride on the interface between uranium metal and oxide. Showing that even small partial pressures of 2mbar at 80 degrees centigrade can cause transformation of the uranium metal.

Introduction

The rich nuclear history of the UK gives a diverse portfolio of waste nuclear material so to investigate this a degree of control and flexibility is required in sample production. For this approach Bristol has used dedicated uranium based thin film deposition system. This allows production of samples of epitaxial single crystal uranium metal, uranium oxide or bi-layers of metal and oxide, controlling stoichiometry, crystal structure and multi components.

The Bristol thin film actinide group acts as a team and as such many are involved in a multitude of projects. The focus of this summary will be on the work lead by the first author who has additionally aided with the projects of S Rennie, L Costelle and R S Springell.

Hydride formation on uranium metal surfaces is an important safety consideration as the resulting compound is pyrophoric, therefore storage considerations require knowledge of the formation of hydride. To investigate this thin film epitaxial uranium metal layers were grown with an oxide to mimic the oxide-metal interface in the real storage condition. This then has been exposed to a hydrogen partial pressures at a range of temperatures and times explore the kinetics of hydride formation.

Uranium dioxide is now the predominant fuel in the UK civil nuclear fleet and interest lies in the effect of the radiation damage throughout life on the stability and corrosion in storage and disposal. Thin films of single crystal epitaxial UO_2 produced by reactive DC sputtering are irradiated with a number of different ions to cause damage or implantation in order to mimic the evolution of virgin fuel to spent. This damage is characterised through a distortion in the lattice and is observed by X-ray Diffraction (XRD) however this technique is most sensitive to high electron density elements and therefore predominantly the information recovered is due to the uranium. Alternatively conduction of heat through a sample is dominated by phonons and particularly by those modes containing light elements, in this case oxygen. Therefore the thermal conductivity of a sample would give additional complementary information on the damage to the structure. This measurement is to be conducted by a 3omega method requiring development of a rig suitable for thin films.

Methodology Details

Hydriding

The thin films are produced as an epitaxial uranium layer (via a buffer) on a-plane Al_2O_3 with either a deposited UO_2 or Pd layer or exposed to air to form a 'native' oxide. These samples are then placed in sealed vessel and evacuated down to $1x10^{-5}$mbar at 110°C in order to remove any adsorbed contaminants from the air before being exposed to a partial pressure (2-500mbar) of H_2 at temperature (80-200°C) to cause hydride formation. The effect of the hydride is then characterised through a combination of XRD, X-ray Reflectivity (XRR) and Second Ion Mass Spectroscopy (SIMS).

Irradiation

Thin films of epitaxial UO_2 are produced on a range of substrate to give different orientations (SrTiO, YSZ and CaF) which are subsequently irradiated at Dalton Cumbria Facility (DCF) or Surrey Ion Beam Centre

(SIBC). Radiation damage in the films is produced by irradiation with He^{2+} ions at 2.1MeV at the DCF to a level of 0.15 displacements per atom.

Results and Discussion

Hydriding

This investigation has shown indications of hydride formation through consumption of uranium metal at 80°C with a H_2 partial pressure of 4mbar. The rate of consumption of metal is dependent on the orientation of the uranium film. Confirming that the metal is transformed into hydride poses problems as it does not form a crystalline phase and so is difficult to detect by standard diffraction. SIMS was utilised in this case to find the H and UH rich region, figure 1. At higher temperatures 150°C and pressures 500mbar a distinct hydride layer is formed between the metal and the oxide, which is not crystalline but can be determined as separate by XRR and complementary information from the XRD.

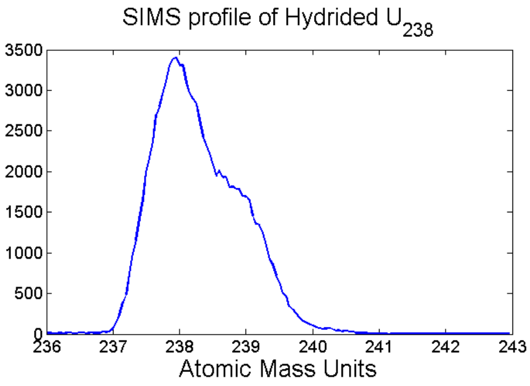

Figure 1: SIMS atomic mass scan at the U metal-oxide interface showing UH indicative of the hydride formation.

Analysis of XRD Bragg peaks illustrates differences in rate of consumption of metal and formation of hydride is also seen with different layers above the uranium. A UO2 deposited by reactive DC sputtering is uniform and results in a linear removal of metal with time. A 'native' oxide grown naturally in air slows the uranium metal consumption and follows a parabolic rate with time, figure 2.

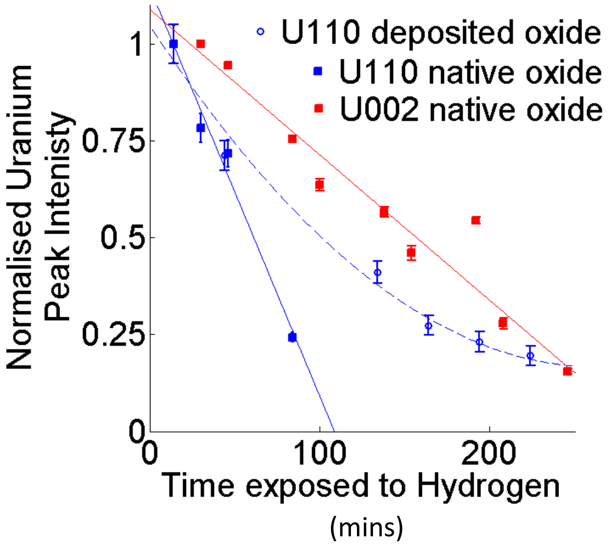

Figure 2: Consumption of U metal as observed by Bragg peak reduction when exposed to 2mbar H_2 at 80°C.

Other bulk work on uranium metal suggests that a crystalline hydride can form given defects and stresses in the metal to nucleate a crystalline growth. This aspect is missing from the single crystal thin film starting case and as such should be perused as an additional variable for future experiments.

Irradiation

Irradiating samples with different ions at different energies simulates the two different radiation damage events that fuel encounters during life in the reactor. He^{2+} at 2.1Mev illustrates the damage from neutrons and Xe or Cs at 40kev is indicative of the recoil implantation from fission daughter products.

Both types of damage have been seen to significantly affect the lattice structure as observed by XRD. In the case of He^{2+} damage an expansion in the lattice is seen, figure 3. This is through uniform accommodation of defects in the lattice caused by the irradiation. In the case of the heavier ion implantation (Xe Cs 40Kev) a significant loss in crystallinity is observed suggesting that the damage leads to a disordering of the atoms in the original lattice, figure 3.

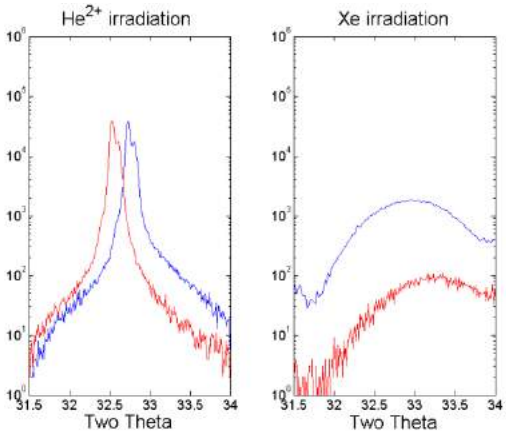

Figure 3: Blue undamaged, red irradiated. Left He^{+2} irradiated 200nm 001 UO_2 showing no loss in intensity only lattice expansion. Right Xe irradiated 80Å 001 UO_2 showing loss of crystalline material and lattice contraction.

The damage caused by He^{2+} irradiation has also been studied by AR-TEM which highlighted ‘bubble’ like features that maybe He bubbles or voids which are a collection of the dislocations formed, figure 4.

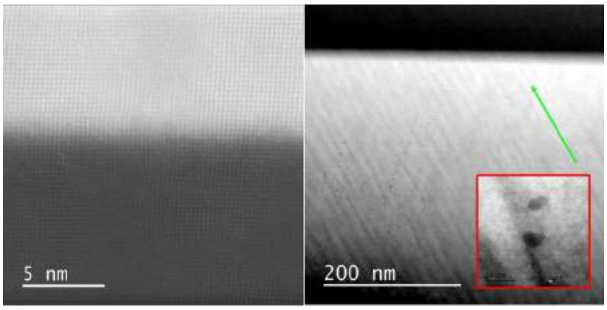

Figure 4: Left atomic resolution image of undamaged UO_2 thin film interface with a YSZ substrate. Right He^{2+} irradiated UO_2 film illustrating the FIB artefact direction in green and the highlighted ‘bubble’ features in red.

The development of a 3omega system at Bristol has completed the initial testing stages illustrating that measurement of thermal conductivity in bulk substrates matches literature values and that values from thin film samples on substrates is different and distinct from this. Now progress will be made to reduce noise in the system through production of a printed circuit board and improvement to the electrical conduction between the circuit and the deposited wire used a both source and probe of heating.

Conclusions and Future Work

A number of hydriding tests have been undertaken on engineered interfaces between single crystal uranium metal and different oxides showing that the metallic crystallography and the type of oxide has a considerable impact on the consumption of uranium and the formation of uranium hydride. Future steps are to increase the complexity of the system by introducing defect structures to investigate crystalline hydride formation. This linked with TEM of the interfaces can lead to a complete picture of the modes of formation of the pyrophoric uranium hydride for informing of safe storage and disposal.

Initial irradiation experiments of UO_2 epitaxial single crystal thin films has shown that the two major types of structural damage can be simulated for use in further experiments. This is a crucial step in increasing the complexity of the system investigated in a controlled way towards Spent Nuclear Fuel.

The 3omega system once updated will be used to completed measurements of UO_2 thin films with differing levels of damage. To corroborate the values found a thermal probe AFM will be used. These results will give information about the radiation damage accommodated through displacement of oxygen atoms in the lattice.

Acknowledgements

Thanks to DISTINCTIVE consortium for additional funds. Thanks also go to the project students Josh Fletcher, Nathan Brown, Lucy Welburn and Kamran Lamb.

Thanks to the Surrey Ion Beam Centre and Dalton Cumbria Facility for the work on irradiation.

Thanks to Gerry Lander for useful discussion.

Localized corrosion behaviour of uranium based materials

L. Costelle[1], R. Springell[1], S. Rennie[1], J. E. Darnbrough[1] and R. Burrows[2]

*Correspondence: Leila.costelle@bristol.ac.uk

[1] Interface Analysis Centre, University of Bristol, Bristol BS2 8BS, United Kingdom
[2]National Nuclear Laboratory, 102B Stonehouse Park, Sperry Way, Stonehouse, Gloucester GL10 3UT, United Kingdom

Abstract

In the present project, we design uranium microelectrodes using uranium thin films and expose their surfaces to a range of chemical conditions to study the localized corrosion behaviour in uranium-based materials. We use a range of electrochemical tests in order to probe the dynamic changes to the electrode surface and calculate the corrosion rate. The arising experimental results will be used as important parametric input for calculations of the likely long-term degradation of Spent Nuclear Fuels in variety of potential storage and disposal scenarios.

Introduction

The corrosion of uranium by hydrogen is a destructive process. The principal reaction involves the formation of a metal hydride precipitate which has a lower mass density than that of the parent metal and has been observed to follow a localized, spatially heterogeneous, and random pattern of initiation on uranium surfaces. However, electrochemically, there is a lack of understanding of these localized processes in uranium, because of the difficulty associated with the tiny current from the nucleated pits, which is always swamped by the overall passive current from the surface, and the difficulty to identify the time of initiation or the location of a single attack among many.

Conventional macro-electrodes are not suited for the study of these mechanisms as they tend to dilute the responses evident in the localised processes. However, the use of microelectrodes, based on uranium thin films, enabled us to isolate the effect and investigate it without the parallel response of a surface undergoing an entirely different reaction.

Methodology Details

Microelectrode design

Single-crystal and poly-crystalline thin films of U are grown on glass substrates using a dedicated dc magnetron sputtering facility at the University of Bristol under UHV conditions. The films were then mounted on chemically resistant epoxy to insulate the samples, giving exposed areas of ~ 2 – 4x10^{-6} cm^2. Electrical connection was achieved through conductive epoxy to wires (Figure 1).

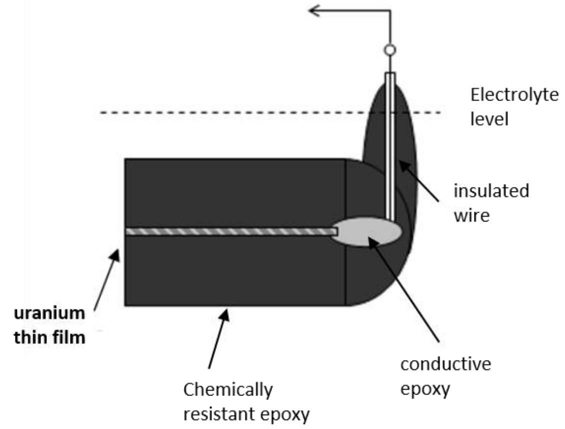

Figure 1 Uranium microelectrode design

Characterisation

Electrochemical tests employed a standard three electrode set-up with the U microelectrode as working electrode. As auxiliary electrode we used a platinum mesh mounted on a Pt rod. The reference electrode was a Ag/AgCl double-junction electrode (Thermo Scientific™ Orion™ 900200 Sure-Flow™) with a potential of +246 mV vs. standard hydrogen electrode (SHE). Electrolytes were prepared from high purity deionised water and AnalaR sodium hydroxide reagent.

Free corrosion potential studies were carried out using a Gamry potentiostat (Interface 1000E) with data collection using Gamry Framework software and data analysis using Gamry Anal Chem and Z-view softwares. Potentiodynamic polarisations were recorded in the range of ±250mV vs. open circuit potential (OCP) with a scan rate of 0.1mV/s. AC impedance involved the application of 20mV excitation at OCP over the frequency range 10^6 to 0.1 Hz. The corrosion rate was calculated by analysis according to a simple equivalent circuit.

Results and Discussion

The AC impedance spectra possess a single time constant and a Warburg diffusion impedance which is apparent at the lower frequency limit, similar to what is observed with conventional macroelectrode (Figure 2).

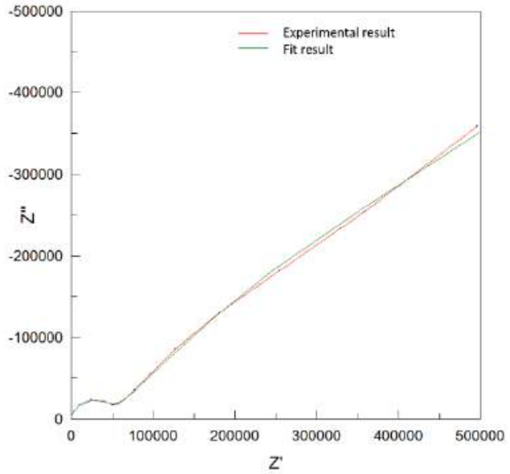

Figure 2 Impedance spectra of uranium microelectode in aqueous solutions of pH 7.

The results of dynamic polarisation tests show that increasing the electrolyte pH results in a anodic shift of the E_{corr} value and an increase in the corrosion current density (Figure 3). In addition, the polarisation curves exhibit current densities five orders of magnitude higher than those obtained using conventional macroelectrodes in similar conditions (similar pH). This shows how the use of microelectrodes can effectively be used to study the localized corrosion behaviour in uranium.

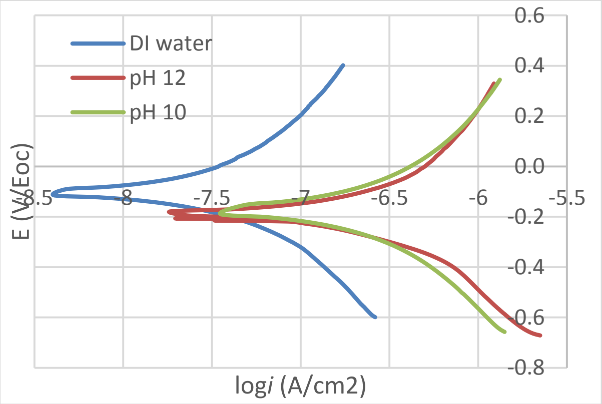

Figure 2 Polarisation curves of uranium microelectrodes in aqueous solutions of pH 7 (DI water), 10 and 12.

Ongoing and future Work

Building a portable ultra-high vacuum (UHV) chamber for active samples

We are actually working on the design of a portable sample storage device with ultra-high vacuum and inert gas overpressure and suitcase capabilities. The objective is to investigate the corrosion mechanisms of radiolytic dissolution and hydride formation in spent nuclear fuels. Therefore it is of paramount importance to isolate the samples from the ambient before we get them characterized using synchrotron and neutron experiments. This will allow us to detect changes in the surface structure of the fuels at the Angstrom level and the strong sensitivity of neutrons to the presence of hydrogen, means that we are able to detect the formation of uranium hydride in the nanometre regime as it is first initiated, without the parasitic contribution of contaminant from the ambient.

Radiation Driven Reactions at the Surface of Uranium Dioxide

S. Rennie*[1], J. E Darnbrough[1], L. Costelle[1], E. Lawrence Bright[1], J. Sutcliffe[1], I. Griffiths[1], J. Rawle[2], R. Gwilliam[3], C. Jeynes[3], T. B. Scott[1], and G. H. Lander[4], R. S. Springell[1]
*Email: Sophie.rennie@bristol.ac.uk
[1] Interface Analysis Centre, University of Bristol (Bristol BS2 8BS, UK)
[2] Diamond Light Source (Harwell Science and Innovation Campus, Harwell OX11 0DE, UK)
[3] Nodus Lab, University of Surrey (Guildford, Surrey, GU2 7XH, UK)
[4] European Commission, JRC, Institute for Transuranium Elements (Postfach 2340, D-76125 Karlsruhe, Germany)

Abstract

In order to ensure resilient, long-term storage for nuclear material it is critical to have a thorough understanding of the reactions occurring at the surface of stored uranium oxides. This project aims to explore this topic in further detail through studying radiation induced oxidative *dissolution of uranium dioxide thin films*. Building on our previously developed experimental technique, we have expanded upon our initial measurements to investigate the effect of crystal orientation on the dissolution of UO_2. These measurements were conducted on the I07 beamline at the Diamond Light Source in March 2016 and a full analysis of the experimental results is currently underway. However, preliminary analysis has shown crystal orientation to significantly affect the rate of UO_2 dissolution, with the [111] film appearing far more resilient to radiation induced corrosion than either the [001] or [110] orientations.

Introduction

With the ever increasing demand for energy and the need for a more sustainable future, providing improved energy solutions has become a pressing challenge for nations across the world [1]. With nuclear power presenting a reliable, carbon-free solution, many countries have chosen to invest heavily in nuclear technology, resulting in high level waste (HLW) increasing globally, by around 12,000 tonnes each year [2]. With uranium oxides comprising the vast majority of HLW generated by modern society, it is critical that a safe and efficient storage strategy is developed for these materials. Despite the recent advancement in HLW containment systems, eventual failure will expose the surface of nuclear material to reactive environments, which may lead to degradation and corrosion of the fuel surface, releasing harmful radionuclides in to the environment [3]. It is therefore crucial that we acquire a fundamental understanding of the reactions occurring within a failed storage environment in order to develop accurate, long term corrosion models of nuclear waste.

Radiation Induced Oxidative Dissolution

Previous studies suggest that within a failed nuclear storage container, the corrosion of UO_2 is primarily driven by oxidative dissolution [4]. This is where the surface of UO_2 is oxidised to give the readily soluble U^{6+} ion, resulting in the dissolution of the fuel matrix [4]. While the groundwater present within a failed storage container does not comprise the oxidation products (H_2O_2, $OH^\bullet$) required to drive this reaction, they are instead generated via water radiolysis, initiated by residual radiation fields of the stored fuel [5-6], Fig. 1.

The focus of this research will therefore be to investigate the impact of oxidative dissolution on the surface of uranium oxides. The key aim is to expose uranium dioxide samples to a simulated failed storage environment in order to monitor the changes in surface morphology of UO_2.

Experimental Methodology

A Thin Film Approach

Spent nuclear fuel (SNF) possesses a great deal of complexity, including defects, He bubbles, microscopic cracking, and fission daughter products. When investigating the oxidative dissolution of SNF, the individual effects of these complexities become difficult to isolate, and thus highly complicated to analyse.

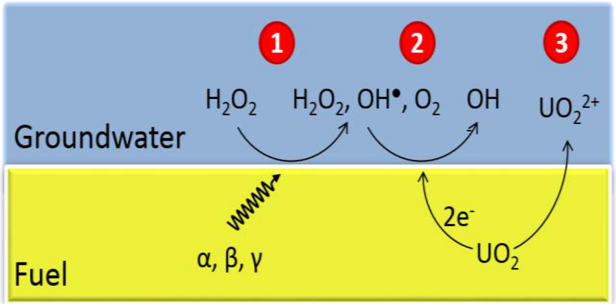

Figure 1: *Oxidative dissolution of UO_2 via radiolysis of groundwater in a failed geological disposal facility. 1) Radiolytic production of oxidants via interaction of groundwater with residual radiation fields. 2) Cathodic reduction of oxidants. 3) Anodic oxidation and dissolution of the UO_2 fuel.*

This project therefore aims to remove much of this complexity in order to first understand the corrosion mechanism for an idealised UO_2 surface, before systematically increasing material complexity. To achieve this, idealised epitaxial UO_2 thin films have been grown via Reactive DC Magnetron Sputtering at the University of Bristol. To investigate the reactions taking place at film/water interface in the presence of strong radiation fields, we have developed an experimental technique that induces dissolution of a UO_2 surface using an intense beam of x-rays, mimicking the radiation fields found at the surface of spent nuclear fuel. Initial experiments were carried out using an [001] oriented, single crystal UO_2 thin film, where synchrotron diffraction was used to measure variations in the film morphology at the Angstrom length-scale. This work has been published in Faraday Discussions [7] and will be summarised in this report.

In March 2016 we conducted a further synchrotron experiment to expand on these first measurements. Here we investigated the effect of two further variables on the dissolution of UO_2: crystal orientation and fission product damage. While the analysis from these experiments is still in progress, here we will present the preliminary findings on the effect of crystal orientation on radiation induced UO_2 dissolution.

Simulating Corrosion with Synchrotron Radiation

To investigate the effect of oxidative dissolution on the surface morphology of uranium dioxide, a series of synchrotron x-ray diffraction experiments have been conducted at both BM28, ESRF and I07, Diamond Light Source beamlines.

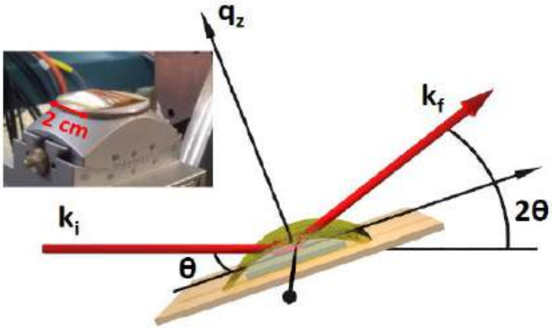

Figure 2: *Schematic of the experimental set-up used at the Diamond Light Source, where k_i and k_f are the incident and exit wavevectors, ϑ the angle of incidence with respect to the detector 2ϑ and q_z the wavevector momentum transfer. The thin layer surface tension cell (insert) holds a fixed volume of water over the sample during x-ray irradiation.*

To simulate the oxidising environment required for oxidative dissolution to occur within a failed geological disposal facility, a layer of milliQ water was maintained across the surface of the UO_2 film using a thin layer surface tension cell, Fig 3. The film, entirely covered by the water, was then exposed to a 17.116keV x-ray beam in order to radiolyse the water and produce the oxidation products (H_2O_2, $OH^\bullet$) required for the dissolution process to occur. X-ray Reflectivity (XRR) and high angle x-ray diffraction were then used to probe the changes in surface morphology of the UO_2 film after exposure to milliQ water in the presence of a strong radiation field.

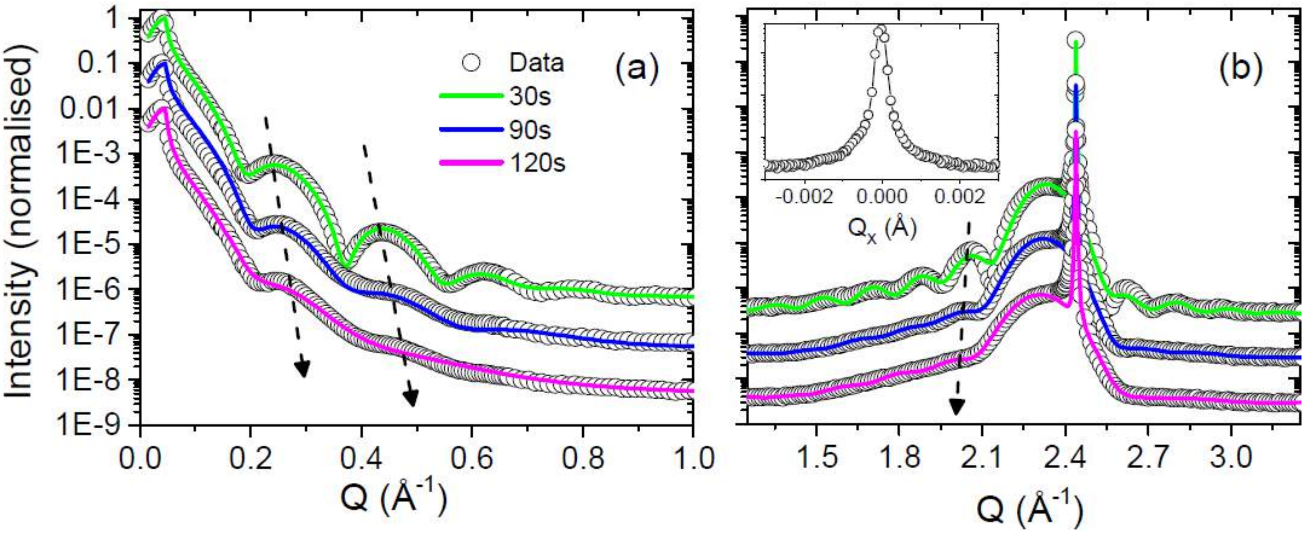

Figure 3: *Panel (a) shows x-ray reflectivity and panel (b) shows high angle diffraction data, measured at exposure times of 30 s, 90 s and 120 s, the experimental data are represented by the open black circles and the fitted calculations by the solid green, blue and magenta lines, respectively. The insert of panel (b) shows the rocking curve of the (002) Bragg peak for the 30 s exposure. The dashed black arrows indicate an increase in fringe separation as a function of exposure time, which suggests a concomitant loss of material.*

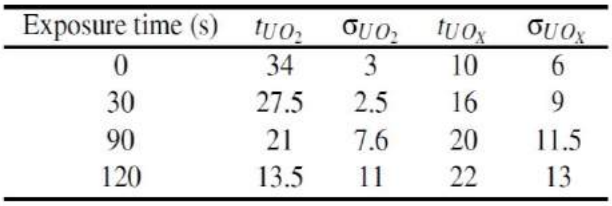

Exposure time (s)	t_{UO_2}	σ_{UO_2}	t_{UO_X}	σ_{UO_X}
0	34	3	10	6
30	27.5	2.5	16	9
90	21	7.6	20	11.5
120	13.5	11	22	13

Table 1: *Parameters used in the fitted calculations to model the experimental reflectivity and high angle diffraction data. All values are in Å, where* t_{UO2} *is the thickness of the* UO_2 *and* σ_{UO2} *is the root mean squared roughness,* t_{UOX} *and* σ_{UOX} *are the thicknesses and roughnesses of the top layer of complex oxide, respectively.*

Results and Discussion

Published Results

Initial experiments carried out at synchrotron beamlines BM28, ESRF and I07, Diamond Light Source, using single crystal [001] oriented UO_2 thin films were used to study the effect of radiolysis at the fuel interface. As shown in Fig. 3, a combination of X-ray Reflectivity (XRR) and high angle x-ray diffraction were used to probe changes in the thickness, roughness, electron density, crystallinity and dissolution of the film on exposure to milliQ water radiolysed by the x-ray beam for a series of exposure times. Data are presented for three exposure times, 30 s (green), 90 s (blue) and 120 s (magenta), where the data are shown as open black circles and fitted calculations are represented by solid lines. The XRR data was fitted using the Parratt recursion method [8], using the GENX computer program. These fitted calculations are based on a structural model of the UO_2 film that consists of a layer of crystalline UO_2 with the standard bulk density and a surface layer of reduced electron density, labelled UO_X.

The fitting parameters, including layer roughnesses are summarised in Table 1. While this experiment was successful in providing a detailed insight into the oxidative dissolution of the ideal UO_2 single crystal surface [7], further work is required to investigate the precise mechanism that is responsible for the observed corrosion.

Ongoing Work

The Effect of Crystal Orientation

The effect of crystal orientation on radiolysis induced UO_2 dissolution was investigated by applying the previously described experimental technique for [001], [110] and [111] oriented UO_2 thin films. XRR and XRD measurements were carried out for following exposure times: 30s, 60s, 90s, 120s, 150s, 210s, 270s and 330s. While a full analysis of these data sets is still in progress Fig. 4 shows a comparison of the XRR measurements before corrosion and after an exposure time of 330s, for each film orientation. From these scans alone it is clear that there is a crystal orientation effect, with the [111] oriented UO_2 being significantly more resilient to radiation induced surface corrosion, with only 7.8 Å of film being corroded over the course of 330s, compared with 42.9 Å and 51.5 Å for the [110] and [001]

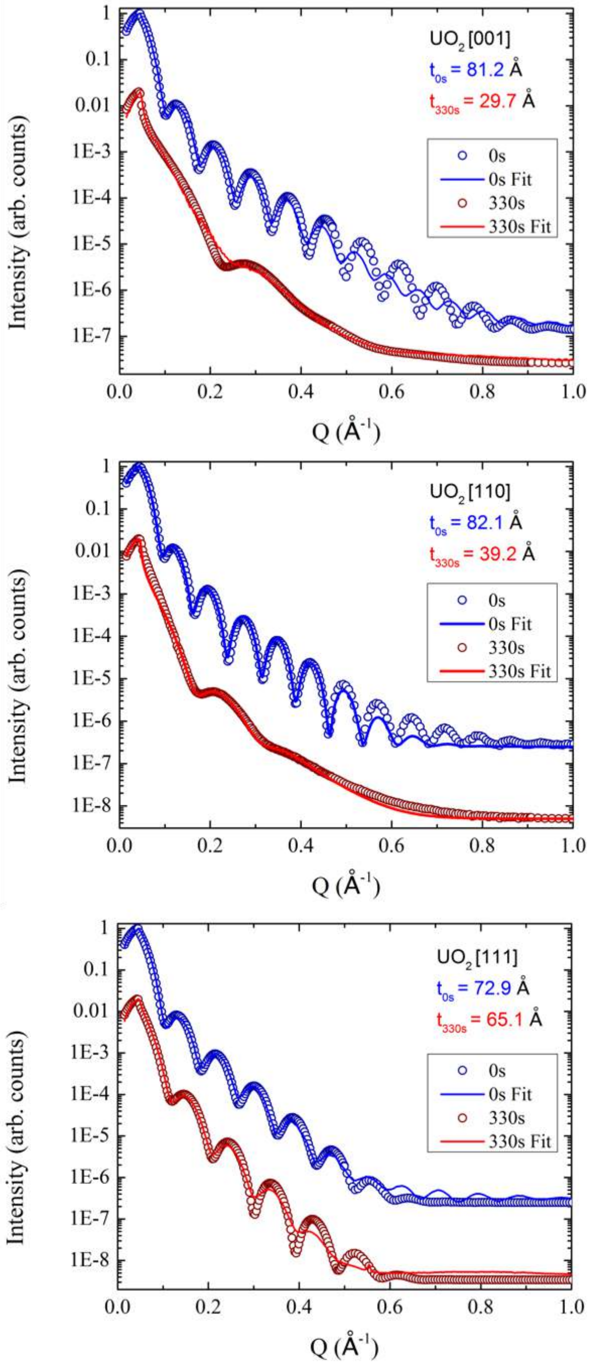

Figure 4: *XRR profile comparison of 0s and 330s corrosion of [001], [110] and [111] oriented* UO_2 *thin films, where t is the film thickness. Corrosion rates differ between each of the orientations, with the [111] oriented film being significantly more resistant to radiolysis induced dissolution than the [001] and [110] orientations.*

orientations. Further analysis for each of the measured exposure times will enable us to better understand how the dissolution reaction progresses for each orientation, and further elucidate the reasons for the observed differences in rates of dissolution.

Conclusions and Future Work

Building on our previous synchrotron experiments, epitaxial UO_2 thin films have been used to systematically investigate the impact of crystal orientation and fission product damage on the radiation induced dissolution of UO_2 surfaces. This approach enables us to study the complexities found within spent nuclear fuel in isolation, which is particularly advantageous for the validation of long term storage models of nuclear materials.

Initial results from the investigation into crystal orientation demonstrate that the rate of dissolution differs significantly between the principle UO_2 directions. The [111] oriented films appear to be far more resilient to the dissolution process, than both the [110] and [001] orientations. However further experimental analysis is required to understand the progression of the dissolution reaction in further detail, in order to elucidate the reason for the observed differences in dissolution rates.

Measurements were also carried out to investigate the effect of fission product damage on UO_2 dissolution. This was achieved using UO_2 thin films that had been implanted with Xe and Cs ions at the Surrey Ion Beam Centre. Analysis of these results is currently being performed.

Acknowledgements

Sophie Rennie would like to thank the AWE and EPSRC for providing the PhD funding that supports this research. The authors would also like to thank the EPSRC for funding the DISTINCTIVE consortium grant on nuclear waste.

References

[1] U. Strandberg and M. Andren, Journal of Risk Research 12 (2009) 879-895.

[2] World Nuclear Association, Available at: http://www.worldnuclear.org/info/inf103.html [Acessed: January 2013].

[3] D. W. Shoesmith, Journal of Nuclear Materials 282 (2000) 1-31.

[4] D. W. Shoesmith, Nuclear Waste Management Organization, (2007).

[5] O. Roth, PhD Thesis, University of Stockholm (2008).

[6] M. G. Bailey, L. H. Johnson and D. W. Shoesmith, Corrosion Science 25 (1985) 233-238.

[7] R. S. Springell et al., Faraday Discussions (2015) DOI: 10.1039/C4FD00254G.

[8] L. G. Parratt, Phys. Rev., 1954, 95, 359.

Oxidation of Carbides Including Carbide Nuclear Fuels

C. Gasparrini*[1], R. Podor[2], D. Horlait[1,3], D. Shepherd[4], S. May[4], P. Durham[4], S. Everall[4], D. Coppersthwaite[4] and W.E. Lee[1]

*Correspondence: c.gasparrini14@imperial.ac.uk

[1] Centre for Nuclear Engineering and Dpt. Materials, Imperial College London, Exhibition Road, SW7 2AZ, London, UK
[2] Institut de Chimie Séparative de Marcoule (ICSM), Bagnols-sur-Cèze, France
[3] CNRS, Centre d'Etudes Nucléaires de Bordeaux-Gradignan, UMR 5797, Chemin du Solarium, 33175 Gradignan, France
[4] National Nuclear Laboratory Preston, Preston, PR4 0XJ, Lancashire, UK

Abstract

Oxidation of depleted uranium carbide (UC) fuel pellets from Dounreay was investigated using isothermal oxidation of UC pellet fragments crushed in air atmosphere and inert atmosphere in a TGA/DSC for heat of combustion evaluation. Oxidations on fragments performed in a muffle furnace from 873-1173 K were used to investigate the influence of time and temperature on the final oxide product characteristics: conversion, specific surface area (SSA) and oxide stoichiometry and morphology. Preliminary results show that, for a given time, oxidation performed at 873K gives greater SSA and conversion than when higher temperatures are used.

Prior to this work, a preliminary study of oxidation of dense hot pressed ZrC specimens was performed from 1073 – 1473 K. Oxidation in furnaces was performed for kinetics investigations and characterisation of the interface between ZrC/ZrO_2. *In situ* analysis performed on ZrC with an HT-ESEM was used to examine the influence of crack propagation on the Maltese Cross shape development of the oxide.

Introduction

Uranium carbide[1,2] (UC) and mixed uranium plutonium carbide[3,4] (U,Pu)C have the potential to be used in the nuclear industry as nuclear fuels for Generation IV fuel reactors thanks to their higher metal atom density and better thermal conductivity when compared to the most common mixed oxide fuels[4,5]. While these carbides offer improved properties during use, at the end of their fuel cycle they cannot be safely disposed without being conditioned into a suitable oxide wasteform as they are reactive and pyrophoric[6]. The aim of this work is to study the oxidation of depleted uranium carbide fuels that have been stored for several decades at the Dounreay site, Scotland, and to convert them into a suitable oxide wasteform that meets repository specifications (specific surface area (SSA), conversion and carbon content). Experimental work has been performed on depleted UC crushed pellets in the National Nuclear Laboratory (NNL) facilities in Preston, UK. The main parameters investigated during this oxidation study from 873 – 1173 K are the influence of temperature and time on the oxide product characteristics (oxide morphology, SSA, conversion and carbon content). Heat of combustion from UC pellets crushed in air or inert atmosphere has also been investigated.

Before getting access to the NNL nuclear site preliminary work was performed on a non active carbide material, zirconium carbide (ZrC), at Imperial College, Department of Materials. This carbide material has potential to be used in the nuclear industry as an inert matrix in carbide fuels or as a structural component in tristructural-isotropic (TRISO)[7,8] fuel particles for Generation IV fuels reactors. Advantageous properties of ZrC include high melting point (around 3700 K[9]), and high thermal conductivity (20 $Wm^{-1}K^{-1}$ at 300 K[10]). Oxidation studies were performed on dense hot pressed specimens of ZrC from 1073-1473 K for kinetics analysis and characterization of the ZrC/ZrO_2 interface on samples cross sections. *In situ* oxidation was performed with a state-of-the-art characterisation technique: high-temperature environmental scanning electron microscopy (HT-ESEM) in collaboration with the Marcoule Institute of Separative Chemistry, France. The *in situ* study was performed to investigate the mechanism of formation of the typical Maltese cross[11] morphology of the oxide.

Methodology Details

Uranium Carbide

Oxidation studies on depleted UC were carried out by TGA/DSC-MS on fragments of about 50 mg in weight crushed in air atmosphere or inert atmosphere.

Oxidation on UC fragments of about 1 g in weight were performed in a muffle furnace from 873 – 1173 K in air atmosphere. The initial material and the oxide product were thoroughly characterised using SEM-EDX, XRD and BET.

Zirconium Carbide

Specimens of ZrC were cut from bulk discs produced by hot pressing commercial ZrC powder (Grade B, Starck, Germany) by electrical discharge machining method. After density characterisation, 1cm side cubic specimens were oxidised in a furnace with air atmosphere from 1073-1473 K. Cuboids specimens with size 4×4×0.5 mm^3 were oxidised in a HT-ESEM at 1073 K in a 2mbar oxygen atmosphere. Characterisation on partly oxidised sample cross sections was performed via SEM and TEM.

Results and Discussion

Uranium Carbide

Temperature has a great influence on U_3O_8 oxide morphology (evaluated both via naked eye on the oxide product and via SE images, Figure 1), SSA and conversion. Oxidation performed at lowest temperature used in this study, 873 K, gave the highest value of SSA.

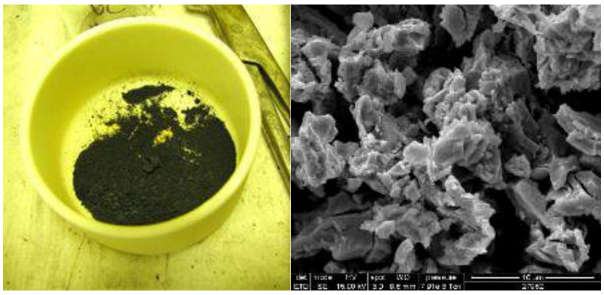

Fig 1. Photograph of a UC specimen oxidized at 873 K for 4h (left) and SEI of the U_3O_8 oxidized product: details of oxide morphology

Zirconium Carbide

The oxide layer growth on ZrC assumes a particular shape, as reported for other carbides of the group IV, V and VI of the transition metals, the so called Maltese cross. *In situ* investigations were performed on hot pressed ZrC samples in a HT-ESEM by monitoring the surface and edges of the sample. Crack formation and propagation from the corners to the inner unoxidised carbide core plays a major role in the formation of this Maltese cross (see Figure 2).

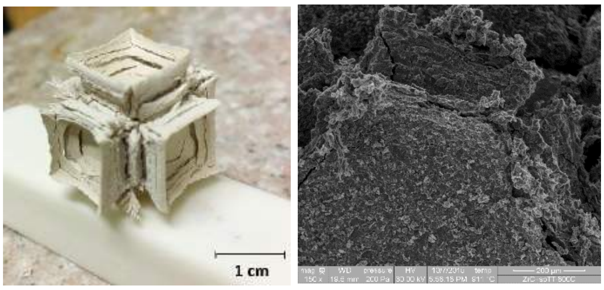

Fig 2. Photograph of a ZrC specimen oxidized at 1273 K for 4h (left) and SEI of ZrC specimen oxidized for 300 min at 1073 K in a 2 mbar oxygen atmosphere in a HT-ESEM (right): details of crack formation at the corners and propagation towards the inner carbide core

Conclusions and Future Work

The project aim is to give industry information about an optimized UC conditioning process. Preliminary results show that oxidation performed on UC fragments in air at low temperatures (873 K) gives highest SSA. Oxidation performed at 1173 K for different times shows that sintering of the oxide occurs as the SSA decreases by increasing the reaction time. Investigation of oxide conversion and remnant carbon left content needs to be performed. Specifications from industry are needed in order to tailor this oxidation experimental study to meet requirements for a suitable oxide wasteform.

The formation of the Maltese Cross shape of the oxide during ZrC oxidation was investigated by an *in situ* technique: HT-ESEM. Its mechanism of formation comprises of three steps: delamination of edges – crack formation at corners – microcracks propagation and debonding of the interface. ZrC/ZrO_2 interface characterisation was also part of this study and was performed by TEM, HRTEM and FIB-SIMS.

Understanding of the oxidation of a mixed carbide material (U,X)C (with X=Ce, Zr, Pu) will give invaluable data on the oxidation process used in the industry as a reprocessing step or as a conditioning step prior disposal for next generation mixed carbide nuclear fuels.

Acknowledgements

We thank the EPSRC DISTINCTIVE (Decommissioning, Immobilisation and Storage soluTIons for NuClear wasTe InVEntories) Consortium for their financial support of this project (EPSRC Industrial Case Award EP/M507428/1 grant and the DISTINCTIVE EP/L014041/1 grant).

References

1. Berthinier, C., Rado, C., Dugne, O., Cabie, M., Chatillon, C., Boichot, R. & Blanquet, E. Experimental kinetic study of oxidation of

uranium monocarbide powders under controlled oxygen partial pressures below 230°C. *J. Nucl. Mater.* **432,** 505–519 (2013).

2. Berthinier, C., Coullomb, S., Rado, C., Blanquet, E., Boichot, R. & Chatillon, C. Experimental study of uranium carbide pyrophoricity. *Powder Technol.* **208,** 312–317 (2011).

3. Duguay, C. & Pelloquin, G. Fabrication of mixed uranium–plutonium carbide fuel pellets with a low oxygen content and an open-pore microstructure. *J. Eur. Ceram. Soc.* **35,** 3977–3984 (2015).

4. Mazaudier, F., Tamani, C., Galerie, a. & Marc, Y. On the oxidation of (U,Pu)C fuel: Experimental and kinetic aspects, practical issues. *J. Nucl. Mater.* **406,** 277–284 (2010).

5. Rodriguez, P. Mixed plutonium-uranium carbide fuel in fast breeder test reactor. *Bull. Mater. Sci* **22,** 215–220 (1999).

6. Dell, M. & Wheeler, V. J. The ignition of uranium mononitride and uranium monocarbide in oxygen. *J. Nucl. Mater.* **21,** 328–336 (1966).

7. Lee, W. E., Gilbert, M., Murphy, S. T. & Grimes, R. W. Opportunities for advanced ceramics and composites in the nuclear sector. *J. Am. Ceram. Soc.* **96,** 2005–2030 (2013).

8. Minato, K., Ogawa, T., Fukuda, K., Nabielek, H., Sekino, H., Nozawa, Y. & Takahashi, I. Fission product release from Zrc-coated fuel particles during postirradiation heating at 1600 C. *J. Nucl. Mater.* **224,** 85–92 (1995).

9. Jackson, H. F., Jayaseelan, D. D., Manara, D., Casoni, C. P. & Lee, W. E. Laser melting of zirconium carbide: determination of phase transitions in refractory ceramic systems. *J. Am. Ceram. Soc.* **94,** 3561–3569 (2011).

10. Jackson, H. F. & Lee, W. E. Properties and characteristics of ZrC, book section 2.13. *Comprehensive Nuclear Materials - Volume 2* (2012). doi:10.1016/B978-0-08-056033-5.00085-9

11. Opila, E. J. & Jacobson, N. S. in *Ceramics Science and Technology : Volume 4 - Applications* (Wiley).

The Behaviour of Spent Nuclear Fuel in Wet Storage

Elizabeth Howett[1], Colin Boxall*[1], and David Hambley[2]

*Correspondence: c.boxall@lancaster.ac.uk

[1] *Engineering Department, Lancaster University, Lancaster LA1 4YW*
[2] *National Nuclear Laboratory, Central Laboratory, Seascale, Cumbria CA20 2PG*

Abstract

The project aims to investigate the behaviour of Spent Nuclear Fuel (SNF) in interim storage, specifically AGR fuel in storage ponds at Sellafield. Corrosion behaviour will be studied in order to assess the validity of extended storage periods. Studies will be carried out on UO_2, SIMFUEL and AGR cladding samples separately and in binary systems. Once these initial experiments have been completed, analogous experiments will be carried out on real spent AGR fuel. To date studies have been carried out on the corrosion behaviour of sensitised and unsensitised stainless steel cladding and cladding analogue samples in simulant pond water with varying temperature, chloride concentration and pH.

Introduction

The Thermal Oxide Reprocessing Plant (THORP) at Sellafield is due to close in 2018. Future un-reprocessed spent nuclear fuel (SNF) will be sent to a GDF (geological disposal facility) although this is currently not expected to be available for receipt of SNF before 2075. Between THORP closing and the GDF opening, AGR SNF will be held in interim wet storage in ponds containing demineralised water dosed with NaOH (to pH≈11.4 at 24°C) which acts as a corrosion inhibitor, at sites such as Sellafield. Current storage periods are typically less than 10 years, although this may extend to as long as 100 years after THORP closes. It therefore necessary to determine if the SNF can be stored safely in the same manner without significant degradation of the SNF over this time scale.

AGR cladding can be breached due to inter-granular Stress Corrosion Cracking (igSCC) or damaged during dismantling. The former may be at least in-part facilitated by the steel cladding becoming sensitised to corrosion processes due to its in-reactor irradiation history. If the cladding is breached, the fuel itself can also become exposed. Evolution of both the steel & UO_2 surfaces upon consequent exposure to pond water can be considered as corrosion processes and so conveniently studied by electrochemical methods.

In order to accommodate all future AGR SNF, a new racking system for the Thorp receipt and Storage pond has been proposed. This new storage arrangement will mean that fuel will be packed closer together, causing a rise in temperature of the fuel and the pond water within the storage racks compared to that which would be expected in the current storage arrangement. Current assessments indicate that rack water temperature could be up to approximately 60°C with an average of around 45°C. For this section of the project the corrosion behaviour of both sensitised and unsensitised samples is studied by linear sweep voltammetry to assess short time corrosion susceptibility of these materials at existing and proposed pond temperatures as well as a pond maloperation temperature of 90°C.

Methodology Details

A series of linear sweep voltammetry (LSV) experiments were carried out on several samples of unsensitised and sensitised 20/25/Nb SS (AGR cladding) in pond water simulant with varying temperature. Figure 1 shows the experimental set-up, where CE is the counter electrode (platinum mesh), WE is the working electrode (the SS sample) and RE is the reference electrode (Ag/AgCl), the circuit here represents the potentiostat. The potential was swept from -0.8V to 1.6V in most cases, some experiments started at the open circuit potential of the sample. The scan rate was 10mV/s for the majority of the experiments.

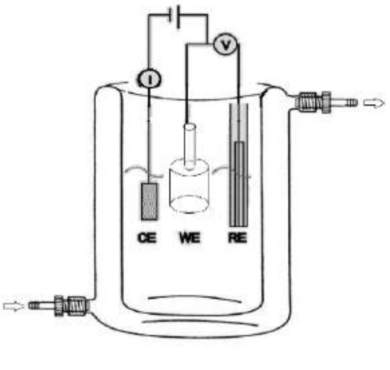

Figure 1: Experimental set-up for voltammetry

Results and Discussion

In the first instance experiments were carried out on unsensitised 20/25/Nb SS to show the effect of temperature on the corrosion behaviour on time scales typical of LSV experiments. Figure 2 shows a plot of tafel plot at four temperatures (room temperature, 45ºC, 60ºC and 90ºC) and a plot of the corrosion and potential for the onset of transpassivity at each of these temperatures.

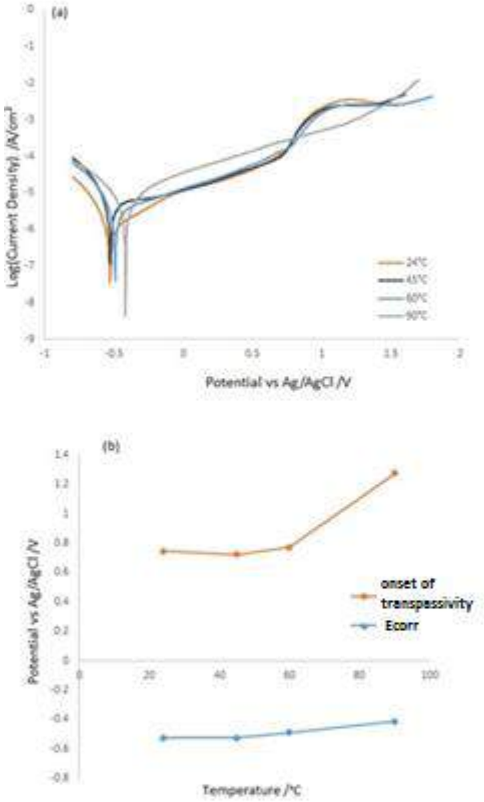

Figure 2: Plot of the effect of increasing temperature on the corrosion behaviour of unsensitised 20/25/Nb SS in simulant pond water, pH≈11.4 (a) and from this graph the change in E_{corr} and onset of transpassivity with temperature can be determined, a plot of which is seen here (b).

E_{corr} and potential of the onset of transpassive behaviour remain separated by at least 1.3V in the temperature range 20-90°C. Therefore in the case of unsensitised 20/25/Nb it appears that, on the timescale of the LSV experiments conducted here, there is no localised pitting or crevice corrosion threat at any of the temperatures studied.

Similar experiments were carried out on heat treated 20/25/Nb SS, Figure3. From these it was found that the sample heated at 1150°C for half an hour then aged at 600°C for 48hours showed enhanced susceptibility to transpassive corrosion behaviour at 90ºC compared to non-heat treated samples, demonstrated by comparing the tafel plots of the heat treated sample to those of unsensitised 20/25/Nb SS, suggesting that the heat treated samples have been sensitised at least in part i.e. the Cr concentration at the grain boundary has been depleted to less than 12%.

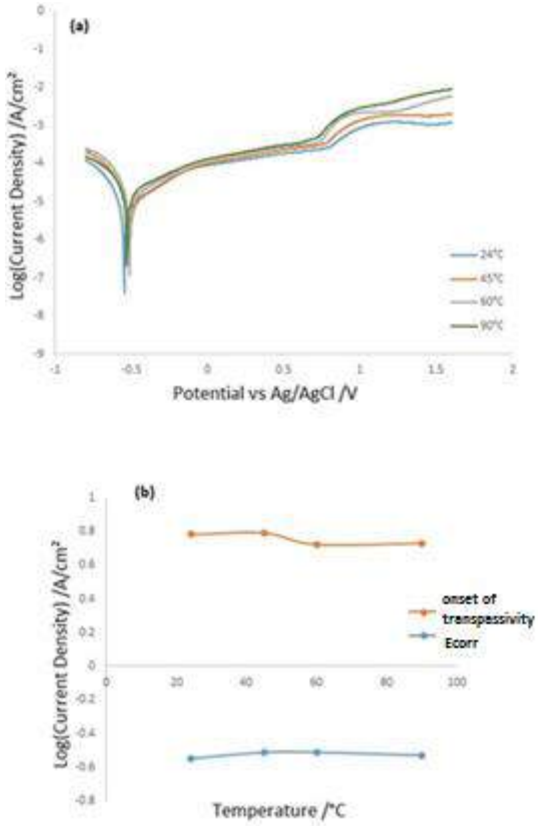

Figure 3: Effect of temperature change on 20/25/Nb SS (heated at 1150°C for half an hour and then at 600°C for 48hours) in simulant pond water, pH≈11.4 (a) and from this graph the change in E_{corr} and onset of transpassivity with temperature can be determined, a plot of which is seen here (b).

Increasing the temperature of the simulant pond water (pH≈11.4) below 90ºC causes only minor changes in the general electrochemical behaviour of the sensitised 20/25/Nb, again Figure 3. Taken as a whole, the data of Figure 3 show that, over the timescale of a typical LSV experiment, there is no threat of in-pond localised pitting or crevice corrosion for the heat treated 20/25/Nb samples at any of the temperatures studied here – despite the apparent sensitisation alluded to above.

In the event of a rise in chloride concentration in the ponds, it is necessary to investigate the effect on [Cl^-] on the corrosion behaviour of sensitised 20/25/Nb SS. The tafel plots obtained for varying concentration along with a graph of the corrosion and breakdown potentials can be seen in Figure 4.

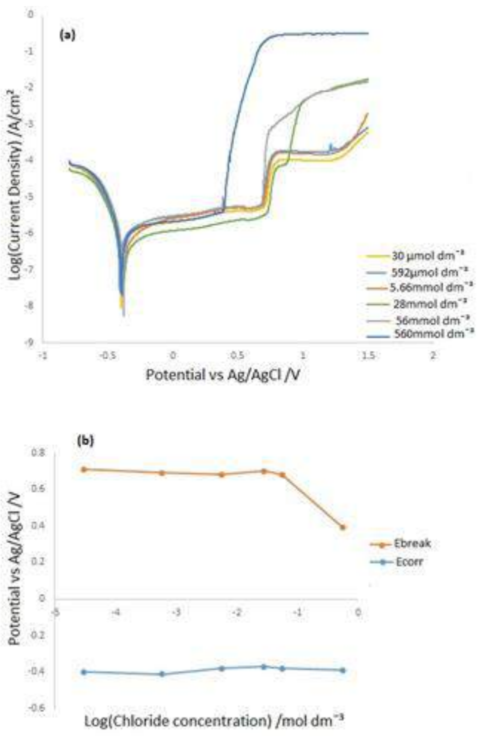

Figure 4: 20/25/Nb (heated at 1150°C for a half hour then 48hours at 600°C) in pond water dosed to pH≈11.4 and then the chloride concentration was increased.

Figure 4 shows a secondary process (proposed to be derived from hexachloroferric electrochemistry) occurring in the post transpassive region, the onset of which appears to shift in the cathodic direction with an increase in chloride concentration.

Experiments were also carried out to investigate the effect of pH on the corrosion behaviour of heat treated 20/25/Nb SS., the results of which can be seen in Figure 5. At pH>9.2 at 24°C, the onset of transpassive behaviour can be seen at E > ~0.75 V. At pH<9.2, the system is passive over the potential range studied in these experiments. Results are similar at 90°C but the potential for the onset of transpassivity has decreased.

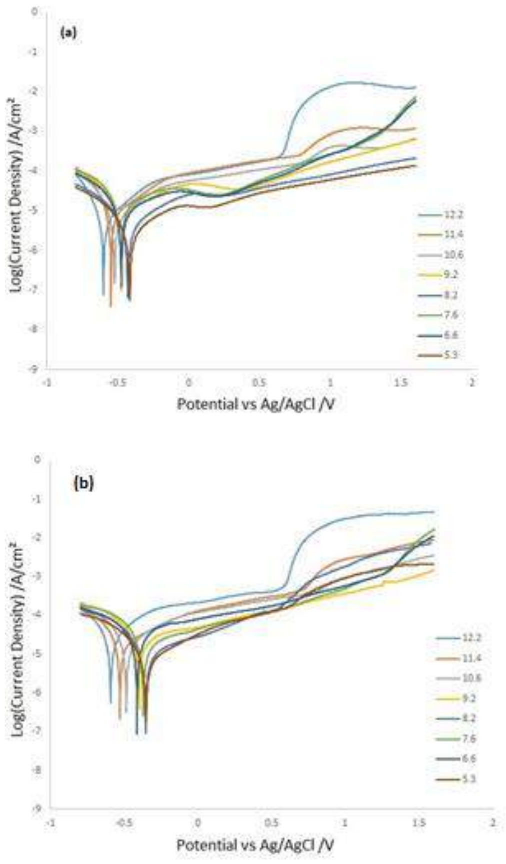

Figure 5: Effect of pH variation on the corrosion behaviour of 20/25/Nb heated at 1150°C for a half hour and then 48hours at 600°C, in simulant pond water at 24°C (a), and 90°C (b).

Conclusions and Future Work

The above studies relate to the corrosion behaviour of unsensitised and simulants for sensitised 20/25/Nb (AGR cladding) stainless steel as a function of pH, temperature and chloride concentration. These tests aim to demonstrate whether a pond water pH of 11.4 at 24°C provides sufficient corrosion protection, if increasing the temperature of the pond water will remove this protection and if in the event of a rise in chloride concentration the steel could be compromised. Intergranular attack in the form of transpassive behaviour is observed on nearly all samples, both sensitised and unsensitised, but typically only under condition of high oxidative stress. Tests at 1ppm Cl^- at 24°C and 45°C at pH≈11.4 indicate an E_{corr}-E_b separation of over a volt indicating that intergranular attack is unlikely under open circuit conditions on the timescale of the experiemnts conducted here. More broadly, the results demonstrate the following with respect to the initiation of corrosion:

- **With respect to pH**: that it is advantageous in terms of minimising corrosion to dose the ponds to pH≈11.4, corrosion potential –

breakdown potential differences are typically over 1V at this pH.

- **With respect to chloride concentration**: that much higher chloride concentrations, e.g. 5.6 mmol dm^{-3}, than those expected in pond water, e.g. 30 µmol dm^{-3}, are necessary to cause significant cathodic movement in breakdown potential and thus the onset of intergranular attack.
- **With respect to temperature**: Generally, there appears to be no localised corrosion threat to fuel cladding as the electrolyte temperature is increased in the range 24°C-90°C assuming that the fuel has not undergone stress corrosion cracking or intergranular attack (during its time in the reactor or during the dismantling process) before submersion in the ponds.

These short duration linear sweep voltammetry experiments provide preliminary indications that dosing pond water to a pH≈11.4, with an expected chloride concentration of ~1ppm, provides corrosion protection at the temperatures studied, 24°C (current conditions), 45°C (projected future pond temperature), 60°C (predicted peak operating conditions) and 90°C (potential maloperations / fault condition). However, in order to gain a more complete assessment of corrosion susceptibility experiments over extended periods of time must be carried out.

Acknowledgements

This work is supported by the National Nuclear Laboratory, Lancaster University and the Lloyd's Register Foundation *via* provision of a PhD studentship. The Lloyd's Register Foundation helps to protect life and property by supporting engineering-related education, public engagement and the application of research.

Transitioning of Spent AGR Fuel from Wet to Dry Storage

James Goode*[1], Bruce Hanson and David Harbottle

*Correspondence: pmjbg@Leeds.ac.uk

[1] *Institute of Particle Science and Engineering, University of Leeds, Leeds, LS2 9JT*

Abstract

Upon removal from a reactor spent AGR fuel (SNF) is placed into water storage to remove decay heat and provide shielding prior to reprocessing. Empirical evidence with long stored fuel suggests that fuel can be stored in caustic dosed ponds for at least 25 years without failures. With the closure of Thorpe and the end of reprocessing the current NDA roadmap has SNF being kept in caustic dosed ponds until 2038 followed by direct disposal to a geological disposal facility in 2075. No decision has yet been made as to how fuel will be stored between 2038 and 2075. One option that is being considered is interim dry storage. This project is investigating whether AGR fuel can be dried suitably for dry storage to be a viable option.

Introduction

The UK government has made the strategic decision to stop spent fuel reprocessing and adopt an open fuel cycle. Empirical evidence has shown that caustic dosing allows fuel to be safely wet stored for at least 25 years and the Thorp receipt and storage pond (TR&S) will be used for the this purpose until 2038. In the long term the fuel will need to be transferred to a geological disposal facility (GDF) however since this is not expected to be available until 2075[1] a decision will need to be made in the future as to how the fuel will be stored during the interim period of approximately 35 years.

One option that has been considered for this is the use of dry storage. Dry storage is being utilised in many countries for the storage of LWR and MTR fuels however little research has been carried out into the dry storage of fuels utilising stainless steel (SS) cladding such as AGR fuel. Consequently considerable work will be required to ensure that a safety case can be made for such work, and the current PhD project intends to begin working in this area.

The work so far has centred around producing specimens for testing. Post storage examination of failed fuel has shown that historic failures during storage have been due to intergranular corrosion (IGC) [and stress corrosion cracking (SCC) 1]. Caustic dosing of ponds has shown that IGC can be prevented by caustic dosing of the pond water to pH 11.4. While the pond water is highly controlled SS is also susceptible to pitting corrosion when chlorides are present.

Water can be present as free water which may be trapped in pores or free on the surface or and bound water which may be chemisorbed or physiosorbed to the surface oxide. Free and untrapped water can be removed with little difficulty by simple evaporation but bound and trapped water may be more difficult.[2]

Preliminary work as part of an MSc project using aluminium samples found that surface oxides had a significant quantity of bound water which could be removed relatively easily by heating.

This initial work is establishing whether the same is true for SS samples or whether the presence of bound water can be essentially ignored.

Methodology Details

Stainless steel samples (SS) were prepared for TGA/DSC analysis as well as SEM/EDX and XPS. Two forms of SS were used; AISI 310 alloy was obtained from Goodfellows Metals Ltd and an unirradiated length of cladding from an AGR fuel pin was obtained from NNL (20/25). These samples were then treated in different ways.

Sample Designation	Treatment
AR	As received samples. No treatment.
HNO_3	Samples boiled in 65% nitric acid with 0.1% Cr(VI) ions to encourage IGC.
NaOH	Samples held in autoclave containing deminarlised water dosed to pH 11.4 with NaOH (to simulate long term pond storage).
$FeCl_3$	Samples held in 6% $FeCl_3$ and 1% HCl for 24 hours to encourage pitting corrosion.

Table 1. SS sample treatments.

Results and Discussion

SEM images of 310 samples (Figure 1) have shown that in the as received state there are differences in the two surfaces of the sheet with grain boundaries being visible on side 2, presumably as a result of the rolling work. These differences are no longer visible following treatment. As expected the HNO3 samples shows clear evidence of IGC resulting in some grain dropping. The FeCl3 sample shows evidence of pits developing.

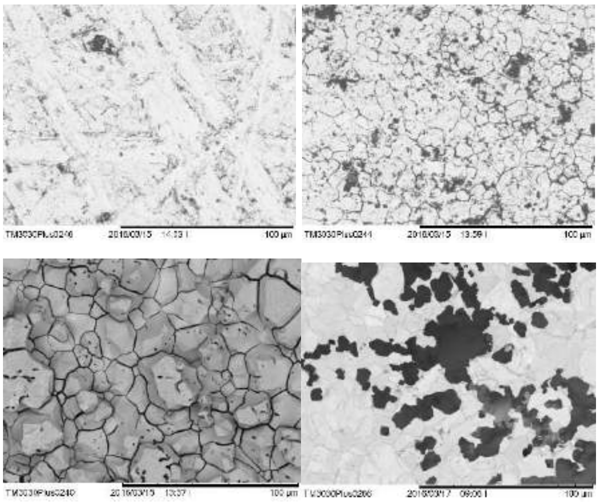

Figure 1. 310 SS samples. Clockwise from top left; AR side 1, AR side 2, HNO3 and FeCl3.

SEM images of the 20/25 samples again shows differences in surfaces for the inside of the fuel pin, the outside of the fuel pin and the area on the top of the rib. Visual examination by eye shows that the inner surface has a matt finish in comparison to the outer surface which can be explained by the rougher finish observed in SEM images.

°

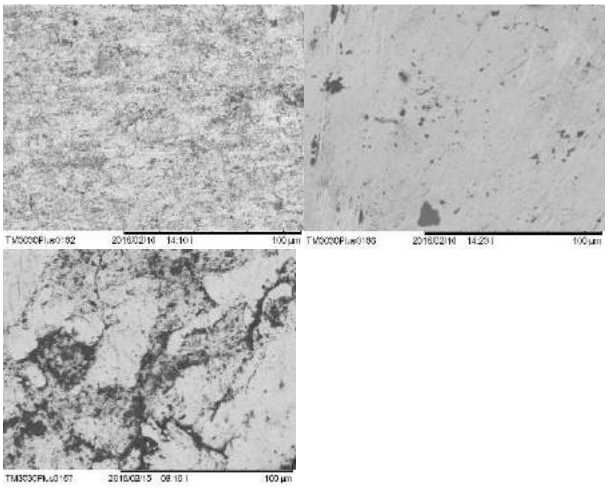

Figure 2. AR 20/25 samples. Clockwise from top left; inner surface, outer surface and top of rib.

Figure 3 shows the 20/25 samples following corrosion in the nitric acid solution. The inner surface and rib top appear to show evidence of IGC which is present on the outer surface. This would suggest that the machining process by which removes material forms the ribs also gives some protection to the material. It also means that in the event of a fuel pin flooding due to a pin hole pins may corrode from the inside out and as such a simple visual inspection may not be sufficient to assess for damage.

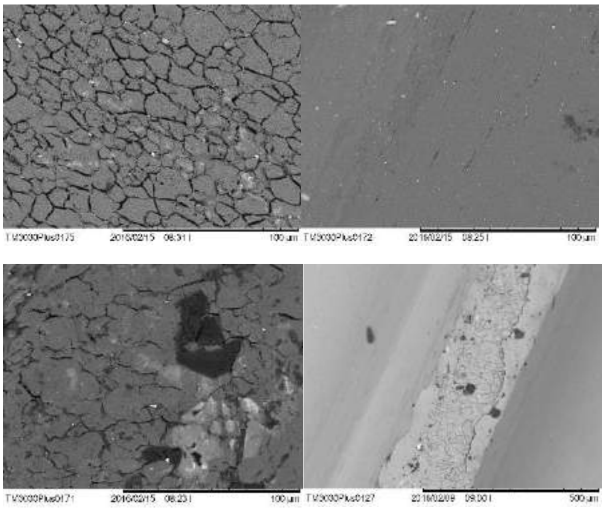

Figure 3. 20/25 HNO3. Inner surface, outer surface, rib top and across the rib top.

Figure 4 shows the TGA/DSC curves for a 310-HNO_3 sample. Run 1 is the first time the sample was heated and run 2 was the same sample heated again approximately 15 hours later. The curves show almost identical behaviour and no sudden mass drop indicative of water loss from drying which would be expected in run 1 when water is most likely to be present. This suggests that there is no significant water retention on the sample surface when samples suffer from IGC.

Similar curves were obtained from all samples tested indicating that bound water is likely to be of little concern for drying spent AGR fuel.

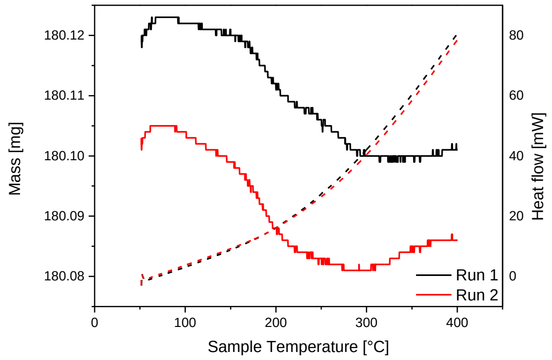

Figure 4. TGA/DSC curves for a 310-HNO3 sample.

Figure 5 shows MS spectra of the off gas from the Run 1 TGA shown above. The TGA was carried out under a nitrogen purge and this explains the overall increase in N and N2 as the chamber was purged after sample insertion. Similarly the nitrogen purge also explains the drop in O, O2 OH and water. No peaks in OH or water are present confirming that there are no low levels of water being given off that are not detected by mass change (an initial heating run was carried our prior to sample tests to flush system after connection of MS to TGA. This showed a significant jump in OH and water as the system was purged indicating that the system is sensitive enough to pick up such peaks).

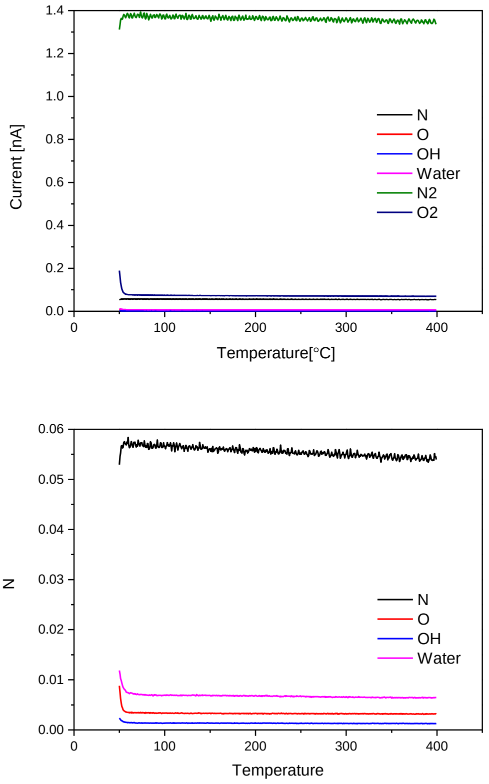

Figure 5. MS curves for off gas from 310-HNO3 sample (top-full plot, bottom zoomed image).

Conclusions and Future Work

The purpose of the work carried out to date was to make an assessment of whether the quantities of bound water on a spent AGR fuel pin are significant enough to be of concern for dry storage and consequently for drying tests. The data obtained so far would suggest that this is not the case. Further XPS work will be carried out to confirm whether there is really any water present and of so in what quantities. The work has however shown that there is a different corrosion behaviour between the inside and outside of the fuel cladding which may well need to be accounted for.

Sample preparation is now concentrating on producing samples of cladding with through cladding SCC so that trapped water can be simulated and these samples will be used drying tests in a drying rig that has been built for this purpose.

Acknowledgements

I would like to thank the EPSRC Grant Number EP/L014041/1 and the DISTINCTIVE consortium for funding my research.

References

1 Kyffin, J. The technical case for interim Storage of AGR fuel and development of a programme of further work, in Manchester, IChemE, 9-11 April.

2 Anon *ASTM C-1553-Standard Guide for Drying Behaviour of SNF*, n.d.

Characterising the Chemical and Physical Properties of the UK's Depleted, Natural and Low-enriched Uranium Stockpile with Regard to the Suitability of Alternative Disposal Routes

M. Druce*[1], M. Horstwood[2], M. Felipe-Sotelo[1], A. Milodowski[2] and D. Read[1]

*Correspondence: M.Druce@lboro.ac.uk

[1] Loughborough University, Epinal Way, Loughborough, LE11 3TU, UK
[2] British Geological Survey, Nicker Hill, Keyworth, Nottingham, NG12 5GG, UK

Abstract

The UK owns an estimated inventory of depleted, natural and low-enriched uranium (DNLEU), including that from military and foreign sources, of around 200,000 tonnes. It is classified as a 'zero-value asset' but might be re-classified as waste in the future and would need to be consigned for disposal. The material is stored in a variety of chemical forms and there is currently a lack of data surrounding the secondary phases that might develop under disposal conditions. This project focuses on identifying the paragenetic sequences of minerals that could be formed under different disposal concepts and gathering the necessary thermodynamic and kinetic data. Depleted uranium oxide (UO_3 and UO_2) pellets and uranium metal will be introduced to static solutions of 95% saturated calcium hydroxide, synthetic seawater and synthetic groundwater under both oxic and anoxic conditions. In addition, uranium oxide pellets will be encapsulated using cement-based grouts and surrounded by synthetic groundwater to simulate groundwater interaction with encapsulated DNLEU. Uranyl silicates such as uranophane and the weeksite group are possible secondary phases giving a uranium solubility on the order of 10^{-6} to 10^{-8} mol dm^{-3} and a dissolution rate in groundwater of approximately 10^{-7} g cm^{-2} day^{-1}, though these estimates require confirmation. The results from this project will improve the experimental database and consequently, the accuracy of safety models that are used to predict the fate of DNLEU on disposal. This will clarify whether DNLEU could be disposed of directly in powdered form or requires encapsulation and whether it should be disposed of within specifically designed vaults or may be used in service and transport tunnels in place of backfill.

Introduction

Depleted, natural and low-enriched uranium is a by-product of the nuclear industry. It is formed through uranium enrichment activities that produce depleted uranium (DU) tails or via the reprocessing of spent fuel to recover uranium so that it can be re-enriched and reused. DNLEU is characterised by its isotopic composition; depleted and natural uranium (NU) compositions are shown in Table 1. Low-enriched uranium (LEU) is defined as uranium enriched to more than 0.72% ^{235}U but less than 20% by mass [1].

Table 1 Isotopic composition of depleted and natural uranium [2]

Isotope	Half-life (years)	% Abundance in Depleted Uranium	% Abundance in Natural Uranium
^{234}U	2.46×10^5	6.00×10^{-4}	5.40×10^{-3}
^{235}U	7.04×10^8	0.20	0.72
^{238}U	4.47×10^9	99.80	99.27

The estimated UK inventory for DNLEU, including that from military and foreign sources, is approximately 200,000 tonnes. This is currently considered a 'zero-value asset' and the Nuclear Decommissioning Authority (NDA) has statutory responsibility for it. However they are exploring the possible inclusion of uranics into the design of the repository in anticipation of it being re-classified as waste. Owing to the volume of DNLEU, this inevitably means that some will need to be disposed of. The predominant chemical form of uranium in the inventory is depleted uranium hexafluoride (UF_6) from enrichment activities. To enable disposal, the UF_6 will be converted to the more geochemically stable triuranium octoxide (U_3O_8). The second most abundant chemical form is uranium trioxide (UO_3) from reprocessing activities. Depleted uranium metal, uranium dioxide (UO_2) and some miscellaneous DNLEU is also present [3].

Re-use options for DNLEU, such as fabricating mixed-oxide (MOx) fuel or down-blending with high-enriched uranium (HEU), have the capacity to utilise large quantities of the DNLEU stockpile. However, it could also be disposed of in a purpose built vault or emplaced in the service and transport tunnels in place of backfill [1]. If either of these options is considered then the wasteform needs to be suitable. The NDA has suggested encapsulation of U_3O_8 in a cementitious grout emplaced in a stainless steel canister [4] since disposal in a powdered form might not be suitable due to the increased risk of inhalation during the operational period. This constraint has since been challenged and options for disposal include powdered U_3O_8, UO_3 or UO_2 in a stainless steel canister [1]. The latter could be encapsulated using a cement-based grout if it is considered appropriate. However, owing to the half-life of uranium (4.5×10^9 years), there is no engineered barrier system that can be guaranteed to contain DNLEU in the long term [1].

In the case of disposal by encapsulation in grout and deposition in a geological disposal facility (GDF), four main areas can be defined within and around the GDF, according their chemical conditions; the near-field, the alkaline disturbed zone, the deeper far-field, and the shallower far-field. The near-field chemical conditions will be dominated by hyper-alkaline cement equilibrated water with little carbonate present and pH 12.5 - 10. Initially, the near-field will be oxidising and as the intruding groundwater equilibrates, a reducing environment will be established with an Eh approaching -800 mV [5]. Secondly, the alkaline disturbed zone is a high pH environment where minerals from the host rock interact with the alkaline plume from the GDF. The deeper far-field host rock will provide a major change in groundwater chemistry as saline waters with a pH of 7 – 9 and maintained reducing conditions with little carbonate interact with the uranium. Finally, the shallower far-field will mean the uranium interacts with fresh groundwater at a pH of 6 – 8 and less reducing, high carbonate conditions [6].

Owing to the chemotoxic and radiotoxic properties of uranium, it is imperative that safety models can accurately describe the fate of DNLEU upon disposal. Experimental thermodynamic and kinetic data are required for both the dissolution of the primary uranium species in the waste as well as the formation of secondary uranium phases under the conditions expected in the GDF. This project focuses on establishing thermodynamic and kinetic data for paragenetic sequences of uranium minerals and characterisation of solubility limiting phases under three potential chemical environments encountered during the evolution of the waste, namely a Ca-rich alkaline solution, groundwater and seawater.

Proposed Methodology

Three solutions will be prepared; a 95% saturated calcium hydroxide, $Ca(OH)_2$, solution will be used as a simulant of intermediate cement pore water at pH 12.5. A synthetic seawater stock will be made up as an analogue for saline groundwater and a fresh groundwater modelled on the composition of the Borrowdale Volcanic basement rock at Sellafield. The seawater and groundwater compositions are given in Table 2.

Table 2 Composition of synthetic seawater based on an American Society for Testing and Materials (ASTM) standard practice [7] and fresh groundwater using the groundwater composition of the Borrowdale Volcanic basement groundwater at Sellafield [8]

Component	Concentration in Synthetic Seawater (mol dm^{-3})	Concentration in Synthetic Fresh Groundwater (mol dm^{-3})
Na	8.40×10^{-4}	5.62×10^{-1}
K	3.76×10^{-5}	9.90×10^{-3}
Ca	1.02×10^{-3}	1.01×10^{-2}
Mg	5.35×10^{-4}	5.34×10^{-2}
Cl	3.90×10^{-3}	5.62×10^{-1}
S_{tot}	4.18×10^{-5}	9.39×10^{-3}
TIC*	2.49×10^{-5}	2.29×10^{-3}
Fe	1.10×10^{-5}	-
Sr	-	1.60×10^{-4}
Si	1.75×10^{-4}	-
Al	2.93×10^{-9}	-
Br	-	8.26×10^{-4}
B	-	7.35×10^{-5}
F	-	5.26×10^{-5}
pH	8	7

*TIC = total inorganic carbon

Under anoxic conditions UO_2 and UO_3 pellets together with U metal will be placed in each solution and stored in a glove box under N_2 atmosphere. Iron strips will be mounted to the sample containers for the $Ca(OH)_2$ and seawater experiments to lower the Eh to between -200 and -600 mV to represent the reducing conditions expected to be established in the repository [5]. In addition, a parallel batch will be established under oxidising conditions exposed to the atmosphere and without the metal iron strips. One aim of these experiments is to determine the rates of dissolution and formation of secondary uranium minerals that form under their respective conditions. This will be determined by analysis of the supernatant using inductively coupled plasma – mass spectrometry (ICP-MS). After 6, 12 and 18 months the solid samples will be removed for thorough mineralogical characterisation using micro X-ray diffraction (µ-XRD), environmental scanning electron microscopy (ESEM), multi-collector (MC)-ICP-MS, particle induced X-ray emission (PIXE) and time-resolved laser fluorescence spectroscopy (TRLFS).

In addition to these experiments there will be cross-comparison between UO_3 and UO_2 pellets encapsulated in cement grouts to determine whether there is comparability in the phases formed. These experiments will also provide a more realistic approach in terms of solid – solution ratio. Two grouts will be used for the encapsulation experiments; pulverised fly ash (PFA):ordinary Portland cement (OPC) (3:1), and granulated ground blast furnace slag (GGBS):OPC (9:1). The encapsulated uranium oxide pellets will then be submerged in a synthetic groundwater for 12 and 18 months. The solutions will be analysed using ICP-MS to determine dissolution rates. At the end of each experiment the blocks will be sectioned and the solid samples analysed to characterise the evolution of the uranium minerals as well as determination of diffusion profiles within the grouts.

Expected Results and Discussion

The uranium waste forms are likely to undergo rapid dissolution and oxidation. They are expected to quickly saturate the pore water in the repository and in turn initiate nucleation and growth of U(VI) mineral phases. At a later stage, the repository environment will decrease in Eh [5]. However, this change in Eh may not be enough to force the reduction of U(VI) to U(IV). Therefore, the bulk of the uranium may still be in the form of U(VI) with some U(IV) [8]. It is expected that uranium mineral paragenesis will follow the systematic route from uranium oxides, through oxy-hydroxides to silicates, including alteration products that are related to the specific groundwater chemistry [9].

Silicates such as uranophane, $Ca(UO_2)_2(SiO_3OH)_2(H_2O)_5$, and the weeksite group, $M_2(UO_2)_2(SiO_5)_3.4H_2O$ where M is a monovalent cation, have been highlighted as possible solubility limiting phases. If the concentration of phosphate is high enough then minerals from the autunite group, hydrated uranyl phosphates, e.g. $Ca(UO_2)_2(PO_4)_2.10\text{-}12H_2O$, could form [6]. Thermodynamic calculations suggest solubility limits for uranyl silicates in the far-field are 10^{-6} to 10^{-8} mol dm^{-3}, and it could be possible for uranium concentrations to reach 10^{-5} mol dm^{-3} in some groundwaters [6]. Kinetic studies report initial uraninite dissolution rates of approximately 10^{-7} g cm^{-2} day^{-1} though after the formation of a passive mineral layer on the uraninite surface, further dissolution could be reduced to around 2×10^{-8} g cm^{-2} day^{-1}. The formation of schoepite, $(UO_2)(OH)_2(H_2O)$, would increase the rate of dissolution to approximately 1-2 × 10^{-6} g cm^{-2} day^{-1} [10].

It is imperative to understand the thermodynamic and kinetic properties of the secondary minerals that form later in the paragenetic sequence because these are the effective solubility limiting phases. The range of experiments covered in this project aim to increase our understanding of DNLEU disposal and the data collected will significantly improve the accuracy of safety models. This will be used to test whether the waste form needs to be immobilised or can be disposed of as uranium oxide powders, and whether a purpose built vault is necessary or if disposal in the service and transport tunnels in place of backfill would be conceivable.

Acknowledgements

M.D. would like to thank the Central England NERC Training Alliance (CENTA) consortium for funding his PhD and for a comprehensive doctoral training programme. He also thanks M. Isaacs for his advice and assistance in numerous aspects of this project.

References

[1] NDA, “Geological disposal - Investigating the impacts of managing depleted, natural and low-enriched uranium through geological disposal,” 2015.

[2] W. Burkart, P. R. Danesi, and A. Bleise, “Properties, use and health effects of depleted uranium (DU): a general overview,” *J. Environ. Radioact.*, vol. 64, pp. 93–112, 2003.

[3] R. D. Wilmot, “Uranium IPT: Phase 2 - Post Closure Safety of DNLEU Disposal,” 2015.

[4] NDA, “Geological Disposal Generic transport system designs,” 2010.

[5] Amphos, “Model of the Redox conditions in the near field of a cementitious geological disposal facility (GDF) Final report,” 2009.

[6] A. Bath and D. Read, “Uranium IPT: Phase 2 - Conceptual Model of Far-field Uranium Transport,” 2015.

[7] ASTM International, “D1141-98 Standard Practice for the Preparation of Substitute Ocean Water,” 2013.

[8] A. Bath and D. Read, “Uranium IPT: Phase 2 - Uranium and its Daughters in the Far Field,” 2015.

[9] L. J. Bonales, C. Menor-Salván, and J. Cobos, “Study of the alteration products of a natural uraninite by Raman spectroscopy,” *J. Nucl. Mater.*, vol. 462, pp. 296–303, 2015.

[10] V. Ivanov and I. B. Popov, “Kinetics of dissolution of stoichiometric uraninite,” *Radiochemistry*, vol. 53, no. 2, pp. 160–163, 2011.

Microstructural Characterisation of AGR Cladding Material

C. Barcellini[1,2,*], S. Dumbill[3], S. Pimbott[1,4], E. Jimenez-Melero[1,2]

*email: chiara.barcellini@postgrad.manchester.ac.uk

[1] *Dalton Cumbrian Facility, Westlakes Science and Technology Park, University of Manchester, Moor Row, Cumbria, CA24 3HA, UK*
[2]*School of Materials, University of Manchester, Oxford Road, Manchester, M13 9PL, UK*
[3]*National Nuclear Laboratories, Central Laboratory, Sellafield, Seascale, Cumbria, CA20 1PG, UK*
[4]*School of Chemistry, University of Manchester, Oxford Road, Manchester, M13 9PL, UK*

Abstract

The safe interim storage of AGR irradiated fuel in water ponds requires a detailed knowledge of the corrosion behaviour of the fuel cladding material. The systematic study of corrosion relies on the availability of sensitised 20Cr25Ni Nb-stabilised stainless steel, ideally with a microstructure close to that produced by neutron irradiation but less radioactive. The aim of this PhD project is the production of sensitised specimens using an intense beam of protons, and to develop thereupon an understanding of the mechanisms driving the radiation-induced segregation of chemical species in the vicinity of grain boundaries. Advanced electron/X-ray techniques are to be used to investigate the damaged structures resulting from the irradiation experiments, in order to compare them with those of claddings removed from the reactor core. A profound knowledge of the behaviour of 20Cr25Ni Nb-stabilised stainless steel under irradiation, however, starts with the characterisation in the pre-irradiation conditions (cold-rolled and annealed). Analytical electron microscopy has been used to investigate the distribution of solute elements, the nature and location of precipitates, together with the crystallographic orientation and grain boundary characteristics of the matrix in non-irradiated specimens. This will constitute the reference for the assessment of the effects of proton irradiation on this material.

Introduction

British nuclear fuel strategy has changed in the last years. In 2018 the reprocessing operation in THORP is scheduled to end. Therefore, the AGR fuel will interim be stored in water ponds, pending packaging and disposal. Long wet storage challenges the cladding integrity; therefore studies on the ageing degradation characteristics are strongly needed. One of the possible challenges is linked with the corrosion resistance of 20Cr25Ni Nb-stabilised stainless steel claddings.

The interim storage of irradiated AGR fuel in water ponds requires a very detailed knowledge of the corrosion behaviour of the fuel cladding material. The systematic study of corrosion relies on the availability of sensitised 20Cr25Ni Nb-stabilised stainless steel. Irradiating the material seems to be the best way to achieve the sensitisation, since thermally-sensitised samples do not present a microstructure comparable to that of the claddings removed from the reactor core.

Protons beams have already been used to simulate neutron effects in other austenitic stainless steels with very promising results. For this reason, irradiation of AGR cladding material with an intense beam of protons looks like to be the best approach for the production of sensitised samples, with a microstructure similar to that of neutron-irradiated steel, but reduced or no radioactivity. This will open the door to the systematic study in this project on the effect of irradiation on the structure and chemistry of these materials. The result of this project will provide a valuable input to predict reliably the corrosion resistance of the AGR spent fuel in storage conditions.

The characterisation of the microstructures obtained by proton irradiation is fundamental in order to assess if the sensitisation obtained can be compared with neutron-damaged structures. However, the profound knowledge of the non-irradiated microstructure is also important, in order to assess the effects of irradiation on the material.

For this reason, the work done in the first year of this project has mainly focused on the investigation of the (non-irradiated) annealed structure. In the following sections, the main results are presented and discussed. The details of the first proton irradiation are also reported.

Experimental

Sample Preparation

A 94x26mm^2 cold-worked sheet of 20Cr25Ni Nb-stabilised stainless steel with a thickness of 7.7mm was provided by Westinghouse. This sheet was annealed for 40min at 930°C in inert atmosphere, in order to simulate the final heat treatment received by the AGR fuel cladding materials. The samples for Scanning Electron Microscopy (SEM) characterisation have been prepared by mechanical grinding, and final electro-polishing using an electrolyte composed of 60ml perchloric acid (3.6%), 600ml of methanol (99.99%) and 360ml of 2-butoxyethanol (99.99%). An analogous procedure has been used for preparing samples for the Transmission Electron Microscopy (TEM). In this case the samples were pre-thinned to 100µm, and then 3mm-diameter disks were punched and subsequently electro-polished using the chemical solution previously mentioned. The sheet sample used in the proton irradiation experiment was prepared on both sides by mechanical grinding and polished down to 0.25µm finish.

Irradiation Experiment

One 26x26mm^2 sheet sample of 20Cr25Ni Nb-stabilised stainless steel was successfully irradiated with a 3MeV proton beam. The experiment took place in September 2015 at the Dalton Cumbrian Facility of the University of Manchester.

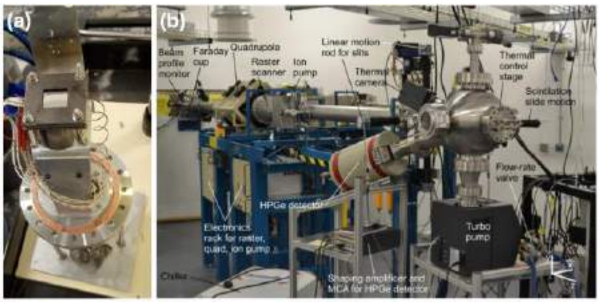

Fig. 1. (a) Sample stage and (b) principal components of the beam line used for the sample irradiation at Dalton Cumbrian Facility [1].

The sample was mounted on the stage shown in Fig. 1a, and two thermocouples were spot welded on its surface in order to monitor the temperature of the sample close to the irradiated area. We placed a ceramic heater at the bottom of the sample in order to heat the sample during the irradiation. Indium (melting point = 156°C) was used to improve the thermal contact between the back block where the heater is housed and the sample, so as to achieve a uniform heating of the sample during the experiment.

In Fig. 1b an image of the beam line used is reported. The sample stage is mounted at the end of the vacuum chamber with the sample surface lying perpendicular to the incoming beam. This beam line has tantalum slits installed in front of the sample to optimise the beam position on the sample, electromagnetic lens to raster the beam on the sample surface, and a thermo-camera used to continuously monitor in situ the temperature distribution on the sample surface. A detailed description of the facility used for the irradiation experiment can be found in [1].

In Table 1 the parameters used in this proton irradiation experiment are listed. The sample was continuously irradiated for 2.5 days with a beam of 3MeV protons. The average current was 10µA, while the average temperature 350°C. The sample heating was achieved by both the proton beam itself and the heater placed at the back of the sample. The average dose rate was 1.8x10^{-6}dpa/s, which is significantly higher than the dose rate expected in a thermal reactor (2x10^{-8}dpa/s [2]).

Table 1. Relevant parameters of the proton irradiation experiment.

Particle	proton
Energy	3MeV
Average Current	9.8 μA
Average Temperature	350°C
Irradiated Area	$1.44cm^2$
Time	$59h$
Dose Rate	$1.8 \cdot 10^{-6}$dpa/s

The damage induced in the crystalline structure was simulated using the SRIM software [3]. In Fig. 2 the Bragg curve for this irradiation is shown. The maximum damage, 3.6dpa, is reached at 36µm from the irradiated surface, while the damage at the 60% from the Bragg peak (22µm from the irradiated surface) is much lower, and amounts to only 0.3dpa.

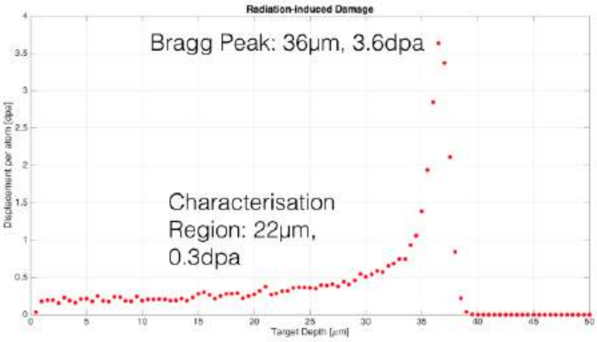

Fig. 2. Radiation-induced damage profile due to a 3MeV proton beam interacting with the 20Cr25Ni Nb-stabilised stainless steel.

The activation of stainless steel is expected for proton irradiations above 2.8MeV. The 20Cr25Ni Nb-stabilised stainless steel sample became radioactive. Three weeks after the end of the experiment were enough for the decay of the short-lived isotopes, such as Co-55 ($t_{1/2}$=0.3days) and Cu-61 ($t_{1/2}$=0.14days). At this moment in time (more than 100 days from the irradiation), the sample activity is only due to the long-lived isotopes of cobalt produced by the nuclear reactions with protons, such as Co-57 ($t_{1/2}$=271days).

Results and Discussion

The microstructural characterisation of the 20Cr25Ni Nb-stabilised stainless steel has so far focused on the annealed sample, in order to have a reference microstructure to study later on the proton irradiated samples. The composition of the austenitic matrix has been measured using Energy Dispersive Spectroscopy (EDS), see Fig. 3.

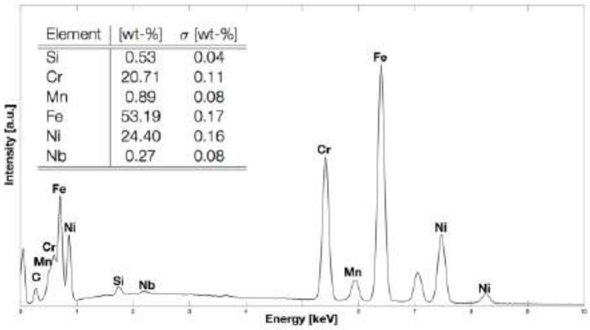

Fig. 3. Typical chemical spectrum of the austenitic matrix.

In order to assess the texture of the matrix of non-irradiated 20Cr25Ni Nb-stabilised stainless steel specimen, Electron Back-Scattered Diffraction (EBSD) measurements have been performed. In Fig. 4a an EBSD map of a large area (64094μm^2) is reported. The data analysis allowed us to detect 3783 individual austenite grains (face-centred cubic, FCC) and their orientation relative to the sample coordinate system.

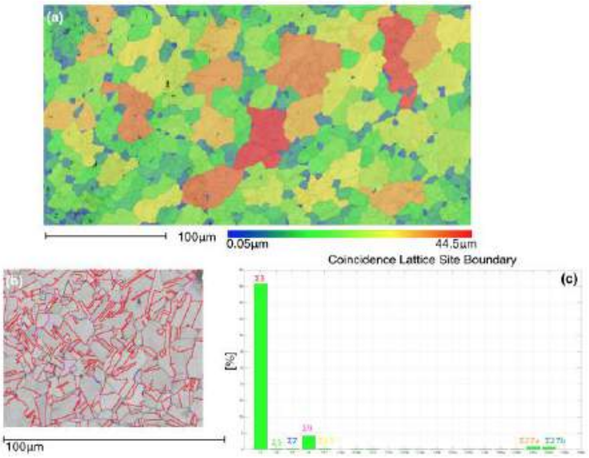

Fig. 4. (a) EBSD map of the austenitic matrix, showing the grains in different colours according to their dimension (b) detail of the EBSD map showing in red twin boundaries, in light green CLS Σ5, in blue CLS Σ7, in magenta CLS Σ9, in yellow CLS Σ11, in dark green CLS Σ27a and in orange CLS Σ27b (c)

Grain boundaries were labelled when the misorientation angle between neighbouring regions was greater than 10°. We have observed a significant amount of twins (51% of the boundary length), most probably formed during the annealing of the sample at 930°C, i.e. annealing twins. Other types of coincidence lattice site (CLS) boundary have been detected and are shown in Fig. 4b. A histogram of the CLS frequency in the sample is shown in Fig. 4c.

Disregarding grains divided by twin boundaries, the average grain size has been estimated to be ~9.2μm. This number is in agreement with the grain size reported by Ramaswamy *et al.* in a recrystallized specimen of 20Cr25Ni Nb-stabilised stainless steel [4]. According to this reference, the recrystallization of this stainless steel grade is completed after 1h at 900°C for a 50% cold-worked specimen, and after 1h at 1000°C the grains start to grow. In the case of a lower thickness reduction during cold working, the recrystallization is slower at same temperature, but the final grains obtained are larger. For instance, in a 25% cold-worked specimen annealed at 950°C for 1h the grains have an average diameter of 14μm. Also Powell et al. found a fully recrystallized material with average grain size of 14μm after 30% cold work and annealing at 930°C for 1h [5]. Full recrystallization in AGR cladding material after 1h at 930°C has also been reported by Ecob [6]. Therefore our specimen under analysis may be partially recrystallized, since our heat treatment was shorter, i.e. only 40min at 930°C.

The inverse pole figures of the matrix along the rolling, normal and transverse direction (RD, ND, and TD, respectively) can be seen in Fig. 5. The grains in the sample are not randomly oriented, but their <101> direction is preferentially aligned with the specimen normal direction. The sample has a texture due to the prior cold rolling and partial recrystallization, with the {101} planes lying along the specimen rolling plane.

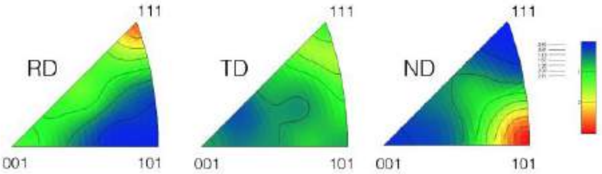

Fig. 5 Inverse pole figures of the non-irradiated sample along the rolling, normal and transverse direction (RD, ND, and TD, respectively). Units are in multiples of a random distribution (mrd).

In Fig. 6 some SEM micrographs at different magnifications of the steel specimen are shown. The general features of this material can be appreciated in Fig. 6a. A large amount of crystalline grains of the matrix, a few of them decorated with precipitates, can be observed. Small and spherical, big and elongated particles and clusters of them can be observed. At higher magnification (Fig. 6b), we can see that the smaller particles are intra-granular, while the bigger ones have grown mainly along the grain boundaries. Fig. 6c and 6d show the details of two clusters grown along grain boundaries.

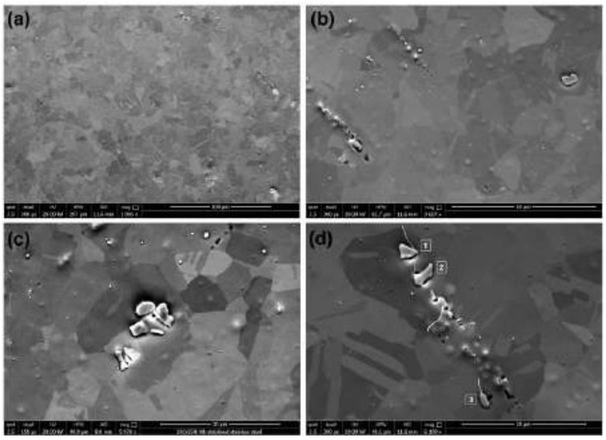

Fig. 6. (a) Scanning electron micrograph of 20Cr25Ni Nb-stabilised stainless steel after a 40min heat treatment at 930°C in inert atmosphere. (b) Grain boundaries free from precipitates. (c) Clusters of Nb-rich particles and isolated spherical precipitates. (d) Cluster of Nb-rich particles grown along a grain boundary of the matrix.

The composition of the biggest particles was also measured using energy dispersive spectroscopy. They are, as expected, Nb-rich particles mostly precipitated during the heat treatment. The annealing at 930°C has been specially designed to induce the Nb-C precipitation, leaving chromium free in the matrix to contribute to the corrosion resistance (stabilisation process).

The composition of some particles shown in Fig. 4c is reported in Table 2. EDS is unfortunately not suitable to detect light elements such as carbon or nitrogen. Besides that, the electron-sample interaction volume at an accelerating voltage of 20kV is large enough to include not only the precipitates but also part of the austenitic matrix. For this reason some elements of the matrix are also present in the EDS spectrum.

Table 2 Chemical composition of selected Nb-rich particles.

	Particle 1		Particle 2		Particle 3	
Element	[wt-%]	σ [wt-%]	[wt-%]	σ [wt-%]	[wt-%]	σ [wt-%]
Cr	4.32	0.08	5.3	0.08	7.65	0.09
Mn	-	-	0.2	0.07	0.57	0.07
Fe	8.17	0.1	10.43	0.11	16.06	0.13
Ni	3.04	0.1	4.04	0.1	6.2	0.11
Nb	84.47	0.15	80.04	0.16	69.53	0.18

The electron beam of a Scanning Electron Microscope is not small enough to allow the analysis of the small precipitates in the samples, since those precipitates have dimensions in the order of few nanometers. For this reason, we have extended our characterization work to Transmission Electron Microscopy (TEM). Fig. 7a and 7b show two examples of nano-scale precipitates observed by TEM. The cluster in Fig. 7a is composed of structures with dimensions ranging from 30 to 250nm, while the single particles in Fig. 7b are less than 30nm in size.

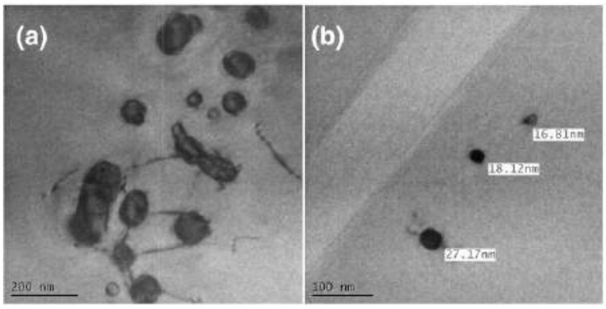

Fig. 7. Bright field TEM images of (a) one precipitate cluster composed of particles of dimensions ranging from 30 to 250nm, (b) small isolated precipitates.

Conclusions and Future Work

The investigation of the annealed 20Cr25Ni Nb-stabilised stainless steel specimen has been reported and discussed. The characterization has mainly focused on the crystallographic orientation and the grain boundary characteristics of the austenitic matrix, and also on the NbC precipitate size and spatial distribution. In the following months, the characterisation of the grain boundaries containing other (nano-scale) phases will be performed. We will also proceed with the characterisation of the first proton irradiated sample. We plan to extract samples at different depths from the surface, and therefore presenting different levels of damage, and to analyse them using electron microscopy. Radiation-induced defects will be related to the amount of damage in the crystalline structure and to variations of the grain boundary chemical composition. The results obtained will be compared with literature data about neutron-irradiated AGR cladding material. In the summer 2016, a second sample will be proton irradiated at the Dalton Cumbrian Facility. The aim of this second irradiation is to reach a level of damage comparable to that obtain in the previous irradiation, but at a considerably higher temperature, 650°C, in order to assess the dependence of the radiation-induced segregation phenomenon on the irradiation temperature.

References

[1] P. T. Wady, A. Draude, S. M. Shubeita, A. D. Smith, N. Mason, S. M. Pimblott, E. Jimenez-Melero, Nucl. Instr. Meth. Phys. Res. A 806 (2016) 109.

[2] J. M. Perks, A. D. Marwick, C. A. English, in proceedings of Radiation-induced Sensitisation of Stainless Steel, D. I. R. Norris, Berkeley Nuclear Laboratories, 1986.

[3] R.E. Stoller, M.B. Toloczko, G.S. Was, A.G. Certain, S. Dwaraknath, F.A. Garner, Nuclear Instr. Meth. Phys. Res B 310 (2013) 75.

[4] V. Ramaswamy, A. E. Sumner, D. R. F. West, J. Iron Steel Inst. 206 (1968) 85.

[5] D. J. Powell, R. Pilkington, D. A. Miller, Acta Metall. 36 (1988) 469.

[6] R. C. Ecob, R. C. Lobb, V. L. Kohler, J. Mater. Sci. 22 (1987) 2867.

A Life Cycle Approach to Nuclear Waste Management

Andrea Paulillo*[1], Dr. Stephen Palethorpe[2], Andrew Milliken[3], Roland Clift[4] and Paola Lettieri[1]

*Correspondence: andrea.paulillo.14@ucl.ac.uk

[1] Department of Chemical Engineering, University College London, Torrington Place, London, WC1 E7JE, United Kingdom
[2] National Nuclear Laboratory, Workington, Cumbria, CA14 3YQ, United Kingdom
[3] Sellafield Ltd., Sellafield, Seascale, Cumbria, CA20 1PG, United Kingdom
[4] Centre for Environmental Strategy, University of Surrey, Guildford, Surrey, GU2 7XH, United Kingdom

Abstract

Nuclear waste management has always been a much debated topic and a key driver for decisions within the nuclear industry. A standardised global approach has not yet been developed and at present many countries are re-considering their position. In the UK the reprocessing of Spent Nuclear Fuel (SNF) is projected to stop, but no clear indication about the future approach has been given. This contribution sets out the early stages of an approach to compare the possible alternatives based on Life Cycle Assessment (LCA), which is widely used in other sectors to assess the overall environmental burdens of a product or a service across the whole life cycle – i.e. from cradle to grave. The LCA may serve to support decision-making processes within the nuclear industry and, provided that it is used in an open and transparent way, to improve public attitudes towards nuclear energy. To date few LCA studies within the nuclear industry have been carried out, the main issue being the lack of a standardised methodology to evaluate the impacts of radionuclides. The present study proposes a new framework for this purpose, and aims to demonstrate its application in an LCA study of the current UK approach to the management of spent nuclear fuel based on a mixture of data collated on site and from literature. The final results of the study will eventually show the overall environmental footprint of the reprocessing of Spent Nuclear Fuel, in terms of both radiological and non-radiological impacts. A "hot spot" analysis will also be performed to highlight the critical processing step.

Introduction

Nuclear energy, as a source of low-carbon dispatchable or base-load electricity, plays a key role for the achievement of sustainability goals [1]. In 2013, nuclear energy accounted for 17% of UK, 24% of European and 11% of worldwide electricity supply [2]- the lowest value since 1982 [3], mainly caused by the 2008 economic crisis and the Fukushima-Daichii accident which led to a total shutdown of Japan's nuclear reactors. However, nuclear energy seems to be on the rise again: according to the World Nuclear Association [4], there are currently 65 nuclear reactors under construction around the world. This figure includes the first plants announced in the 21st century for the UK and USA. However, one of the biggest challenges facing the expansion of nuclear energy is to find a sustainable approach for the management of solid nuclear wastes.

For the purpose of this paper, two main approaches may be identified for the management of Spent Nuclear Fuel (SNF) assemblies: Direct disposal (i.e. open fuel cycle) and Reprocessing with the aim of manufacturing fuel to be recycled back into the Nuclear Power Plants (NPPs) (i.e. closed fuel cycle). In both cases, waste is processed into a final manageable form, either containing spent fuel assemblies or Higher Active Wastes (HAW) [1] or Low Level Waste (LLW). An internationally accepted approach for disposal of HAW has yet to be agreed, but many countries are planning to dispose of them in deep repositories built several hundred meters underground in a geologically stable environment. This is the preferred approach to be taken in the UK, but the siting and design of repository has not been finalised. The UK approach has been to reprocess most (but not all) of the UK's spent nuclear fuel at the Sellafield site. Spent fuel from the UK's Magnox reactors is reprocessed in the Magnox Reprocessing Plant, due to be closed at the end of 2020. The spent reactor fuel from the UK's Advanced Gas-Cooled Reactors (AGRs) and international Light Water Reactors (LWRs) is sent to the Thermal Oxide Reprocessing Plant (THORP), due to be closed at the end of 2018. It is the intention of the Nuclear Decommissioning Authority (NDA) that future arisings from nuclear generation in the UK will be stored without intermediate reprocessing pending final

---

[1] High (HLW) and Intermediate (ILW) are together known as Higher Active Wastes (HAWs)

processing and disposal in the Geological Disposal Facility (GDF). After the failure of the 2013 consultation exercise [5], the process to decide on siting a repository has been reviewed and restarted. According to the timeline set up by the revised siting process, construction of the GDF is not expected to start for at least 25 years; with construction and operation of the facility projected to last for approximately 100 years [5]. Thus the UK is facing a number of important decisions over the future of its nuclear energy industry. Life Cycle Assessment (LCA) represents a tool that could be used to compare alternative strategic options within the nuclear industry by evaluating their environmental performances. The use of the LCA methodology has spread considerably all over the world during the last decade. The methodology underpinning concepts and details have been explained in a previous DISTINCTIVE paper [6] and hence won't be repeated here. The results of an LCA study of the nuclear cycle might be used to support the decision making-process within the nuclear industry and, provided that it is used in an open and transparent way, to improve public attitudes towards the nuclear energy. Until now, few LCA studies of the nuclear cycle have been reported, the main obstacle being the inclusion of ionising radiation within the LCA framework for impact assessment (LCIA). In fact not one reported LCA study has considered the impacts of radionuclide releases from operation of nuclear reactors or from nuclear waste. The goal of the present study is to introduce a novel approach for assessing the impact of radionuclide releases both as direct discharges (i.e. liquid and aerial) and from management of solid wastes in a GDF within the LCIA framework. The approach will then be demonstrated and validated in an LCA study carried out upon the UK approach to the management of SNFs. Several environmental impact categories will be analysed and a "hot spot" analysis will be performed to identify the more polluting sections of the process. Results of the study will show the overall environmental footprint of the UK reprocessing step of spent nuclear fuel in terms of both radiological and non-radiological impacts.

The Risk-based methodology

The standard impact categories conventionally used in LCA studies do not take into account the impacts of radionuclide releases either as process emissions in the form of liquid and gaseous discharges or arising over time from radioactive solid wastes. However, exclusion of these impacts inevitably affects the validity and completeness of the study. With this regard a number of approaches have been proposed; though among those, only few have been operationalised and their usage remains much restricted. A new framework for the assessment of both direct emissions of radionuclides and solid radioactive waste in the impact assessment phase of LCA is proposed in this work. It is based on the PhD work of Solberg-Johansen [7] and hereby updated and amended for a more effective inclusion within the LCA framework. A simple diagram of this methodology is shown in Figure 1.

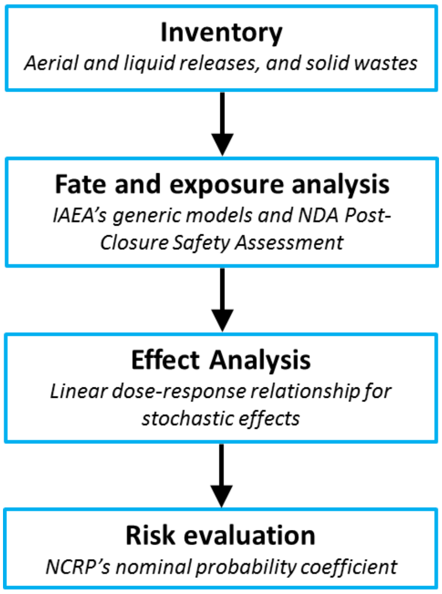

Figure 1 Diagram of the risk-based approach

The starting point is the inventory which comprises the collection and analysis of data regarding liquid and aerial releases, and solid wastes produced by the process. Following the inventory phase, the fate and exposure analysis is carried out with the aim of modelling the transport of radionuclides through the environment (from the source to the receptor or environmental compartment) and through the food chain (from the environment to human beings). The fate and exposure analysis is based on two models: the International Atomic Energy Agency's (IAEA) generic models [8] and the UK NDA Generic Post–Closure Safety Assessment (PCSA) [9]. The former constitutes a simple but robust assessment methodology for the estimation of radioactive doses from routine releases of aerial and liquid radioactive emissions. The latter is a generic exercise performed by the Radioactive Waste Management Ltd. (RWM) with the aim of supporting the environmental safety case of the future national GDF, in which the impact of the storage of nuclear solid waste in a GDF located in a higher strength rock is assessed. The end point of these models is the adsorbed dose, defined as the quantity of ionizing radiation adsorbed per unit mass of the recipient, evaluated for a specific receptor commonly referred as "critical group". The critical group is defined as the member(s) of the public most exposed to radiation due to operations at a given site. The main difference between the two models lies in the timeframe considered. The IAEA models assess the actual impact of current radionuclide releases, whereas the NDA PCSA estimates the future risks arising from solid nuclear wastes buried in a deep GDF. The latter risks start to arise a thousand years after the closure of the GDF and peak after about a million years. The peak value has been considered as the reference risk value for each radionuclide and type of waste. Figure 2 shows an example of the radiological risk as a function of time from different waste types buried in a GDF as estimated by the NDA.

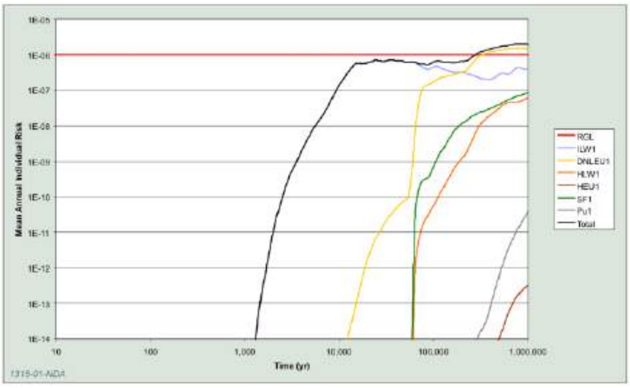

Figure 2 Total mean radiological risk against time showing contributions from the different waste types buried in a GDF[10].

However, different types of radiation can cause different effects in biological tissues and different organs may be more or less susceptible to irradiation. The exposure analysis takes in consideration those aspects by converting the adsorbed dose into an effective dose by means of a linear dose-response relationship for stochastic effects at low doses [11]. Eventually the estimated effective dose is converted into a risk of detrimental effect by using the International Commission on Radiological Protection's (ICRP) nominal probability coefficient for stochastic effects [11]. Notably, the different timeframes of the impacts of direct discharges (aerial and liquid) and solid wastes constitute a big challenge. As the risk associated with direct discharges refers to a current impact and the one arising from solid waste represents a potential impact in the distant future, they are not directly comparable; therefore, their relative significance requires fundamental consideration and discussion. A number of approaches have been used in LCA to deal with different timeframes (e.g. the approach for carbon storage by Levasseur et al [12]), but none encompasses such great differences in scale. Therefore, at this stage the impact of direct discharges and solid wastes will be kept separate within different impact categories.

Life Cycle Model

As previously mentioned, an LCA study including the above proposed methodology will be carried out upon the UK approach to the management of SNF – mainly national AGRs and international LWR spent fuels. The purpose is to the demonstrate and validate the methodology and produce a comprehensive picture of the environmental footprint of the nuclear waste management processes In this study, information about the materials and energy used throughout the process as well as the emissions and waste produced have been and will be collated from different, reliable sources as explained below. Three different units have been identified in the foreground system for the process at issue: Thermal Oxide Reprocessing Plant (THORP), MOX fuel manufacturing plant and the Geological Disposal Facility (GDF). In Figure 3 the process as a whole and the main links between the different units is depicted. The THORP is the latest of the reprocessing plants at Sellafield, where the reprocessing of national AGR and international LWR spent fuel assemblies is carried out. The assemblies are delivered to the site in transport flasks. They are held in THORP's Receipt and Storage Pond for a number of years to allow decay of the highly radioactive fission products with short half-lives. The fuel then undergoes a multi-stage reprocessing. From Fuel Receipt and Storage the fuel elements are transferred to the section known as Head End where the fuel assemblies are sheared and the fuel dissolved in nitric acid. The fumes arising from the dissolvers are treated by the dedicated Dissolver Off-Gas (DOG) Plant. From Head End, the clarified fuel liquor solution is transferred to the Chemical Separation Plant where, firstly, uranium and plutonium are separated from the fission products and then uranium is separated from plutonium (PUREX Process). These liquors are then transferred to the Uranium Finishing and Plutonium Finishing Plants. The process as a whole produces a number of aerial, liquid and solid streams which are treated in ancillary plants. Intermediate level liquid wastes are sent to the Low Active Effluent Monitoring Tank (LAEMT) for marine discharge, while intermediate level solid waste from fuel dissolution is sent to Cement Encapsulation and storage and low level solid waste to Vault Storage. Off-gases are sent to gas treatment before stack discharge. Information about disposal containers and encapsulation procedures have been taken from the UK Derived Inventory [13]. Data regarding those plants and processes will be collated on site by the author. The MOX fuel manufacturing plant is simulated in the model to manufacture MOX fuel from the Plutonium and Uranium powders produced by THORP. Notably the MOX plant was shut down in 2011 and its flowsheets and datasets are currently not available. Thus currently it has been modelled using the data available in the Ecoinvent database [14]. In the analysis, the encapsulated solid wastes are modelled as being sent to the national GDF; this is the long-term plan although, as mentioned above, the facility does not yet exist. Information about the construction, operational requirements and capacity of the GDF has been taken from the UK Nuclear Decommissioning Authority's (NDA) Generic Disposal Facility Designs [9]. Notably this analysis is based upon the current UK approach and status of plants; therefore, with regard to the THORP and MOX plants, only operational environmental impacts have been taken into account. This is not the case for the GDF; as it has not been built, the construction has also been considered along with the proposed operation. However, this assumption makes the assessment specific to the UK.

Conclusions and Future Work

With the aim of enabling LCA practitioners to carry out comprehensive studies upon the nuclear industry and filling the current gap among standard impact categories, a new framework has been proposed. The risk-based approach comprises of four steps and assesses the impact of direct radioactive releases and nuclear solid wastes. In order to validate the methodology. a Life Cycle Assessment study on the reprocessing of Spent Nuclear Fuels in the UK is being carried out. The LCA scenario comprises of three main units: Thermal Oxide Reprocessing Plant (THORP), MOX fuel manufacturing plant and Geological Disposal Facility. A mixture of data collated on site and from literature will be used for the foreground system. A parallel work is also being carried out with the aim of developing an alternative approach base on the multimedia fugacity model concept [15]. Their comparison is expected to give key information regarding the validity of the approaches. Moreover, other existing and future nuclear waste management processes will also be considered for further studies and comparison.

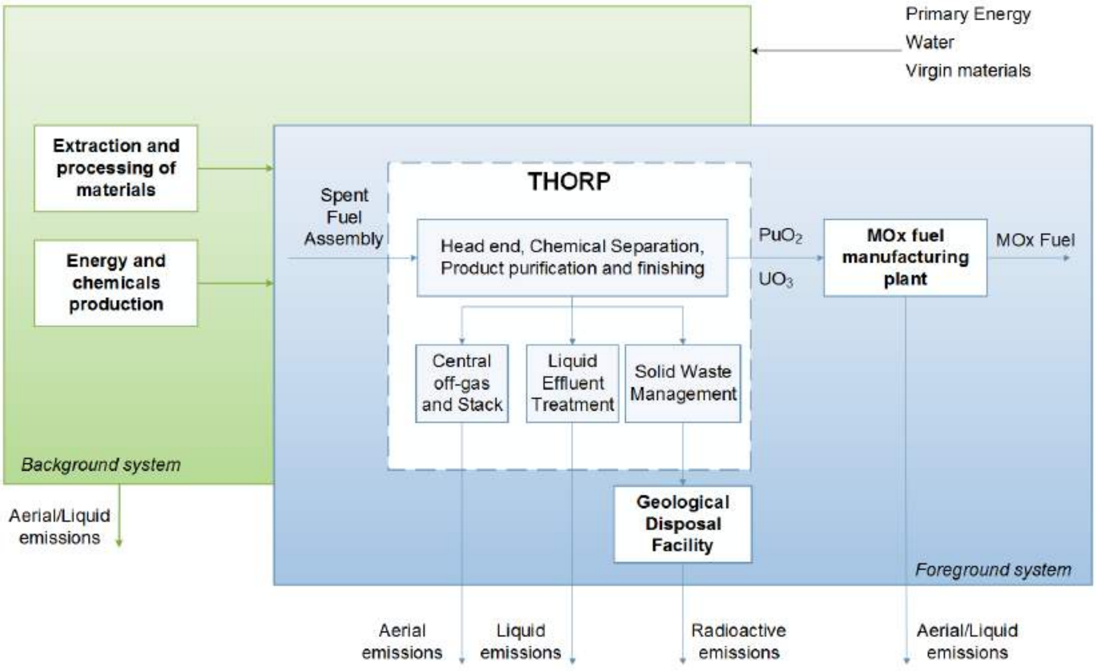

Figure 3 Schematic diagram of the reprocessing step of Spent Nuclear Fuel

References

[1] Royal Commission on Environmental Pollution, "Energy - The changing climate," *The Stationary Office,*. 2000.

[2] U.S.Energy Information Administration, "International Energy Outlook 2013," 2013.

[3] IAEA, "International Status and Prospects for Nuclear Power 2014," 2014.

[4] World Nuclear Association, "World Nuclear Power Reactors & Uranium Requirements." [Online]. Available: World Nuclear Power Reactors & Uranium Requirements.

[5] Department of Energy and Climate Change, "Implementing Geological Disposal," no. July, 2014.

[6] A. Paulillo, S. Palethorpe, R. Clift, and P. Lettieri, "A Life Cycle approah as a desicion tool for nuclear waste management," in *DISTINCTIVE 1st annual meeting*, 2015.

[7] B. Solberg-Johansen, "Environmental Life Cycle Assessment of the Nuclear Fuel Cycle," University of Surrey, 1998.

[8] IAEA, "Generic Models for Use in Assessing the Impact of Discharges of Radioactive Substances to the Environment - Safety Series," Vienna, 2001.

[9] NDA, "Geological Disposal: Generic post-closure safety assessment," 2010.

[10] NDA, "The 2013 UK Radioactive Waste Inventory: Radioactivity Content of Wastes," 2014.

[11] ICRP, "The 2007 recommendations of the International Commission on Radiological Protection. ICRP publication 103.," *Ann. ICRP*, vol. 37, no. 2–4, pp. 1–332, 2007.

[12] A. Levasseur, M. Brandão, P. Lesage, M. Margni, D. Pennington, R. Clift, and R. Samson, "Valuing temporary carbon storage," *Nat. Clim. Chang.*, vol. 2, no. 1, pp. 6–8, 2011.

[13] NDA, "Development of the Derived Inventory Based on the 2007 UK Radioactive Waste Inventory," 2010.

[14] B. P. Weidema, C. Bauer, R. Hischier, C. Mutel, T. Nemecek, J. Reinhard, C. O. Vadenbo, and G. Wernet, "The ecoinvent database: Overview and methodology, Data quality guideline for the ecoinvent database version 3," 2013.

[15] D. Mackay, *Multimedia Environmental Models: The fugacity approach*, Second edi. CRC Press, 2001.

Theme 2 – PuO_2 and Fuel Residues
DISTINCTIVE 2nd Annual Meeting
Bristol, UK
19th – 20th April 2016

Computational modelling of PuO_2 ageing and fuel residues

Nathan A. Palmer* and Mark S.D. Read*

*Correspondence: NAP131@student.bham.ac.uk, M.S.D.Read@bham.ac.uk

School of Chemistry, University of Birmingham, Edgbaston, Birmingham, B15 2TT

Abstract

Static lattice simulations of PuO_2 have been performed using the GULP (General Utility Lattice Program) code in combination with interatomic potentials available in the literature. Simulation results include intrinsic defect energies and mechanical properties of PuO_2, which have been used to select the most appropriate analytical form of the short range potential for further refinement by empirical fitting. The fully ionic model incorporating the core-shell model as used by Read et al. (2014) [1] and Jackson et al. (1986) [2] in modelling PuO_2 is shown to be the most appropriate. The formation energies of intrinsic defects and binding energies of Frenkel pairs and Schottky defects have been predicted. The Uchida et al. (2014) [3] partially ionic model has shown the greatest agreement with experimental data for the oxygen Frenkel pairs. All of the potentials used predict that the formation of oxygen Frenkel pairs are energetically preferred to plutonium Frenkel pairs in PuO_2. Furthermore, they all predict that the formation of Schottky defects where the oxygen ion pairs are further apart are marginally energetically preferred.

Introduction

Ageing mechanisms associated with the storage of PuO_2 are poorly understood. The generation, stability and mobility of fission products in addition to the role of the surface oxide layer being key factors. Computational modelling techniques employ robust interatomic potentials derived from empirical fitting to experimental data to predict bulk and surface structures and their defect chemistry. The application of these modelling techniques to the simulation of defect chemistry provides valuable insight into furthering the understanding of ageing mechanisms associated with PuO_2 at the atomic scale.

Computational techniques

Empirical interatomic potentials

The atomistic simulations presented here employ the same methodology for the treatment of perfect and defective lattices as employed in previous studies of PuO_2 and UO_2 by Read et al [1], [4]. The atomistic approach to modelling crystal structure and associated properties involves the definition of interatomic potential functions to simulate the forces acting between ions and expresses the total energy of the system as a function of atomic coordinates.

For actinide oxides, the calculations are commonly formulated within a Born model representation, with the total energy, $V(r_{ij})$ partitioned into long-range Coulombic interactions and a short-range analytical function, $\phi(r_{ij})$ to model interactions attributed to the repulsion between electron charge clouds, van der Waals attraction, etc. described by:

$$V(r_{ij}) = \frac{q_i q_j}{4\pi\varepsilon_0 r_{ij}} + \phi(r_{ij}) \qquad \textbf{(1)}$$

q_i and q_j represent formal ionic charges and r_ij the interatomic distance. The short-range interaction combines a number of components including non-bonded interactions (electron repulsion and van der Waals attraction) and electronic polarizability.

A number of standard analytical functions are available for the non-bonded potential, but for ionic or partially ionic materials the most commonly used is the Buckingham form described by Eq. (2). The form of the Buckingham potential may be justified from a theoretical perspective since the repulsion between overlapping electron densities, due to the Pauli principle, takes an exponential form at reasonable distances.

$$\phi(r_{ij}) = A_{ij}\exp\left(\frac{-r_{ij}}{\rho_{ij}}\right) - \frac{C_{ij}}{r_{ij}^6} \qquad \textbf{(2)}$$

Eq. (2) contains a repulsive exponential and an attractive term due to dipolar interactions with constants A_{ij} ρ_{ij} and C_{ij} obtained via empirical fitting. In this case, the total potential is called a 'Born-Mayer-Huggins' (BMH) potential. From surveying the literature, a range of models for the PuO_2 potential have been published. These are broadly classed as either fully ionic (full formal ionic charge) or partially ionic models.

The core-shell model

To model polarisation of ions, a simple core-shell model developed by Dick and Overhauser (1958) [5] has been widely and successfully used in atomistic simulations of UO2 and PuO_2 and indeed many other ionic oxides by Lewis and Catlow (1985) [6]. In the core-shell model, a core and a massless shell are connected by a spring. The core usually contains all the mass of the ion and the total electronic charge of the ion comprised of the core and shell charge, as shown in Fig.1. Illustration of the core and shell connected by a 'spring' of spring constants k_2 and k_4. q_c and q_s are the electric charges of the core and shell respectively [7].

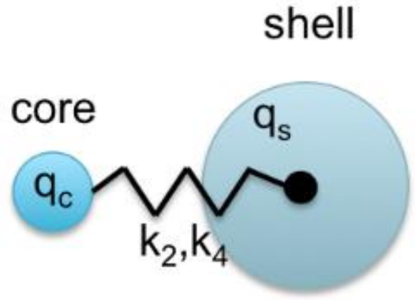

Fig.1. Illustration of the core and shell connected by a 'spring' of spring constants k_2 and k_4. q_c and q_s are the electric charges of the core and shell respectively [7].

The short-range interactions act on the shell, whilst the long-range Coulomb potential acts on both the core and the shell. The free-ion polarizability is given by

$$\alpha = \frac{q_s^2}{k} \qquad (3)$$

k is the harmonic spring constant, a variable parameter, and q_s^2 is the shell electric charge. The potential associated with the interaction between the core and the shell is given by [4]

$$V(r) = \frac{1}{2}k_2 r^2 + \frac{1}{24}k_4 r^4 \qquad (4)$$

r is the radial separation between the core and shell. k_2 is the harmonic spring constant and k_4 is the anharmonic spring constant, for anharmonic interactions between the core and the shell [4].

The available potentials for PuO_2 were implemented in GULP to investigate mechanical properties and intrinsic defect energies. By comparing to reported data, the most suitable analytical form of the potential is chosen. Only one partially ionic model by Uchida et al. (2014) [3] gave required defect energy optimisation in GULP, and four full ionic models were successfully used, with only one presented here by Read et al. (2014) [1] and Jackson et al. (1986) [2]. The analytical form of the potentials are very different for the O-O interaction, but both are of BMH type for the Pu-O interaction, although a Morse potential is used by Uchida et al. [3] in which partial charges of 56.5% are assigned to ion cores, whereas in the fully ionic model, full formal charges are assigned to the ions, modelled using the core-shell model.

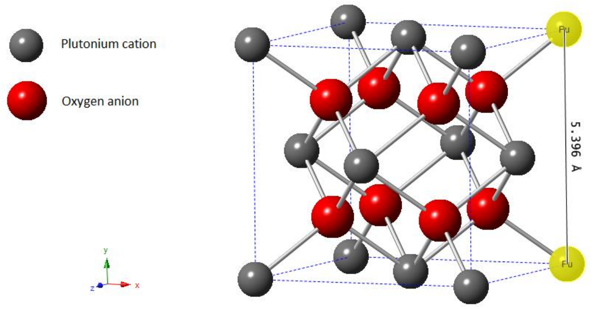

Fig.2. The unit cell of PuO_2. Note only Pu-O bonds are shown.

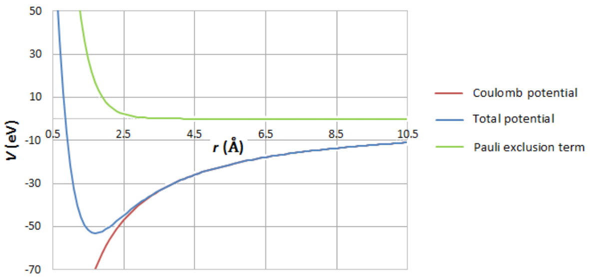

Fig.3. Pu-O interatomic potential by Read et al. (2014) [1], where the C_{ij} parameter is set to zero to avoid unphysical divergence of the total potential as the interatomic separation tends to zero.

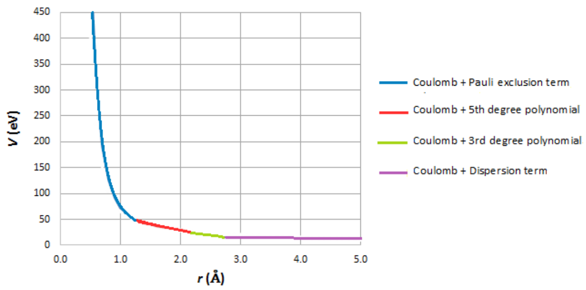

Fig.4. O-O Buckingham 'four-range' potential by Jackson et al. (1986) [2].

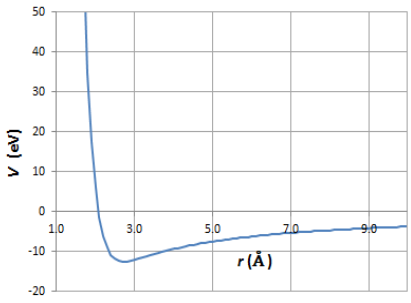

Fig.5. Pu-O interatomic potential by Uchida et al. (2014) [3].

Crystal properties

GULP has been used to determine a range of crystal properties, including structural, mechanical and optical, which are used to guide choice on the most appropriate analytical form of potential for empirical fitting. These properties are predicted from the potential e.g. elastic constants, which are a measure of the materials response to deformation, given by [8]

$$C_{ij} = \frac{1}{V}\left(\frac{\partial^2 U}{\partial \varepsilon_i \partial \varepsilon_j}\right) \qquad (5)$$

V is the volume, U is the internal energy and ε_i and ε_j represent the strains in the orthogonal directions labelled i and j. In a cubic crystal, there are only three unique elastic constants of C_{11}, C_{12} and C_{44} [8].These elastic constants are used to determine other mechanical properties such as bulk, shear and Young's moduli.

Defect formation energies

In GULP, the well-used Mott-Littleton method [9] was used to calculate defect formation energies. There is a two-region approach in the lattice, where regions surrounding the defect are allowed to relax in response to the defect. This is shown in Fig.6. Illustration of regions I and IIa surrounding a central defect in the Mott-Littleton method [4]. The inner region I is relaxed explicitly, with the ions being most perturbed by the defect. In region IIa, the ions experience a harmonic potential. Outside these two regions is region IIb where it is assumed the ions experience a Coulomb interaction only with the defect, which extends out indefinitely in an infinite lattice, but is excluded in the defect energy calculation.

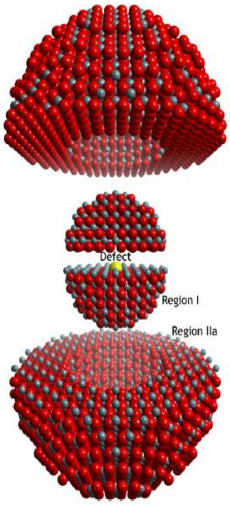

Fig.6. Illustration of regions I and IIa surrounding a central defect in the Mott-Littleton method [4].

Results and Discussion

After surveying the literature, available potentials were used in GULP to predict properties of PuO_2 and intrinsic defect energies. There were four sets of potentials of full ionic type and one set of partially ionic type implemented in GULP. The range of predicted properties of PuO_2 consist of structural, mechanical and optical properties. The intrinsic defects modelled consist of oxygen and plutonium Frenkel pairs and Schottky (tri-vacancy) defects. All simulation results are compared with experimental values to select the most appropriate analytical form of potentials for PuO_2.

Crystal properties of PuO_2

Table 1. PuO_2 crystal structural and mechanical properties.

Potentials by	Property	Calculated	Experimental	% deviation
Read et al. (2014) [1] **and Jackson et al. (1986)** [2]	Lattice constant: a_0 (Å)	5.39812	5.39819 ^{a}	0.001
	Elastic constants (GPa):			
	C_{11}	408.6	430.6 ^{b}	5.12
	C_{12}	130.2	128.4^b	-1.41
	C_{44}	67.301	67.3^b	-0.002
	Bulk modulus, B (GPa)	223.0	178.0^C	-25.28
Uchida et al. (2014) [3]	Lattice constant: a_0 (Å)	6.95295	5.39819^a	-28.80
	Elastic constants (GPa):			
	C_{11}	103.7	430.6^b	75.92
	C_{12}	55.5	128.4^b	56.74
	C_{44}	33.7	67.3^b	49.93
	Bulk modulus, B (GPa)	71.6	178.0^c	59.78

Ref [10], b- Ref [11], c- Ref [12].

Table 2. PuO_2 optical properties.

Potentials by	Dielectric constant	Calculated	Experimental	% deviation
Read et al. (2014) [1] **and Jackson et al. (1986)** [2]	Static, ε_0	15.92	19.27^a	17.39
	High frequency, ε_∞	3.23	3.0^b	-7.52
Uchida et al. (2014) [3]	Static, ε_0	2.27	19.27^a	88.23
	High frequency, ε_∞	-	3.0^b	-

a- Ref [11], b- Ref [13]

Comments

It is clear from the above that the potentials by Read et al. (2014) [1] and Jackson et al. (1986) [2], which are fully ionic incorporating the core-shell model, is far superior to the potentials by Uchida et al. (2014) [3] which is a partially ionic model where there are only ion cores with partial charge. From comparing to other fully ionic models, this particular model gives the closest agreement with experimental data of crystal properties of PuO_2.

Intrinsic defect energies in PuO_2

Oxygen and plutonium Frenkel pairs

For the oxygen Frenkel pairs, the interstitial position was fixed at position $(\frac{1}{2},\frac{1}{2},\frac{1}{2})$, whilst the oxygen vacancy was positioned at $(-\frac{1}{4},-\frac{1}{4},\frac{1}{4})$ and $(-\frac{1}{4},-\frac{1}{4},-\frac{1}{4})$ for 'O F.P.1.' and 'O F.P.2.' respectively. There was only one plutonium Frenkel pair simulated, where the plutonium interstitial is at position $(\frac{1}{2},\frac{1}{2},\frac{1}{2})$ and the plutonium vacancy is at position $(0,0,0)$.

Table 3. Defect energies of oxygen and plutonium Frenkel pairs in PuO_2.

Potentials by	O F.P. 1. E_D^f per defect (eV)	O F.P. 2. E_D^f per defect (eV)	Reported E_D^f per defect (eV)	O F.P.1. $B.E.$ per defect (eV)	O F.P.2. $B.E.$ per defect (eV)	Pu F.P. E_D^f per defect (eV)	Reported E_D^f per defect (eV)	Pu F.P. $B.E.$ per defect (eV)
Read et al. (2014) [1] and Jackson et al. (1986)[2]	2.12	2.07	1.36-1.46^a, 1.74^b	-0.54	-0.59	7.87	7.595^b	-2.16
Uchida et al. (2014) [3]	1.73	1.86	1.36-1.46^a, 1.74^b	-0.54	-0.41	5.48	7.595^b	-2.43

a - Ref [14], experimental data on oxygen diffusion, b – Ref [15], DFT+U method.

Schottky defects

Three Schottky defects were simulated, each differing by the position of an oxygen vacancy as shown in Fig. 7.

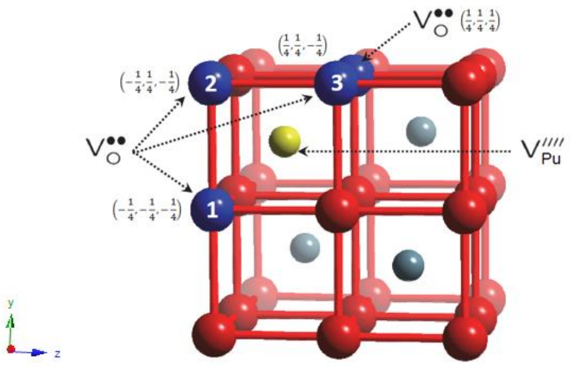

Fig.7. PuO_2 unit cell showing the three unique Schottky defects, varying with the position of the second oxygen vacancy.

Table 4. Defect energies of Schottky defects in PuO_2.

Potentials by	Schottky 1 E_D^f per defect (eV)	Schottky 2 E_D^f per defect (eV)	Schottky 3 E_D^f per defect (eV)	Reported E_D^f per defect (eV)	Schottky 1 $B.E.$ per defect(eV)	Schottky 2 $B.E.$ per defect (eV)	Schottky 3 $B.E.$ per defect (eV)
Read et al. (2014) [1] and Jackson et al. (1986)[2]	1.93	1.93	2.11	2.503^b	-1.61	-1.61	-1.44
Uchida et al. (2014) [3]	1.71	1.79	2.04	2.503^b	-2.38	-2.30	-2.05

b – Ref [15], DFT+U method.

Comments

For the oxygen Frenkel pair defect formation energies, the potentials by Uchida et al. (2014) [3] gave closer agreement with the reported values than the potentials by Read et al. (2014) [1] and Jackson et al. (1986)[2] indeed other potentials investigated. Nevertheless, both the potentials overestimate the experimental values. It is clear the formation of oxygen Frenkel pairs is energetically preferred than for plutonium. For the Schottky defect energies, the potentials predict marginal differences for the three types simulated. There is an agreement that the 'Schottky 3' is least energetically preferred, which is due to the higher interaction energy (primarily electrostatic) between the oxygen ion pair, as the oxygen ions are closest together in this configuration.

Conclusions and Future Work

From the static lattice simulations, the most appropriate analytical form of potentials has been chosen to be a fully ionic model using the core-shell model, as the Read et al. (2014)[1] and Jackson et al. (1986) [2] potentials for PuO_2 gave generally the closest agreement with experimental data for PuO_2. It is clear that these potentials give a robust description of the PuO_2 crystal lattice, as expected from their derivation. Consequently, this will be the form used in deriving a new PuO_2 potential by empirical fitting. This will be achieved by using a fitting code, and using relevant and recent data on PuO_2 to refine potential parameters. Once derived, the potential will be further validated by experimental data and it will be applied in future modelling techniques, such as molecular dynamics simulations. Other common oxides of plutonium may also be investigated such as Pu_2O_3. In addition to using GULP, the molecular dynamics program DL_POLY and the surface simulation program METADISE will be used to investigate the defect chemistry and radiation damage in PuO_2, both in the bulk lattice and at surfaces.

Acknowledgements

The computations performed in this work used the University of Birmingham's BlueBEAR HPC service, used for high performance computing at the University [16]. Thanks are given to the NDA, NNL and the EPSRC for the provision and funding of this iCASE studentship, which is part of the DISTINCTIVE Consortium [17].

References

1. Read, M.S.D., S.R. Walker, and R.A. Jackson, Derivation of enhanced potentials for plutonium dioxide and the calculation of lattice and intrinsic defect properties. Journal of Nuclear Materials, 2014. 448(1–3): p. 20-25.

2. R.A. Jackson, A.D.M., J.H. Harding, C.R.A. Catlow, Philos. Mag. A, 1986. 53(1): p. 27-50.

3. Uchida, T., et al., Thermal expansion of PuO2. Journal of Nuclear Materials, 2014. 452(1–3): p. 281-284.

4. Read, M.S.D. and R.A. Jackson, Derivation of enhanced potentials for uranium dioxide and the calculation of lattice and intrinsic defect properties. Journal of Nuclear Materials, 2010. 406(3): p. 293-303.

5. Dick Jr, B. and A. Overhauser, Theory of the dielectric constants of alkali halide crystals. Physical Review, 1958. 112(1): p. 90.

6. Lewis, G.V. and C.R.A. Catlow, Potential models for ionic oxides. Journal of Physics C: Solid State Physics, 1985. 18(6): p. 1149.

7. Piezo Institute. Available from: http://www.piezoinstitute.com/news/force-field-developments-in-pzt-modelling

8. Gale, J.D., General Utility Lattice Program (User Manual), Version 4.2, Nanochemistry Research Institute, Department of Chemistry, Curtin University: Perth, WA, Australia. p. 50-51.

9. Mott, N.F. and M.J. Littleton, Trans. Faraday Soc., 1938: p. 485.

10. R. Belin, P.V., M. Reynaud, P. Raison, J. Appl. Crystallogr., 2004. 37(6): p. 1034–1037.

11. Meis, C. and J.D. Gale, Computational study of tetravalent uranium and plutonium lattice diffusion in zircon. Materials Science and Engineering: B, 1998. 57(1): p. 52-61.

12. Idiri, M., et al., Behavior of actinide dioxides under pressure: UO2 and ThO2. Physical Review B, 2004. 70(1): p. 014113.

13. Haire, R.G., Advance in Plutonium Chemistry 1967-2000. American Nuclear Society, 2000.

14. Murch, G. and C. Catlow, Oxygen Diffusion in UO sub 2 , ThO sub 2 and PuO sub 2. J. Chem. Soc., Faraday Trans. II. 83(7): p. 1157-1169.

15. Lu, Y., Y. Yang, and P. Zhang, Charge states of point defects in plutonium oxide: A first-principles study. Journal of Alloys and Compounds, 2015. 649: p. 544-552.

16. Birmingham Environment for Academic Research. Available from: https://intranet.birmingham.ac.uk/it/teams/infrastructure/research/bear/index.aspx.

17. Distinctive Consortium. Available from: http://distinctiveconsortium.org/.

Real-time fast-neutron plutonium assay for storage and ageing applications

R. Sarwar*[1], C. H. Zimmerman[2] and M. J. Joyce[1]

*Correspondence: r.sarwar@lancaster.ac.uk
[1] Engineering Department (Lancaster University, Lancaster, UK LA1 4YR)
[2] The Central Laboratory (The UK National Nuclear Laboratory, Sellafield, Cumbria, UK CA20 1PG)

Abstract

Nuclear safeguards is the discipline that ensures that civilian nuclear installations are not being misused to pursue weapons and that associated materials are not diverted to illegal usage. The well-established techniques for verifying this include passive/active radiation monitors using one of several detection methods including gamma-ray tomography, neutron coincidence counters using He-3 detectors and the Cherenkov viewing device etc. Each method has its benefits but individual limitations too. Additionally, the development of advanced fuel-cycle material, such as mixed-oxide (MOX) fuel has indicated further limitations of existing safeguard techniques due to presence, for example, of multiple actinides acting like neutron sources having signatures comparable to plutonium. A solution to this can be achieved by using liquid scintillation detectors (LSD) for fast neutron multiplicity analysis or coincidence counting. These detectors are sensitive to both fast neutrons and gamma radiation. The primary advantage of using such detectors is that they enable an extremely short gate time (three orders of magnitude lower than He-3 detectors) to be used, allowing reduced accidental coincidences and thus being able to detect higher orders of multiplicity.

This studentship is supported by the National Nuclear Laboratory as part of the EPSRC DISTINCTIVE consortium along with Lancaster University with the aim of (i) identifying the multiplicity distribution of a sample in real-time using liquid scintillation detectors to discriminate between different isotopes and (ii) exploiting (α, n) reactions to distinguish the uncorrelated events from the correlated neutrons. This report primarily focuses on the design and development of a real-time system capable of the rapid data processing needed to this end. This is required due to the very short pulse length (in the order of 50-70 ns) originating from LSD when radiation is detected. Moreover, considering practical geometry of an experimental setup (i.e. several rings of detectors surrounding a source within a radius of 50-100cm) and the high speed at which fast neutrons travel, it is expected that fission neutrons will theoretically arrive at the detector after within 20 to 40 ns of the fission event taking place. Hence it is imperative that the system is capable of sampling the detector response at 200 MHz or higher. This feat was achieved utilizing a platform based on System-on-Chip Field-Programmable Gate Array (SoC–FPGA) which combines a dual-core Cortex-A9 embedded core with a FPGA fabric using a high-bandwidth interconnecting link. The system is capable of constructing neutron coincidence distributions in real-time by sampling up to 16 detectors every 5 ns over a user-defined gate-width or coincidence window. This distribution can then be unfolded to carry out neutron multiplicity analysis.

Introduction

During spontaneous and induced fission a significant number of neutrons are produced that are difficult to distinguish from one another. For neutrons, the number may range from zero to ten while photons often exhibit a wider range in multiplicity. This distribution of number of emitted particles, while being a statistically-random event, is called the neutron multiplicity distribution [1]. Figure 1 shows the multiplicity distributions of a number of fissioning isotopes. It is clear that isotopes of individual elements (i.e. Pu-238, Pu-240 and Pu-242) do not vary a great deal in this respect. However, comparing different elements (i.e. plutonium versus curium versus californium) indicates that these distributions are quite different. Identifying this difference in experiments using liquid scintillation detectors has the potential to assist in the identification of the elemental composition of a sample of nuclear material.

In theory, neutron multiplicity analysis refers to counting the number of neutrons that are emitted per fission event. However, since it is rarely possible to associate detected neutrons with their particular fission event, the number of neutrons that are detected within a specified interval of time (also called the gate-width or detector window) is determined in order to construct a coincidence distribution. This method is often referred to as *neutron coincidence counting*. Although there are several methods [2] of detecting multiplicity from such neutron coincidence distributions, the primary focus is usually the Rossi-α Method [3] as per the discussion of this work.

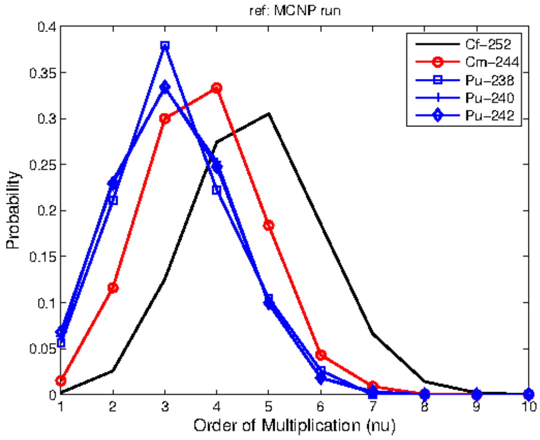

Figure 1 Multiplicity distribution from MCNP6 simulations

The Rossi-α Method allows direct observation of the behaviour of fission neutrons following a fission event by measuring the time distribution of neutron pulses following every triggering pulse [3]. This exploits the fact that the probability of having one fission event followed by multiple neutron detections within a small time interval can be divided into two components: (i) *real* counts or neutrons from a given fission event and (ii) *accidental* counts associated with neutrons from other sources or that have been scattered in the environment. Although this is a well-established method that is used with He-3 detectors [4], the difference in physics of detection of radiation between He-3 and liquid scintillation detectors, the requisite electronics and the unfolding methodology needed to use it with liquid scintillation detectors must be revisited.

The studentship supported by the National Nuclear Laboratory on this topic is part of the EPSRC DISTINCTIVE consortium along with Lancaster University with the aim of (i) identifying the multiplicity distribution of a sample in real-time using liquid scintillation detectors to discriminated between different isotopes and (ii) exploiting (α, n) reactions to identify the uncorrelated events from the correlated neutrons. This report aims to outline progress in the development of a system capable of determining the multiplicity of fissile materials using LSD in real-time.

Methodology Details

Implementation

The Rossi-α method was implemented in Altera DE1-SoC Development Board. This board was chosen for the high speed and flexibility of Field-Programmable Gate Array (FPGA) needed to implement the digital circuitry and also to take advantage of the dual-core ARM processor to send data from the device to a host computer avoiding any bottleneck in data acquisition.

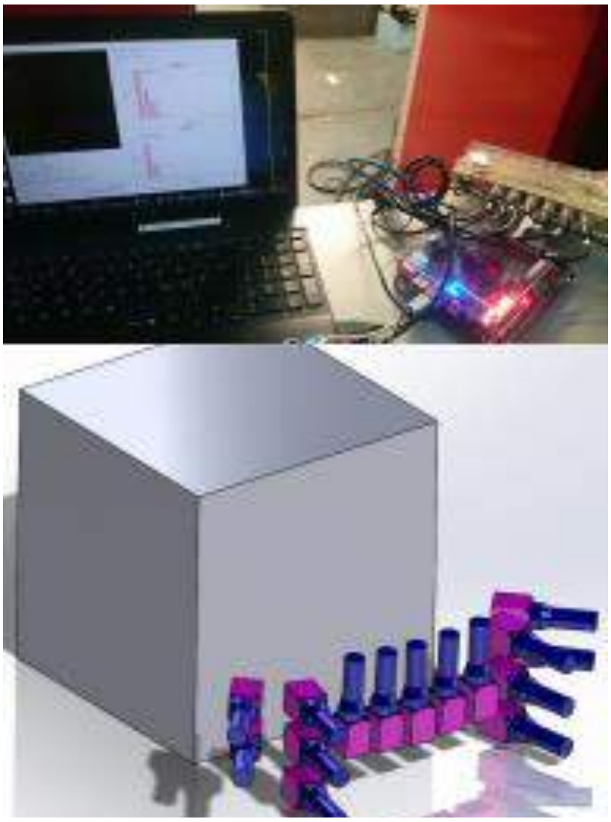

Figure 1 (Top) The signals MFA are connected to the brown PCB referred to as 'signal hub' which is connected to the DE1-SoC kit which is controlled by the laptop. (Bottom) Experimental setup, with a Cf-252 source inside the steel tank.

The assay utilizes 4-channel real-time mixed-field-analysers (MFA) which are capable of driving two TTL outputs per channel, each indicating if a neutron or gamma ray was detected. The reasons for this choice of device for the project are the following advantages: (i) integration of multichannel processing in one self-contained portable unit driven by the same clock of 250 MHz and (ii) evidence of real-time coincidence assay of plutonium with an assessment of the limiting mass uncertainty achieved with four-channel system. Four of these MFAs were connected in parallel to 15 E-309 liquid scintillators in an assay, providing real-time PSD results. These 16 TTL outputs were compiled together in a “signal hub” and were fed into a field-programmable gate array (FPGA) using 16-bit wide general-purpose input-outs (see Figure 2 (top)). To minimize development time, Altera DE1-SoC Development Kit was used. The device integrates both a FPGA and a dual-core ARM processor in the same fabric using high-speed interlink for fast data transfer. The FPGA samples the input at 200 MHz (once every 5 ns) and implements noise dampening techniques to filter out any undesirable fluctuation from the cabling and the signal hub. The neutron coincidence distribution is then constructed using a one-shot circuit [1] based on a gate-width which is defined by the user via 8-bit sliding-switch that gives an effective range of 5 ns to 1270 ns. Additionally, raw signal data along with timestamp information is transferred to the ARM core which uses the information to construct a Type I Rossi-α distribution. These distributions are then transferred to a host computer or laptop using a 1 Gbps Ethernet connection. The host computer runs a program which receives the data, displays the results and saves the data.

Experimental Setup

In order to test the system, experiments were conducted at Lancaster University which houses a Cf-252 stored inside a steel water tank, as shown in Figure 2 (bottom). When the source is brought to the edge of the tank so as to expose it to the surroundings, it gives off a large number of correlated counts, spitting out 10^7 neutrons per second. This source was exposed to 15 detectors which are connected to the prototype assay detection of large number of correlated events. Using the prototype assay, the foreground coincidence distribution as well as the Rossi—α were then computed using both neutron-only and joint (gamma & neutron) signals. This setup is labelled as Exp1-neutron and Exp1-joint.

Results

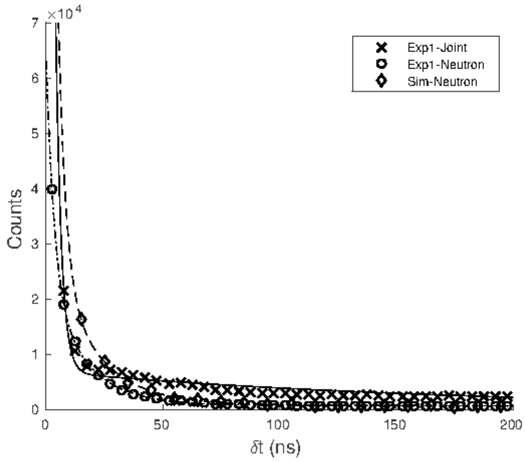

Figure 3 Rossi-α (Top) distribution from Exp. 1 for both neutron-only and joint signals. The α values from Equation 1 for the three set of experiments are 0.3546, 0.1104 and 0.1551, respectively.

Figure 3 is illustrates the Rossi—α distribution for Exp1 for both Joint and Neutron signals, in addition to the simulation results for Neutron signals only. Both Exp1-Neutron and Sim-neutron follow the same trend, with the only difference being lower delta-t due to the fact that the simulation does not take into account detector dead-time correctly.

Figure 4 illustrates the foreground coincidence distribution for Exp1 and Exp2 for both Joint and Neutron signals using a gate-width of 50 ns.

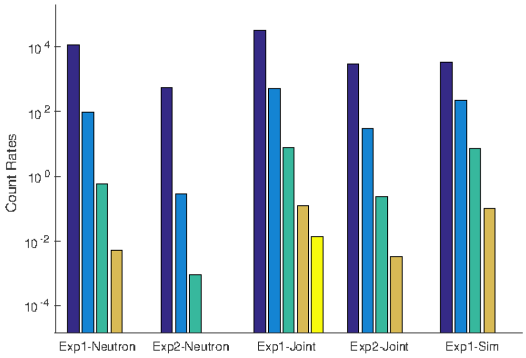

Figure 4 Foreground Neutron coincidence distributions for both neutron-only and joint signals.

Conclusions and Future Work

The project is progressing well. The major research undertaken during the period has been the development of the multiplicity register. Listed below are some of the plans for the upcoming six months:

1. Carry out experiments using sources.
2. Build an assay to accommodate waste drums.
3. Unfolding of the distribution

References

[1] N. Ensslin, Chapter 11: The origin of neutron radiation, in: D. Reilly, N. Ensslin, H. S. Jr. (Eds.), Passive Non-destructive Assay of Nuclear Material, Los Alamos National Laboratory Report,Report LA-UR-90-732, Washington, DC 20555, 1991.

[2] N. Ensslin, Chapter 16: Principles of Neutron Coincidence Counting, in: D. Reilly, N. Ensslin, H. S. Jr. (Eds.), Passive Non-destructive Assay of Nuclear Material, Los Alamos National Laboratory Report,Report LA-UR-90-732, Washington, DC 20555, 1991.

[3] ORNDOFF J. D. (1957) Nucl. Sci. Engng 2,450.

[4] Joyce, M.J.; Gamage, K.A.A.; Aspinall, M.D.; Cave, F.D.; Lavietes, A., "Real-Time, Fast Neutron Coincidence Assay of Plutonium With a 4-Channel Multiplexed Analyzer and Organic Scintillators," in Nuclear Science, IEEE Transactions on , vol.61, no.3, pp.1340-1348, June 2014

The Behaviour of Used Nuclear Fuel in Wet Storage

D. M. Laventine*[1],C. Boxall[1], R. Taylor[2] and D. Woodhead[2]

*Correspondence: d.laventine@lancaster.ac.uk

[1] *University of Lancaster, Lancaster, LA1 4YR, UK*
[2] *Central laboratory, B170, National Nuclear Laboratory, Sellafield, CA20 1PG, UK*

Abstract

We have developed a method which enables direct gravimetric measurement of water adsorption onto CeO2 thin films. Porous CeO2 films were fabricated from a surfactant based precursor solution. The absorption of water onto the CeO2 coating at different relative humidities was studied in a closed reactor. Quartz Crystal Microbalance (QCM) gravimetry was used as a signal transducer, as changes in crystal resonant frequency due to absorbed mass are directly and linearly related to mass changes occurring at the crystal surface.

Introduction

The product of approximately 50 year's civil nuclear fuel reprocessing, about 100 tonnes of Pu are stored at the UK Sellafield site alone. With minor differences, the storage system is very similar to the US approach (DOE standard: stabilization, packaging, and storage of plutonium-bearing materials, DOE-STD-3013-2012, Washington, D.C., 2012). Specifically, the general form of this Pu is as calcined plutonium dioxide (PuO_2) powder usually contained within a series of nested stainless steel cans with the outer can welded to maintain storage integrity, although the characteristics of UK PuO_2, predominantly derived from the Magnox and THORP reprocessing plants, are somewhat different from US PuO_2. Current UK plans are to store in cans long term for several decades with the UK Nuclear Decommissioning Authority (NDA) estimating UK Pu stocks will remain in storage for at least 30-50 years, and possibly until 2120.[1] Whilst PuO_2 is also produced from reprocessing operations in e.g. France, storage times are generally much shorter before incorporation into MOX fuel. Thus, the UK situation is unique in relation to PuO_2 characteristics, expected duration of storage and amount stored.

Under certain circumstances, Pu stores have been observed to cause gas generation within the can and consequent pressurisation of the storage package. This comprises one of the most serious fault scenarios that must be considered in the safety cases for long term PuO_2 storage and avoided in practice. Whilst empirically or phenomenologically derived criteria are used to maintain safe storage conditions, the fundamental mechanisms that lead to pressurisation are poorly understood, although samples withdrawn from can headspaces indicate that the gas is oxygen deficient with a high hydrogen content. 5 main routes to gas production have been suggested:

- Helium accumulation from alpha decay;
- Decomposition of polyethylene packing material;
- Steam produced from adsorbed water during self-heating of cans;
- Radiolysis of adsorbed water;
- Generation of H_2 by chemical reaction of PuO_2 with H_2O, also producing a postulated PuO_{2+x}.

Methodology

Water adsorption on PuO_2 has previously been investigated by measuring headspace pressure, as a function of temperature within a closed system containing a fixed quantity of PuO_2 in the presence of varying amounts of deliberately added water [2].

This involves making a number of assumptions relating to the pressure-volume-temperature behaviour of the headspace of the closed system, usually based on the behaviour of an ideal gas, in order to estimate the mass of water adsorbed at the PuO_2 surface. Assuming ideality at high temperatures and pressures is problematic and, at best, only gives an indirect measurement of water adsorption on PuO_2. Water adsorption on PuO_2 has also been investigated as a function of relative humidity at 25°C [2-4], These studies, however, were not carried out at the high temperatures that can exist within a THORP derived plutonium dioxide storage containers, with Pu238 having a high thermal output of 560 W/kg. Thus, there currently exists a gap in the knowledge regarding the exact mass of water which adsorbs on PuO_2 powders in the closed, heated conditions within a PuO_2 storage container.

Ceria (CeO_2) is widely used as a non-radioactive PuO_2 surrogate due to its oxidation state, ionic radius and fluorite crystal structure. We have proposed to deposit thin films of ceria onto piezo-active crystals and use QCM methodology to directly measure any mass changes under a range of temperatures and humidities. The mass changes, combined with accurate measurements of surface area, can then be used to calculate the amount of water adsorbed onto the ceria surface and the thermodynamic requirements for its desorption [5].

Thin films of ceria and urania have been deposited onto piezo-active crystal wafers through spin-coating precursor salt aqueous solution followed by calcination. Scanning electron microscopy and x-ray fluorescence was used to determine the thickness and roughness of the layers produced. The coated crystals were mounted within the pressure vessel using a custom made crystal holder which exposed both faces of the crystal to the pressurized environment of the vessel, so preventing breakage. The holder had a maximum operating temperature of 200 °C and was constructed of PTFE.

The change in mass resulting from deposition or desorption of water onto or from the metal oxide coating could then be directly measured by Quartz Crystal Microbalance (QCM) methodology. This is a well-established gravimetric device that measures the change in resonant frequency of a piezo-electrically active crystal as mass is added or removed from the surface. The linear relationship between frequency shift and mass change on the crystal surface is described by the Sauerbrey Equation.

Results and Discussion

Measurement of the mass changes using the above methods was performed in a sealed pressure reactor, allowing control of the temperature, pressure and humidity. A number of studies were undertaken that allowed the adsorption of water to be measured under a variety of real-world applicable conditions. The crystals employed in the initial ceria model studies were SiO_2 quartz, and evince a cubic temperature-frequency relationship.

Ceria

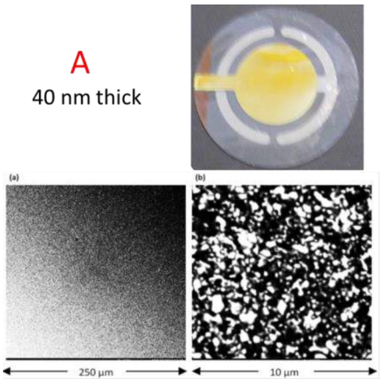

Figure 1. SEM of a CeO_2 coated (40 nm thick) quartz crystal.

Initial experiments at room temperature (21°C) showed that water was absorbed onto the ceria surfaces over a period of about 12 hours from saturated humit atmospheres (fig. 1).

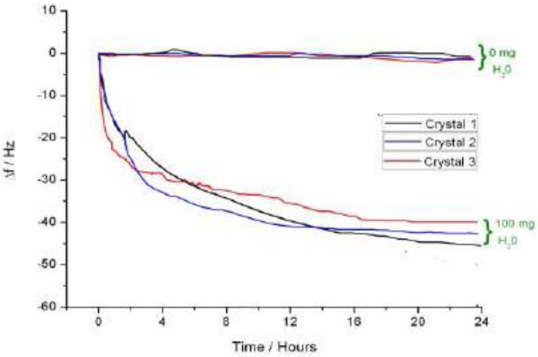

Figure 2 Graph showing the reduction in frequency of a CeO_2 coated (40 nm thick) quartz crystal due to adsorption of water.

Variation of the temperature (and hence the relative humidity) allowed the surface area and the number of monolayers of water to be calculated using the BET equation.

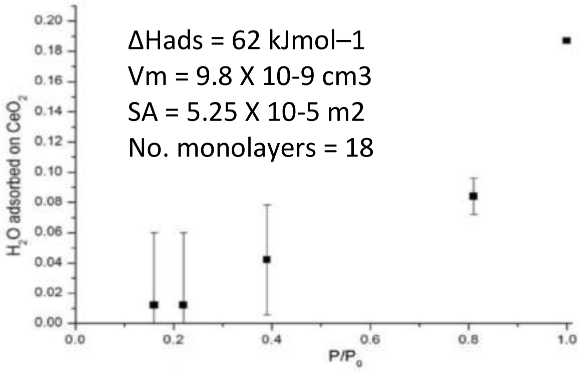

ΔHads = 62 kJmol–1
Vm = 9.8 X 10-9 cm3
SA = 5.25 X 10-5 m2
No. monolayers = 18

Figure 3 Graph showing the absorption of water onto a CeO_2 coated (40 nm thick) quartz crystal at different humidities.

Urania

Urania (U_3O_8) thin films approximately have been synthesised on $GaPO_4$ crystal electrodes, which have a linear temperature-frequency correlation, allowing more accurate measurement of the frequency (and hence mass) changes at higher temperatures.

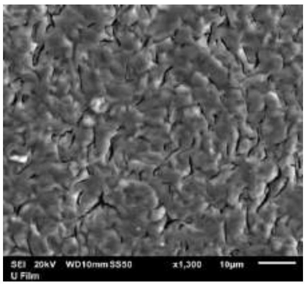

Figure 4. SEM of a U_3O_8 coated (40 nm thick) $GaPO_4$ crystal.

QCM measurments indicate about 18 ug of urania is deposited, which would be equivalent to a 28 nm thick layer. XRF measurements of the layer thickness give an average thickness of approximately 42nm (fig. 5), indicting a porosity of 35%.

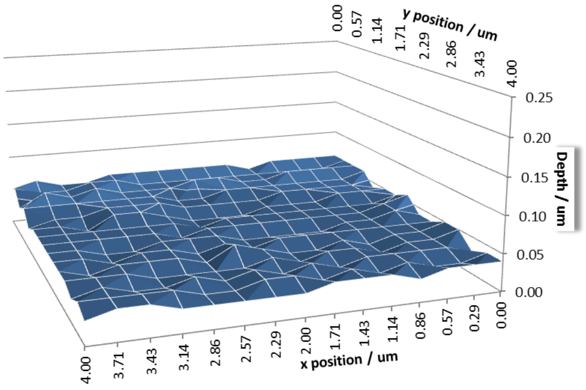

Figure 5. XRF map of a U_3O_8 coated (40 nm thick) $GaPO_4$ crystal.

Conclusions and Future Work

CCeria and Urania thin films have been synthesised on piezo-active crystals, and their thickness and porosity measured. Absorption of water onto these surfaces is ongoing. Subsequent to this optimisation and validation of the initial results, the experimental set up will be transferred to the National Nuclear Laboratories at Sellafield. These facilities will allow the use of radioactive plutonium oxide and investigation of its interactions with water.

Acknowledgements

This work was funded by the UK’s National Nuclear Laboratory, the EPSRC and further supported by the Lloyd’s Register Foundation (LRF), a UK registered charity.

References

[1] Gilchrist, P., *Plutonium Strategy: Current Position Paper.* Nuclear Decommissioning Authority, 2011.

[2] J. M. Haschke, T.E. Ricketts, J. Alloy Compd., 252, 148-156, 1996.

[3] M.T. Paffett, D. Kelly, S.A. Joyce, J. Morris, K. Veirs, J Nucl Mater, 322 (2003) 45-56.

[4] J.L. Stakebake, J Phys Chem-Us, 77 (1973) 581-586.

[5] C Lu, O. Lewis, J. Appl. Phys., 43, 4835, 1972.

Water Adsorption on Actinide Oxide Surfaces

B. E. Tegner*[1], A. Kerridge[2], and N. Kaltsoyannis*[1]

*Correspondence: bengt.tegner@manchester.ac.uk, nikolas.kaltsoyannis@manchester.ac.uk

[1] School of Chemistry (The University of Manchester, Oxford Road, Manchester, M13 9PL, UK)
[2] Department of Chemistry (Lancaster University, Bailrigg, Lancaster, LA1 4YW, UK)

Abstract

The interactions between water and the actinide oxides UO_2 and PuO_2 are important when considering the long-term storage of spent nuclear fuel. However, experimental studies in this area are severely limited by plutonium's intense radioactivity, and hence we have recently begun to investigate these interactions computationally. In this summary we report the results of first principles calculations of the interaction of water with UO_2 and PuO_2. Strongly-correlated effects are taken into account using a Hubbard corrected potential, which enables us to perform efficacious plane-wave density functional calculations of extended systems. In particular, we compare results of water adsorption on UO_2 (111) and PuO_2 (111) with the corresponding results on CeO_2, focusing on the energetics and structural properties of molecular versus dissociative adsorption, for both partially and fully covered surfaces.

Introduction

One of the problems with nuclear energy is the long term storage of nuclear waste, spent nuclear fuel and the products of fuel reprocessing. Our particular project concerns the civilian stores of highly radioactive plutonium dioxide. Presently, the UK's PuO_2 is stored as a powder in stainless steel storage containers, while the government decides its long term fate. However, some of these steel containers have started to buckle, leading to the hypothesis that gas build up, possibly from water vapour due to desorption or the production of hydrogen gas due to the radiolysis of water, causes some of the containers to pressurize. We are exploring these suggestions computationally.

Methodology Details

The calculations were performed using VASP 5.4.1 [1-4], a plane-wave DFT code using Projector-Augmented Wave (PAW)-pseudopotentials [5, 6] to describe the ions and employing Monkhorst-Pack (MP) [7] grids for the *k*-space integration. All calculations used a plane wave cut-off of 650 eV and a MP-grid of 5×5×1 k-points for the Brillouin zone sampling. The generalized gradient approximation of Perdew, Burke, and Ernzerhof (PBE) [8, 9], with a Hubbard correction [10, 11], was used for the exchange-correlation. The surface is constructed using a repeating slab of 16 - 24 AnO_2 units arranged in four or six layers with 18 Å of vacuum between each slab.

Results and Discussion

The AnO_2 (111) Surface

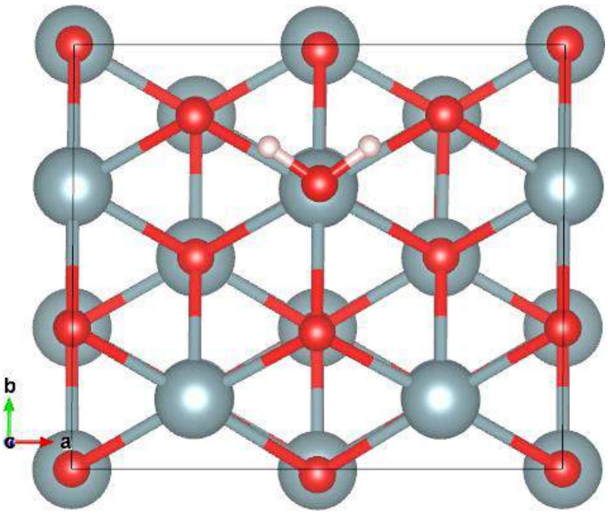

Figure 1 Single water molecule adsorbed molecularly on the 2 × 2 UO_2 (111) surface, yielding a coverage of 25%, i.e. ¼ of a monolayer. U atoms in grey, oxygen in red and hydrogen in white.

A ball-and-stick representation of the (111) surface at low coverage is shown in figure 1. The calculated adsorption energies of molecularly and dissociatively adsorbed water on UO_2 (111) and PuO_2 (111) is shown in table 1 below.

System	0.25 ML	0.5 ML	0.75 ML	1.0 ML
$UO_2 + H_2O$	-0.36	-0.51	-0.52	-0.49
UO_2 + OH + H	-0.44	-0.40	-0.26	-0.13
$UO_2 + H_2O$ [12]	-0.61	N/A	N/A	-0.60
UO_2 + OH + H [12]	-0.68	N/A	N/A	-0.32
$PuO_2 + H_2O$	-0.40	-0.47	-0.46	-0.44
PuO_2 + OH + H	-0.32	-0.29	-0.21	-0.07
$CeO_2 + H_2O$ [13]	-0.56	-0.60	N/A	-0.57
CeO_2 + OH + H [13]	-0.59	N/A	N/A	-0.15

Table 1 Water adsorption energies (eV) per molecule on the UO_2 (111) and PuO_2 (111) surfaces, with results for UO_2 from Bo et al. [12] and for CeO_2 from Molinari et al. [13].

Corresponding data on UO_2 from Bo and co-workers [12] and on CeO_2 from Molinari and co-workers [13] are shown for comparison, and selected interatomic distances are shown in table 2.

Distance (Å)	UO_2 (111) (0.25 – 1.0 ML)	UO_2 (111) (0.25 – 1.0 ML) [12]	PuO_2 (111) (0.25 – 1.0 ML)	CeO_2 (111) (0.25 – 1.0 ML) [13]
$H_W - O_{1S}$	1.96 – 2.28	1.66	2.00 – 2.23	1.99 – 2.13
An_{1S} / Ce_{1S} – O_W	2.62 – 2.69	2.60 – 2.73	2.62 – 2.68	2.62
An_{1S} / Ce_{1S} – O_WH_W	2.18 – 2.26	2.29 – 2.36	2.20 – 2.26	2.22
An_{1S} / Ce_{1S} – $O_{1S}H_W$	2.33 – 2.44	N/A	2.30 – 2.43	2.41
$O_{1S}H_W$ – O_WH_W	1.61 – 2.39	N/A	1.57 – 2.29	1.65

Table 2 Selected interatomic distances for molecularly and dissociatively adsorbed water on the UO_2 (111) and PuO_2 (111) surfaces at coverages from 0.25 to 1.0 monolayers, with results for UO_2 from Bo et al. [12] and for CeO_2 from Molinari et al. [13]. H_W and O_W denote the hydrogen and oxygen atoms belonging to the water molecule whereas An_{1S}/Ce_{1S} and O_{1S} denote the outermost surface atoms.

Comparing the data, we find close similarity between CeO_2 and UO_2/PuO_2, particularly at full coverage. This strengthens the idea of using CeO_2 as a non-radioactive analogue of the actinide oxides for experimental water adsorption studies.

The AnO_2 (110) Surface

We have recently started work on the (110) surface. This surface is more featured compared to the (111) surface which forces us to increase the slab size to six layers and adsorb on both sides of the slab to improve symmetry and avoid dipole effects. A ball-and-stick representation of the (110) surface at low coverage is shown in figure 2.

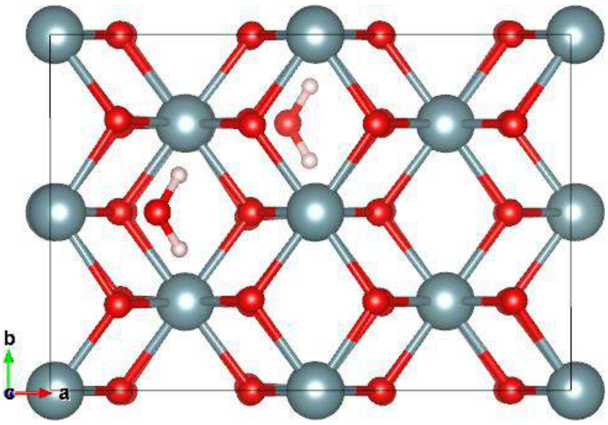

Figure 2 Water adsorbed on the 2 × 2 UO_2 (110) surface, yielding a coverage of 25%, i.e. ¼ of a monolayer. U atoms in grey, oxygen in red and hydrogen in white.

Calculated adsorption energies for molecularly and dissociatively adsorbed water on UO_2 (110) and PuO_2 (110) are shown in table 3 below.

System	0.25 ML	0.5 ML	1.0 ML
$UO_2 + H_2O$	-0.93	-0.74	-0.65
UO_2 + OH + H	-1.39	-1.05	-1.00
$PuO_2 + H_2O$	-0.29*	-0.73	-0.75*
PuO_2 + OH + H	-0.03*	-0.94	-0.91
$CeO_2 + H_2O$ [13]	-0.85	-0.76	N/A
CeO_2 + OH + H [13]	-1.12	-1.00	-0.21

Table 3 Water adsorption energies (eV) per molecule on the UO_2 (110) and PuO_2 (110) surfaces, with results for CeO_2 from Molinari et al. [13]. The starred results are work in progress, and subject to change.

Corresponding data on CeO_2 from Molinari and co-workers [13] are again shown for comparison, and selected interatomic distances are shown in table 4.

Distance (Å)	UO_2 (110) (0.25 – 1.0 ML)	PuO_2 (110) (0.25 – 1.0 ML)	CeO_2 (110) (0.25 – 1.0 ML) [13]
$H_W - O_{1S}$	2.13 – 2.26	2.14 – 2.21	2.07
An_{1S} / Ce_{1S} – O_W	2.73	2.72	2.67
An_{1S} / Ce_{1S} – O_WH_W	2.15	2.12	2.14
An_{1S} / Ce_{1S} – $O_{1S}H_W$	2.44 – 2.58	2.44 – 2.49	2.48 – 2.58
$O_{1S}H_W$ – O_WH_W	3.11	3.05	1.92

Table 4 Selected interatomic distances for molecularly and dissociatively adsorbed water on the UO_2 (110) and PuO_2 (110) surfaces at coverages from 0.25 to 1.0 monolayers, and results for CeO_2 from Molinari et al. [13]. H_W and O_W denote the hydrogen and oxygen atoms belonging to the water molecule whereas An_{1S}/Ce_{1S} and O_{1S} denote the outermost surface atoms.

Comparing the data, we again find close similarity between CeO_2 and UO_2/PuO_2, with the added observation that unlike the (111) surface, there is a clear preference for dissociative adsorption at all coverages on the (110) surface, supporting the idea of a fully hydroxylated surface.

Conclusions and Future Work

Water adsorption energies and distances on the UO_2 (111) surface look very similar to previous work by Bo and co-workers, increasing confidence in the validity of our computational approach. Moreover, the resulting adsorption energies and distances on the AnO_2 (111) and (110) surfaces also compare well with corresponding values on CeO_2, particularly at full coverage, strengthening the notion that CeO_2 can be used as an actinide oxide analogue.

Moving forwards, we will continue to study water adsorption on the (100) surfaces of both actinide oxides, before progressing to more complex systems such as reduced surfaces.

Acknowledgements

We would like to thank Howard Sims at the National Nuclear Laboratory, and Jeffrey Hobbs and Helen Steele at Sellafield Ltd for helpful discussions.

We are also grateful for access to ARCHER, the UK's National Supercomputing Service (http://www.archer.ac.uk), *via* the HEC Materials Chemistry Consortium, which is funded by EPSRC (EP/L000202). We also thank University College London for computing resources *via* Research Computing's "Legion" cluster (Legion@UCL) and associated services, and the "Iridis" facility of the e-Infrastructure South Consortium's Centre for Innovation.

References

[1] G. Kresse and J. Hafner, Phys. Rev. B, 47, 558, (1993).

[2] G. Kresse and J. Hafner, Phys. Rev. B, 49, 14251, (1994).

[3] G. Kresse and J. Furthmüller, Comput. Mat. Sci., 6, 15, (1996).

[4] G. Kresse and J. Furthmüller, Phys. Rev. B, 54, 11169, (1996).

[5] P. E. Blöchl, Phys. Rev. B, 50, 17953, (1994).

[6] G. Kresse and D. Joubert, Phys. Rev. B, 59, 1758, (1999).

[7] H. J. Monkhorst and J. D. Pack, Phys. Rev. B, 13, 5188, (1976).

[8] J. P. Perdew, K. Burke and M. Ernzerhof, Phys. Rev. Lett., 77, 3865, (1996).

[9] J. P. Perdew, K. Burke and M. Ernzerhof, Phys. Rev. Lett., 78, 1396, (1997).

[10] S. L. Dudarev, D. Nguyen Manh and A. P. Sutton, Philosophical Magazine Part B, 75, 613 (1997).

[11] A. I. Liechtenstein, V. I. Anisimov and J. Zaanen, Phys. Rev. B, 52, R5467, (1995).

[12] T. Bo, J. Lan, Y. Zhao, Y. Zhang, C. He, Z. Chai and W. Shi, J. Nucl. Mat. 454, 446 (2014).

[13] M. Molinari, S. C. Parker, D. C. Sayle and M. S. Islam, J. Phys. Chem. C 116:7073, (2012).

Adsorption of Chloride and Water on CeO_2 as a precursor to PuO_2 studies

S. Sutherland-Harper*[1], S. Pimblott[1], J. Hobbs[2], R. Taylor[3], C. Pearce[4], F. Livens[1] and N. Kaltsoyannis[1]

*sophie.sutherland-harper@postgrad.manchester.ac.uk

[1] University of Manchester, Oxford Road, Manchester, England
[2] Sellafield Ltd., Sellafield, Seascale, Cumbria, England
[3] National Nuclear Laboratory, Sellafield, Seascale, Cumbria, England
[4] Pacific Northwest National Laboratory, Washington, USA

Abstract

A quantity of plutonium dioxide powders in storage at the Sellafield site in Cumbria has become contaminated with chloride ions from the degradation of polyvinyl chloride (PVC) within the package, along with moisture from the atmosphere; chloride and water are thus adsorbed to the surface of PuO_2. This `high chloride` PuO_2 must be dried prior to repackaging in welded cans for safe, long term storage. Therefore an interfacial study of water- and Cl^--contaminated PuO_2 is essential to understand its properties and develop a treatment process. Due to difficulties in working with plutonium, using analogues is important to optimise analytical techniques and to provide more complete predictions of the probable behaviour of PuO_2 in advance of plutonium-active experiments. This review summarises recent findings of Cl^--contaminated ceria (CeO_2) as an analogue, using X-Ray Diffraction and Infrared Spectroscopy, Ion Chromatography and Scanning/Transmission Electron Microscopy - Energy Dispersive Spectroscopy for analysis.

Introduction

There are currently over 100 tonnes of PuO_2 stored at the Sellafield site in Cumbria as the product of reprocessing spent fuel from nuclear reactors. During some of the early reprocessing operations between 1970 and 1975, powder production was placed into a packaging system consisting of a screw top aluminium inner container, inside 2 layers of PVC and placed into an steel outer container. The PVC has degraded due to the heat and radiation emitted by the PuO_2 and contaminated around 5 tonnes of the PuO_2 with chloride from the evolved HCl as well as adsorbed moisture from the atmosphere. The leading option for plutonium disposition in the U.K. is to re-use the PuO_2 as a mixed-oxide (MOX) fuel for new-build nuclear reactors, but it must be stored safely and securely in the meantime. Repacking this material for interim storage in welded cans in the new Sellafield Products and Residue Store is planned but this requires meeting specific conditions for acceptance (CFA); most notably the material must be dried to meet a low loss on heating (LOH) condition. Therefore understanding how the material will behave when dried in a retreatment plant as well as how Cl^-—contaminated PuO_2 evolves over time is necessary. Past experiments have revealed a recalcitrant fraction of Cl^- within PuO_2 that cannot be leached out under the conditions studied. It is ideal for PuO_2 to have an oxidation state of 4+, which is insoluble in water, so it will not leach as much as +5 or +6 in groundwater. PuO_2 is both toxic and radiotoxic, so using non-toxic analogues with the same oxidation state and similar properties to PuO_2, such as CeO_2, ThO_2 and UO_2, is beneficial as it avoids dangerous and expensive laboratory work.[1] Investigations on these analogues should provide an insight into the expected behaviour of contaminated PuO_2, particularly with respect to physical effects, despite the fact that plutonium will have radiological effects, which cerium does not, and a different affinity for various oxidation states in solid form (Pu (IV) exists in solid form and Pu (III) in liquid, whereas Ce (III) and (IV) both exist in the solid phase). This project summary includes details of recent results from X-Ray Diffraction (XRD), Infrared (IR) Spectroscopy, Scanning Electron Microscopy-Focussed Ion Beam (SEM-FIB) and Transmission Electron Microscopy-Energy Dispersive Spectroscopy (TEM-EDS).

Methodology Details

CeO_2 synthesis

Cerium nitrate hexahydrate (0.0416 mol dm^{-3}) in nitric acid (0.2 mol dm^{-3}) and oxalic acid (0.68 mol dm^{-3}) in water were mixed together using the oxalate precipitation method at 25 ± 0.5 °C, filtered *in vacuo* and washed with nitric acid (50 mL, 0.01 mol dm^{-3}) and water (50 mL). The solid was collected on a PVDF membrane (pore size 0.22 μm) and air dried overnight, producing cerium oxalate (white powder). This was calcined at either 500 or 900 °C to produce CeO_2 of High Specific Surface Area (HSSA, yellow powder) or

Low Specific Surface Area (LSSA, cream powder), respectively.

Cl^- contamination

A small vial containing CeO_2 powder was put inside a bigger vial containing HCl (~5 mL, ~37%). The big vial was sealed and left for 7 days.

Analysis

XRD was measured on a Brücker D8Advance and crystal sizes were calculated using Topas software, IR Spectroscopy on a Thermo scientific Nicolet iS5, SEM-EDS was done using an FEI XL30 ESEM-FEG and FIB-TEM were carried out at Pacific Northwest National Laboratory (USA).

Chloride was leached from the samples overnight, using sodium hydroxide (0.1 mol L^{-1}). They were then diluted x20, spiked with 0.05 mL fumaric acid and analysed by ion chromatography (IC) (Dionex ICS-5000 Analytical IC), using the NaOH solution as a blank.

Results and Discussion

X-Ray Diffraction

Previous XRD results of CeO_2 made by NNL showed no extra phases appearing after Cl^--contamination. However, upon contamination of freshly made CeO_2, a cerium chloride heptahydrate phase appears in the sample bulk (Fig. 1), making the powder heterogeneous. This behaviour is probably due to different contamination conditions and HCl concentrations being used, compared to NNL's synthesis.

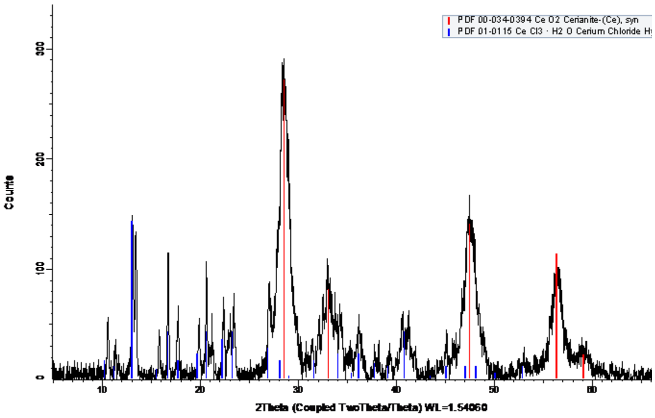

Figure 1 XRD pattern of Cl^--contaminated HSSA CeO_2 (red Bragg peaks = cerianite, blue = cerium chloride heptahydrate).

This is not the case for contaminated LSSA CeO_2 (Fig. 2), as no extra phases are detected in the bulk of the sample. It behaves much like the samples made by NNL.

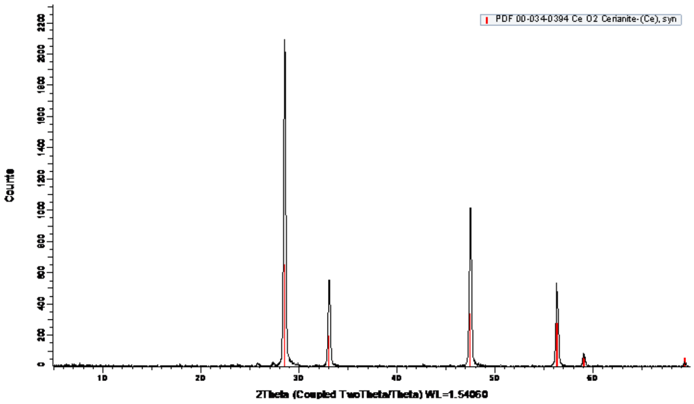

Figure 2 XRD pattern of Cl^--contaminated LSSA CeO_2 (red Bragg peaks = cerianite).

Infrared Spectroscopy

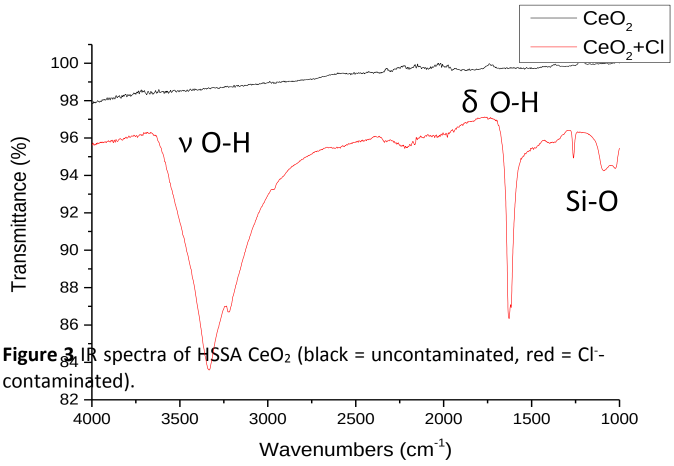

Figure 3 IR spectra of HSSA CeO_2 (black = uncontaminated, red = Cl^--contaminated).

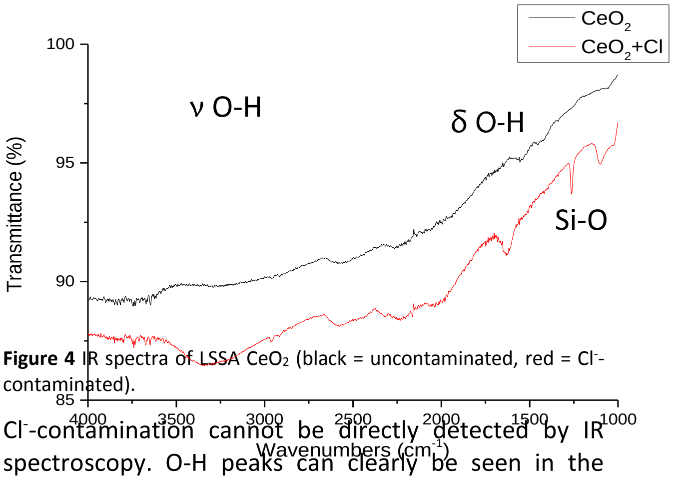

Figure 4 IR spectra of LSSA CeO_2 (black = uncontaminated, red = Cl^--contaminated).

Cl^--contamination cannot be directly detected by IR spectroscopy. O-H peaks can clearly be seen in the contaminated spectra (Figs. 3 and 4) at ~3,300 (ν) and ~1,600 (δ) cm^{-1}. This suggests a link between Cl^- concentration (shown in previous X-Ray Photoelectron Spectroscopy (XPS) results) and the amount of water adsorbed, i.e. if Cl^- is present on the surface of CeO_2, water will be as well, despite being contaminated with conc. HCl vapour. Similar to the previous Cl^- XPS results, the intensity of the contaminant water peaks here is greater for the higher SSA particles (Fig. 3), as more surface area is available for sorption relative to volume. Si-O peaks are also present, due to contaminating the samples using glass vials. HDPE bottles will be used in future to prevent this occurring again.

Ion Chromatography

Cl^- has 3 forms when adsorbed to the surface of CeO_2: one volatilises as a gas upon heat treatment, one is physically bound to the surface and leaches off in caustic solution and the third is chemically bound and does not leach off in caustic solution. Ion chromatography of the leachable Cl^- (Fig. 5) shows how much difference surface area makes to the adsorption of contaminants.

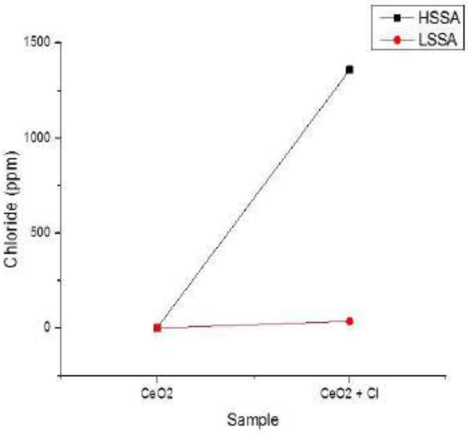

Figure 5 Concentrations of Cl^- leached from CeO_2 particles before and after contamination by ion chromatography.

Similar to previous XPS and IR spectroscopy, IC shows that the concentration of Cl^- increases dramatically with surface area. It also proves that even though LSSA CeO_2 is exposed to concentrated HCl vapour, the maximum amount of Cl^- leached off is only 35.4 ppm (far less that the HSSA value of ~1,360 ppm). This is encouraging, as it means that particles of a lower surface area (particles which are larger) are an insignificant concern, compared to HSSA particles. Performing IC on heat treated particles will provide more information on whether this leachable fraction volatilises off the CeO_2 surface or remains bound to it.

Scanning Electron Microscopy-Energy Dispersive Spectroscopy

Ideally, the CeO_2 particles should have the same shape as PuO_2 (Fig. 6), in order to act as a true surrogate. These PuO_2 flakes are hexagonal in shape at 5 µm.

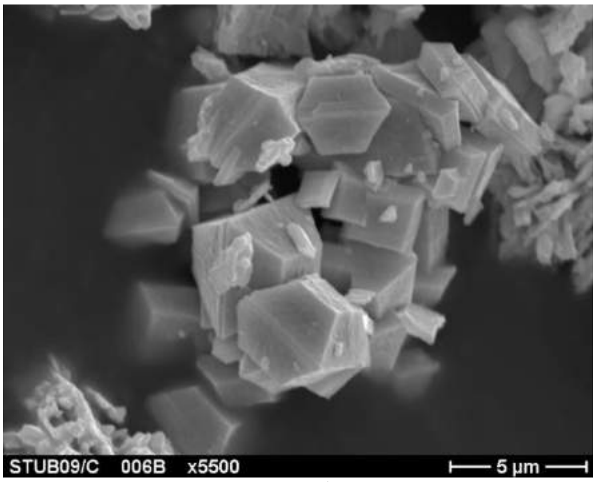

Figure 6 SEM image of PuO_2 particles.[2]

However, the CeO_2 particles synthesised have more irregular shapes at this scale (Fig. 7). There is also no change in appearance between uncontaminated and contaminated LSSA CeO_2, which agrees with IC, that hardly any Cl^- has been adsorbed to make much difference.

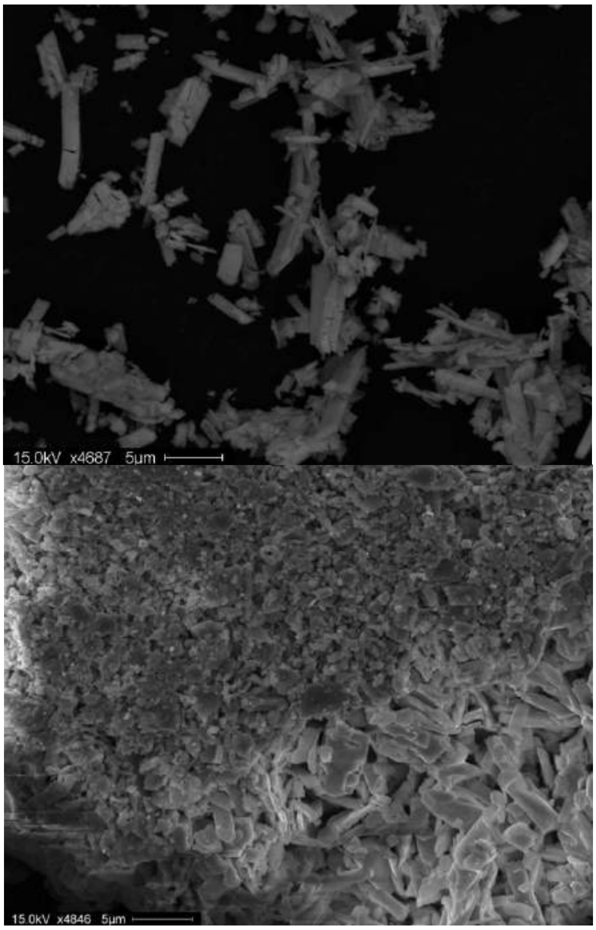

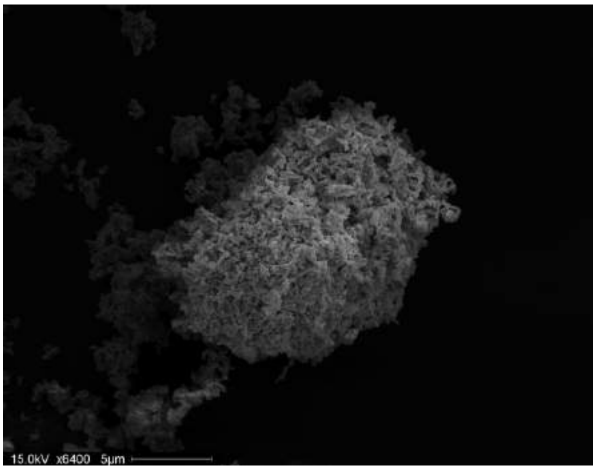

Figure 7 SEM image of CeO_2 particles (top = HSSA, middle = LSSA and bottom = LSSA + Cl^-).

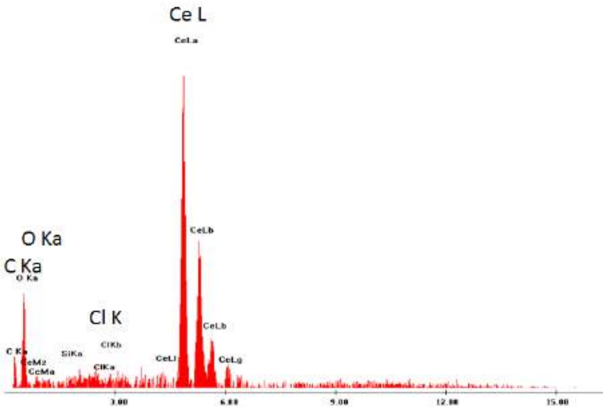

Figure 8 EDS spectrum of Cl^--contaminated LSSA CeO_2.

Even though EDS is only being used as a qualitative analysis technique, not quantitative, the amount of Cl^- on the surface of contaminated LSSA CeO_2 is below the limit of detection (LOD) of the instrument (0.1 %wt).

Transmission Electron Microscopy-Energy Dispersive Spectroscopy

Images of heat treated HSSA CeO_2 (Fig. 9) from NNL, where contaminated CeO_2 has been heated at 900 °C for 2 hours, show that the crystals have sintered and are, in fact, hexagonal in shape (similar to PuO_2 particles on a nano scale). This means that PuO_2 and CeO_2 synthesised at high temperatures should behave in the same way. The EDS spectrum also shows that after contaminated HSSA CeO_2 has been heat treated, the amount of Cl^- remaining on the surface is below the LOD.

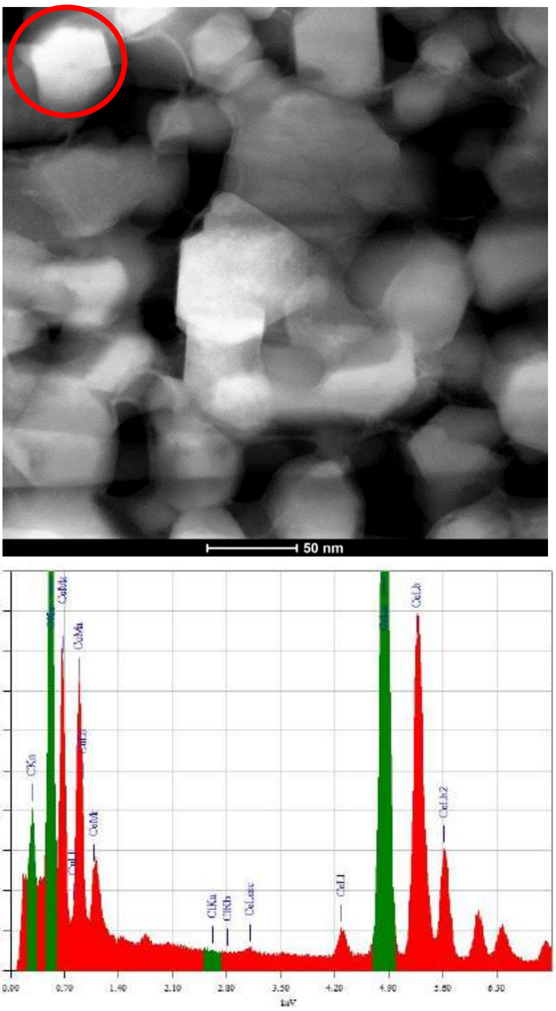

Figure 9 TEM image (top) and EDS spectrum (bottom) of HSSA Cl^--contaminated CeO_2 particles heat treated at 900 °C.

Conclusions and Future Work

An additional cerium chloride heptahydrate phase (unseen in samples prepared by NNL) appears after contamination in HSSA CeO_2, suggesting heterogeneity, but not LSSA. XPS can detect changes in Cl^- concentration, but IR spectroscopy only detects changes in water, with a possible link between the two contaminants. Cl^- on HSSA CeO_2 drops below the LOD of EDS after heat treatment at 900 °C, but Cl^- on contaminated LSSA CeO_2 (both on the surface and leachable) is also below the LOD of EDS and only 35 ppm is detectable by IC.

Future work will involve contaminating CeO_2 with a range of HCl vapour concentrations and relative humidities, followed by heat treatment. Analysis of recent XPS results with *in situ* heating and Mass Spectrometry will be performed, to detect volatilised substances. The same experiments will be carried out at ITU, Germany, using CeO_2, ThO_2 and UO_2 thin films, fresh PuO_2 from ITU and aged Magnox PuO_2 from Sellafield.

Acknowledgements

John Waters (UoM, XRD)

Jon Fellowes (UoM, SEM-EDS)

Libor Kovarik (PNNL, TEM-FIB)

Alastair Bewsher (UoM, IC)

References

1 C. Campbell, C. Gregson, R. Orr, H. Sims, R. Taylor and K. Webb, *NNL, National Nuclear Laboratory, Sellafield*, 2014, **12869**, 1–68.

2 R. J. Taylor, *Update on experimental work at NNL underpinning Sellafield plutonium storage*, 2013.

Theme 2 – PuO_2 and Fuel Residues
DISTINCTIVE 2nd Annual Meeting
Bristol, UK
19th – 20th April 2016

Radiolysis of H_2-O_2 mixtures of relevance to long term storage of PuO_2

L. Jones*[1], H.S. Sims[2], R.M. Orr[3] and S.M. Pimblott[1]

*Correspondence: Luke.jones-2@manchester.ac.uk

[1] School of Chemistry (University of Manchester, Dalton Cumbrian Facility, Westlakes Science Park, Moor Row, Cumbria, CA24 3HA, UK)
[2] National Nuclear Laboratory (NNL, Culham Science Centre, Abingdon, Oxfordshire, OX14 3DB, UK)
3 National Nuclear Laboratory (NNL, Sellafield Central Laboratory, Sellafield, Seascale, Cumbria, CA20 1PG, UK)

Abstract

Radiolysis of adsorbed water on the surface of PuO_2 could lead to the build-up of potential detonable atmospheres of H_2 and O_2 during long term storage of this product. This project aims to investigate the radiolysis of H_2-O_2 mixtures to determine the extent of recombination of these gases. This research was undertaken at the Dalton Cumbrian Facility utilising ^{60}Co γ rays and accelerated He^{2+} ions as sources of ionising radiation. Gas chromatography was used to analyse post-irradiated samples.

Introduction

The UK currently has the largest stockpile of civil separated plutonium in the world. It is a by-product of reprocessing spent nuclear fuel from the UK's fleet of nuclear reactors [1]. The majority of plutonium is stored at the Sellafield site as PuO_2 powder. There are two product streams at Sellafield by which this powder is formed. Magnox PuO_2 is obtained from spent fuel from Magnox reactors which used uranium metal as fuel, while PuO_2 product from THORP is obtained from spent fuel from AGR reactors, which use UO2 as the fuel type.

The final stages of the finishing process for PuO_2 powder is calcination at high temperatures (> 600 °C), this ensures removal of organics and volatiles from PuO_2. The moisture content is required to be less than 0.5 wt.% before the product can go into storage, which is in line with the United States Department of Energy standard [2].

After calcination, the PuO_2 product is packaged in multi-can containers. In the UK there are two designs. Magnox PuO_2 is packaged in a screw top aluminium can, placed inside a polyethylene bag and welded into a stainless steel outer can. The atmosphere inside the can is a 50:50 mix of argon and air. PuO_2 from the THORP product line is packaged in a stainless steel three can system with a pure argon atmosphere [3, 4].

The default option for this stockpile is long term storage, with the Sellafield site plan suggesting the material will be stored until the site end point in 2120.

Whilst in storage, the cans are a dynamic system. PuO_2 and its radioactive daughters undergo decay and generate heat. This environment will potentially lead to chemistry occurring with the overlying headspace and any adsorbed species on the oxide surface. A number of processes may occur which could lead to pressurisation of the cans and possible can failure. Therefore an understanding of the radiation chemistry of the gas phase in the presence of an oxide surface is of importance.

One such process is the radiolysis of adsorbed water, which could lead to potential detonable atmospheres inside the storage canisters.

Methodology Details

Gas Mixing

A bespoke manifold has been designed and commissioned to be able to mix various ratios of H_2-O_2 and Ar gas. The schematic is shown in Figure 1

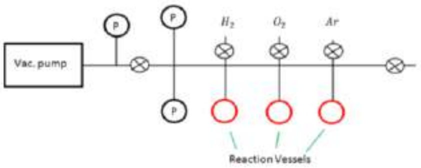

Figure 1: Bespoke gas mixing manifold made from 316-SS Swagelok fittings

Irradiation Sources

A Foss Therapy Model 812 self-shielded irradiation source is utilised to perform gamma irradiations. The irradiator is capable of delivering a dose rate between 400 and 4 Gy min^{-1} depending on attenuation and distance from the sources.

An NEC 5 MV tandem ion accelerator is utilised to perform ion irradiation studies. The accelerator is capable of delivering a beam of positive ions of light charged particles (H^+ and He^{2+}) up to energies of 10 and 15 MeV respectively. Samples are placed at the end of one of the accelerator's six beam lines where irradiations and/or analysis can be carried out *in-situ*. In this research, 5.5 MeV He^{2+} ions will be used to simulate the α decay of plutonium-238.

Analysis

The GC used in this research is an SRI Instruments Multiple gas analyser #1, equipped with a thermal conductivity detector (TCD). The stationary phase is a 6 ft. long, 1/8 " diameter packed column of molecular sieve 13X beads. The mobile phase is high purity argon (99.999% pure), specifically chosen to increase the sensitivity of the instrument towards H_2 measurements.

Results and Discussion

The following section details the results of radiolysis of three mixtures of H_2-O_2-Ar gas. These mixtures are:

- Equal volumes of H_2 and O_2 (stoichiometry 5 : 5 : 90 H_2-O_2-Ar (by volume));
- Water stoichiometry of H2 and O2 (stoichiometry 5 : 2.5 : 92.5 H_2-O_2-Ar (by volume)); and
- O_2 excess atmospheres (stoichiometry 2.5 : 5 : 92.5 H_2-O_2-Ar (by volume))

Figure 2 details depletion of H_2 as a function of dose using ^{60}Co γ rays

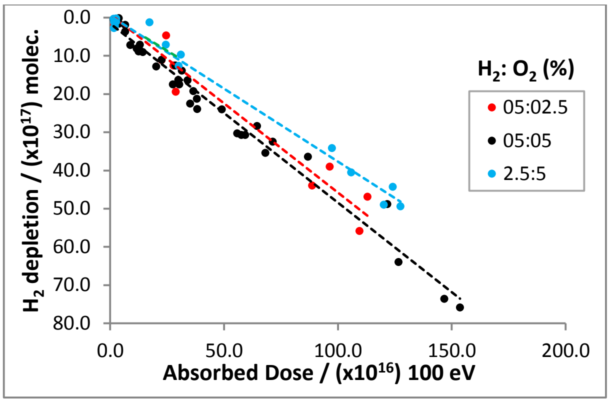

Figure 2: Results of gamma radiolysis of different ratios of H_2-O_2-Ar illustrating H_2 depletion as a function of absorbed dose

Table 1 outlines the calculated G (-H_2)-values for these three systems and associated errors

System (H_2-O_2-Ar (by volume))	*G*(-H_2) / molecules 100 eV^{-1}	Error (σ_{slope})
5 : 2.5 : 92.5	4.66	± 0.37
5 : 5 : 90	4.68	± 0.13
2.5 : 5 : 92.5	3.81	± 0.12

Table 1: Calculated G(-H_2) values for several different ratios of H_2-O_2-Ar gas using gamma radiation

These values are a similar order to those attained by Dautzenberg [5]. The order of this system is still not agreed upon in literature, with both zero and first order kinetics discussed [5,6]. From the calculated G(-H_2) it is possible to apply a first order kinetic nature to the results as depletion of H_2 increases with increasing initial H_2 concentration, however the concentration of O_2 also changes in these systems. The calculated G(-H_2) values in Table 1 do not increase in proportion to the increase in H_2 concentration therefore zero order is also likely.

Figure 3 details depletion of H_2 as a function of dose using 5.5 MeV He^{2+} ions.

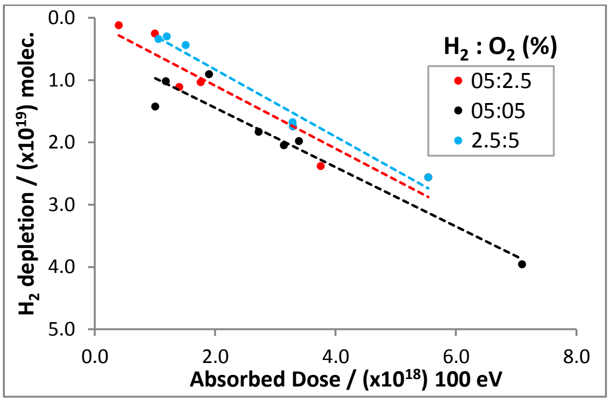

Figure 3: Results of He^{2+} radiolysis of different ratios of H_2-O_2-Ar illustrating H_2 depletion as a function of absorbed dose

Table 2 outlines the calculated G(-H_2)-values for these three systems and associated errors

System (H_2-O_2-Ar(by volume))	*G*(-H_2) / molecules 100 eV^{-1}	Error (σ_{slope})
5 : 2.5 : 92.5	5.04	± 0.72
5 : 5 : 90	4.76	± 0.61
2.5 : 5 : 92.5	5.38	± 0.46

Table 2: Calculated G(-H_2) values for several different ratios of H_2-O_2-Ar gas using He^{2+} radiation

The G(-H_2) values calculated in Table 2 are of the same magnitude as seen in Table 1 for gamma irradiations indicating the depletion of H_2 is independent of radiation energy and type. The increased errors are due to a reduced sample population.

Figure 4 is a compiled data set of H_2 depletion data for the three gaseous systems of interest utilising both gamma and He^{2+} radiation sources.

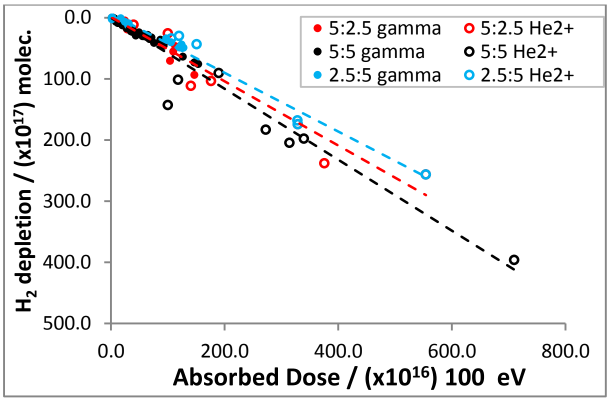

Figure 4: Results of gamma and He^{2+} radiolysis of different ratios of H_2-O_2-Ar illustrating H_2 depletion as a function of absorbed dose

From this figure it is clear that H_2 continues to be depleted at high absorbed doses, with no steady state between H_2-O_2 recombination and radiolysis of water vapour being reached

Conclusions and Future Work

It is clear there is no Linear Energy Transfer (LET) effect on this gaseous system as G(-H_2) values are independent of radiation type. H_2 continues to be depleted at high doses indicating that the rate of H_2-O_2 recombination is faster than the rate of water radiolysis as a steady state is not reached.

Inclusion of a metal oxide powder would provide a better simulation of PuO_2 storage canisters. This would provide a better mechanistic understanding of the system. Firstly inactive PuO_2 surrogates such as CeO_2 and ZrO_2 should be utilised before experiments with PuO_2 powder could be undertaken.

Acknowledgements

This project was jointly funded by the EPSRC and Sellafield Sites Ltd.

Paul Cook and Jeff Hobbs (both of Sellafield Sites Ltd. for advice and reference

References

[1] *Management of the UK's plutonium stocks: a consultation on the long-term management of UK owned separated civil plutonium*, 2011, Department of Energy and Climate Change. p. 12-13.

[2] *Stabilization, Packaging, and Storage of Plutonium-Bearing Materials*, D.o. Energy, Editor 2012.

[3] Cook, P., H.E. Sims, and D. Woodhead, *Safe and Secure Storage of Plutonium Dioxide in the United Kingdom.* Actinide Research Quarterly, 2013(2): p. 20-25.

[4] Sims, H.E., et al., *Hydrogen yields from water on the surface of plutonium dioxide.* Journal of Nuclear Materials, 2013. **437**(1-3): p. 359-364.

[5] Dautzenberg, D., *Gamma-radiolysis of Hydrogen Oxygen Mixtures 1 Influences of Temperature, Vessel Wall, Pressure and Added Gases (N2, AR, H2) on the Reactivity of H2/O2-Mixtures.* Radiation Physics and Chemistry, 1989. **33**(1): p. 61-67.

[6] Benjamin, B.M. and H.S. Isbin, *Recombination of Hydrogen and Oxygen in Presence of Water Vapour under Influence of Radiation.* Energia Nucleare, 1966. **13**(4): p. 165-172.

Ceramic wasteforms for actinide disposition

Shikuan Sun, Martin Stennett and Neil Hyatt

*Correspondence: shikuan.sun@sheffield.ac.uk

Immobilisation Science Laboratory, Department of Materials Science and Engineering, The University of Sheffield,
(Mappin Street, Sheffield S1 3JD, United Kingdom)

Abstract

Pyrochlore ceramic and zirconolite glass-ceramic wasteforms are the potential host phases for actinide disposition. Composition – processing – structure relations in a series of pyrochlore related wasteforms (prototypically $CaCeTi_2O_7$ and $CaUTi_2O_7$) were investigated in this work, using Rietveld modelling of powder X-ray and neutron diffraction data and analysis of Ce and U L_3 edge XANES. An almost single phase Ce pyrochlore with composition of $Ca_{0.60}Ce_{0.92}Ti_{2.27}O_7$, was synthesised and the first reliable structure determination made from analysis of neutron diffraction data (space group *Fd-3m*, a = 10.1462(4) Å). In addition, the synthesis of uranium betafite pyrochlore ceramics, was investigated at 1320°C in flowing N_2 from $CaTiO_3$, TiO_2, ZrO_2 and U_3O_8 as raw precursors. The betafite phase was obtained in high yield (> 85%) and a mean uranium oxidation state of 4.3±0.1 was determined by U L_3 edge XANES; all U_3O_8 was incorporated into the ceramic host phase.

Introduction

A wide range of ceramic matrices have been proposed as potential candidates for the disposition of actinides [1,2]. In particular, titanate ceramics with the pyrochlore structure are promising matrices for the immobilisation of plutonium, due to their chemical durability and radiation tolerance [3]. In the present work, cerium pyrochlore, prototypically $CaCeTi_2O_7$, was first studied as a model system for ceramic disposition of Pu. Because of the size similarity between tetravalent cerium (0.97 Å, CN = 8) and tetravalent plutonium (0.96 Å, CN = 8), cerium pyrochlore is a potentially useful analogue ceramic wasterform from a crystallographic viewpoint [4]. Targeting the single phase of cerium pyrochlore, the chemical composition, crystal structure and oxidation state of the as-prepared pyrochlore products were investigated.

In addition, the preparation of synthetic uranium betafite pyrochlore, prototypically $CaUTi_2O_7$, was investigated. Betafite ceramics were fabricated at waste loading of 35 wt% and 45 wt%, using U_3O_8 as the uranium source. Metallic Fe and Ni was added to assess the effect of an imposed partial oxygen pressure on the wasteform phase assemblage and microstructure. The mean uranium oxidation state was investigated to understand the effect of chemical stoichiometry, processing conditions, and metal additions on the role of uranium as a charge balancing species.

Methodology Details

Preparation

Cerium pyrochlore samples were prepared by solid state reaction between $CaCO_3$, CeO_2 and TiO_2. These raw materials with various molar ratios of Ca:Ce:Ti were mixed, in an effort to obtain a single phase pyrochlore product. Reagents were mixed using planetary milling containing Si_3N_4 milling media and isopropanol as a carried fluid. The mixed precursors were reacted in alumina crucibles at 1250°C for 10 h in air with a ramp rate of 5°C/min.

Uranium betafite were prepared by adding U_3O_8 to the oxide precursor material ($CaTiO_3$, TiO_2 and ZrO_2) at two different U_3O_8 waste loading – 35 wt% and 45 wt%, corresponding to the nominal stoichiometries $Ca_{0.96}U_{0.48}Zr_{0.18}Ti_{2.20}O_7$ and $Ca_{0.87}U_{0.67}Zr_{0.16}Ti_{2.01}O_7$. The raw materials were mixed using rotary ball milling for 16 hours. For the waste-loading of 45 wt% U_3O_8, additional samples were fabricated with 10 wt% Fe and 10 wt% Ni metallic buffer. The mixture was pressed in a stainless steel die using 1.5 tonnes loads. The resulting powder compact were then placed in alumina crucibles and sintered in flowing N_2 at 1320°C for 2 hours, with a ramp rate of 5°C/min.

Characterisation

The phase analysis of the samples was performed by X-ray diffraction (XRD, D2 Phaser, Bruker, λ = 1.5406 Å). Quantitative phase analysis by Rietveld refinement was performed using the GSAS suite of programs [5]. Neutron diffraction data of Ce-pyrochlore were acquired at room temperature on the High Resolution Powder Diffractometer using Ge (733) monochromator with the wavelength λ = 1.1969 Å at NIST Centre for Neutron Research, USA. Ce and U L_3 edge X-ray absorption spectroscopy data were acquired on beamline B18 at Diamond Light Source and Beamline X23A2 at the National Synchrotron Light Source (USA), respectively. For the bulk specimens, the density was measured by the Archimedes method and the microstructure was observed using a scanning electron microscope (SEM, TM3030, Hitachi). Semi-quantitative compositional information was acquired using energy dispersive spectroscopy (EDS, Bruker Quantax 70).

Results and Discussion

Cerium pyrochlore

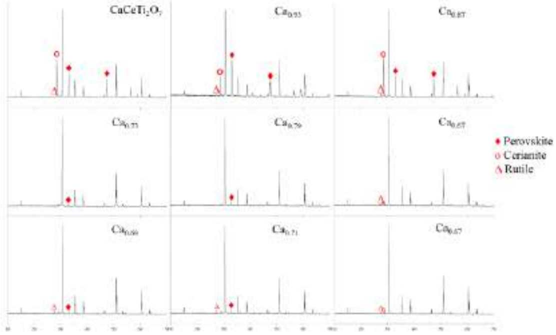

Figure 1. XRD patterns of the products with decreasing the amount of Ca in the starting material. Perovskite: ♦, rutile: Δ and cerianite: o. All other reflections are due to Ce-pyrochlore phase.

Initially, the synthesis of a pyrochlore with the ideal stoichiometry $CaCeTi_2O_7$ was attempted. However, a considerable amount of perovskite and cerianite impurity were detected in the product. The amount was determined to be as follows: pyrochlore, 58.0 wt%; perovskite, 30.1 wt%; cerianite, 10.7 wt%; and rutile, 1.2 wt%. This result is in agreement with previous studies which concluded that synthesis of ideal $CaCeTi_2O_7$ pyrochlore could not be achieved [6].

According to Helean et al. [7], $CaCeTi_2O_7$ pyrochlore was stabilised for Ca deficient stoichiometry, although single phase compositions could still not be achieved. Therefore, we made a careful study of the synthesis of pyrochlore compositions involving Ca deficiency with an excess of Ti for charge balance. As shown in Figure 1, the relative intensity of the Bragg reflections associated with the impurity phases decreased with increasing Ca / Ti ratio in the nominal composition. Finally, a near single phase Ce-pyrochlore was obtained for the nominal composition $Ca_{0.61}Ce_{1.08}Ti_{2.12}O_7$; the chemical composition was determined by quantitative EDS analysis to be $Ca_{0.60}Ce_{0.92}Ti_{2.27}O_7$. The pyrochlore structure ($A_2B_2O_7$) can accept excess TiO_2 considering B cation substitution on to the A cation lattice with charge compensation by forming A cation vacancies, which was consistent with the modelling predictions of Ebbinghaus et al. [8]. Therefore, subsequent refinement of neutron diffraction was performed by assuming the excess Ti cation located in Ca/Ce site (*16d*). The results of Rietveld profile refinement for the as-prepared pyrochlore was presented in Table 1. The profile refinement was given in Figure 2, where a calculated pattern (solid line) has been fitted to measured data points (dots). The difference between the experimental data and calculated fit was displayed below these and indicated a good fit to the data; the tick marks indicated expected peak positions in the calculated profile. The cation non-stoichiometric pyrochlore exhibit cubic symmetry (space group Fd-3m). A small quantity of TiO_2 impurity was observed in the product without the existence of the perovskite and cerianite impurities. The final refined results in ND were a = 10.1462(4) Å, which were slightly smaller than the previously reported lattice parameter 10.1477 Å [7].

Table 1 Refined structural parameters for cerium pyrochlore from Rietveld analysis of neutron powder diffraction data.

Space group: *Fd-3m* a = 10.1462(4) Å					
Atom	Site	x	y	z	U_{iso} × 100(Å^2)
Ca1^a	16d	0.5	0.5	0.5	0.532
Ce1^a	16d	0.5	0.5	0.5	0.532
Ti1^a	16d	0.5	0.5	0.5	0.532
Ti2^b	16c	0	0	0	0.859
O1^b	48f	0.3267(2)	0.125	0.125	1.333
O2^b	8b	0.375	0.375	0.375	1.482

Powder statistics: χ^2 = 2.428 R_{wp} = 5.48%, R_p = 4.41%
a) Occupancy fixed according to quantitative EDS stoichiometry: n_{Ca} = 0.30; n_{Ce} = 0.46, n_{Ti} = 0.14; b) Occupancy $n_{Ti,O}$ = 1.

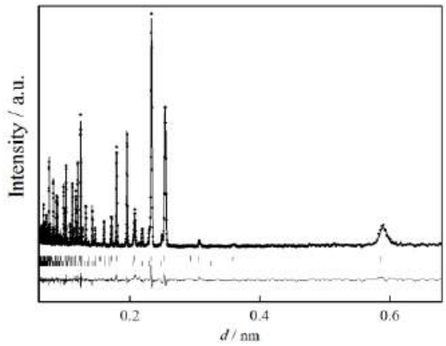

Figure 2. Neutron diffraction of nearly pure Ce-pyrochlore refined in space group *Fd-3m*. Fit: solid line; observed data: dot and allowed reflections: tick marks. The impurity of TiO_2 is included.

The Ce L_3 edge X-ray absorption near edge structure (XANES) of $Ca_{0.60}Ce_{0.92}Ti_{2.27}O_7$ is shown in Fig. 3 and from comparison of the spectra with those of reference compounds, it is apparent that the XANES of Ce-pyrochlore closely resemble those of CeO_2, and to a lesser extent those of $SrCeO_3$, demonstrating that Ce^{4+} with CN = 8 was the dominant species in Ce-pyrochlore phase (i.e. Ce^{4+} in an environment similar to CeO_2). The amount of Ce^{3+} was estimated to be 10 % of total Ce by linear combination fitting of reference spectra using the program Athena [9]. The average oxidation state of Ce was thus estimated to be 3.9 v.u (with the experimental error ±0.1).

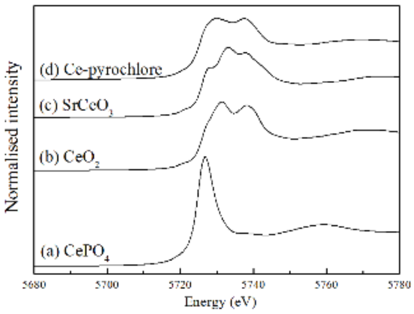

Figure 3. Ce L_3 X-ray absorption near edge spectra (XANES) of Ce-pyrochlore.

Uranium betafite

XRD analysis of uranium betafite compositions, demonstrated the formation of a pyrochlore compound as the major phase in all samples. Reflections that could not be attributed to a pyrochlore were also observed indicating the formation of one or more secondary phase. The pyrochlore reflections compared well with the reported pattern of $Ca_{0.92}U_{1.08}Ti_{1.99}O_7$ [JCPDS45-1477, Ref. 10]. This indicated that isostructural compounds had been formed with space group of *Fd-3m* in this study. It should be noted that no residual U_3O_8 remained in all as-prepared ceramics.

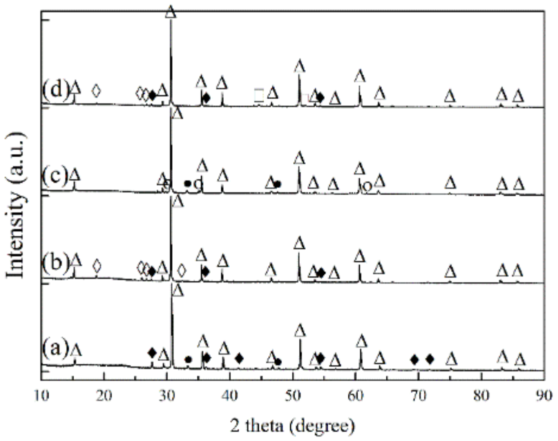

Figure 4 XRD patterns of the product after sintering with 35 wt% U_3O_8 (a), 45 wt% U_3O_8 (b), 45 wt% U_3O_8 and 10 wt% Fe (c) and 45 wt% U_3O_8 and 10 wt% Ni (d) at 1320°C in flowing N_2. Betafite: Δ, rutile: ♦, perovskite: ●, brannerite: ◊, ulvospinel: o and nickel: □.

The chemical composition of the betafite phase in the sample with 35 wt% and 45 wt% U_3O_8 was determined by EDS as $Ca_{1.13}U_{0.55}Zr_{0.17}Ti_{2.15}O_7$ and $Ca_{1.09}U_{0.67}Zr_{0.15}Ti_{2.10}O_7$, respectively, revealing that the U deficiency in the A site was balanced by the excess Ca and Zr/Ti. Rietveld refinement of XRD patterns was performed for the quantitative phase analysis (QPA). The mass fraction of betafite phase was determined to be 84.80 wt%, 94.38 wt%, 86.42 wt% and 85.82 wt% for the product with the U_3O_8 loading of 35 wt%, 45 wt%, and 45 wt% with Fe and Ni buffer, respectively. Note that QPA demonstrates that synthesis of ceramics with a high betafite yield is possible at relatively low temperature (1320°C) in contrast to the conclusions of previous studies (< 75 wt% at 1450°C, Ref. 11)

Full densification of betafite ceramics was nearly achieved (> 98.0% of TD) for the sample with 35 wt% and 45 wt% U_3O_8. A relative density of 86.9% was measured for the sample with iron addition, which agreed with the considerable porosity observed in SEM (not given in this summary).

U L_3 XANES of the as-obtained betafite samples were measured and compared with UTi_2O_6, $U_{0.5}Y_{0.5}Ti_2O_6$ and $CaUO_4$ as standards for U^{4+}, U^{5+} and U^{6+}. All the as-prepared samples showed XANES spectra similar to UTi_2O_6, indicating that the majority of uranium in the product should be tetravalent. Construction of a calibration line, relating the absorption edge energy to oxidation state, allowed the average uranium oxidation state of the samples to be estimated. The values of the average oxidation state were calculated to be 4.4, 4.2, 4.3 and 4.3 (within experimental error ± 0.1) for the products with U_3O_8 loading of 35 wt%, 45 wt%, and 45 wt% with Fe and Ni buffer, respectively. The average oxidation state of uranium determined by XANES was close to that determined by the chemical formula.

Although the synthesis of near single phase betafite was obtained with the stoichiometry $Ca_{1.25}U_{0.75}Ti_2O_7$, the samples were relatively porous (around 80% of theoretical density) after sintering in argon at 1400°C and were characterised by an average U oxidation state of 4.7+ [12]. The lower average U oxidation state and enhanced densification observed in this study should improve the stability of these materials to aqueous dissolution which is advantageous for geological disposal (given the lower solubility of U^{4+}).

Conclusions and Future work

A series of pyrochlore wasteforms were fabricated to understand composition – processing – structure relations for actinide disposition. Results shown that (1) near single phase Ce-pyrochlore was stabilised by A-site vacancies, with an average Ce oxidation state of 3.9 ± 0.1 v.u.; (2) U-betafite ceramics were obtained in 85 wt% yield with up to 98% theoretical density and a mean uranium oxidation state of 4.3 ± 0.1 v.u.; no residual U_3O_8 was detected in the ceramics.

Future experiments will seek to understand the radiation resistance and the dissolution rate of pyrochlore ceramics.

Acknowledgements

This work was funded in part by EPSRC under grant EP/L014041/1 - Decommissioning, immobilisation and storage solutions for nuclear waste inventories (DISTINCTIVE). This work was performed in the MIDAS Facility at The University of Sheffield, which was established with support from the Department for Energy and Climate Change. NCH is grateful to the Royal Academy of Engineering and the Nuclear Decommissioning Authority for funding. We thank Dr Ewan Maddrell at the National Nuclear Laboratory for useful discussions.

References

1. W. E. Lee, M. I. Ojovan, M. C. Stennett, N. C. Hyatt, *Adv. Appl. Ceram*., 105 (2006), pp. 3.
2. O. Terra, N. Dacheux, F. Audubert, R. Podor, *J. Nucl. Mater.*, 352 (2006), pp. 224.
3. R. C. Ewing, W. J. Weber, F. W. Clinard, *Prog. Nucl. Energy*, 29 (1995), pp. 635.
4. P. A. Bingham, R. J. Hand, M. C. Stennett, N. C. Hyatt, M. Harrison, *Mater. Res. Soc. Symp. Proc.*, 1107 (2008), pp. 421.
5. A. C. Larson, R. B. von Dreele, Los Alamos National Laboratory Report LAUR (2000), pp. 86-748.
6. L. A. J. Garvie, H. Xu, Y. Wang, R. L. Putnam, *J. Phys. Chem. Solids*, 66 (2005) pp. 902.
7. K. B. Helean, A. Navrotsky, E. R. Vance, M. L. Carter, B. Ebbinghaus, O. Krikorian, J. Lian, L. M. Wang, J. G. Catalano, *J. Nucl. Mater.*, 303 (2002) pp. 226.
8. C. R. Stanek, L. Minervini, R. W. Grimes, *J. Am. Ceram. Soc*., 85(2002) pp. 2792.
9. B. Ravel, M. Newville, *J. Synchrotron Radiat*., 12 (2005), pp. 537.
10. F. J. Dickson, K. D. Hawkins, T. J. White, *J. Solid State Chem.*, 82 (1989) pp. 146.
11. E. R. Vance, G. R. Lumpkin, M. L. Carter, D. J. Cassidy, C. J. Ball, R. A. Day, B. D. Begg, *J. Am. Ceram. Soc*., 85(2002) pp. 1853.
12. M. James, M. L. Carter, Z. Zhang, Y. Zhang, K. S. Wallwork, M. Avdeev and E. R. Vance, *J. Am. Ceram. Soc*., 93 (2010) pp.3464.

Developing Glass-Ceramic Wasteforms for the Immobilisation of Pu-Bearing Waste-Streams

S. M. Thornber*[1], M. C. Stennett[1] & N. C. Hyatt[1]

*Correspondence: sthornber1@sheffield.ac.uk

[1] *The University of Sheffield, Hadfield Building, Mapping Street, Sheffield, S1 3JD, UK*

Abstract

The UK has 140 tonnes of separated civil PuO_2 stored at the Sellafield site. The strategy for dealing with this stockpile involves reuse in nuclear fuels, however a significant fraction has been identified as higher activity waste requiring immobilisation into stable wasteforms. This project is fundamental to gaining knowledge and understanding of zirconolite based glass-ceramics as future wasteforms for specific streams of these plutonium wastes. Consolidated using a hot isostatic press, an optimised formulation has been achieved to progress with waste incorporation experiments.

Introduction

The UK's current policy for dealing with the plutonium stockpile stored at the Sellafield site involves reuse as nuclear fuel where possible[1], however, a significant fraction of the stockpile is unsuitable for retrieval of the Pu and has been classified as higher activity waste.[2] We are developing suitable wasteforms and technologies for the immobilisation of these highly variable wastes, for which current vitrification methods are unsuitable.

Some Pu-wastes have significant quantities of impurities and glass formers. Glass-ceramics are being developed for the low purity Pu-residue waste-streams to provide flexibility for incorporating the extensive range of impurities that are retained in the amorphous glass matrix whilst partitioning the actinides into the durable ceramic phase. Coupling zirconolite with a glass component maintains the high loading capacity and durability properties of the ceramic, whilst adding the flexibility and ease of processing of the glass.[4] Zirconolite readily accepts Pu into its structure as seen through its use in Synroc-C and natural analogues show excellent radionuclide retention even when completely metamict.[6, 7]

Hot isostatic pressing is a thermal treatment method whereby high temperature and pressure consolidate dense, durable materials, with significant volume reductions and subsequent cost savings compared to current vitrification methods.[3–5] HIPing is flexible toward processing different matrix materials including glass, glass-ceramic, ceramic and metal encapsulants. Due to the immense variability in Pu-residue waste-streams it is essential to utilise a method that is not limited to specific processing parameters and is capable of processing these diverse wastes.

Development of glass-ceramic wasteforms at The University of Sheffield

This project is at the forefront of current research and development taking place in the UK on the consolidation of HIPed Pu-residue wasteforms. The project aims to develop zirconolite based glass-ceramic systems whilst considering the crystalline phase assemblage and stability, waste incorporation and the effect of mineralisers on waste digestion.

The formation of zirconolite in the glass-ceramic systems is thermodynamically unfavourable to other phases; sphene ($CaTiSiO_5$), zircon ($ZrSiO_4$) and rutile (TiO_2).[8] In recent work, the crystalline phase stability with respect to the glass composition has been investigated with the aim to determine a formulation that optimises the yield of zirconolite. The glass composition and glass fraction were varied to fabricate a qualitative phase map of the crystalline phase assemblage. All samples were consolidated inside hermetically sealed stainless steel canisters at 1250 °C for 4 hours under 103 MPa of isostatic pressure.

Method

A matrix of samples investigating the effect of glass fraction and composition on the crystalline phase assemblage were fabricated with varying Al_2O_3 concentrations, according to the target glass phase $Na_2Al_{1+x}B_{1-x}Si_6O_{16}$, where x=0, 0.2, 0.4, 0.6, 0.8, 1.0, and increasing glass fractions; 30 wt%, 50 wt% and 70 wt%. All samples were packed into stainless steel canisters and all volatiles were removed before being HIPed at 1250 °C for 4 hrs under 103 MPa of pressure.

Results

Zirconolite forms as the product in one of two competing reactions generally resulting in an assembly of up to 4 crystalline phases; zirconolite ($CaZrTi_2O_7$), sphene ($CaTiSiO_5$), zircon ($ZrSiO_4$) and rutile (TiO_2).[8] Such phases have different radiation tolerances and volume expansion behaviour with respect to actinide alpha decay, which ultimately results in stress relief cracking of the final wasteform. Hence, it is important to maximise the formation of zirconolite and minimise the presence of the unwanted phases sphene, zircon and rutile.

The XRD traces in Figure 1 demonstrate how the Al_2O_3 concentration in the glass phase affected the crystalline phase assemblage. Increasing the Al_2O_3 content significantly reduced the presence of the unwanted phases shown by the decrease in relative peak intensities in Figure 1 (top XRD pattern). Consequently, a higher yield of zirconolite was achieved.

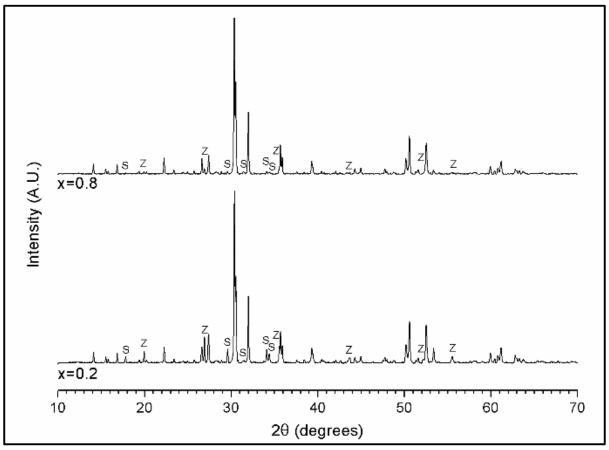

Figure 1. XRD plot showing the effect of increasing Al in $Na_2Al_{1+x}B_{1-x}Si_6O_{16}$ glass on the intensity of peaks corresponding to unwanted phases; sphene (pdf-card 01-085-0395) and zircon (pdf-card 04-007-5058) (labelled as S and Z, respectively). All unlabelled peaks correlate to zirconolite (pdf-card 04-007-6895).[9]

The effect of increased Al_2O_3 in the glass composition in stabilising the desired zirconolite phase was observed for all ceramic / glass ratios. However, a higher glass fraction resulted in a higher yield of undesired phases. Figure 2A and 2B are micrographs of a 30 wt% glass fraction sample and a 50 wt% glass fraction sample, respectively, with glass composition $Na_2Al_{1.4}B_{0.6}Si_6O_{16}$, showing the increase of undesired phases associated with the higher glass fraction. At 30 wt% glass, the undesired phases were gradually reduced such that the 70 wt% ceramic / 30 wt% glass formulation afforded only zirconolite as the crystalline phase for the $Na_2Al_2Si_6O_{16}$ glass. As well as removing undesired phases and the risk of stress release cracking, it is important to maximise the yield of zirconolite, the actinide host phase, in order to maximise the actinide loading capacity of the wasteform. A higher loading capacity reduces the overall number of wasteform packages requiring processing and the costs associated with post-processing storage, maintenance and disposal.

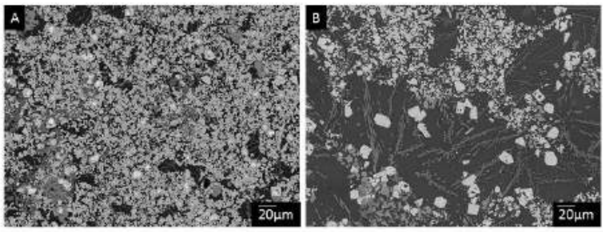

Figure 2. SEM micrographs comparing the microstructures and phase assemblage of A) 30 wt% glass fraction and B) 50 wt% glass fraction. Both samples have the same glass composition $Na_2Al_{1.4}B_{0.6}Si_6O_{16}$.[9]

Conclusions and Future Work

The crystalline phase assemblage is highly controlled by the glass composition and fraction of the glass-ceramic wasteform. By increasing the Al_2O_3 concentration in the glass phase and having a higher ceramic fraction, an optimised formulation was obtained. The 70 wt% ceramic / 30 wt% glass formulation, with glass phase $Na_2Al_2Si_6O_{16}$, attained a single crystalline phase assemblage of zirconolite. Current work is investigating the waste incorporation and wasteform properties of the optimised formulation.

Acknowledgements

This work was funded in part by EPSRC under grant EP/L014041/1 - Decommissioning, immobilisation and storage solutions for nuclear waste inventories (DISTINCTIVE), and by award of a Nuclear Decommissioning Authority sponsored EPSRC DTG-CASE award to ST. This work was performed in the MIDAS Facility at The University of Sheffield, which was established with support from the Department for Energy and Climate Change. NCH is grateful to the Royal Academy of Engineering and the Nuclear Decommissioning Authority for funding. We thank Dr Ewan Maddrell at the National Nuclear Laboratory for useful discussions.

References

[1] Nuclear Decommissioning Authority (NDA), *Progress on approaches to the management of separated plutonium - Position paper - v1.0*. Nuclear Decomissioning Authority, 2014.

[2] Nuclear Decommissioning Authority, *Conditioning of Plutonium Residues by Hot Isostatic Pressing and Options for packaging and Disposal (pre-conceptual stage) Summary of Assessment Report*. 2009.

[3] C.R. Scales, E.R. Maddrell, N. Gawthorpe, B.D. Begg, S. Moricca, and R.A. Day, “Development of a Process for the Immobilisation of Actinide Containing Residues on the Sellafield site;” in ICEM, 2005.

[4] R.A. Day, S. Moricca, M.W.A. Stewart, B.D. Begg, E.R. Maddrell, C.R. Scales, and N. Gawthorpe, “Technical Demonstration of Zirconolite Glass-Ceramics Processed in a Hot Isostatic Press: An

Option for Immobilisation of Actinide Containing Residues at Sellafield;" in ICEM, 2005.

[5] B. D. Begg, R. A. Day, S. Moricca, M. W. A. Stewart, and E.R. Vance, "Low-risk waste forms to lock up high-level nuclear waste;" in *WM'05*. Arizona, 2005.

[6] S. Moricca, C. Orcutt, M.W.A. Stewart, W. Bermudez, E.R. Vance, T. Eddowes, R. Persaud, and D. Taylor, "Hot isistatic pressing of synroc for nuclear waste disposal.;" in *Adv. Powder Metall. Part. Mater. - Part 4*. Nashville, Tennessee, 2012.

[7] F. Bellatreccia, G. Della Ventura, E. Caprilli, C.T. Williams, and G.C. Parodi, "Crystal-chemistry of zirconolite and calzirtite from Jacupiranga, Sao Paulo (Brazil)," *Mineral. Mag.*, **63** [5] 649–660 (1999).

[8] E. Maddrell, S. Thornber, and N.C. Hyatt, "The influence of glass composition on crystalline phase stability in glass-ceramic wasteforms," *J. Nucl. Mater.*, **456** 461–466 (2015).

[9] S. Thornber, E. R. Maddrell, M. C. Stennett, and N. C. Hyatt, "The Consolidation of Glass-Ceramic Wasteforms by Hot Isostatic Pressing: Sample Optimisation;" in *WM16 Conf. Proc.* Phoenix Arizona USA, 2016.

Understanding actinide sorption and binding to cement materials for radioactive waste management

Antonia S. Yorkshire*[1], John L. Provis[1], Neil C. Hyatt[1] and Claire L. Corkhill[1]

*Correspondence: asyorkshire1@sheffield.ac.uk

[1]*University of Sheffield, NucleUS Immobilisation Science Laboratory, Department of Materials Science & Engineering, Sheffield, UK*

Abstract

Intermediate level waste (ILW) in the UK is currently immobilised using cementitious encapsulation. Cement hydrate phases, which form during the dissolution of cement clinker and pozzolanic additives, are capable of binding radionuclides on the long timescales required during storage and disposal of ILW. This study is focused in particular on the sorption of plutonium, and other actinides, onto fly ash (FA) and blast furnace slag (BFS) cement grouts associated with the encapsulation of plutonium contaminated materials (PCM) and other ILW, respectively. FA cement was synthesised and analysed using scanning electron microscopy (SEM) and X-ray diffraction (XRD) to establish key hydrate phases that may be involved in the uptake and retention of actinides. Hydrotalcite is a BFS cement hydrate phase that is concurrently being prepared for preliminary sorption studies.

Introduction

The baseline treatment strategy for ILW in the UK is encapsulation in a cementitious grout, with eventual disposal in a geological facility. Plutonium contaminated material (PCM) waste is a sub-category of ILW that includes materials contaminated with isotopes of Pu, in addition to other actinides associated with plutonium decay.[1] PCM encompasses materials associated with the handling of plutonium during fuel reprocessing, including HEPA filters; PVC gloves; glassware, and metals and masonry that form the structural materials used in plutonium handling facilities.[2] There is thought to be in excess of 20 000 m^3 of PCM awaiting disposal at the Sellafield site.[3]

The current method for PCM storage is super-compaction and encapsulation in steel drums that are infilled with a fly ash/Portland cement (FA/PC) grout[2,4]

Portland cement clinker undergoes hydration reactions on contact with water to form cement hydrate phases. These phases have the potential to sorb and bind radionuclide species in aqueous solution. Studies have shown, in particular, that calcium silicate hydrate (C-S-H) phases are able to sorb metal cations (e.g. Sr^{3+}, Cm^{3+} and Eu^{3+}) as well as actinides (e.g. U^{6+}).[5–7]

Additionally, supplementary cementitious materials (SCM), such as FA and blast furnace slag (BFS), added to cement blends can also undergo reaction to form secondary cement hydrate phases which may act as further sorbents for radionuclides.

FA is an aluminosilicate glass that is a by-product of coal combustion, used in PCM encapsulation. Other ILW streams tend to be immobilised in a BFS grout; BFS arising from iron extraction processes.

This report will focus primarily on the 1:1 FA/PC cement blend commonly used for PCM encapsulation.[4] SEM and XRD analyses were adopted to identify the key cement hydrate phases present in this cement blend. Further work is described, which will involve batch sorption studies carried out using aqueous suspensions of individual hydrate phases, initially with U(VI) as the sorbate actinide of choice to obtain sorption isotherms. Preliminary analysis has been carried out on the BFS hydrate phase hydrotalcite to determine its suitability for initial sorption tests.

Methodology Details

Cement blend synthesis and curing

Cement paste was formulated at a ratio of 1:1 FA/PC (wt %) and w/s = 0.33 with 5 min mixing time in a Kenwood benchtop mixer. The resulting mixture was transferred into centrifuge tubes and cured at 20°C. The hardened cement paste was sampled at 12, 28 and 90 days curing time for analysis. Hydration was stopped using solvent exchange in acetone.

Cement characterisation

Samples were mounted in epoxy resin and polished to a 1 µm finish using diamond paste for SEM imaging and energy dispersive X-ray (EDX) analysis. Back scattered electron (BSE) images were recorded and EDX maps were counted for 10 minutes. Powder XRD was carried out with particle sizes <63 µm. Measurements were taken between 8° to 70° 2θ, with step a size of 0.02° and a 2 s counting time per step.

Hydrotalcite characterisation

Synthetic hydrotalcite was obtained from Sigma Aldrich. Powder XRD measurements were taken between 10° to 70° 2θ, with a step size of 0.02° and a 0.5 s counting time per step.

Results and Discussion

For the purpose of this report, the 12 and 90 day cement characterisation analyses have been omitted. 28 day curing was considered sufficient time for the initial cement hydrate products to establish and for secondary hydrate phases to begin to nucleate.

SEM: FA/PC 28 days

Figure 1 shows a SEM micrograph of a cenosphere (hollow) type FA particle reacting after 28 days curing The oxygen EDX map indicates the density of the phases present, confirming the hollow nature of the particle. Calcium present throughout the structure verifies the formation of C-S-H gel, which comprises the bulk of the cement matrix. C-S-H and portlandite ($Ca(OH)_2$) are the components of hardened cement paste that lead to early setting strength. Area **A** corresponds to higher concentrations of calcium, suggestive of portlandite formation intermixed within the C-S-H phase. Pozzolanic reactions occur between aluminium and silicon oxides (from FA), portlandite and water to form secondary hydrate phases. An intermixed portlandite phase would therefore promote reaction of the FA particle shown. Silicon and aluminium are primarily concentrated in areas of FA, however there is also evidence of their incorporation within the C-S-H structure.

Formation of ettringite ($Ca_6(Al_2O_6)(SO_4)_3.32H_2O$) or AFm ($Ca_4(Al_2O_6)(SO_4).12H_2O$) type phases are evident from sulfur EDX. From the sulfur map alone, it is difficult to distinguish between the two phases. Magnesium and iron are also present in the structure, likely as periclase (MgO) and iron oxides respectively, also as a FA component. Magnesium appears to be well dispersed throughout the structure and incorporated into the C-S-H phase. Iron, however, is confined only within a few FA particles.

The presence of sodium and potassium demonstrate the high alkalinity of PC. Such conditions result in the dissolution of FA, further contributing to pozzolanic activity, as shown in **Figure 2**.

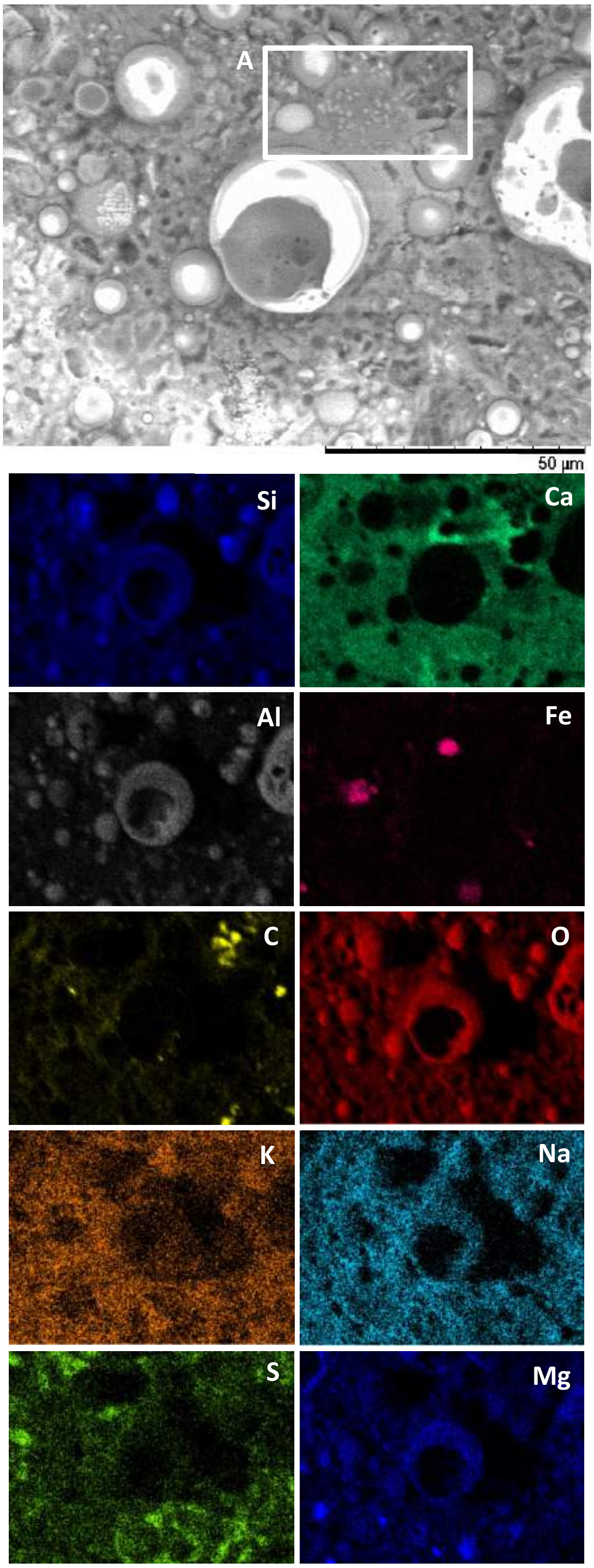

Figure 1: BSE SEM micrograph of a 300 µm FA particle (top) starting to react at 28 days with corresponding EDX maps.

XRD: FA/PC 28 days

The XRD pattern obtained for the 28 day FA grout is

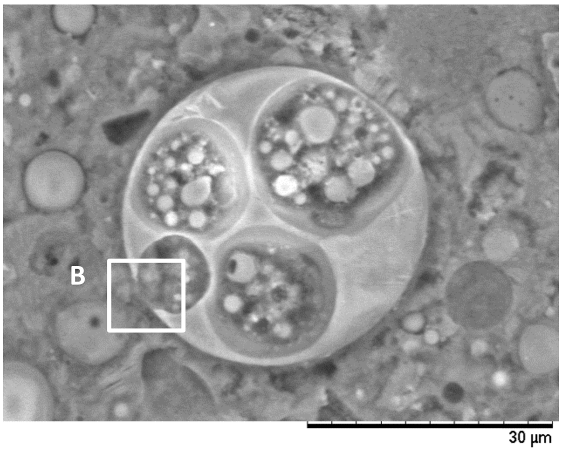

Figure 2: SEM micrograph of a 300 µm plerosphere type FA particle; a cenosphere containing smaller FA particles within its structure. Area **B** shows evidence of this alkali induced dissolution of FA.

shown in **Figure 3** and indicates the crystalline phases formed in the hardened cement paste. Characteristic peaks for portlandite and ettringite confirm the presence of these hydrate phases inferred from EDX measurements. A set of peaks between 31° to 34° 2θ corresponding to unreacted calcium silicates indicate that the cement clinker has not fully hydrated after 28 days. Quartz (SiO_2), mullite ($3Al_2O_32SiO_2$) and periclase are residual minerals from FA. There is also evidence of calcite formation, indicative of carbonation of the sample in air, which is further supported by the detection of carbon by EDX (see **Figure 1**). The diffuse scattering region is found between 20° to 40° 2θ which indicates the amorphicity of other phases forming, such as C-S-H.

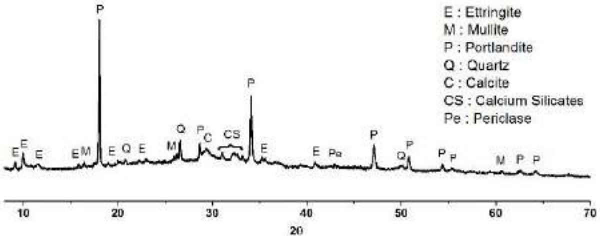

Figure 3: XRD pattern for 1:1 FA/PC at 28 days curing. Crystalline phases are labelled.

Hydrotalcite

Hydrotalcite ($Mg_6Al_2CO_3(OH)_{16}{\cdot}4(H_2O)$) is a layered double hydroxide that has previously been established as an important hydrate phase in BFS cements.[4] **Figure 4** shows the XRD pattern of synthetic hydrotalcite and the corresponding Miller indices, with **Figure 5** displaying the crystal structure.

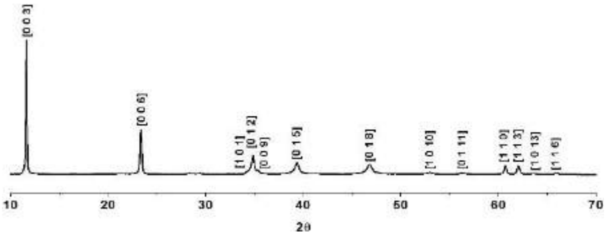

Figure 4: XRD pattern for synthetic hydrotalcite and corresponding Miller indices.

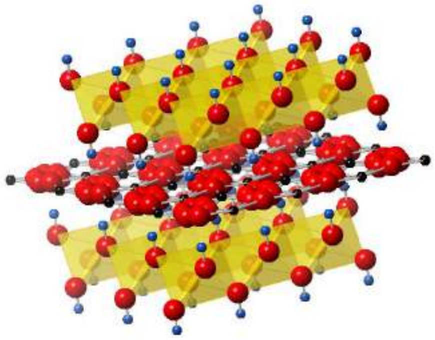

Figure 5: Crystal structure of hydrotalcite adapted from Belloto *et. al.*[8]

Previous studies[9] have shown the ability of thermally treated hydrotalcite to uptake anions in aqueous solution. As a layered double hydroxide, hydrotalcite has an associated interlayer that may act as site for the sorption of radionuclides.

Conclusions and Future Work

The nature of this work has allowed identification of key cement hydrate phases found in FA cements, possibly pertaining to the uptake and retention of actinides from PCM waste. Although hydrotalcite is a slag cement phase, studies using this mineral phase will form a basis to the general understanding of radionuclide sorption to cement grouts related to ILW.

Future work

The individual FA hydrate cement phases that have been identified will be synthesised and characterised. Each phase will be subject to sorption studies, initially using $UO_2(NO_3)_2$ to obtain sorption isotherms. Later studies will involve use of Ce as a surrogate for Pu, with the eventual aim of carrying out higher activity Pu studies. Solid state characterisation will be a useful tool for inferring the mechanism of uptake. Solid state NMR analysis will be used to determine the coordination environment of Al-27 and Si-29, and any changes thereafter as a consequence of radionuclide uptake. Microfocus-XAS will allow direct characterisation of the coordination of radionuclide species associated with the hydrate phase structures.

Acknowledgements

This research was performed in part at the MIDAS Facility, at the University of Sheffield, which was established with support from the Department of Energy and Climate Change. The authors would also like to thank the Nuclear Decommissioning Authority for sponsorship of the project and the National Nuclear Laboratory for industrial supervision.

References

1. *Introduction to plutonium contaminated material (PCM) issues*, NDA Waste & Nuclear Materials Department, Position Paper W&NM/PP/008, (2008).

2. Egan, M., Paulley, A. & Towler, G. *Treatment of Plutonium Contaminated Material at Sellafield,* Report QRS-1372A-1, Sellafield Ltd., (2008).

3. Aggarwal, S., Angus, M. J. & Ketchen, J. *Sorption of radionuclides onto specific mineral phases present in repository cements*, AEA Report NSS/R312, Windscale; Cumbria, (2000).

4. *Treatment of Plutonium Contaminated Material at Sellafield*, Stakeholder Consultation Briefing Note, http://sellafieldsites.com/wp-content/uploads/2012/08/PCM-brochure-low-res.pdf

5. Tits, J., Wieland, E., Müller, C. J., Landesman, C. & Bradbury, M. H., "Strontium binding by calcium silicate hydrates." *J.Colloid Interface Sci.* **300,** 78–87 (2006).

6. Tits, J., Stumpf, T., Rabung, T., Wieland, E. & Fanghänel, T., "Uptake of Cm(III) and Eu(III) by Calcium Silicate Hydrates: A Solution Chemistry and Time-Resolved Laser Fluorescence Spectroscopy Study." *Environ. Sci. Technol.* **37,** 3568–3573 (2003).

7. Harfouche, M. *et al.,* "EXAFS study of U(VI) uptake by calcium silicate hydrates." *J.Colloid Interface Sci.* **303,** 195–204 (2006).

8. Belloto, M. *et al.* "A re-examination of hydrotalcite crystal chemistry." *J. Phys. Chem.* **10,** 8527–8534 (1996).

9. Lu, L., He, J., Wei, M., Evans, D. G. & Duan, X. "Uptake of chloride ion from aqueous solution by calcined layered double hydroxides: Equilibrium and kinetic studies." *Water Res.* **40,** 735–743 (2006).

Computational Studies of Water Adsorption on UO_2 and PuO_2 Surfaces

J. Wellington*[1], A. Kerridge[2], and N. Kaltsoyannis*[3]

*Correspondence: joseph.wellington@ucl.ac.uk
nikolas.kaltsoyannis@manchester.ac.uk

[1] Department of Chemistry, University College London, 20 Gordon Street, London WC1H 0AJ, UK
[2] Department of Chemistry, Lancaster University, Bailrigg, Lancaster LA1 4YB, UK
[3] School of Chemistry, The University of Manchester, Oxford Road, Manchester M13 9PL, UK

Abstract

Density functional theory (DFT) and the periodic electrostatic embedded cluster method (PEECM) are used to study AnO_2 bulk and surfaces (An = U, Np, Pu). Water adsorption was investigated on the (111) and (110) surfaces of UO_2 and PuO_2 with 1 to 4 water molecules adsorbing on the cluster dissociatively or molecularly. Water adsorption on the (110) surface is stronger than on the (111). A mixture of molecular and dissociative adsorption is found to be most favourable on the (111) surface, while dissociative adsorption is seen to be most favourable on the (110) surface. Water in a second layer is found to have hydrogen bonding with the surface and hydroxyls present at the surface. Oxygen 1s binding energies show that molecular and dissociative adsorption could be distinguished by X-ray photoelectron spectroscopy (XPS) on the AnO_2 surfaces.

Introduction

Of the world's c. 250 tonnes of separated plutonium, more than 100 tonnes are stored at Sellafield in the UK as PuO_2 powder in sealed steel cans. Under certain circumstances, gas generation may occur in these cans, with consequent pressurization. Five routes to gas production have been suggested: (i) helium accumulation from a decay; (ii) decomposition of polymeric packing material; (iii) steam produced by H_2O desorption from hygroscopic PuO_2 due to self-heating; (iv) radiolysis of adsorbed water; and (v) generation of H_2 by chemical reaction of PuO_2 with H_2O, producing a postulated PuO_{2+x} phase. The last three mechanisms, all involving PuO_2/H_2O interactions, are complex, interconnected and poorly understood.

Both experimental and theoretical studies of water adsorption are more abundant on UO_2 than on PuO_2, therefore our inclusion of UO_2 in this study allows us to compare the results obtained here with previous studies.

Theoretical studies comparing water adsorption between the UO_2 and PuO_2 surfaces have found water adsorption to be more favourable on the UO_2 than the PuO_2 surface,[1] however, these studies only considered the water molecules adsorbing dissociatively. Comparing the (111) and (110) surfaces, theoretical studies have predicted adsorption of water to be stronger on the (110) than the (111) surface, regardless of whether the adsorption is molecular or dissociative.[1,2] Comparing dissociative and molecular adsorption, recent studies have predicted fully dissociative adsorption to be stronger than fully molecular. However, a mixture of dissociatively and molecularly adsorbed water was seen to be the most stable structure on UO_2.[2] For PuO_2, dissociative adsorption has been predicted to be more stable than molecular adsorption on the (110) surface.[3]

Experimental studies of water adsorption on PuO_2 surfaces have shown that water adsorbs via a multi-step process. Initial strong chemisorption due to dissociation of water, forming a hydroxylated surface, is followed by successive layers of H_2O physisorbed above the hydroxylated layer.[4]

In this study we use the PEECM, where a portion of the surface is described quantum mechanically, and the rest of the system is approximated by point charges. Our main aim is to study the adsorption of water on the (111) and (110) surfaces of UO_2 and PuO_2, although we also report other cases where we have used the PEECM.

The PEECM offers certain advantages over more traditional periodic boundary condition approaches: all of the analysis tools of molecular quantum chemistry can be applied, it is relatively straightforward to employ hybrid DFT, and defects and vacancies can be studied in isolation.

Computational Details

All calculations were performed with the TURBOMOLE6.5[5] program. DFT with the PBE0 (hybrid-GGA) exchange-correlation functional was used for all calculations.

PEECM

All calculations were performed using the PEECM[6]. In this approach, the system is split into three regions: an inner explicit cluster region, which is treated quantum mechanically as described above; the outer embedding region, which consists of point charges; and an intermediate embedding region, consisting of negative point charges and effective core potentials (ECPs) (Figure 1).

The infinite outer embedding region recreates the Madelung potential of the bulk system; formal charges were used for the ions in this region, +4 for actinide ions and -2 for oxygen ions. The ECPs used in the intermediate embedding region were the Ce CRENBL ECPs, employed in order to avoid overpolarization of the electron density in the explicit cluster, whilst -2 charges again represented the oxygen ions. The Ce CRENBL ECP, which corresponds to a +4 charge when used without any basis functions, was used since no actinide ECPs corresponding to a +4 charge were available. The 8-coordinate Ce(IV) ionic radius, 0.97 Å, is very similar to that of U(IV), 1.00 Å, Np(IV), 0.98 Å, and Pu(IV), 0.96 Å.

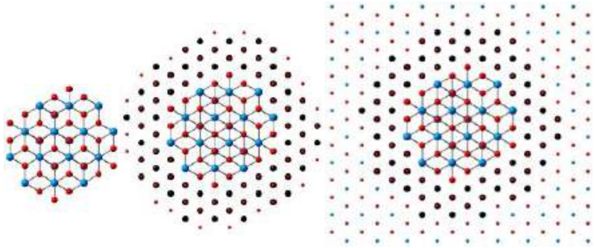

Figure 1 Embedding of quantum mechanical (QM) cluster in PEECM scheme. Left, QM cluster, actinide ions in blue, oxygen ions in red. Middle, QM cluster embedded in intermediate region of ECPs (black) and -2 point charges (small red), representing actinide and oxygen ions respectively. Right, QM cluster and intermediate region embedded in infinite array of +4 (small blue) and -2 (small red) point charges representing the actinide and oxygen ions respectively.

Results and Discussion

Electronic Structure of Bulk UO_2, NpO_2 and PuO_2

We have shown previously that the PEECM, with the use of a hybrid DFT functional, is able to correctly predict actinide dioxides to be insulators, with the composition of the valence and conduction bands agreeing with experiment.

Water Adsorption on UO_2 and PuO_2 Surfaces

Water can adsorb onto AnO_2 surfaces in two ways: molecularly, where the water molecule remains intact on adsorption, or dissociatively, where an O-H bond is broken. Molecular adsorption on the (111) surface occurs with an oxygen adsorbing above an actinide ion and two hydrogen atoms pointing towards two surface oxygen atoms. Dissociative adsorption forms two hydroxyl groups: a surface hydroxyl, formed from a hydrogen of the water molecule binding to a surface oxygen, and an adsorbed hydroxyl, where an OH group of water adsorbs above an actinide ion. These adsorptions are shown in Figure 2.

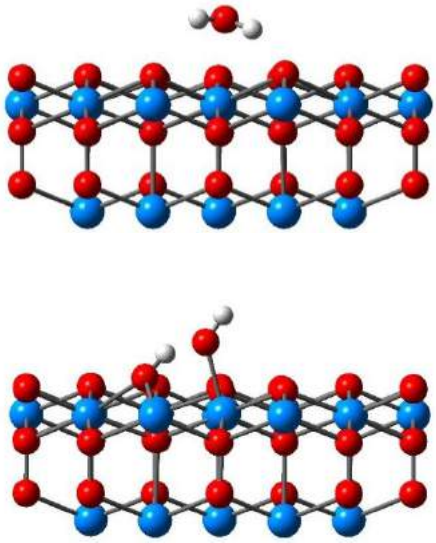

Figure 2 $U_{19}O_{38}$ cluster of the (111) surface with water adsorbing molecularly (top) and dissociatively (bottom). Uranium atoms shown in blue, oxygen atoms in red and hydrogen atoms in white. The cluster is shown in the plane of the surface.

As with the (111), there are two types of adsorption on the (110) surface: molecular and dissociative. Molecular adsorption occurs with the hydrogen atoms tilted towards the surface, the oxygen atom is now not directly above the actinide ion (Figure 3). Dissociative adsorption again forms two hydroxides, the adsorbed hydroxide has its oxygen above the actinide ion and its hydrogen tilted towards a surface oxygen, while the surface hydroxide has its hydrogen angled towards another surface oxygen ion. (Figure 3).

In our project summary from last year we reported water adsorption energies for the UO_2 and PuO_2 (111) and (110) surfaces using the SV(P) basis set. After this we noted that increasing the basis set size (up to the QZVP level) significantly decreased the adsorption energy, and we presented these results in a paper for the WM2016 conference. However, calculating water adsorption energies with the QZVP basis set is computationally expensive, and we sought a way to obtain adsorption energies in agreement with those calculated at the QZVP level but without the significant computational cost. Accounting for the basis set superposition error in the calculations with the counterpoise (CP) method, we have obtained adsorption energies at the SV(P) level in good agreement with our results at the QZVP level.

We have therefore performed single point energy calculations at the SV(P) level with the CP on all our structures. Although the adsorption energies change significantly (up to 0.6 eV), the trends in our results do not. We still see slightly stronger adsorption of water on the UO_2 than PuO_2 surfaces, as well as stronger adsorption on the (110) than (111) surface. On the (111) surface the difference between molecular and dissociative adsorption is small, with a mixture of both being most stable, while on the (110) surface dissociative adsorption is clearly favoured. We have also included dispersion effects into our calculations using the Grimme D3 parameters.[7] With the D3 parameters we see an increase in all adsorption energies (0.1-0.3 eV), although again there is no change in the trends observed.

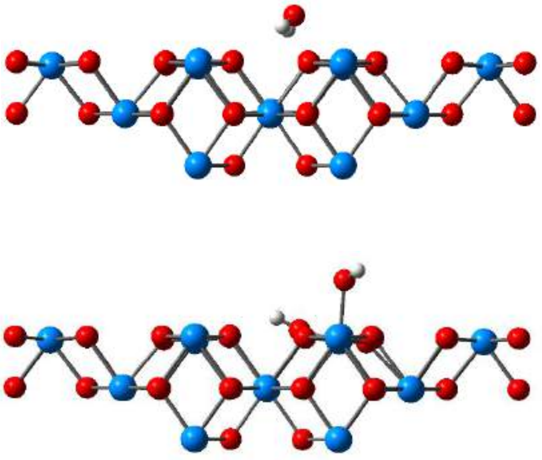

Figure 3 $U_{25}O_{50}$ cluster of the (110) surface with water adsorbing molecularly (top) and dissociatively (bottom). Uranium atoms shown in blue, oxygen atoms in red and hydrogen atoms in white. The cluster is shown in the plane of the surface.

Second Layer Water

Due to the larger adsorption energies on the (110) than (111) surface, and dissociative adsorption being more favourable than molecular adsorption on the (110) surface, we decided to consider the fully hydroxylated (110) surface of UO_2 and PuO_2 when investigating a second layer of water adsorption. We also decided to consider the fully hydroxylated surface as experimental studies have seen that water in the first layer is dissociatively adsorbed on PuO_2 powder.[4]

We optimized the geometry of a water molecule positioned above our hydroxylated $U_{25}O_{50}$ cluster representation of the (110) surface. The water molecule sits close to the surface forming 4 hydrogen bonds: one with a surface oxygen atom, and 3 to hydroxyl groups at the surface (Figure 4).

The adsorption energy of a water molecule in the second layer on the UO_2 (110) surface was calculated to be -0.40 eV. This is ~0.5-0.6 eV smaller than molecular adsorption of water in the first layer at the surface, although still considerably stronger than physisorption.

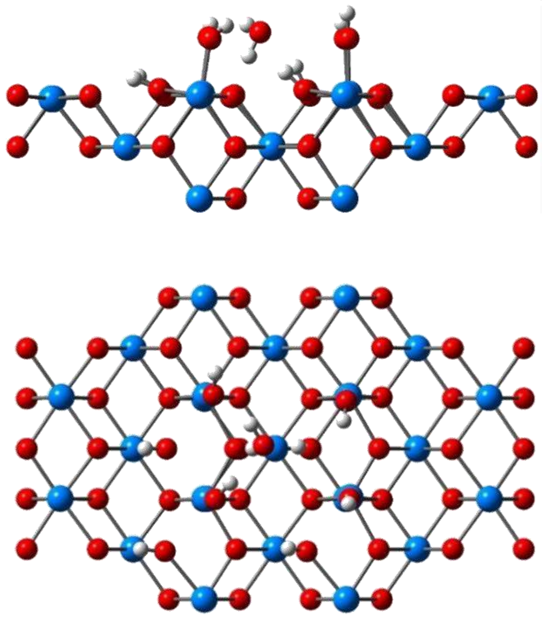

Figure 4 $U_{25}O_{50}$ cluster of the (110) surface with water adsorbing in the second layer onto a hydroxylated surface. Uranium atoms shown in blue, oxygen atoms in red and hydrogen atoms in white. Top view shows cluster in the plane of the surface, bottom view is perpendicular to the surface.

Oxygen 1s Binding Energies

The binding energies of oxygen 1s electrons can be measured experimentally using XPS. In surface systems the O 1s electron binding energy has been used to distinguish between oxygen atoms in the surface layer, subsurface layers, and in water adsorbed on the surface, as well as being able to distinguish between water adsorbed molecularly or dissociatively on surfaces.[8,9] We have calculated the O 1s binding energies for oxygen atoms in CeO_2, UO_2 and PuO_2 cluster representations of the (111) and (110) surfaces to see how the energy differs between subsurface and surface atoms, as well as between water molecules and hydroxyls adsorbed on these surfaces.

The absolute O 1s binding energies cannot be compared between different clusters, and so we cannot compare the absolute energy between the (111) and (110) surfaces. Therefore, we compared shifts in the O 1s binding energy. The shifts we calculated are the difference between the 1s binding energy of the oxygen atom we are interested in (an atom at the surface, in a water molecule, or in a hydroxyl group) and the 1s binding energy of a reference oxygen atom in the same cluster. The reference oxygen atom is always fully coordinated and in the second layer.

On the UO_2 (111) clean surface (where no water has been adsorbed), we found that 3rd layer (subsurface) oxygen atoms had the strongest O 1s binding energies, while 1st layer (surface) oxygen atoms had the weakest.

We then calculated shifts in the O1s binding energies of water and hydroxyls adsorbed on the (111) and (110) surfaces of CeO_2, UO_2 and PuO_2. Of these oxygen atoms, those in water molecules are seen to have the strongest 1s binding energy (0.8-1.3 eV stronger than the reference oxygen atom), followed by surface hydroxyls (0.1-0.6 eV stronger than the reference oxygen atom), while adsorbed hydroxyls have the weakest O 1s binding energy (0.2-0.8 eV weaker than the reference atom). This was true across all three dioxide systems and both (111) and (110) surfaces. The difference between the water and the hydroxyl binding energies is higher on the (110) than the (111) surface; indicating that it would be easier to distinguish between molecular and dissociative adsorption on the (110) surface.

PEECM and the Quantum Theory of Atoms in Molecules (QTAIM)

In addition to using the PEECM to study water adsorption on actinide dioxide systems, we have also used the method to investigate environmental effects on the electron density topology in $UO_2Cl_4Cs_2$, $U(Se_2PPh_2)_4$ and $Np(Se_2PPh_2)_4$ using the QTAIM.[10] In these systems we found that the environment (whether the central molecule of the system was in the gas phase or embedded in PCs via the PEECM) had little effect on the topology of the electron density.

Conclusions and Future Work

The PEECM was used to investigate water adsorption on UO_2 and PuO_2. The results show that adsorption is much stronger on the (110) surface, there is little difference between molecular and dissociative adsorption on the (111) surface, but there is a larger difference on the (110) surface where dissociative adsorption is seen to be more favourable.

Initial investigations of water adsorption on the second layer of the UO_2 and PuO_2 (110) surfaces has begun, and water is seen to bind to the surface as well as first layer hydroxyls. We will continue our investigation of multiple layers of water adsorption, initially creating a full second layer of water on the (110) surface.

By calculating O 1s binding energies, we see that surface and subsurface oxygen atoms in AnO_2 can be distinguished. We also see that molecular and dissociative water adsorption on the AnO_2 surfaces can be distinguished.

The PEECM is a suitable technique to be used for studying surface defects such as oxygen vacancies. The PEECM allows us to study these defects in isolation. We will initially investigate the energy required to create an oxygen vacancy at the (111) and (110) surfaces, and see how the presence of oxygen vacancies affects the adsorption of water on the surfaces.

Acknowledgements

We are grateful to the National Nuclear Laboratory, UCL and the M3S Centre for Doctoral Training for financial support for a PhD studentship to JW. We also thank UCL for computing resources via the Research Computing “Legion” cluster (Legion@UCL), “Grace” cluster and associated services, and also the “Iridis” facility of the e-Infrastructure South Consortium’s Centre for Innovation.

References

[1] Z. Rák, R.C. Ewing, U. Becker, Surf. Sci. 608 (2013) 180–187. doi:10.1016/j.susc.2012.10.002.

[2] T. Bo, J.-H. Lan, Y.-L. Zhao, Y. Zhang, C.-H. He, Z.-F. Chai, et al., J. Nucl. Mater. 454 (2014) 446–454. doi:10.1016/j.jnucmat.2014.09.001.

[3] G. Jomard, F. Bottin, G. Geneste, J. Nucl. Mater. 451 (2014) 28–34. doi:10.1016/j.jnucmat.2014.03.012.

[4] J.M. Haschke, T.E. Ricketts, J. Alloys Compd. 252 (1997) 148–156. doi:10.1016/S0925-8388(96)02627-8.

[5] R. Ahlrichs, M. Bär, M. Häser, H. Horn, C. Kölmel, Chem. Phys. Lett. 162 (1989) 165–169. doi:10.1016/0009-2614(89)85118-8.

[6] A.M. Burow, M. Sierka, J. Döbler, J. Sauer, J. Chem. Phys. 130 (2009) 174710. doi:10.1063/1.3123527.

[7] S. Grimme, J. Antony, S. Ehrlich, H. Krieg, J. Chem. Phys. 132 (2010) 154104. doi:10.1063/1.3382344.

[8] J.T. Newberg, D.E. Starr, S. Yamamoto, S. Kaya, T. Kendelewicz, E.R. Mysak, et al., Surf. Sci. 605 (2011) 89–94. doi:10.1016/j.susc.2010.10.004.

[9] X. Zhang, S. Ptasinska, J. Phys. Chem. C 118 (2014) 4259–4266. doi:10.1021/jp411977p.

[10] J.P.W. Wellington, A. Kerridge, N. Kaltsoyannis, Polyhedron (2016) doi:10.1016/j.poly.2016.02.048.

Synthesis and ion exchange properties of zirconogermanates

R.George*[1] and Dr J.A.Hriljac[1]

*Correspondence: RXG034@bham.ac.uk

[1] School of Chemistry, University of Birmingham, Edgbaston, Birmingham, UK B15 2TT.

Abstract

The synthesis of materials for ion exchange and subsequent disposal of radionuclides will be explored in this work; the concept being the formation of open framework materials with high selectivity for caesium and strontium that can be thermally transformed into dense phases for disposal. The successful synthesis of the germanium form of the natural mineral umbite ($K_2ZrSi_3O_9.H_2O$) and subsequent ion exchange results show both caesium and strontium uptake by Ge-Zr-umbite. Further work focused on the fine tuning of ion exchange properties by partial doping into the material.

Introduction

The synthesis of novel ion exchange materials for uses in nuclear waste management and environmental remediation is a key area of research. Much effort is being placed in designing materials with high selectivity and ion exchange capacity, especially in relation to caesium and strontium. The established methodology for the removal of these radionuclides in the UK involves the use of a natural zeolite material clinoptilolite[1], but future waste streams and POCO activities may be bettered tackled with other systems.

One family of materials which have been widely investigated are mixed octahedral and tetrahedral framework metal silicates, due to potentially interesting ion exchange properties and better chemical and radiation stability than aluminosilicate zeolites. Altering the composition of these metal silicates by substituting in different metal ions affects the properties, making it a great tool for modification of the product [2]. Materials have been synthesised with a range of metals such as Zr [3], Sn [4] and Ti [5] in the silicate framework. This allows for fine tuning of the materials properties by either total substitution or partial doping into the structure. It has been of great interest to introduce a wide range of different metal atoms into the framework in order to develop materials that can be of use industrially as cation-exchangers.

One of these types of materials, a natural zirconosilicate mineral umbite ($K_2ZrSi_3O_9.H_2O$) has been synthesised with both Sn and Ti as the octahedral component, for which the ion exchange properties have been explored in the literature [6]. Umbite is of further interest as it can be thermally converted to a dense wadeite ($K_2ZrSi_3O_9$) structure which could act as a final wasteform.

The focus of this work will be on the variation of the tetrahedral component of umbite, potentially allowing for further tunability of the materials properties. For this we have chosen germanium, which is chemically similar to silicon but has a larger ionic radius.

Methodology Details

Germanate synthesis

The fumed silica (Sigma) and germanium dioxide (Gerald wise and co) were added to potassium hydroxide (Sigma) dissolved in deionised water. To the stirring mixture zirconyl chloride octahydrate (Sigma) was added until dissolved. The mixture is then stirred for a further hour to allow it to homogenise. The resulting mixture was then transferred to a 45ml Teflon liner and placed in a Parr autoclave at 200°C. The autoclave was then heated for 1 to 7 days. The resulting white solids were then washed in deionised water and dried overnight at 60°C.

Ion exchange

0.1M solutions of strontium and caesium nitrate (Sigma) were added to 0.2-0.5g of sample. This was then shaken for 24 hours before being washed and dried overnight at 60°C. Samples were prepared for XRF as either a loose powder or pellet.

Any compounds synthesised were analysed using Powder X-ray diffraction (XRD) on a Bruker D8 Advance using a Cu Kα source at room temperature. Phase matching was performed using the EVA software from known databases.

Results and Discussion

Initial synthesis attempts of a germanium umbite focused on the direct replacement of silica with germanium dioxide. This was done by using a batch composition and conditions widely used by our group, however direct substitution of SiO_2 for GeO_2 did not result in Ge-Zr-umbite. A subsequent literature search gave a new batch composition; this used a much more dilute starting solution relative to the silicon umbite synthesis [7]. This presented a potential issue with GeO_2 solubility as the solution was far less basic than that in the Si-umbite synthesis. It was decided that a synthesis time of one week should give the material plenty of time to form, it could be possible to decrease this time in future experiments so length of time was not an initial issue.

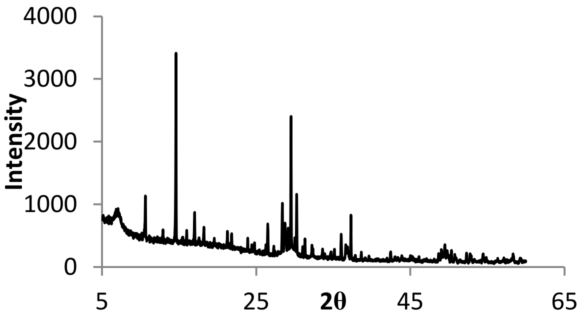

Figure 1: Product from a 7 day Ge-Zr-Umbite synthesis

The resulting material was confirmed to be Ge-Zr-umbite, as seen in figure 1; however the methodology used resulted in small quantities of sample and a lengthy synthesis time. As a result more experiments were designed to improve sample turnover and scale up the synthesis. Reducing the synthesis time proved to be very simple, initial attempts reduced the synthesis time down to 24 hours. These showed no difference in crystallinity, as seen in figure 2, when compared to the seven day preparation and as a result a 24 hour synthesis seemed the optimal time length.

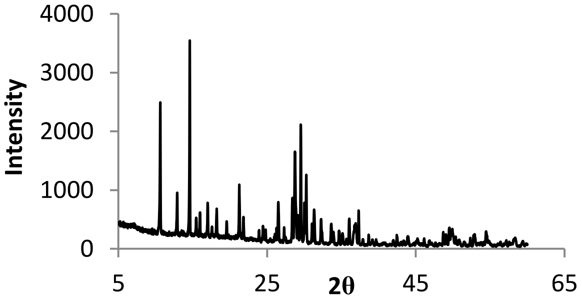

Figure 2: Product from a 24 hour Ge-Zr-umbite synthesis

The final step was to improve the amount of sample synthesised each time, this would allow us to run ion exchange experiments on the material. Utilising a systematic approach we were able to increase the amount of sample formed during each batch to approximately 2g. As a reliable scaled up synthesis had been achieved, a series of ion exchange experiments were planned to test Ge-Zr-umbite for its caesium and strontium uptake.

Preliminary ion exchange experiments used a 0.1M solution of caesium or strontium nitrate. Ge-Zr-umbite showed both caesium and strontium uptake as seen in tables 1 and 2.

Table 1: Caesium exchange data

Element	Weight %	Mole%
Ge	25.02	49.3
Zr	14.51	22.8
K	7.39	27.0
Cs	0.83	0.89

Table 2: Strontium exchange data

Element	Weight %	Mole%
Ge	27.97	49.3
Zr	16.99	23.8
K	8.09	26.5
Sr	0.28	0.41

It was decided to see if the ion uptake of this material could be improved and as mentioned a key area of focus is on the tunability of umbite. It was decided to also synthesise a range of partially doped umbites. Once again this was done by simply replacing silica for germanium dioxide in the starting reaction mixture. By synthesising a range of mixed Ge/Si materials, it would be possible to see the impact of doping on ion exchange properties. This should allow for some degree of composition optimisation to give the best ion exchange properties.

Synthesis of a mixed 50/50 Ge/Si material is possible; this is shown by a shift to lower 2θ in the XRD of the mixed system compared to that of Si-umbite. However this is also the maximum doping limit for a mixed Ge/Si system. Anything above 50% results in the formation of a $K_2ZrGe_2O_7$ phase which is not of interest. This phase is also an impurity in each mixed Ge/Si umbite synthesised and as a result it is not possible to get an accurate value for the level of germanium doping. Until this is resolved no ion exchange studies can be carried out.

Conclusions and Future Work

The early results for the synthesis of the Ge-Zr-umbite seem promising with early exchange data showing some degree of caesium and strontium uptake. Despite the mixed Ge/Si systems proving to be difficult to synthesise phase pure, further scope may focus on systems with mixed octahedral metals. By doping into the octahedral site we may have another chance to alter ion exchange properties.

Another area of future work will focus on the thermal conversion of Ge-Zr-umbite to see what phases result. This will also be done for the exchanged samples to see if the potential final wasteform can accommodate caesium and strontium. These final phases will all need to be characterised with thermal conversion pathways analysed.

The final area of work will focus on synthesising a sodium form of Zr-Ge-umbite, either through direct synthesis or ion exchange. By forming the sodium form it is hope that ion exchange properties may improve when compared to the potassium form of Ge-Zr-umbite.

Acknowledgements

The authors would like to thank the school of chemistry and the ESPRC for the funding provided. We would also like to thank advantage west midlands for providing the equipment required to carry out the experiments.

References

[1] A.Dyer, A.Chimedtsogzol, L.Campbell and C.Williams, *Micropor.Mesopo. Mat*, 2006, **95**, 172-175.

[2] S.D.Sharma, K.G.Varshney and S.C.Mojumdar, *J Therm Anal Calorim,*2012,**108**, 843-850.

[3] S.Ferdov,U.Kolitsch,O.Petrov,V.Kostov-Kytin,C.Lengauer and E.Tillmanns, *Micropor.Mesopor.Mat*, 2005, **81,** 79–86.

[4] F.Pan, X.Lu, Y.Wang, S.Chen, T.Wang and Y.Yan, *Micropor.Mesopor.Mat,*2014, **184** 134–140.

[5] Y.Zou, R.Wang, Z.Zhang, G.Li and S.Qiu, *Micropor.Mesopor.Mat, 2013*, **182,** 178–184.

[6] C.S.Fewox,A.Clearfield and A.J.Celestian, *Inorg. Chem*,2011, **50**, 3596–3604

[7] J.Plevert, R.Sanchez-Smith, T.M.Gentz, H.Li, T.L.Groy, O.M.Yaghi and M.O'Keeffe, *Inorg.Chem*, 2003,**42,** 5954-5959.

Synthesis and studies of Barium doped $Cs_2TiNb_6O_{18}$ - A new Cs-waste form

G.Day*[1], G. Cutts[1], T.Chen[1], and J.A. Hriljac[1]

*Email: gxd988@bham.ac.uk

[1] *University of Birmingham, Birmingham, UK*

Abstract

$Cs_2TiNb_6O_{18}$ has the potential to be an excellent waste form for the immobilisation of radioactive caesium. A previous study revealed that $Cs_2TiNb_6O_{18}$ is the major Cs-containing phase produced when Cs-loaded IONSIV, a commercial ion exchanger, is hot isostatically pressed (HIPed).[1] $Cs_2TiNb_6O_{18}$ demonstrates excellent chemical durability which compared well to the Cs containing phase hollandite in SYNROC.[2]

Introduction

^{137}Cs is one of the primary heat generating radio nuclides in nuclear waste. It is a strong beta-gamma emitter with a half life of approximately 30 years.[3,4] It is often the radionuclide accidently released into the biosphere on account of its high environmental mobility.[5–7]

Crystalline Silicotitanate (CST) with a formula $Na_2Ti_2O_3(SiO_4)\cdot 2H_2O$, is an inorganic ion exchanger which was developed by the Sandia National Laboratory and Texas A&M University.[4,8,9] CST demonstrates tremendous properties, possessing excellent selectively for Cs over a wide pH range, excellent radiation stability and importantly, is compatible with final waste forms making it a great candidate for radioactive Cs clean-up.[4,5,9,10] It is well known that varying the composition in CST by doping $Nb^{(V)}$ for $Ti^{(IV)}$ enhances the exchange capabilities for Cs.[1,5] Universal Oil Products (UOP) and Sandia in a joint collaboration commercialised this product labelled as IE-911, an engineered form of Niobium doped CST.

A recent study demonstrated that Cs-loaded IE-911 could be immobilised into a suitable waste form through hot isostatic pressing (HIPing).[1,6] HIPing is suitable for immobilising a variety of nuclear wastes into dense robust crystalline waste forms ideal for final disposal.[6] The major Cs waste form produced from HIPing was identified as $Cs_2TiNb_6O_{18}$. This phase demonstrated exceptional leach rates which compared well to other ceramic Cs waste forms such as hollandite.[1] Hollandite is a well studied Cs waste form which is a major component of SYNROC.[11,12] It is known that hollandite, formula $(Ba,Cs)_xAl_{2x}Ti_{8-2x}O_{16}$, is chemically durable and reported to be able to retain the transmutation products of ^{137}Cs ***(figure 1)*** .[2,11–17] The release of a β^- particle in the transmutation process is able to simultaneously reduce $Ti^{(IV)}$ to $Ti^{(III)}$ meaning Ba can be retained in the hollandite structure.[17] It is not yet known how $Cs_2TiNb_6O_{18}$ will respond to the transmutation of $^{137}Cs^+$ to $^{137}Ba^{2+}$.

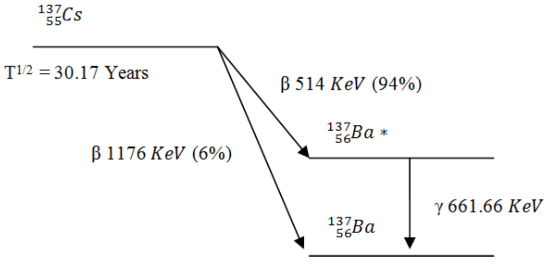

Figure 1. Transmutation of ^{137}Cs *Adapted from reference* [18]

It was envisaged a similar process that occurs in hollandite could also take place in $Cs_2TiNb_6O_{18}$. In this scenario the β^- particle could reduce either the $Nb^{(V)}$ or $Ti^{(IV)}$ to balance the overall charge giving ***formulas 1.1*** and ***1.2***. Proof of barium substitution could therefore provide decent evidence that $Cs_2TiNb_6O_{18}$ is able to retain Ba and be a suitable final waste form for Cs immobilisation.

1.1 $Cs_{2-x}Ba_x\mathbf{Ti^{(IV)}_{1-x}Ti^{(III)}_x}Nb_6O_{18}$

1.2 $Cs_{2-x}Ba_xTi\mathbf{Nb^{(V)}_{6-x}Nb^{(IV)}_x}O_{18}$

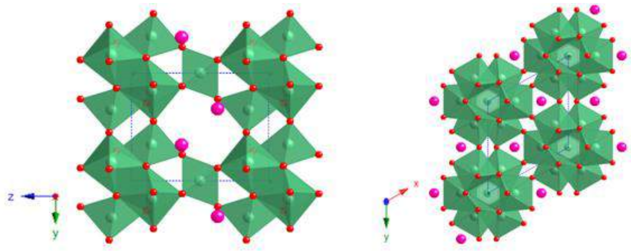

Figure 2. Crystal Structure of $Cs_2TiNb_6O_{18}$. Sourced from Desgardin et al [19]. Left hand side view down a axis. Right hand side, view down c axis.

Methodology Details

Preparation of Materials

Samples were synthesised using both sol gel and traditional solid state techniques based on those outlined by Desgardin et al [19] and Balmer et al [20].

Characterisation of materials

X-ray diffraction (XRD) experiments were carried out on a Bruker D8 Diffractometer in transmission mode using a Cu kα1 1.5406 X-ray source. Wavelength dispersive X-ray fluorescence spectroscopy was carried out using a Bruker S8 Tiger (WDXRF). Scanning electron microscopy (SEM) studies were performed using a Philips XL30 ESEM-FEG with an Oxford Inca 300 EDX system operating at 10 kV. Transmission electron microscopy (TEM) experiments were carried out using JEOL JEM-2100F equipped with a EDAX Genesis XM 4 system 60, a double tilt holder and SEI/BSE detector operating at 200 kV in STEM mode.

Static defect calculations

Novel atomic potentials have been empirically derived through a Reverse Mote Carlo methodology using code developed by the group. Static calculations have been performed using the GULP (General Utility Lattice program) code. [21] Defects in the $Cs_2TiNb_6O_{18}$ system have been approximated at infinite dilution and as clusters using the Mott-Littleton (two-region) approach.

Results and Discussion

The results discussed here are related to Ba doped samples where the charge compensation is achieved through doping excess $Ti^{(IV)}$ for $Nb^{(V)}$ giving the formula $Cs_{2-x}Ba_xTi_{1+x}Nb_{6-x}O_{18}$. Although not necessarily realistic these samples provided a decent starting point in order to confirm Ba doping in the phase of interest.

Elemental analysis was carried out using X-ray fluorescence (XRF) spectroscopy. Samples were prepared into fusion beads by heating to 1050°C dissolved in appropriate flux. The results shown in ***table 1*** within a decent error agree with the expected increase in Ba concentration with increased Ba doping. Following this further analysis was then carried out in order to identify whether Ba had actually incorporated into the desired phase.

Table 1 XRF $Cs_{2-x}Ba_xTi_{1+x}Nb_{6-x}O_{18}$

Sample/x	Expected Ba/ wt%	XRF Ba/ wt%
0.05	0.60	0.53(3)
0.10	1.19	1.13(4)
0.15	1.79	1.77(4)

XRD analysis of $Cs_2TiNb_6O_{18}$ confirmed that it crystallises in the trigonal structure (structure shown in ***figure 2***), with the space group $P\overline{3}m1$. It was thought that Ba substitution would occur directly on the Cs site and therefore not change the symmetry of the system. Initial XRD results shown in ***figure 3*** suggested that the symmetry of the system had not been changed and therefore Ba potentially had been incorporated into the structure.

On closer inspection of the XRD patterns, some additional impurity peaks to what was expected were found. These impurities were able to be identified as $BaTiNb_4O_{13}$, $BaTi_3Nb_4O_{17}$ and $Ti_2Nb_{10}O_{29}$. GSAS analysis enabled an estimate of the impurity phases which is summarised in ***table 2***.

Table 2 GSAS analysis Weight fractions $Cs_{2-x}Ba_xTi_{1+x}Nb_{6-x}O_{18}$

Phase	x=0.05	x=0.10	x=0.15
$Cs_2TiNb_6O_{18}$	95.11(2)	91.52(5)	88.19(5)
$BaTi_3Nb_4O_{17}$	2.2(3)	1.1(5)	4.9(3)
$BaTiNb_4O_{13}$	0	3.9(5)	4.7(3)
$Ti_2Nb_{10}O_{29}$	2.7(4)	3.5(8)	2.2(5)
Total Ba %	0.35	0.88	1.62
Expected Ba %	0.60	1.19	1.79

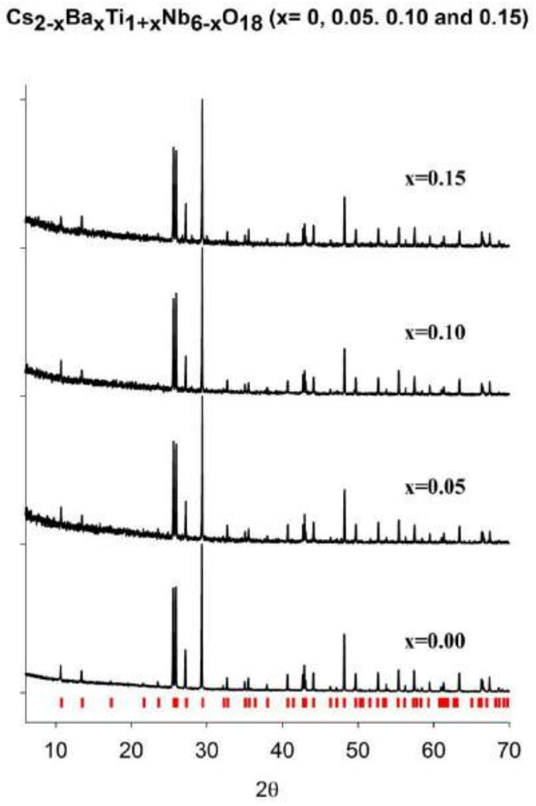

Figure 3. X-ray diffraction (5-70°) $Cs_{2-x}Ba_xTi_{1+x}Nb_{6-x}O_{18}$ (x=0.00, 0.05, 0.10 and 0.15)

The weight fractions of phases calculated in ***table 2*** suggest that there may be a small amount of Ba doping in the $Cs_2TiNb_6O_{18}$ phase. The stiochiometric amount of Ba initially reacted and that suggested by XRF is consistently higher than the level of Ba impurities calculated using GSAS. Lower level Ba samples were synthesised in order to investigate this, however due to the associated errors with weight fraction analysis at lower Ba level, any discrepancies between GSAS analysis and XRF were discarded. Additional analysis was carried out in order to confirm the location of Ba.

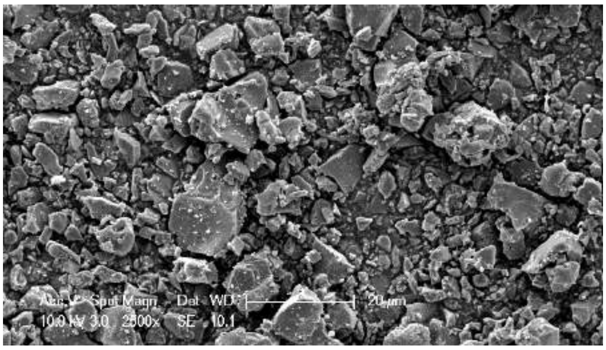

Figure 4. SEM SE Image $Cs_{2-x}Ba_xTi_{1+x}Nb_{6-x}O_{18}$ (x=0.1)

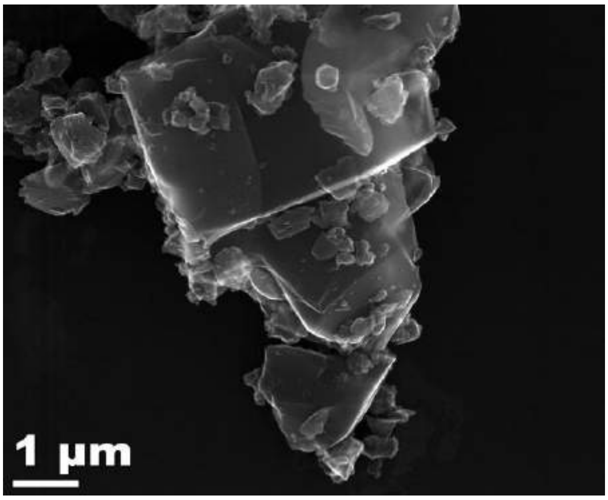

Figure 5. *TEM Image Ba doped* $Cs_2TiNb_6O_{18}$

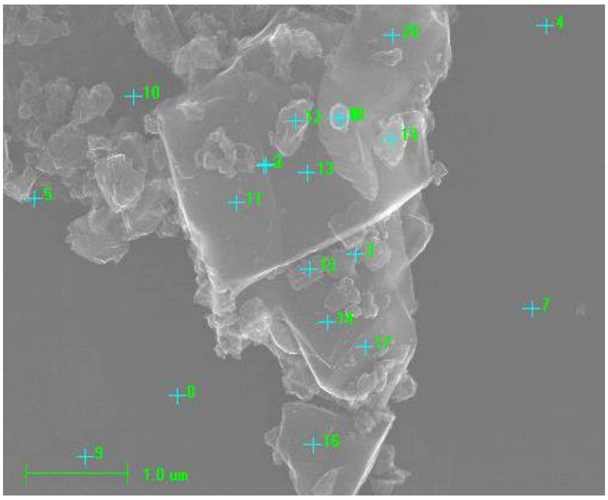

Figure 6. *TEM/EDX Point analysis Ba doped* $Cs_2TiNb_6O_{18}$

SEM studies ***(figure 4)*** apart from displaying the morphology were unable to yield much more information. TEM studies (***figure 5 and 6)*** were carried out and with the higher energy, smaller sized beam better detection of Ba was achieved compared to SEM. Multi point EDX analysis ***(figure 6)*** identified at least two phases in the sample. A very high concentration of Ba, alongside Ti and Nb was detected around point 12, suggesting a Barium titanium niobate impurity, leaving the pure un-doped $Cs_2TiNb_6O_{18}$ parent material at point 13. In summary TEM indicates it is unlikely any Ba has been incorporated into the target phase.

Defect calculations

A series of defect calculations have been performed involving a number of charge compensating mechanisms for the incorporation of Ba in the $Cs_2TiNb_6O_{18}$ structure. Cluster defect energies were calculated according to the following Kroger-Vink notations;

Scheme 1: $Ti^{(IV)}/Ti^{(III)}$

$$BaO + \frac{1}{2}Ti_2O_3 + Cs_{Cs}^{X} + Ti_{Ti}^{X} \rightarrow Ba_{Cs}^{\bullet} + Ti_{Ti}' + TiO_2 + \frac{1}{2}Cs_2O$$

Scheme 2: $Nb^{(V)}/Nb^{(IV)}$

$$BaO + NbO_2 + Cs_{Cs}^{X} + Nb_{Nb}^{X} \rightarrow Ba_{Cs}^{\bullet} + Nb_{Nb}' + \frac{1}{2}Nb_2O_5 + \frac{1}{2}Cs_2O$$

Scheme 3: $Nb^{(V)}/Ti^{(IV)}$

$$BaO + TiO_2 + Cs_{Cs}^{X} + Nb_{Nb}^{X} \rightarrow Ba_{Cs}^{\bullet} + Nb_{Nb}' + TiO_2 + \frac{1}{2}Cs_2O$$

Table 4. *Fractional coordinates Site1 and 2 Ti/Nb*

Ti/Nb Sites	Fractional coordinates		
Site 1	0.0000	0.0000	0.5000
Site 2	0.1700	-0.1700	0.1457

The preference for the charge compensation on each site has been assessed. Initial results suggest there is a preference for charge compensation on site 1 *(Δ ≈ 2.5 eV)* for scheme 1, which is in contrast to scheme 3 which has a slight preference for site 2 *(Δ ≈ 1 eV)*. A large preference for charge compensation on site 2 has been calculated for scheme 2, with a difference of *ca.* 10.5 eV between the two sites.

A large negative binding energy, (*ca.* -13 eV) has been calculated for site 2 scheme 2, suggesting it is much more favourable for the charge compensating Nb^{IV} to be in close proximity to the Ba impurity. This was not the case for the other schemes investigated with binding energies ranging from -0.675 to 0.212 eV, showing little or no preference for clustering.

Further to these results, solution energies will be calculated in order ultimately find which of the three schemes is most energetically favourable, of which the results will be presented later.

Conclusions and Future Work

Initial XRD and XRF results led to some amount of uncertainty to what level of Ba can incorporate in the $Cs_2TiNb_6O_{18}$ phase. The identification of impurities particularly at higher levels of Ba doping did hint that the Ba cation may not be suitable for the crystallographic Cs site which may be down to cation size. Lower level Ba doped samples were synthesised but the subsequent studies were unable to unambiguously confirm the incorporation of Ba.

Consequent TEM studies however did firmly imply the formation of minor Ba impurities phases at low level leaving the pure parent phase un-doped. Further TEM/EDX work on these materials is planned in order to yield more information regarding the identity and weight fraction of Ba impurities. Furthermore, additional synthesis with more vigorous conditions is planned in order to try and drive Ba into the parent phase. Further simulations are also intended in order to assess the stability of Ba in the $Cs_2TiNb_6O_{18}$ structure.

Acknowledgements

Thank you to the School of Chemistry, University of Birmingham for funding and equipment and also advantage west midlands. Acknowledgements to Dr. J.A.Hriljac, Dr. Tzu-Yu Chen and Geoff Cutts for their invaluable assistance in this work. Further thanks to Dr. Yina Guo from the University of Limerick for collecti;ng the STEM data.

References

1. T.-Y. Chen, J. . Hriljac, A. . Gandy, M. . Stennett, N. C. Hyatt, and E. . Maddrell, in *Scientific Basis for Nuclear Waste Management XXXVI, MRS Symp*, 2013, pp. 67–72.
2. A. Ringwood, *Miner. Mag.*, 1985, **49**, 159–176.
3. M. S. Denton and M. J. Manos, in *Phoenix, AZ Conference Proceedings WM2009*, 2009, pp. 1–8.
4. B. Yu, J. Chen, and C. Song, *J. Mater. Sci. Technoology*, 2002, **18**, 206 – 210.
5. V. Luca, J. Hanna, M. Smith, M. James, D. Mithchell, and J. Bartlett, *Microporous Mesoporous Mater.*, 2002, **55**, 1–13.
6. E. Maddrell, *Chem. Eng. Res. Des.*, 2013, **91**, 735–741.
7. A. M. El-Kamash, *J. Hazard. Mater.*, 2008, **151**, 432–445.
8. National-Research-Council, in *Alternatives for High-Level Waste Salt Processing at the Savannah River Site*, National Academies Press, Washington DC, 2000, pp. 55–65.
9. R. G. Anthony, R. G. Dosch, D. Gu, and C. V. Philip, *Ind. Eng. Chem. Res.*, 1994, **33**, 2702–2705.
10. A. Clearfield, L. Bortun, and A. Bortun, *React. Funct. Polym.*, 2000, **43**, 85–95.
11. A. Y. Leinekugel-le-Cocq-Errien, P. Deniard, S. Jobic, E. Gautier, M. Evain, V. Aubin, and F. Bart, *J. Solid State Chem.*, 2007, **180**, 322–330.
12. A. Y. Leinekugel-le-Cocq, P. Deniard, S. Jobic, R. Cerny, F. Bart, and H. Emerich, *J. Solid State Chem.*, 2006, **179**, 3196–3208.
13. I. Donald, B. Metacalfe, and R. Taylor, *J. Mater. Sci.*, 1997, **32**, 5851–5887.
14. S. Stefanovsky, S. Yudintsev, R. Giere, and G. Lumpkin, *Energy, Waste Environ. a Geochemical Persspective*, 2004, **236**, 37–63.
15. L. M. Wang, J. Chen, and R. C. Ewing, *Curr. Opin. Solid State Mater. Sci.*, 2004, **8**, 405–418.
16. A. E. Ringwood, S. E. Kesson, N. G. Ware, W. Hibberson, and A. Major, *Nature*, 1979, **278**, 219–223.
17. L. Bursill, *J. Solid State Chem.*, 1987, **69**, 355–359.
18. J. Namiesnik and P. Szefer, *Analytical Measurements in Aquatic Environments (Google eBook)*, CRC Press, 2010.
19. G. Desgardin, C. Robert, D. Groult, and B. Raveau, *J. Solid State Chem.*, 1977, **22**, 101–111.
20. M. Lou Balmer, Y. Su, H. Xu, E. Bitten, D. McCready, and A. Navrotsky, *J. Am. Ceram. Soc.*, 2001, **84**, 153–160.
21. J. D. Gale and A. L. Rohl, *Mol. Simul.*, 2003, **29**, 291–341.

Theme 3 – Silo Ponds and Legacy Wastes
DISTINCTIVE 2nd Annual Meeting
Bristol, UK
19th – 20th April 2016

Tailored Cs/Sr Ion Exchange in Sn-Umbite by Framework Substitution

T. Chen*[1] and J.A. Hriljac[1]

*Correspondence: t.chen.3@bham.ac.uk

[1] *University of Birmingham*

(School of Chemistry, the University of Birmingham, Edgbaston, Birmingham, UK. B15 2TT)

Abstract

Stannosilicates consisting of heteropolyhedral structure where the simplest units are SnO_6 octahedra and SiO_4 tetrahedra have been raising considerable interest. Current work has focused on the modification of the crystallographic and electrostatic environment in Sn-umbite ($K_2SnSi_3O_9{\cdot}H_2O$) by varying the ratio or species of substitution in the framework (Nb^{5+}, V^{5+}, Sb^{5+}, Y^{3+} and Sc^{3+} for the octahedral site, and Ge^{4+} for the tetrahedral site). The substitutions were confirmed by XRD and XRF. The structural incorporations lead to a slight change of the unit cell volume, suggesting an isomorphous substitution can be achieved. As compared to Sn-umbite, some of the partially substituted phases, for example 25% Nb substituted umbite, show remarkable increases in both Cs and Sr capacity. An increase in ion exchange properties can be explained in terms of their inherent tunnel sizes to accommodate counterions due to partial substitution and bond strengths associated with the charge-neutralising cations and framework oxygens.

Introduction

Although aluminosilicate zeolites are widely used as ion exchange media for removing radioactive Sr and Cs from water in the nuclear industry, there is scope for new materials that have improved stability, ion exchange selectivity and conversion pathways into dense ceramics that retain the Sr and Cs and are suitable for long term storage.

Sn-umbite possesses a framework structure built of $[SnO_6]$ octahedra and long-chain $[SiO_4]$ tetrahedra by corner-sharing, as shown as Figure 1a. There are two unique ion exchange sites in the tunnels. The first exchange site (*Site 1* in Figure 1b) is in a 8-membered ring (8MR) tunnel consisting of six SiO_4 tetrahedra and two SnO_6 octahedra; the second site (*Site 2*) is in another 8MR tunnel composised of four SiO_4 tetrahedra and four SnO_6 octahedra. Water molecules only locate in channels along with Site 2 cations.[1] Some umbite compositions have shown a great ability for Cs and Sr uptake over a wide pH range, however typically much poorer in low pH condition.[1-3] Furthermore, one of the advantages of umbite is that the phase can be thermally transformed to a dense phase wadeite[4, 5], which is considered as a potential ceramic wasteform.

While synthesising new materials for ion exchange is common, tailoring optimum ion exchange properties by rational framework design is also possible. It has been demonstrated that significantly better Cs^+ selectivity can be achieved in some materials by framework substitution, for example, partial Nb^{5+} substitution for Ti^{4+} in the crystalline silicotitanate (CST) structure[6-8] or complete/partial substitution of Ge or Nb in the pharmacosiderite framework[9-11]. The crystallographic and electrostatic environment in which the Cs^+/Sr^{2+} ions are accommodated can be tailored by varying the ratio or species of substitution.

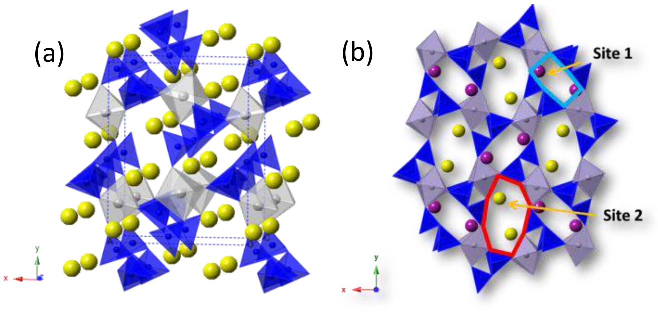

Figure 1 (a) Projections of the structure *Sn-Umbite,* $K_2SnSi_3O_9{\cdot}H_2O$*,* Orthorhombic, $P2_12_12_1$, a = 10.101, b = 13.136, c = 7.157 Å. (b) structural overview of Sn-umbite showing two unique ion exchange sites in the 8MR tunnels

Like these synthetic microporous zeolite-like materials, CST and pharmacosiderite, umbite has exhibited a flexibility to incorporate hetero-elements into the framework containing 6-fold coordinated transition elements. Various tri- and penta-valent elements with similar ionic radii to Sn were selected (Table1) to study the effect of substitution on ion exchange properties. There are two strategies for this project. Firstly, Sn^{4+} is partially (25%) replaced with 5+ elements, such as Nb^{5+}, V^{5+}, and Sb^{5+}. In this case, less K^+ cations will be required for charge neutralisation. Thus, the tunnels become less crowded, therefore more hydrated Cs or Sr can be accommodated. Secondly, Sn^{4+} is partially (25%) replaced by equal amount of trivalent and pentavalent elements, for example (Y^{3+}, Nb^{5+}) or (Sc^{3+}, Nb^{5+}). The size and electrostatic environment of the tunnel inside the umbite framework can be altered but the total K^+ content still remains the same. Sn-umbites with partially substituted 4-coordinated SiO_4 by GeO_4 (10 and 20 at.%) were also prepared for comparison.

Table 1 Ionic radii of selected elements[12]

Site	CN	Element	Ionic Radius(Å)
Octahedral	6	Sn 4+	0.69
		Nb 5+	0.64
		V 5+	0.54
		Sb 5+	0.61
		Y 3+	0.89
		Sc 3+	0.73
Tetrahedral	4	Si 4+	0.29
		Ge 4+	0.40

Methodology Details

Synthesis

The synthesis method of Sn-umbite used in this work is adapted and modified from the literatures reported by Lin et al[13] and Navascues et al.[14] Fumed silica (1 g) was added to a solution of KOH (2.25 g) and KCl (2 g) in water (10 g), a clear solution was obtained. A second solution, containing $SnCl_4 \cdot 5H_2O$ (1.85 g) in water (10 g), was also prepared. Upon mixing, a cloudy solution was formed, which was kept under vigorous stirring for 1 hr. This gel, with a molar composition $Si:K:Sn:H_2O=3.23:12.98:1:228$, was transferred to a Teflon-lined autoclave and treated at 200 °C for 48 h.

A range of substituted Sn-umbites were prepared via direct hydrothermal synthesis. For example, a 25% Nb substituted Sn-umbite can be synthesised following the above mentioned method simply replacing 25 at.% of $SnCl_4 \cdot 5H_2O$ with $NbCl_5$ with fixed molar ratio of K, Si, and H_2O. All the substituted Sn-umbites prepared in this work are listed in Table 2. The starting chemicals for the substitution are $NbCl_5$, GeO_2, $VOSO_4 \cdot xH_2O$, Sb_2O_5, YCl_3, and Sc_2O_3, respectively.

Table 2 List of substituted umbites studied in this work

Code	Substitution	Expected formula
Sn_Si	-	$K_2SnSi_3O_9 \cdot H_2O$
10Ge	10%Ge with Si	$K_2Sn(Ge_{0.1}Si_{0.9})_3O_9 \cdot H_2O$
20Ge	20%Ge with Si	$K_2Sn(Ge_{0.2}Si_{0.8})_3O_9 \cdot H_2O$
25Nb	25%Nb with Sn	$K_{1.75}(Nb_{0.25}Sn_{0.75})Si_3O_9 \cdot H_2O$
25V	25%V with Sn	$K_{1.75}(V_{0.25}Sn_{0.75})Si_3O_9 \cdot H_2O$
25Sb	25%Sb with Sn	$K_{1.75}(Sb_{0.25}Sn_{0.75})Si_3O_9 \cdot H_2O$
25(Y,Nb)	12.5% Y, 12.5% Nb with Sn	$K_2(Y_{0.125}Nb_{0.125}Sn_{0.75})Si_3O_9 \cdot H_2O$
25(Sc,Nb)	12.5% Sc, 12.5% Nb with Sn	$K_2(Sc_{0.125}Nb_{0.125}Sn_{0.75})Si_3O_9 \cdot H_2O$

Characterisation

The powder X-ray patterns of the crystals were collected using X-ray diffraction analysis (Bruker D8 diffractometer Cu-Kα radiation), and a whole pattern fitting method (Pawley fit) and Rietveld refinement of the structures were performed using TOPAS. The elemental compositions were determined using XRF (Bruker S8 Tiger) on loose powders.

Ion exchange evaluation

The Cs and Sr uptake was tested by shaking the materials in 0.1 M $Sr(NO_3)_2$ or $CsNO_3$ solution under batch conditions at V:m = 100:1 (mL:g) for 24 hr at room temperature. The white powders were washed first with water and dried at 50 °C. The Cs and Sr content in the material were evaluated using XRF.

Results and Discussion

(1) Synthesis and characterisation

These materials were successfully synthesised via a hydrothermal route as confirmed by XRD and XRF. The experimental powder XRD pattern of as-synthesised Sn-umbite and the substituted Sn-umbite are very similar but some peak shifts are observed, indicating that umbite structure is preserved upon incorporation. The unit cell parameters of the various umbites have been calculated with a whole pattern fitting using TOPAS, as plotted in Figure 2. The change in the cell dimensions of the substituted Sn-umbites, relatively to the parent Sn-umbite, is expected because of the difference in ionic radii between them and Sn^{4+}. Attempts have also been made to incorporate Te^{4+} (0.97 Å) into the umbite framework, or totally replace Sn with equal amount of trivalent and pentavalent elements. However, none have been successful due to a much larger radius of Te than Sn and the requirement of Sn as skeleton.

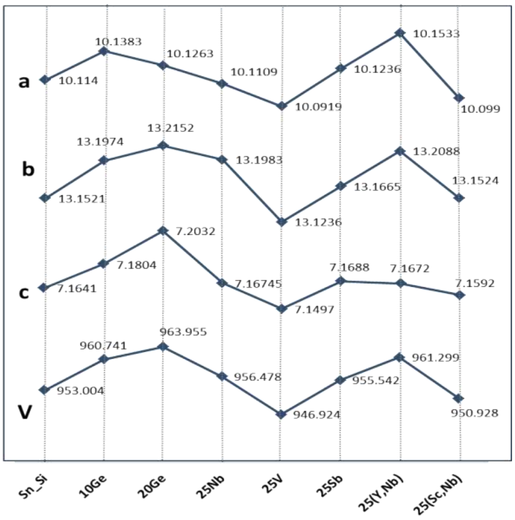

Figure 2 Unit cell parameters of various substituted Sn-umbites (numbers were acquired by a whole pattern fitting method)

Rietveld refinement has been performed to investigate the structural chemistry. As shown in Figure 3, a fairly reasonable fit was achieved for Sn-umbite. However, strict geometrical restraints were required for SiO_4 and SnO_6 to prevent the structure from falling apart during refinement. Furthermore, a serious anisotropic peak broadening was observed in almost every material, making it difficult to achieve a good fit. To resolve this, efforts have been made to improve crystallinity but have not been successful. It was also noted that some of the reflections were not calculated properly, indicating the starting structure model is not entirely correct. It is suggested that neutron diffraction data are required for structural solution since the diffraction is not dominant by the atomic number. In addition, due to the nature of neutron, more intense reflections at high angles can be observed, which are beneficial for refinement.

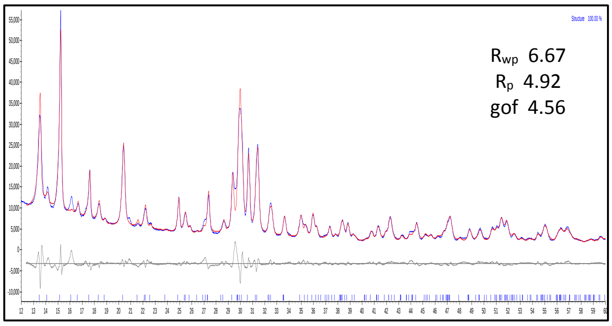

Figure 3 Powder X-ray diffraction pattern and Rietveld analysis of Sn-umbite ($K_2SnSi_3O_9{\cdot}H_2O$). The solid lines are the observed and calculated profiles. Tick marks represent the positions of allowed reflections, and a difference curve on the same scale is plotted at the bottom of the pattern.

(2) Ion exchange tests

As-synthesised materials were evaluated for the removal of Cs and Sr using static batch experiments. The recovered ion exchangers were then analysed by XRF, the molar ratios of Cs or Sr normalised to the sum of octahedral site elements such as Sn, Nb, Y, Sc. These are compared to unsubstituted Sn-umbite in Figure 4, but as samples were not prepared as fused beads the numbers should not be over interpreted.

It is of interests that most of the umbites containing pentavalent elements have a significant improvement in Sr or Cs uptake, apart from V^{5+}. We believe that it is because of the less crowded tunnels formed with fewer charge neutralising K cations, as observed as in Nb substituted CST. Furthermore, the poorest Sr uptake shown in 25%V doped umbite might be correlated with a decrease of unit cell volume which is usually associated with the flexibility to incorporate the counterions.

Ge was also doped in Sn-umbite to replace Si in the tetrahedral sites. They have been prepared successfully and ion exchange tested. A significant decrease in both Cs and Sr uptake was observed in 10% Ge doped umbite, however, the reason is not entirely clear yet. It is suggested that although Ge tend to form 4-fold coordination it can also be 6-fold geometry. More detailed structure investigation is required to prove this suggestion.

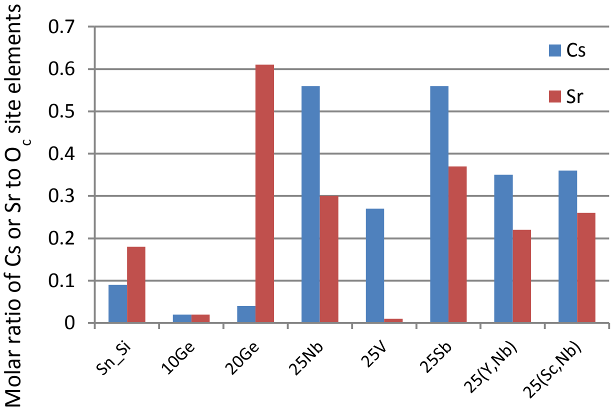

Figure 4 Relative Cs/Sr uptake (in molar ratio) of substituted and unsubstituted umbites.

Conclusions and Future Work

Conclusions

Ion exchange capacity to both Cs and Sr has been significantly improved in 25% Nb, 25% Sb, 25%(Y, Nb) and 25%(Sb,Nb) substituted umbites. It is observed that ion exchange properties are strongly correlated to unit cell parameters. This can be also attributed to other factors such as:

1. Different tunnel/pore size due to partial substitution.
2. When replacing Sn with 5^+ elements such as Nb^{5+} or V^{5+}, less K^+ cations are required for charge neutralisation forming less crowded tunnels to accommodate more hydrated Cs or Sr.

Future Work

1. Due to the unsatisfying refinement based on lab PXRD, synchrotron X-ray or neutron diffraction data are required for solving the crystal structure and investigating the structural effect of the substitution on Cs and Sr exchange behaviour.
2. In addition, atomistic simulation to predict ion exchange sites, framework response to exchange, and potential migration pathways during exchange will be performed in order to assist mechanistic understanding and materials performance optimisation. Fitting of atomistic potentials of tin silicate systems is ongoing.
3. Various ion exchange conditions such as pH control, kinetic, or competitive ions present to monitor the change of K^+, Cs^+, and Sr^{2+} using ICP are required.
4. Attempts have also been made to synthesise hierarchically micro-mesoporous structured zeolites for flow continuous ion exchange process. Hierarchical monoliths or spheres are advantageous due to the better accessibility of reactants to the active sites and the ease of recycle and reuse.

Acknowledgements

We gratefully acknowledge the EPSRC DISTINCTIVE grant for the financial support, and the Advantage West Midlands for the facilities.

References

[1] Fewox, C.S. and A. Clearfield, *Synthesis and characterization of protonated zirconium trisilicate and its exchange phases with strontium.* Journal of Physical Chemistry A, 2008. **112**(12): p. 2589-2597.

[2] Pertierra, P., et al., *Thermal behavior of K2MSi3O9 center dot H2O with the structure of umbite (M = Sn) and kostylevite (M = Pb) minerals.* Thermochimica Acta, 2004. **423**(1-2): p. 113-119.

[3] Doebelin, N. and T. Armbruster, *Microporous titanosilicate AM-2: Ion-exchange and thermal stability.* Microporous and Mesoporous Materials, 2007. **99**(3): p. 279-287.

[4] Xu, H., et al., *Crystal-chemical and energetic systematics of wadeite-type phases A 2 BSi 3 O 9 (A = K, Cs; B = Si, Ti, Zr).* Physics and Chemistry of Minerals, 2005. **32**(5): p. 426-435.

[5] Poojary, D.M., et al., *Syntheses and X-ray Powder Structures of K2(ZrSi3O9)·H2O and Its Ion-Exchanged Phases with Na and Cs.* Inorganic Chemistry, 1997. **36**(14): p. 3072-3079.

[6] Chitra, S., et al., *Optimization of Nb-substitution and Cs+/Sr+2 ion exchange in crystalline silicotitanates (CST).* Journal of Radioanalytical and Nuclear Chemistry, 2012: p. 1-7.

[7] Luca, V., et al., *Nb-substitution and Cs+ ion-exchange in the titanosilicate sitinakite.* Microporous and Mesoporous Materials, 2002. **55**(1): p. 1-13.

[8] Kerlegon, S.M., et al., *Synthetic optimization of crystalline silicotitanate and Nb-substituted crystalline silicotitanate for nuclear waste remediation.* Abstracts of Papers of the American Chemical Society, 2006. **231**: p. 987.

[9] Tripathi, A., et al., *Optimizing Cs-exchange in titanosilicate with the mineral pharmacosiderite topology: framework substitution of Nb and Ge.* Journal of Solid State Chemistry, 2004. **177**(8): p. 2903-2915.

[10] Behrens, E.A., D.M. Poojary, and A. Clearfield, *Syntheses, crystal structures, and ion-exchange properties of porous titanosilicates, HM(3)Ti(4)O(4)(SiO4)(3)center dot 4H(2)O (M=H+, K+, Cs+), structural analogues of the mineral pharmacosiderite.* Chemistry of Materials, 1996. **8**(6): p. 1236-1244.

[11] Behrens, E.A., D.M. Poojary, and A. Clearfield, *Syntheses, X-ray Powder Structures, and Preliminary Ion-Exchange Properties of Germanium-Substituted Titanosilicate Pharmacosiderites: HM3(AO)4(BO4)3·4H2O (M = K, Rb, Cs; A = Ti, Ge; B = Si, Ge).* Chemistry of Materials, 1998. **10**(4): p. 959-967.

[12] Shannon, R.D. and C.T. Prewitt, *EFFECTIVE IONIC RADII IN OXIDES AND FLUORIDES.* Acta Crystallographica Section B-Structural Crystallography and Crystal Chemistry, 1969. **B 25**: p. 925-&.

[13] Lin, Z., J. Rocha, and A. Valente, *Synthesis and characterisation of a framework microporous stannosilicate.* Chemical Communications, 1999(24): p. 2489-2490.

[14] Navascues, N., et al., *Reconstruction of umbite framework variants by atomistic simulations using XRD and sorption data.* Chemical Engineering and Processing, 2008. **47**(7): p. 1139-1149.

Mechanistic studies of uranium corrosion in mixed H_2O-H_2 systems

A.K. Banos*
*Email: Antonis.Banos@bristol.ac.uk

Interface Analysis Centre, University of Bristol

Abstract

The main objective of my PhD research is to investigate and develop a better understanding of the corrosion mechanisms and reaction rates of uranium under waste storage conditions. This requirement hinges on the need to implement safe control, monitoring and identification of corrosion products developing on the uranium-rich radioactive waste awaiting to be retrieved from the radioactive ponds and silos at Sellafield. In order to achieve our objective, the main chemical reaction of uranium with water (H_2O) and the interactions between H_2O, uranium and the reaction products (H_2, UH_3) need to be examined thoroughly. Apart from working solely on the combined system (U-H_2O-H_2), it is also wise to investigate standalone reactions; thus the whole subject may be divided into four main areas:

- U + H_2O (saturated/wet conditions).
- U + H_2 (early hydriding stage).
- UH_3 + H_2O (saturated conditions).
- U + H_2O + H_2 (over pressurised conditions).

Concurrently with the experimental work, two separate and comprehensive reports are being produced which detail the current international understanding of uranium corrosion in water and in hydrogen (rates, mechanisms, controlling influences).

Raman Probe Development for In-situ Nuclear Waste Analysis

K.E Wyness*[1], J.C.C Day [1], and B. Rogerson[2]

*Correspondence: kw14747@bristol.ac.uk

[1] University of Bristol (H H Wills Physics Laboratory, Tyndall Avenue, England)
[2] Sellafield Ltd. (Sellafield, Seascale, England)

Abstract

Sellafield Ltd. is situated in the north east of England and is the UK's nuclear decommissioning site. Within the site, it houses some of the UK's oldest wet storage ponds, with construction from the 1950's. This project seeks to analyse the bottom of the pond environment using Raman Spectroscopy with an in-situ Stand-off probe. Within these ponds a thick layer of sludge (approx. 1m depth) is at the base and is a mixture of nuclear waste, pond infrastructure and organic matter such as algae and windblown debris from its surroundings. This has formed due to decades of corrosion from the aqueous environment. An analysis will dictate the long term strategy for the retrieval and removal of this sludge, so characterising it is essential. The probe geometry and design are imperative for successful data sampling, as organic particulates emit fluorescence when excited by laser interaction, overwhelming the Raman signal the probe is attempting to measure. The probe also has to take data through a body of water. Here is the development to overcome these difficulties by using altering optical set-ups and laser wavelengths.

Introduction

Raman Spectroscopy

With Sellafield wanting a long term storage strategy, a full diagnosis must be completed on all their unknown waste contents. The legacy ponds (pile fuel and FGMSP) are amongst the containers which have unidentified waste products in. Raman spectroscopy is a powerful analytical tool to characterise these products as it detects chemical compounds, which can decipher each foreign specie found within this environment. Using the measurement of inelastic scattering of the vibrational modes associated to each material, Raman spectroscopy can produce an individual spectrum or "fingerprint". From this fingerprint, it is possible to distinguish between two materials with the same elemental components, but in different phases.

Figure 1 Allen et al. demonstrating the oxidation of UO2 into U3O8.

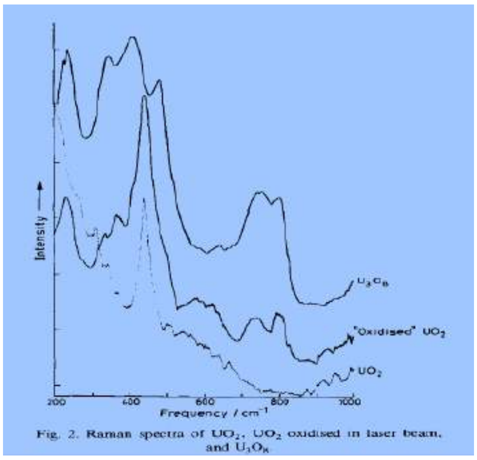

Figure 1. Shows UO_2 in its initial phase, with clear distinction of the $455cm^{-1}$ peak. The sample material is allowed to be oxidised which leads to the eventual production of U_3O_8. Notice the growth of several peaks during this process [1]. Other factors such as stress, strain, heat or pressure on the material will appear in the spectra as artefacts, such as peak shifting, widening or flattening. This could be helpful as the sludge will be formed of many components, with it being under containment in varying pond conditions. Currently there is limited characterisation work performed by NNL and Sellafield with sludge samples, with no in-situ Raman measurements yet taken [2].

Probe Development

Raman Spectroscopy involves the excitation of a material's surface with a laser light source. In this instance this excitation will need to be achieved through a target distance of 1m, passing through water. However there is a limited range of wavelengths that have minimal absorption in water. Figure 2. Pope et al demonstrates that 418nm attenuates the least through water, which therefore is the optimal laser wavelength for the Raman probe to operate at. A 405nm IPS diode laser was selected for the new probe with an operational max power of 30mW. To demonstrate the capabilities of Stand-off Raman [3], the University of Bristol has a preceding probe for this project for open air Stand-off Raman (Figure 3.). With 830nm as the working wavelength, it produces coherent spectra with minimal fluorescence. The principles of Stand-off Raman were established by sampling with this probe, and is the basis for the new optical arrangement. Table 1. compares all elements used with both probe designs.

Figure 2. Pope et al electromagnetic absorption through pure water

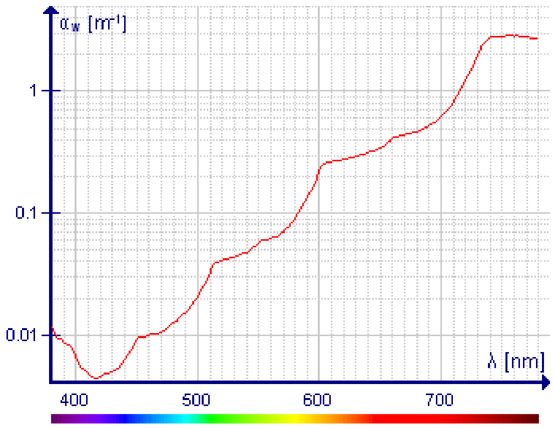

Table 1. Comparison of Probe designs

	Initial Stand Off Raman Probe	*New developed Raman Probe*
Laser Wavelength	830nm	405nm
Laser Power	140mW	30mW
Emission path filters	830nm Semrock Short Pass filter	407nm Semrock laserline clean up filter (with 12 degree slant)
Collection Path filters	830nm Semrock long pass filter 830nm Semrock dichroic mirror	N/A (407nm clean up filter used as a reflective surface) Optional Thorlabs 405nm notch filter (to be applied in biaxial arm)
Optical layout	Coaxial	Coaxial/with additional biaxial configuration
Spectrometer	Headwall	Shamrock 193i Andor
Camera	416 iDus Andor	416 iDus Andor

Methodology Details

Stand-off Raman Testing

When testing the 830nm Raman Probe (see figure 3.), it was important to measure the rate of Raman scattering loss due to distance. A subject material of PTFE, a polymer with several Raman peaks ranging from $200cm^{-1}$- $1300cm^{-1}$, was selected for calibration. The probe was then fixed into position and the PTFE's spectrum was measured at 30cm increments ranging from close range to the maximum distance achievable (0cm-270cm). This was performed several times and each individual peak was examined for a loss in intensity due to distance.

Figure 3. 830nm Stand-off Probe

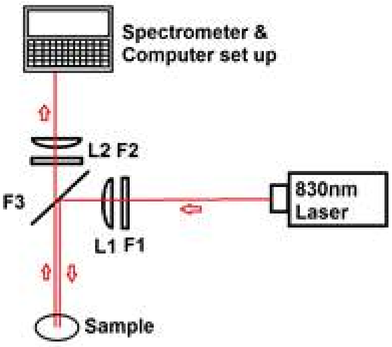

Samples

The probe was used to measure sample material sent from NNL (National Nuclear Laboratory). Powdered calcium carbonate, barium sulphate and magnesium hydroxide were given as appropriate corrosion products from the fuel cladding and pond infrastructure. Segments of concrete were given as the structural material of the ponds. However not all material is Raman active, such as metals. The fuel cladding's main component is magnesium, which is mixed with aluminium to form Magnox. NNL has also provided other non-Raman active samples of magnesium/Magnox turnings, steel and corroded magnesium sludge (CMgS). Further work will need to be carried out to allow them to be measured.

New Wavelength

The developed probe is successfully measuring Raman scattering, with a violet laser (405nm wavelength) being adopted into the design using a single filter configuration. The properties of the laser clean-up filter have been exploited to also reflect any Raman scattering (transmission window ≈ 403nm-407nm at 12°) onto a positioned mirror and collected at a point parallel to the emission path (see figure 4). This set-up has successfully taken multiple spectra, and also minimises the number of optical elements.

Figure 4. 405nm Stand-off Probe

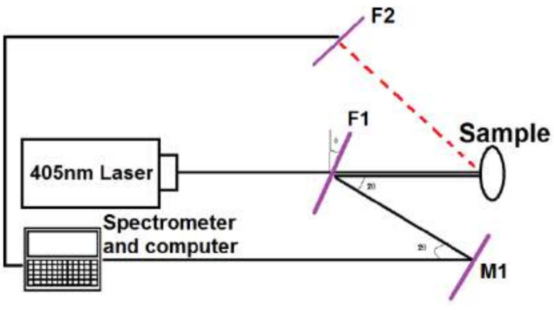

Water based sampling has been trialled. Figure 5 shows the H_2O peak of the O-H bond at around $3500cm^{-1}$.Because of this peak, any Raman scattering in this region is off limits to the sampling. The sample range for the probe is therefore governed by this.

Figure 5. Water Raman spectra measured through a glass flask

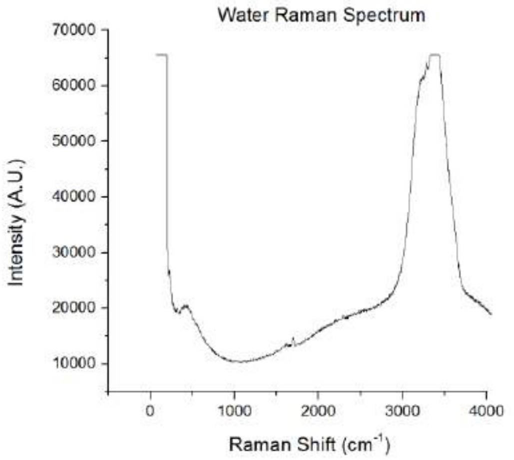

Results and Discussion

Initial Work

The 830nm probe is currently effective at collecting Raman scattering due to the minimal fluorescence generated by the NIR wavelength. Stand-off Raman has been established as a useful technique to this project with lab testing. (figure 6), the probe reached 270cm however Raman scattering could be collected at greater distance. Collecting a spectra was still feasible even at the larger distances. Although the technique has potential to do longer distances than measured, a target distance of 1m has been selected. Due to the other issues this probe

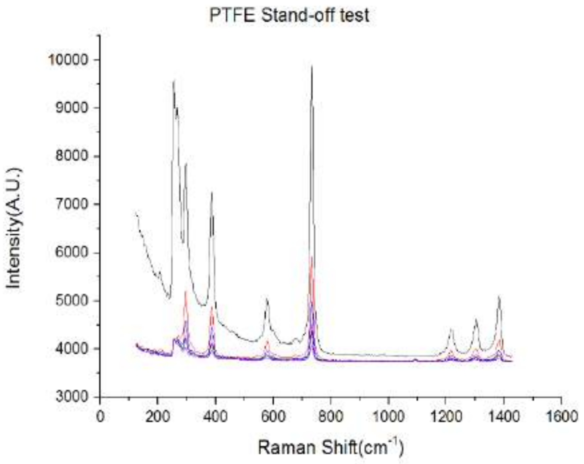

Figure 7. PTFE Raman Spectra – 405nm

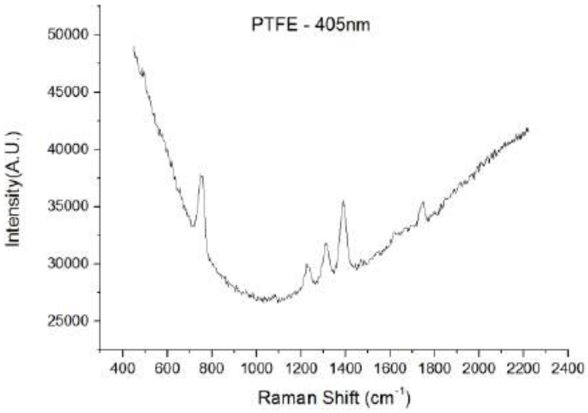

Alternative Wavelength

The 405nm Raman set-up is currently providing inexplicit data. With multiple data sets of PTFE (Polytetrafluoroethylene) taken with the 830nm probe, the expected spectra (Figure 7.) only showed 4 distinguishable peaks out of a possible 8 [4], with the peaks from approx.. 0-700cm^{-1} being overwhelmed by a strong signal.

Due to the optical bench set-up, performing underwater measurements at a depth of 1m is restricted. Sampling a flask of water is sufficient at this current time to measure the Raman spectrum of water. Implementing the optical configuration into a portal probe is the next vital step for testing, with full movement in equipment, any range of distance of air or water can be tested. The 830nm has the minimal fluorescence, as it is out of range of expected fluorescence. However it also has 3 optics filters in comparison to the single 405nm laser clean up filter. Although it is more cost efficient to have less filters, its filtering will need to be improved by adopting another collection path using a biaxial set-up. Figures 8 and 9 proves the difference in probe performance. Magnesium hydroxide is likely be the most abundant product of the sludge, as it is the

Figure 8. Magnesium Hydroxide Raman Spectra - 405nm

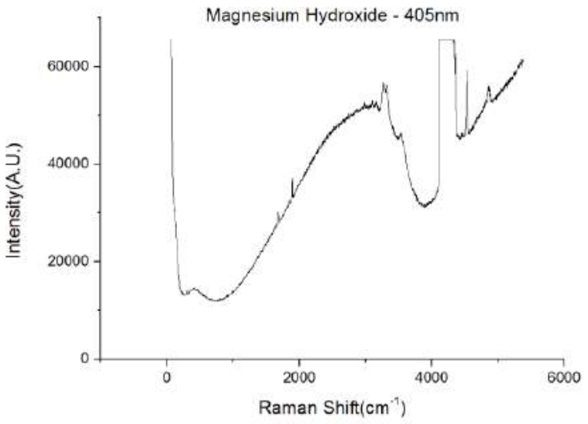

oxidisation of the Magnox fuel cladding. Therefore it is important that the new probe can successfully measure this material. The Raman peaks of magnesium hydroxide [5] are engulfed by the strong fluorescence/laser signal at the start of the spectrum. This follows for the other NNL samples with a Raman peak below roughly $500cm^{-1}$.

Figure 9. Magnesium Hydroxide Raman Spectra - 830nm

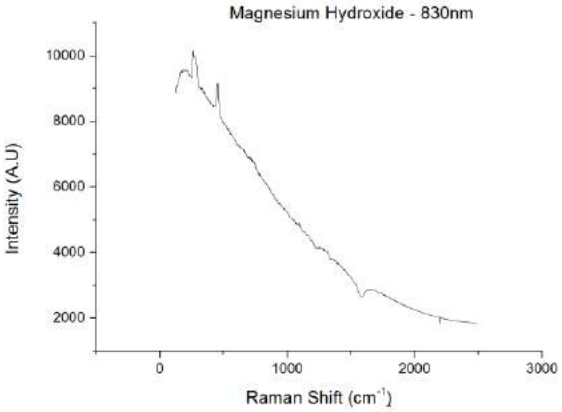

Conclusions and Future Work

Using two different wavelengths clearly exhibits the need to exclude fluorescence within the probe design. Material strongly Raman active will not necessarily need this extra measure, so keeping a coaxial alignment would still be beneficial when sampling. However most of the pond proxy samples produce a strong fluorescent signal, with any Raman signal being overwhelmed. The difference with the developed probe's performance is currently not enough spectral clarity. This will be corrected with further filtering into place, such as a biaxial arm as an optional attachment. This will include a 405nm notch filter to omit the laser light and due to the oblique geometric placement, will only be only to sample at a set distance.

Further work on samples needs to be completed to on the NNL samples. The sludge will contain a large amount of corroded metal. Therefore the proposed plan is for Steel and Magnox metal to be placed into an experimental steel cell with a water crucible. The cells will be placed into ovens over several months ranging from 25- 70 degrees Celsius. These temperatures have been selected in accordance to the residue heat when the fuel is retrieved out of the reactor core, so will simulate the same chemical reaction that occurs within the pond in a favourable timescale.

Acknowledgements

Acknowledgements go to Dr John Day for all his supervision and guidance through this project. Bill Rogerson for being an insight into the industry and overseeing the direction of this assignment.

References

[1] G. Allen, I. Butler "Characterisation of uranium oxides by micro-Raman spectroscopy" Journal of Nuclear Materials 1987 vol: 144 (1-2) pp: 17-19

[2] C. Gregson et al "Combined electron microscopy and vibrational spectroscopy study of corroded Magnox sludge from a legacy spent nuclear fuel storage pond" Journal of Nuclear Materials 2011 vol: 412 (1) pp: 145-156

[3] S. Sharma et al "Stand-off Raman spectroscopic detection of minerals on planetary surfaces Spectrochimica Acta Part A: Molecular and Biomolecular Spectroscopy 2003 vol: 59 (10) pp: 2391-2407

[4] J. Koenig "Raman Scattering and Band Assignments in Polytetrafluoroethylene" The Journal of Chemical Physics 1969 vol: 50 (7) pp: 2823

[5] P.Dawson et al "The polarized infra-red and Raman spectra of Mg(OH)2 and Ca(OH)2"Journal of Physics and Chemistry of Solids 1973 vol: 34 (7) pp: 1217-1225

Glass Degradation in Partially Immersed Water

R. K. Chinnam[1] and W.E. Lee[1]

*Correspondence: r.chinnam@imperial.ac.uk

[1] *Centre for Nuclear Engineering (CNE), Department of Materials, Imperial College London, South Kensington Campus, London SW7 2AZ, UK.*

Abstract

Glass is one of the potential host to contain nuclear wastes for disposal in deep geological repositories. Water which can potentially access repositories can degrade glass and possibly transport radionuclides from vitrified nuclear waste canisters into environment. Global research efforts to understand degradation of host glass in aqueous conditions and its ability to retain radionuclides for thousands of years is in progress. To assess the long term degradation of glass, there is a need to understand many unknown mechanisms and influences. We at Centre for Nuclear Engineering, Imperial College London are developing experimental methods to understand influences of different realistic conditions on glass degradation. We are currently studying glass cracks degradation, glass surface modifications and colloids formation. The document discusses surface modifications of glass when moisture condenses over glass surface.

Introduction

Vitrified nuclear waste disposed of in geological repositories will be protected with a multilayer barrier system. These barriers, during the course of time, will get damaged and can leak water into canisters. In such an event, water can come in contact with glass and activate corrosion. Glass corrosion was classified by Hench and Clark [1] into 5 types, based on the corrosion medium pH and the gel layer formation mechanisms. With increase in pH, the glass corrosion mechanisms and the surface gel layer formation were found to vary. Decades of nuclear glass degradation studies had led to establish sequence of degradation mechanisms that may occur under ideal conditions. Nuclear glass dissolution was said to occur in four stages (1. Hydrolysis, 2. Protective layer and solution saturation, 3. Water diffusion and secondary phase precipitation, and 4. Large precipitation of silicate minerals) [2]. Each stage time frame is not defined and the length of these stages can vary depending on factors such as temperature, pH, composition, renewal rate of the solution. Most previous studies have been dedicated to understanding surface degradation mechanisms of glass [3, 4] and very few considered additional physical and chemical influences that can affect the length of each stage completely immersed in water and is bulk in state without any defects nor other influences. In reality, at the initial stages canisters may not completely but might partially be immersed in water. The effect of partial immersion and water condensation on surface is not reported in literature, hence in this paper we discuss the influence of water condensation on International Simple Glass (ISG).

Methods

The experimental procedure shown in Figure 1 was tested on International Simple Glass (ISG) (provided by James Marra (Savannah River National Laboratory, USA)). The ISG samples were subject to aqueous corrosion in static conditions at 90°C in deionised water for one weeks at pH 7. The ISG was cut into samples of (L × B × H) ~20 mm × 5mm × 2mm size using a diamond blade. These samples were grounded using SiC papers up to 4000 i.e., 2.5µm smoothness.

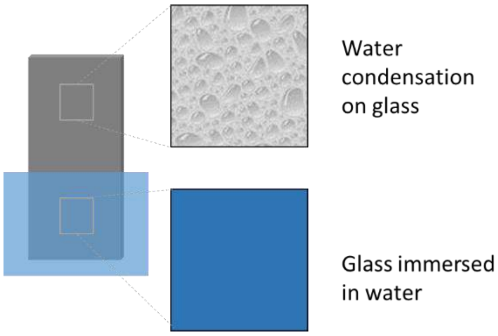

Figure 1 Schematic of ISG Corrosion test setups.

Only half of the sample was immersed in water while the other half was left in air in the container. This experiment was conducted for one and 3 weeks to understand the influence of water condensation on ISG.

Results and Discussions

Figure 2 shows back scattered images of simulated glass which was tested in distilled water for 1 week at 90^{o}C. The stack of images show areas of ISG developing features on the surface during degradation studies. In Figure 2 ISG was observed to develop a thick gel layer at the bottom of sample with gel layer cracking because of water evaporation when dried after removing from container. The gel layer cracking was found to decrease from bottom till water and glass contact region indicating a gradient over gel layer thickness under water. Because of surface tension of glass and static condition of water during experiment a convex layer of water known as meniscus is formed over glass. The meniscus region on ISG was found to precipitate calcium rich phase. Region above meniscus did not get affected by condensation of water, no features or localized chemical changes were found. Area in the top region developed pits due to saturation of water.

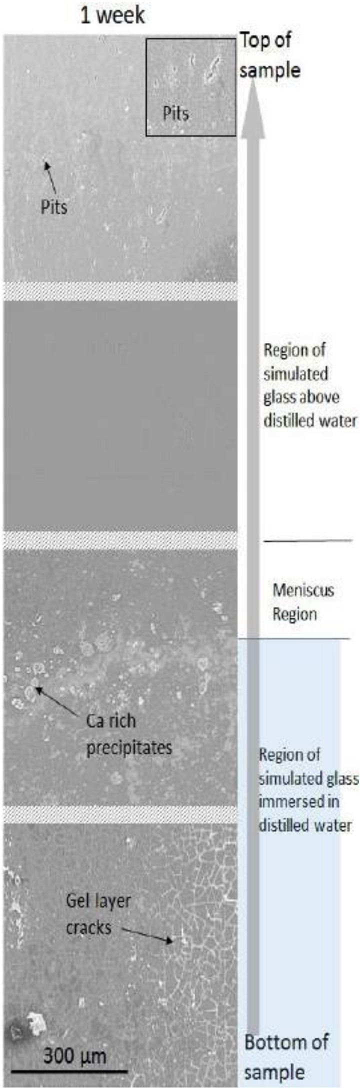

Figure 2 Shows BSE images of ISG tested for degradation in distilled water for 1 week at 90^{o}C. The images are placed in a sequence bottom to top and labelled accordingly

After degrading for 3 weeks, the ISG was found to develop complex morphologies of calcium rich phases on the surface (see figure 3). It was found that the glass immersed in water formed a gel layer while vapor condensed on the surface of the glass above the water. Droplets of water on the glass surface saturated with leachates grew calcium silicate rich phases (see figure 3b and 3c) (confirmed by EDX) and pits (see figure 3d). Similar effects have been found in archaeological glasses where a protective Ca-rich surface layer was found on the surface of glass, this layer hindered inward growth of the dissolution reaction favoring localized pitting. The pitting is caused by water condensation followed by its slow evaporation leading to increased pH [5]. We believe a similar effect is occurring on ISG glass (see figure 3d).

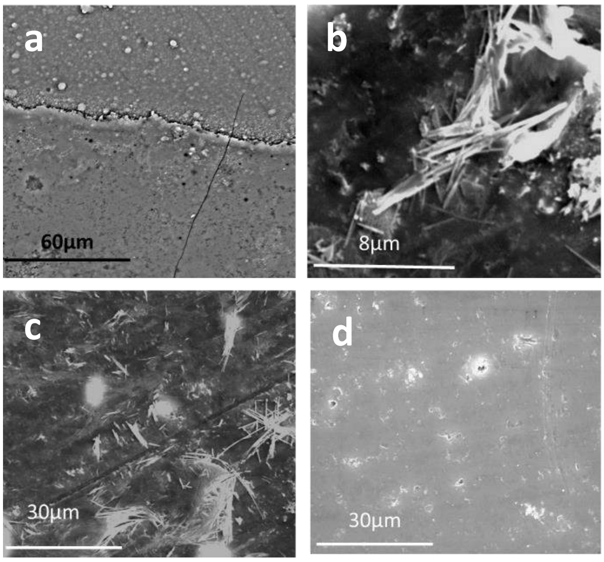

Figure 3 Shows ISG glass surface degraded in partially immersed distilled water for 3 week at 90^{o}C. Description of Figures a, b, c, and d is given in the text.

Conclusions

1. A gel layer thickness gradient from bottom to glass/water boundary is found in ISG.
2. The 1 and 3 weeks degradation of ISG resulted in precipitation of Ca-rich phases and pitting on the surface above water indicating that water condensation can modify glass surface.

References

---

[1] Hench, L. L., & Clark, D. E. (1978). Physical chemistry of glass surfaces. *Journal of Non-Crystalline Solids*, 28, 83–105.

[2] Gin, S., Abdelouas, a., Criscenti, L. J., Ebert, W. L., Ferrand, K., Geisler, T., Vienna, J. D. (2013). An international initiative on long-term behavior of high-level nuclear waste glass. *Materials Today*, *16*(6), 243–248.

[3] Jantzen, C. M., Brown, K. G., & Pickett, J. B. (2010). Durable Glass for Thousands of Years. *International Journal of Applied Glass Science*, 1(1), 38–62.

[4] Gin, S., Abdelouas, a., Criscenti, L. J., Ebert, W. L., Ferrand, K., Geisler, T., Vienna, J. D. (2013). An international initiative on long-term behavior of high-level nuclear waste glass. *Materials Today*, 16(6), 243–248.

[5] McLoughlin, S. D., Hyatt, N. C., Hand, R. J., & Lee, W. E. (2006). The long term corrosion of glasses: analytical results after 32 years of burial at Ballidon. *MRS Proceedings*, 932(3), 59–67.

ACKNOWLEDGEMENTS

The work presented in this paper is carried under DISTINCTIVE CONSORTIUM project funded by EPSRC, under grant #SP/L014041/1, UK.

Low Temperature Immobilisation of Spent Adsorbents from Fukushima

D. Pletser*[1], R. K. Chinnam[1], M. Kamoshida[2] and, W.E. Lee[1]

*Correspondence: D.Pletser@imperial.ac.uk

[1] *Centre for Nuclear Engineering (Imperial College London, SW7 2AZ London, United Kingdom)*
[2] *Center for Technology Innovation (Energy, Research & Development Group,Hitachi, 7-2-1 Omika-cho, Hitachi-shi, Japan)*

Abstract

The clean-up of the Fukushima Daiichi site continues to generate large volumes of spent adsorbents which need to be disposed of permanently, one of the candidates is a low temperature immobilisation process to avoid volatilising radioactive Cs and Sr species. To this end an immobilisation process with a maximum temperature of 600ºC was developed by sintering model waste with glass frit to form a dense Glass Composite Material (GCM) wasteform. A zeolitic model wasteform, chabazite, was sintered with two lead-based glass compositions, lead borosilicate (PBS) and a lead borate (PB) glass composition, at a maximum temperature of 600ºC. Full encapsulation of the zeolitic wasteform was achieved for waste loadings up to 40 wt.% in PBS and 30 wt.% in PB in all cases, with both GCM systems showing foaming. PBS GCM formation was successful at a maximum of 600ºC, while the PB GCM formation was shown to be possible at a maximum temperature of 550ºC.

Introduction

Several water treatment systems are currently in place at Fukushima to remove radionuclides from the contaminated water used to cool the reactor cores, such as the HP-ALPS (High Performance Advanced Liquid Processing System), the high performance multi-nuclide removal equipment. However, the treatment of approximately 500 m^3/day of contaminated water continues to generate large volumes of spent adsorbents, which can be highly radioactive (approximate level of activity concentration of the order of 1E11 Bq/kg to 1E12 Bq/kg). These spent adsorbents are currently stored on-site, but will require immobilisation in a suitable wasteform before being disposed of permanently. The most common radionuclide species present in the effluent cooling water are Cs and Sr species with short half-lives, the longest is Cs-137 with a 30.08 year half-life. The final ILW wasteform will have an estimated repository lifetime of 300 years and will likely be disposed of at a surface storage facility.

Another aspect to consider in any process used to immobilise the adsorbents is Cs and Sr volatilisation. Due to the use of seawater as an emergency coolant and the ingress of groundwater the system has a high chloride content. The high level of chloride could lead to CsCl and SrCl species. Both the chloride species of Sr and Cs are volatile at higher temperatures [1], so to ensure minimal volatilisation a low temperature immobilisation process is sought with a maximum temperature of 600ºC. A fully homogeneous glass wasteform at this temperature is not achievable, as a fully vitreous wasteform incorporating these adsorbents is only achievable above 1100ºC [2].

Radionuclide volatilisation is a problem that has been faced by the nuclear industry in many different clean-up scenarios, including volatilisation from Cs adsorbed onto zeolites. Gray[3] noted that the volatility is significant above 700ºC, and this is echoed by Kamizano *et al.*[4] who notes that volatilisation can be significant above 1000ºC. Furthermore, the presence of chloride species can greatly increase volatilisation, the presence of NaCl in a system can push the volatilisation of Cs to >99% above 1000ºC [4]. Due to the situation at Fukushima Daiichi, the waste has a significant chloride presence that would greatly increase both Cs and Sr volatilisation. For this reason alone classical industrial vitrification techniques are not suited to the immobilisation of this particular waste stream. The volatilisation concerns are too great and a viscous flow sintering process is opted for instead to create a GCM wasteform.

Methodology Details

Two glass compositions were prepared for this study. A lead borosilicate glass (composition in wt.%: PbO 63, B2O3 25 and SiO2 12) was prepared by a melt quench from base oxides. This glass was melted for 2h at 1200ºC in a bottom loaded Lenton EHF 1800 furnace (Carbolite, Hope Valley, UK) using a platinum crucible. A lead borate glass composition (composition in wt.%: PbO 80 and B2O3 20) was prepared by a melt quench from base oxides. This glass was melted for 2 h at 950ºC in a bottom loaded Lenton EHF 1800 furnace (Carbolite, Hope Valley, UK) using a platinum crucible. Both melts were quenched in a large volume of deionised water kept at room temperature. The resulting glass frits were recovered, washed with acetone and dried for 12h at 110ºC. The dried frits were wet ball-milled with ethanol in a planetary ball mill. The ball milling was performed at low frequency (100 Hz) for 5 minutes, with recovered frit of a particle size ≤ 38 µm.

The model waste without Cs and Sr loading was a commercially acquired chabazite. The chabazite used was acquired from Verdi Sp.A (Castelnovo di Sotto, Italy).The chabazite was ground and sieved with the 100 µm - 125 µm fraction retained. The chabazite is initially dried at 110ºC to release any sorbed water. Calcination was performed at 600ºC to remove any volatile species from the chabazite. Calcined (particle size: 100 µm - 125 µm) and glass frit (particle size: ≤ 38 µm) were mixed in a turbula mixer for 12 h to homogenise at different wt.% waste loadings.

After mixing wasteforms were produced by mixing different chabazite (particle size: 100 µm - 125 µm) waste loadings, in 10 wt.% increments, with glass frit (particle size: ≤ 38 µm) for 12 h in a turbula mixer. The mixed powders were loaded into stainless steel ring-shaped (diameter 9.5 mm) moulds and sintered using the optimised sintering profiles. Sintering profile for the PBS system consisted of steps of 2h at 350ºC, 2h at 600ºC and 2h at 550ºC Sintering profile for the PB system consisted of steps of 2h at 350ºC, 2h at 550 ºC and 2h at 500ºC (See Figures 1 and 2).

Produced wasteforms were analysed using SEM (JEOL JSM6400 and JEOL JSM6010) and Energy Dispersive Spectroscopy (EDS) (Oxford Instruments INCA). Surface and cross-sectional Secondary Electron Images (SEI) were taken to examine the microstructure. X-Ray Diffraction (XRD) was performed using a Bruker D2 PHASER.

Sintering Conditions

Initial attempts were done with cold-pressed lead borosilicate samples subjected to a two-step sintering profile, where the first step is to direct sinter the sample at 600ºC for 10 min followed by cooling the sample to 550ºC and annealing for 6h. The sintering step at 600ºC is chosen to activate viscous flow sintering and the subsequent 550ºC annealing is chosen to homogeneously densify the material. The resulting wasteform was found to have a glazed surface, but was bloated [11]. This bloating could to be due to volatilisation of sorbed species from the zeolitic model wasteform. During direct sintering, as soon as the powder compact was introduced into the furnace, the surface lead borosilicate glass particles soften and block all open surface pores. Temperature homogenisation of the bulk would have softened the compact resulting in viscous flow. During this process the release of any volatile material would be blocked by the lack of open porosity. Hence, the gases get trapped and lead to foaming [12]. The chabazite is hygroscopic and a possible source of foaming in the direct sintered compacts is water sorbed on to chabazite. To obtain a denser material, an initial calcination step at 350ºC for 2h was added to volatilise any material or water vapour before the viscous flow of glass occurs. GCM foaming was greatly diminished by evaporating volatile species from the chabazite in an additional sintering step. To further eliminate adsorbed species from the model wasteform an extra calcination step was added to the process. The chabazite was calcined at 600ºC for 2h to remove any possible volatile species that may have adsorbed to the chabazite during processing (Figures 1 and 2).

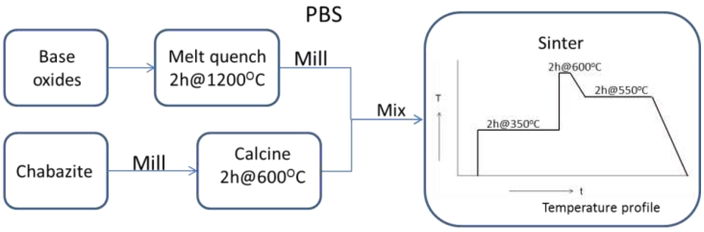

Base oxides: PbO 63wt.%, B_2O_3 25wt.%, SiO_2 12wt.%

Figure 1. Process flow diagram of PBS wasteform

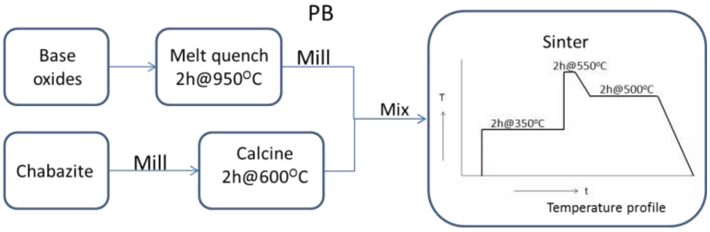

Base oxides: PbO 80wt.%, B_2O_3 20w.t%

production

Figure 2. Process flow diagram of PB wasteform production

Results and Discussion

PBS

To closely mimic the final industrial application the mixed powders were loaded into stainless steel rings before sintering. While optimisation was performed with a 10 wt.% chabazite waste loading, further waste forms were produced in 10 wt.% increments, up to a 40 wt.% waste loading. Due to increasing waste loading of chabazite more adsorbed species need to be eliminated from the wasteform during thermal treatment. This requires a longer treatment step at 350ºC before full viscous flow sintering at 600ºC.

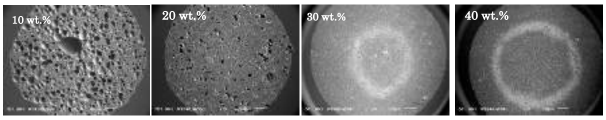

Figure 3. Cross-sectional SEI micrographs of PBS samples.

Cross-sectional SEI in Figure 3 of the different waste loadings in PBS show different microstructures, with especially 10 wt.% exhibiting foaming, however this is decreased at increasing waste loading. The observed halo effect in the 30 wt.% and 40 wt.% is an artefact of the sample preparation for SEM and is due to the resin used for the cold mounting. Work is currently in progress to ensure full densification at all waste loadings.

Cross-sectional SEI micrographs and EDS maps from 10 wt.% (Figure 4), 20 wt.% (Figure 5), 30 wt.% (Figure 6) and 40wt.% (Figure 7) waste loadings reveal homogeneous waste distribution in the vitreous matrix. Each sample shows similar GCM microstructures, with EDS spectra showing different phases in the microstructures. The Al, Si, and K-rich chabazite phases and Pb-rich glass phase became mixed in the final microstructure.

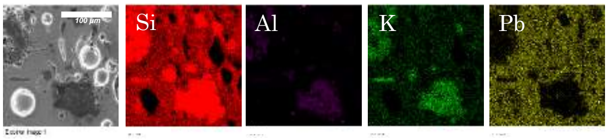

Figure 4. 10 wt.% PBS SEI and EDS micrographs.

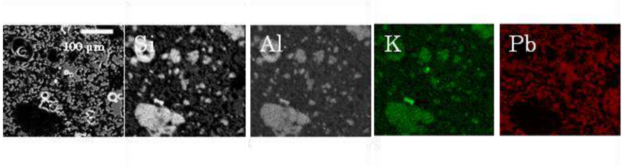

Figure 5. 20 wt.% PBS SEI and EDS micrographs.

The SEI in Figure 4 show the 10 wt.% sample with closed closed porosity, but the SEI in Figure 5 shows the denser microstructure of the 20 wt.% wasteform. In both cases encapsulation of the chabazite in the lead glass matrix is achieved.

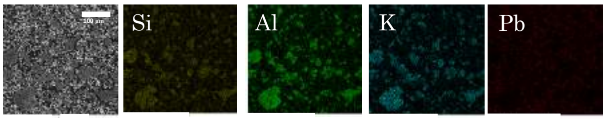

Figure 6. 30 wt.% PBS SEI and EDS micrographs.

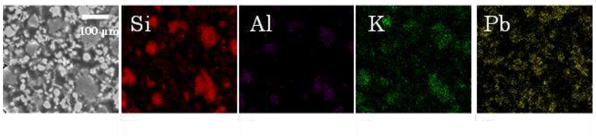

Figure 7. 40 wt.% PBS SEI and EDS micrographs.

At higher waste loadings foaming is greatly diminished. Both Figure 6 and Figure 7, showing 30 wt.% and 40 wt.% waste loading respectively, show a dense microstructure. Due to the higher waste loading initial sintering and pore occlusion is presumed to take longer, giving adsorbed volatiles longer to diffuse out of the wasteform, and leaving dense microstructures. Encapsulation of the chabazite in the lead glass matrix is consistently achieved in all presented wasteloadings.

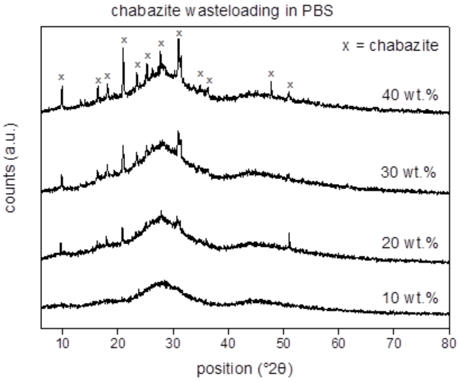

Figure 8. Increasing waste loadings of pre-calcined chabazite in PBS, three-step sintering profile

Figure 8 shows the spectra of increasing waste loading of the pre-calcined chabazite in PBS glass. These samples underwent the sintering profile described previously. In the diffractogram, at 10 wt.% waste loadings the crystalline peaks of the chabazite, denoted by the X, are overlapped by the amorphous halo of the PBS glass. As waste loading increases the relative peak intensity increases and the peaks start showing above the amorphous halo, especially with the 40 wt.% waste loading pattern which exhibits clear crystalline peaks. The fact that such peaks are visible confirms that the crystalline phase has not dissolved into the amorphous glass phase, thereby showing that the created wasteform is indeed a glass-composite.

PB

The PB glass composition lacks the silica phase as a glass former, with the lead phase acting as the glass former. The lack of silica in the glass lowers the melting temperatures and the flow point, leading to lower processing temperatures [5]. The PB frit was mixed with the pre-calcined chabazite and loaded into stainless steel rings before sintering. Waste loading was done in 10 wt.% increments, up to 40 wt.%.

However 40 wt.% waste loading wasteforms did not sinter well, so only up to 30 wt.% samples were analysed. The 350ºC pre-treatment step was retained, to ensure removal of any sorbed volatile species from the chabazite. After this the composites were sintered at 550ºC for 2 h and then treated at 500ºC for a further 2h. Afterwards samples were left to cool in equilibrium in the furnace.

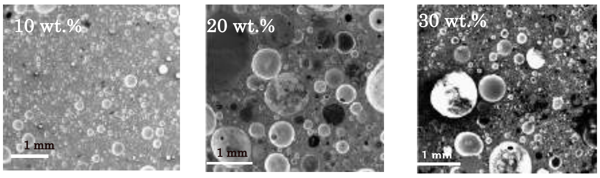

Figure 9. Cross-sectional SE micrographs of PB samples.

PB GCM wasteforms are similar to PBS GCM wasteforms in their foaming behaviour, as seen in the un-optimised PBS samples in Pletser *et al.* [11] and the SEI of the PB in Figure 6. While the microstructures exhibit strong foaming characteristics, encapsulation of the chabazite model waste is achieved for all waste loadings.

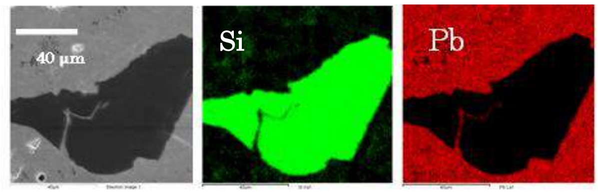

Figure 10. 10 wt.% waste loading PB EDS maps.

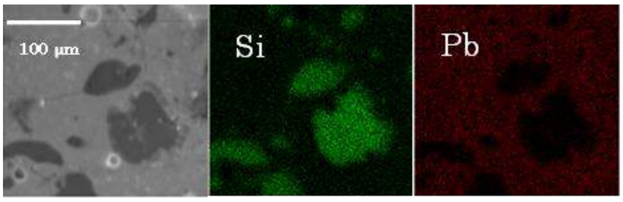

Figure 11. 20 wt.% waste loading PB EDS maps.

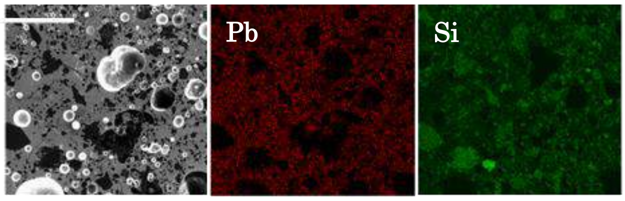

Figure 12. 30 wt.% waste loading PB EDS maps.

EDS maps of all samples show, despite foaming, good encapsulation of the chabazite, revealed by the presence of Si surrounded by lead borate glass, as shown by the Si and Pb maps (Figures 7-9). The successful encapsulation of the model wasteform with the lead borate glass shows that even at temperatures as low as 550ºC a viable GCM wasteform can be produced.

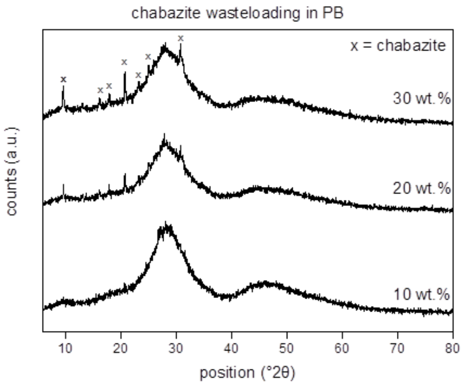

Figure 13. Increasing waste loadings of pre-calcined chabazite in PB, three-step sintering profile

Figure 13 shows a similar pattern to Figure 8 with pre-calcined chabazite in PB glass. Here a maximum 30 wt.% waste loading was achieved. Again at 10 wt.% waste loadings the crystalline peaks are obscured by the amorphous halo, with the crystalline peaks showing above the halo at 30 wt.% waste loading. The visible crystalline peaks, along with the amorphous halo of the glass confirm that the produced wasteforms are glass-composites.

Conclusions and Future Work

Glass composite wasteforms were successfully produced to immobilise volatile Cs and Sr containing waste generated in the clean-up of the Fukushima Daiichi site. The challenge of overcoming a low processing temperature to design a viable model nuclear wasteform was successfully achieved by producing a GCM loaded with chabazite and subjected to direct sintering to form a bulk material with a maximum operating temperature of 600ºC. Two different glass compositions, PBS and a PB composition, were used to produce the wasteforms. These two compositions were studied for their low temperature processing capabilities and their results compared. The release of adsorbed volatile species was enabled by modifying the sintering profile, as during viscous flow sintering a glaze can form on the surface of the wasteform, impeding the diffusion of volatile species, leading to bloating and a foamed microstructure. These initial results open up a promising route of processing for these spent adsorbents and the possibility of low temperature immobilisation of volatile nuclear waste in general.

Further work includes crystallisation studies, in which both PB and PBS frit are being analysed using coupled differential thermal analysis (DTA) - thermogravimetric analysis (TGA) to assess crystallization kinetics of both glass compositions. This work is still ongoing.

While most has concerned itself with the viscous flow sintering behaviour of the glass compositions work has continued to produce loaded Cs loaded wasteforms. For this a Cs loading protocol is being developed to accurately load the chabazite. An accurate Cs loading protocol for up to 12 wt.% Cs using a 24 h reflux with CsCl is being perfected, with successful Cs loading to be confirmed by X-Ray Fluorescence (XRF).

Acknowledgements

The support of Hitachi is gratefully acknowledged.

References

1. M.H. Langowski, J.G. Darab, and P.A. Smith, Volatility Literature of Chlorine, Iodine, Cesium, Strontium, Technetium and Rhenium; Technetium and Rhenium Volatility Testing, Pacific Northwest National Laboratory, Editor. 1996, US Department of Energy,: Oak Ridge, USA.

2. D.M. McPherson, B.W. Bowan, and L.D. Pye. The Dissolution of Zeolitic Compounds in Borosilicate Glass Melts. in International Congress on Glass. 1986. New Delhi, India.

3. W.J. Gray, Volatility of some potential high-level radioactive waste forms. Radioactive Waste Management, 1980. 1(2): p. 147-169.

4. H. Kamizono, S. Kikkawa, S. Tashiro, and H. Nakamura, Volatilization of Cesium from Nuclear Waste Glass in a Canister. Nuclear Technology, 1986. 72(1): p. 84-88.

5. C. Erdogan, M. Bengisu, and S.A. Erenturk, Chemical Durability and Structural Analysis of PbO-B2O3 Glasses and Testing for Simulated Radioactive Wastes. Journal of Nuclear Materials, 2014. 445: p. 154-156.

6. K. Raj and C.P. Kaushik, Glass Matrices for Vitrification and Radioactive Waste, in International Seminar on Science and Technology of Glass Materials. 2009, Institute of Physics: UK.

7. V.S. Yalmali, D.S. Deshingkar, and P.K. Wattal, Chemical Durability of Lead Borosilicate Glass Matrix Under Simulated Geological Conditions, B.A.R.C. Back-End Technology Development Division, Editor. 2002, Government of India: Mumbai, India.

8. W.E. Lee, M.I. Ojovan, M.C. Stennett, and N.C. Hyatt, Immobilisation of Radioactive Waste in Glasses, Glass Composite Materials and Ceramics. Advances in Applied Ceramics, 2006. 105: p. 3-12.

9. A.A. Digeos, J.A. Valdez, K.E. Sickafus, S. Atiq, R.W. Grimes, and A.R. Boccaccini, Glass Matrix/Pyrochlore Phase Composites for Nuclear Wastes Encapsulation. Journal of Materials Science, 2003. 38(8): p. 1597-1604.

10. S. Le Caër, Water Radiolysis: Influence of Oxide Surfaces on H2 Production under Ionizing Radiation. Water, 2011. 3(1): p. 235.

11. D. Pletser, R.K. Chinnam, M. Kamoshida, and W.E. Lee, Immobilisation Process for Contaminated Zeolitic Ion Exchangers from Fukushima. MRS Scientific Basis for Nuclear Waste Management, 2015. Submitted.

12. R.K. Chinnam, S. Molinaro, E. Bernardo, and A.R. Boccaccini, Borosilicate Glass Foams from Glass Packaging Residues, in Ceramic Transactions. 2014. p. 205-210.

Nanoscale Investigation and Control of Radionuclides in Waste Management

E. Cali'*[1], M.P. Ryan[1], and L. Vandeperre[1]

*Correspondence: e.cali14@.imperial.ac.uk

[1] *Department of Materials (Imperial College London, London, UK SW7 2AZ)*

Abstract

The rapid development of the nuclear industry and the associated production of toxic waste has created a large demand for the design of new novel materials aimed at the removal of soluble metals and radionuclides for safe and efficient waste disposal. The recent years' development of magnetic nanoparticles for separation technologies in liquid systems is wide-spread and already in use in medical testing [1–4]. The challenge is to translate this methodology, via surface functionalization to target the species of interest, and to use superparamagnetic behavior for waste form speciation and separation. The potential for magnetic-sorbent structures to be used in waste form separation or removal of RNs from liquid streams has been investigated. Particle development is being carried out and characterization studies performed using TEM-EDX, ATR-FTIR, XRD, DLS and ζ-potential. Preliminary sorption tests with Sr and U have been carried out to evaluate the sample specificity.

Introduction

The Legacy Ponds and Silos (LP&S) at Sellafield Nuclear Site, built to develop an underwater radioactive waste temporary storage system, contain large amounts of waste and sludge from corroded fuel accumulated from the 50s, as well as solubilised metal ions, the removal of which is the target of this project.

Recent years has seen the development of nanotechnologies that have the potential to be used for this application, as nanoparticles offer advantages as nanosensors in rapid and high-throughput detection methods[5]. Specifically, magnetite (Fe_3O_4) nanoparticles (MNPs), given their capability of showing superparamagnetic behaviour if in a particular size range [6], could be a potential tool in separation technologies. Through the application of external magnetic fields, the nanoparticles could be used as adsorbents in water treatment to provide a convenient approach for separating and removing the water contaminants in the LP&S.

The aim of the project is to provide a device capable of selectively target radionuclides and heavy metals in solution and sequester them via specific or non-specific ligand agents, thereby tuning their magnetic properties for sensitive detection. In order for this system to be highly effective, the nanoparticles need to be stable in wastewater systems and, ideally, to regenerate and hence to be reusable for more than one cycle.

As last goal, in collaboration with Loughborough University (Laura Mayne, a PhD student also in EPSRC DISTINCTIVE programme) the MNPs will be silica coated and further used in nanopore technology for contaminant separation purposes. The use of a magnetic core structure will lead to better direction and sensing capability.

Methodology Details

Fe_3O_4 Nanoparticles Synthesis

Magnetite Nanoparticles are prepared *via* a thermal decomposition method of organic iron-oleate complex in the presence of a hydrophobic ligand [7]. Specifically, iron chloride ($FeCl_3 \bullet 6H_2O$) and sodium oleate are dissolved in a mixture of ethanol, DI water and hexane and the solution is heated to 70 °C for four hours. At the completion of the reaction, the upper organic layer is washed and separated from the mixture and the resulting iron-oleate complex is stored in the fridge.

A reaction mixture of the iron-oleate complex, oleic acid and 1-octadecene is heated at 320 °C and kept stirring at that temperature for 30 minutes, when then the solution is cooled down at room temperature and further washed with ethanol in order to precipitate and collect the resulting oleic acid capped-magnetite nanoparticles, which are 12 nm in diameter [7].

Ligand-Exchange Reaction

Water stable and dispersible magnetite nanoparticles are required for their application in wastewater. This feature can be achieved through a ligand-exchange procedure that has recently been optimised.

10 mg of the oleic capped-MNPs are added drop-wise to a mixed phosphate solution of Na_2HPO_4 and KH_2PO_4 (5 mL) [8]. Hexane is then added to the mixture in order to have a 5:1 ratio with the aqueous phase and the sample is stirred at room temperature for 17 hours. When the reaction is complete, the phosphate capped and water stable particles are washed twice in ethanol and DI H_2O, and then re-dispersed in water.

Adsorption tests

Adsorption tests with U and Sr were undertaken in order to study the specificity of the nanoparticles. For each adsorption test 5 mg of phosphate capped-magnetite NPs were incubated with 50 ppm of uranyl nitrate solution for different times, specifically 30 min, 60 min, 90 min, 120 min, 240 min. Before the test, both the particles and the uranium solution were purged with nitrogen for two hours in order to ensure a CO_2-free reaction.

The samples were prepared for ICP-OES analysis by filtrating the liquids three times, after U adsorption, in order to remove the U-PO_4^--MNPs from the analysed supernatants. Each sample was then diluted by half in 2% nitric acid, and blanks and standards were prepared in the same way.

Results and Discussion

The synthesized magnetite nanoparticles result homogeneous in shape and quite monodisperse, with a size distribution very close to 12 nm, as shown in fig. 1. TEM results (fig. 1, left) and DLS data (fig. 1, right) agree in confirming the non aggregation and size characterization of the systems, whereas ATR-FTIR (fig. 2) and XRD (fig. 3) data confirm a relatively high oleic acid coating of the spherical particles, with an approximate calculated surface coverage of ≈ 80 %. The crystalline structure of the samples is confirmed by XRD data which possibly suggest magnetite as the only crystalline structure present.

The ligand-exchange reaction between the hydrophobic coated particles and the hydrophilic phosphate ligand successfully formed water dispersible MNPs, as shown by the FT-IR data reported in fig. 4.

The intense peak in the region between 1200 and 900 cm^{-1} comprises the typical stretching signals of the P-O and P=O bonds, and the band at ~ 950 cm^{-1} can be attributed to the Fe-O-P bond, suggesting a monoprotonated binuclear phosphate complex as the main species.

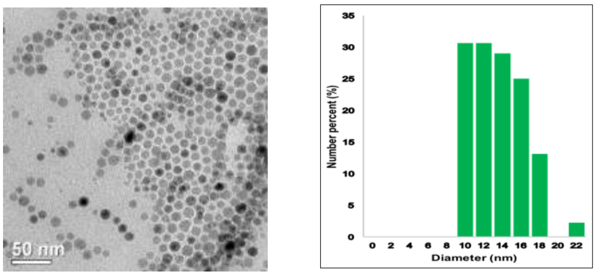

Figure 1. TEM image (left) and size distribution obtained by DLS measurements (right) of 12 nm MNPs samples.

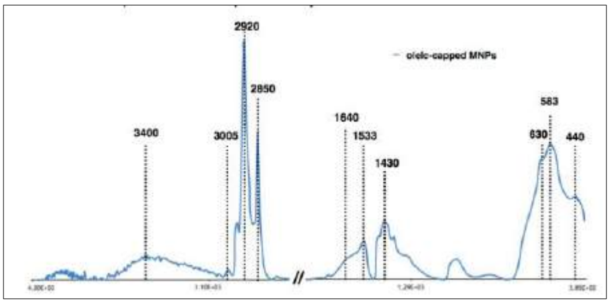

Figure 2. FT-IR spectrum of oleic acid coated-MNPs. The signals at 583 and 630 cm^{-1} correspond to the Fe-O bond stretching; the signals at 2850 and 2950 cm^{-1} correspond to the stretching vibrations of -CH_2- bonds of the oleic acid chain.

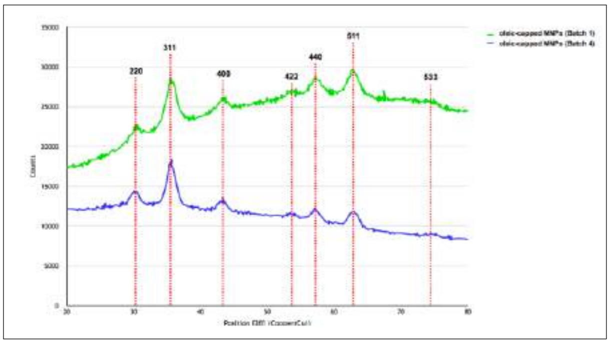

Figure 3. XRD pattern of as-synthesised magnetite NPs from two different samples.

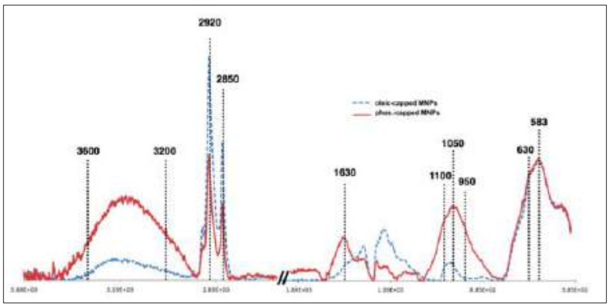

Figure 4. ATR-FTIR spectra obtained for oleic capped-MNPs (blue dashed line) and phosphate capped-MNPs (red line).

ζ-potential analysis shows that the particles are negatively charged at this stage, suggesting that the phosphate-coated MNPs samples are depronotated at pH 7 (fig. 5).

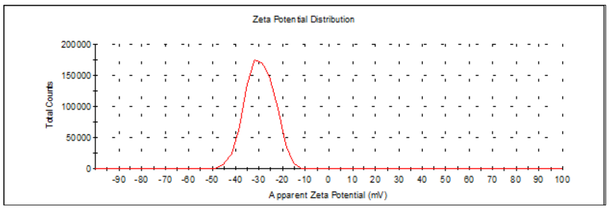

Figure 5. Zeta potential distribution of 12 nm MNPs after the ligand exchange reaction. The phosphate coated-MNPs are negatively charged, with a Zeta Potential value of -28.

Sorption tests with Sr have been firstly carried out. Although the samples seem not to have been effective in the Sr sequester (fig. 6), further studies need to be undertaken as these preliminary tests were conducted in air.

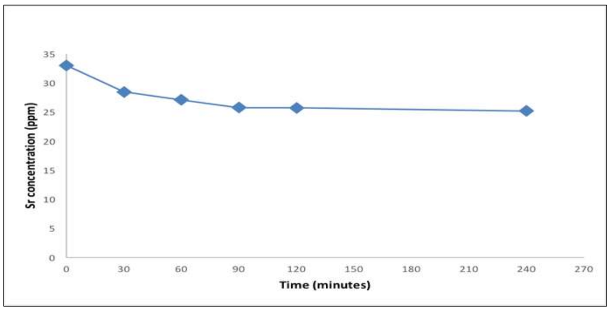

Figure 6. Graph obtained from ICP tests after Sr adsorption on the phosphate coated magnetite NPs. The blank solution measures 33 ppm, and after the different sorption times the amount of Sr not bonded to the MNPs varies from 28-25 ppm, showing a not really selective process.

ICP-OES preliminary results show a rapid U removal for all the different adsorption time systems analysed over a 4 hours' maximum period (fig. 7). Removal of 51-55 % was observed for the four different samples, with small variations with increasing sorption time. The results are promising in terms of rapidity of the sorption process, but might suggest that all the different systems are saturated in U (51 % of U removed after just 30 min).

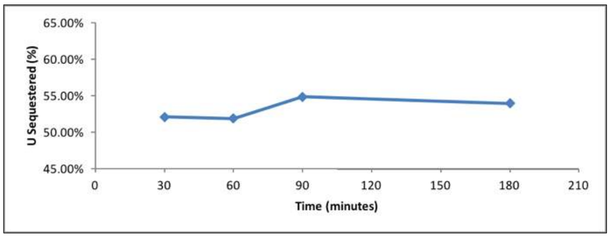

Figure 7. ICP results showing the quantity of U sequestered by the phosphate capped-MNPs. From the first sample (30 min) the U removed is half the amount of the initial concentration.

Conclusions and Future Work

To obtain effective removal of radionuclides and heavy metals from water, magnetite NPs capable of specifically binding the contaminants for removing them from water are necessary. Therefore, a sensing device is to be realised using superparamagnetic magnetite NPs functionalised with specific or non specific ligands. The ligands on the surface of the particles have to show high capacity for the pollutants being investigated, starting from uranium.

Phosphate capped-MNPs have shown to be highly effective for the removal of U in water at pH 7. ICP-OES data have shown a 51-54 % sequester by using 0.002 g of PO_4^--MNPs with a 50 ppm U solution.
Further adsorption tests will help understanding the kinetics of the process and the capacity of the MNPs samples. In order to evaluate the selectivity of the phosphate capped nanoparticles for the Rn ions, co-existing ions will be added in the reaction system at the optimal conditions. Desorption studies will also be carried treating the sorbent systems with various eluents in different concentrations, in order to test the feasibility of regeneration and reuse the adsorbents.
After U and Sr studies will be completed, the attention will be focused on tuning the superparamagnetic nanoparticles' magnetism and changing the ligand in order to achieve the best performing system for adsorbing different heavy metals and Rn.

Acknowledgements

The authors gratefully acknowledge the EPSRC DISTINCTIVE programme for the financial support. We would also like to thank Dr. Jiahui Qi (Materials Dept. - Imperial College) for the help in the development of the sorption studies as well as the invaluable discussions, and Oliver Preedy (Radiochemistry group-Loughborough University) for his contribution to the ICP-OES analyses.

References

1. Tsang, S. C., Caps, V., Paraskevas, I., Chadwick, D. & Thompsett, D. Magnetically Separable, Carbon-Supported Nanocatalysts for the Manufacture of Fine Chemicals. *Angew. Chemie* **116,** 5763–5767 (2004).

2. Gupta, A. K. & Gupta, M. Synthesis and surface engineering of iron oxide nanoparticles for biomedical applications. *Biomaterials* **26,** 3995–4021 (2005).

3. Grasset, F., Duguet, E., Mornet, S. & Vasseur, S. Magnetic nanoparticle design for medical diagnosis and therapy. *J. Mater. Chem.* **14,** 2161–2175 (2004).

4. Li, Z., Wei, L., Gao, M. Y. & Lei, H. One-Pot Reaction to Synthesize Biocompatible Magnetite Nanoparticles. *Adv. Mater.* **17,** 1001–1005 (2005).

5. Wang, L. *et al.* Nanoparticle-based environmental sensors. *Mater. Sci. Eng. R*

Reports **70,** 265–274 (2010).

6. Lu, A.-H., Salabas, E. L. & Schüth, F. Magnetic nanoparticles: synthesis, protection, functionalization, and application. *Angew. Chem. Int. Ed. Engl.* **46,** 1222–44 (2007).

7. Park, J. *et al.* Ultra-large-scale syntheses of monodisperse nanocrystals. *Nat. Mater.* **3,** 891–895 (2004).

8. Li, X., Tang, Y. & Ge, G. Preparation and $ξ$-potential characterization of highly dispersible phosphate --- functionalized magnetite nanoparticles. *Sci. China Physics, Mech. Astron.* **54,** 1766–1770 (2011).

Theme 3 – Silo Ponds and Legacy Wastes
DISTINCTIVE 2nd Annual Meeting
Bristol, UK
19th – 20th April 2016

Ab initio Molecular Dynamics Simulations of Magnesium, Calcium and Strontium Hydrates

O. Lynes*[1], A. Kerridge[2]

*Correspondence: o.lynes@lancaster.ac.uk, a.kerridge@lancaster.ac.uk

[1] *UCL Dept of Chemistry, Gordon St, Kings Cross, London WC1H 0AJ*

[2]*Lancaster University, Bailrigg, Lancaster. LA1 4YW*

Abstract

In order to ensure the safe reprocessing of the legacy waste storage ponds at Sellafield in Cumbria the sludge which has formed at the bottom of the ponds must be characterised. Due to the high radioactivity within the ponds a computational approach offers significant advantages when investigating the behaviour of the various radionuclides which are present and how they adsorb onto the mineral present in the sludge brucite, without the risks associated with working with radioactive materials. This project uses *ab initio* molecular dynamics to quantum chemically study the interactions of magnesium, calcium and strontium ions in a body of water at varying temperatures. The average coordination number and first solvation shell properties have been investigated at 300 K, 350 K and 400 K. Using these methods we have started to develop a picture of the solvation of these ions in order to simulate the behaviour exhibited in the legacy storage ponds.

Introduction

External waste ponds and silos, known as legacy ponds, at Sellafield in North West England have been used to hold spent uranium fuel rods and their associated magnesium alloy cladding (Magnox) since the 1950s. Over time, the corrosion of the Magnox cladding into the mineral brucite ($Mg(OH)_2$) and the variation of external conditions has led to a fine particulate sludge forming in the legacy ponds. This sludge is mainly comprised of brucite and the organic matter which has blown into the ponds; in particular, there are thought to be carbonate and hydroxide complexes of the radionuclide ^{238}U and two of its fission products, ^{90}Sr and ^{137}Cs. These radionuclides will be incorporated into the mineral sludge to varying degrees. The presence of the sludge adds an extra dimension to the reprocessing of the legacy ponds, which cannot proceed until the sludge has been characterised.

By computationally studying the composition of the radionuclides found in the water of the legacy waste ponds we can gain an understanding of their solvation behaviour, before investigating interactions with the sludge itself, and more specifically with the brucite mineral.

Previously this problem has been approached using gas phase Density Functional Theory (DFT) which is used to find the lowest energy conformation of a given system. *Ab initio* molecular dynamics (AIMD) is used to calculate the electronic structure of a given system at regular intervals within a given time period. AIMD generates a trajectory for each atom in a system, meaning in this case that the coordination of the dications in bulk solution environments can be examined in a dynamic context.

The use of *ab initio* molecular dynamics in this project is of great relevance to the development of strategies for the continued storage and disposal of nuclear waste. It represents be the first time this methodology has been used to address this issue, and builds on work previously performed by Kerridge and Kaltsoyannis into the coordination of aquo complexes of strontium.[1]–[3]

Methodology Details

All calculations were carried out with CP2K (version 2.6).[4] The PBE Generalised Gradient Approximation (GGA) exchange-correlation functional was used with Double Zeta Valence Polarised (DZVP) basis sets.[5] The Gaussian Augmented Planewave method (GAPW) was used with Goedecker-Teter-Hutter (GTH) pseudopotentials and periodic boundary conditions with a fixed cell length of 11.99 Å.

Each system is comprised of 64 water molecules, with a central dication of either magnesium, calcium or strontium. A Nosè-Hoover thermostat was used to maintain the temperature of the systems at 300 K, 350 K and 400 K respectively. Each simulation ran for a total simulation time of 40 picoseconds (ps), incorporating a 5 ps equilibration period.

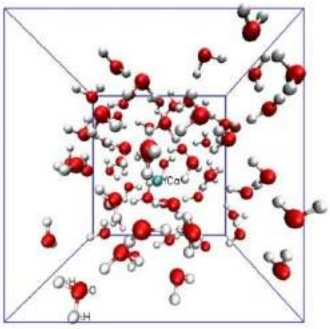

Figure 1: Visual representation of a 64 water molecule cell with a Ca^{2+} ion at its centre

Results and Discussion

Solvation Shell Structure

The radial distribution function g(r) was calculated as an average over every step in the simulation. A running coordination number n(r) was also calculated. The g (r) describes the probability of finding an oxygen ion at that distance from the central ion. The n (r) indicates the number of oxygen ions at a certain distance. A plateau in the n(r) indicates the existence of a well-defined solvation shell.

From these the radii of the first and second solvation shells were derived and are shown in Table 1.

	300K	350K	400K
Mg	2.15 (3.85)	2.15 (3.85)	2.15 (3.85)
Ca	2.35 (4.15)	2.45 (4.15)	2.45 (4.15)
Sr	2.55 (4.25)	2.55 (4.25)	2.65 (4.25)

Table 1: Positions of the maxima of the first (second) peaks of the M-O Radial Distribution Functions, in Å

For Mg the first solvation shell is slightly larger than is seen in both computational (2.08 Å) [6] and experimental literature (2.08 - 2.12 Å)[7], [8] at all temperatures. For Ca the computational literature gives the first solvation shell radius to be 2.36 Å whilst experimental results give a range of 2. 39- 2.46 Å.[9], [10] While at 300 K our result (2.35 Å) is in excellent agreement with that found in previous computational work, at high temperatures calculated values lie within the experimental range.

For Sr, calculated values at all temperatures are very slightly outside the ranges, but still in excellent agreement with previous solvation shell distances found both computationally (2.60 Å)[7], [11] and experimentally (2.57-2.63 Å). [6], [11]

For all systems a second solvation shell is indicated by the radial distribution functions, all of which are significantly lower than reported in the literature for Mg, Ca and Sr (4.3, 4.6, 4.7 Å respectively)[12], [13], but on examining the running coordination number a second shell structure cannot be well defined. It is known that the PBE functional over binds water and requires a high temperature to simulate the liquid phase, this may point to a possible reason why the second solvation shell is underestimated in this case.

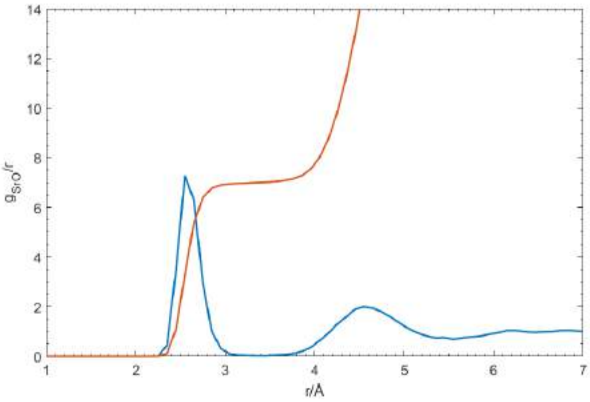

Figure 2: Radial Distribution Function (blue) and running coordination number (orange) for Strontium at 300 K

Coordination Number

The coordination number (CN) for each system at each temperature was calculated using a cut-off distance of 3.4 Å from the ion. The total time spent at each coordination number, or residence time (t_R), is show in Table 2. The coordination number has been analysed according to the direct method protocol detailed by Hofer. *et al* where variation in coordination number is only considered to be a true transition if its duration is longer than 0.5 ps.[14] All instances where a coordination number change occurs for less than 0.5 ps have therefore been ignored in the analysis.

At 300 K, the average coordination numbers of all ions are in good agreement with both computational and experimental data for Mg (6)[15], [12], [16], Ca (6-8)[10], [17], [18] and Sr (6-9)[19]–[21]. At higher temperatures the Mg coordination number remains at 6 for the total simulation time: this is mirrored in both experimental and computational data.

The temperature variation of Ca and Sr coordination numbers has produced some interesting results, shown in Table 2, which are still under investigation. For Ca, increasing the temperature to 350 K leads to a decrease in coordination number from 6 to 4.89, but a further increase in the temperature to 400 K increases the coordination number to 5.85 in line with literature values (6-8). In contrast, an increase in temperature of the Sr system to 350 K shows a slight increase in coordination number from 7 to 7.04, whereas a further increase in temperature to 400 K decreases the coordination number to 6.08. These are still within the literature values (6-9) of first shell coordination number found for strontium, but the long time (15.72 ps) spent at a coordination number of 5 is unusual.

300 K

	CN	t_R /ps (%)	CN
Mg	6	35 (100)	6
Ca	6	35 (100)	6
Sr	7	35 (100)	7

350 K

	CN	t_R /ps (%)	CN
Mg	6	35 (100)	6
Ca	4	7.39 (21.10)	4.89
	5	24.83 (70.96)	
	6	2.78 (7.94)	
Sr	6	7.80 (22.28)	7.04
	7	17.99 (51.40)	
	8	9.21 (26.32)	

400 K

	CN	t_R /ps (%)	CN
Mg	6	35 (100)	6
Ca	5	10.58 (30.22)	5.85
	6	19.14 (54.68)	
	7	5.29 (15.10)	
Sr	5	15.72 (44.92)	6.08
	6	5.55 (15.86)	
	7	9.09 (25.97)	
	8	4.64 (13.25)	

Table 2: Variation in coordination (CN) and residence time (t_R) at each temperature for all systems studied.

Statistically one single trajectory is not sufficient to be used as a definite example of how a system behaves. While there is no one clear reason for the changes in coordination numbers, we note that, when compared to previous AIMD literature the simulation time used here is twice as long.[6], [21] When examining the graphs of the change of coordination number change over time, an example is shown in Figure 3, the lower coordination numbers are seen in the second half of the molecular dynamics run past 20 ps, and the coordination number rises again around 37 ps. A similar pattern is found in our calcium data.

It is possible, and indeed likely, that in some cases that the systems have become trapped in a local energetic minimum, which would explain why such a low coordination number has been seen for a prolonged period of time. To investigate this further, AIMD simulations have been continued for a further 40 ps to ascertain if higher coordination numbers seen in the first 20 ps of the calculation are found on longer timescales.

Also, new AIMD simulations of 40 ps length have also been initiated using different starting geometries to further investigate coordination number dependence on starting geometry.

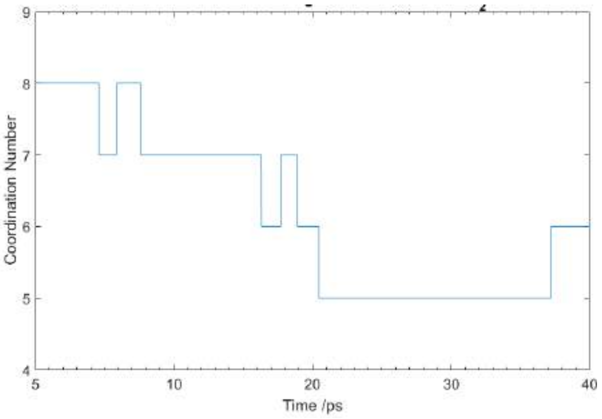

Figure 3: Coordination number over total simulation time for $Sr\cdot(H_2O)_{64}$ at 400 K.

Conclusions and Future Work

From the results presented here it is clear there is much analysis is still needed before the approach can be considered a viable computational model, and clarify while the values for the first and second solvation shell distances vary are in good agreement with literature, the variation in average coordination number as temperature changes is not typical, and why low coordination numbers are seen at higher temperatures.

Calculations have also been performed on systems where two water molecules are replaced with hydroxide ions, in order to investigate the effect of pH. The analysis of these hydrated hydroxide systems will build on work performed by the Kaltsoyannis group at Manchester into the hydrated strontium hydroxides, and investigate proton transfer through the hydration shells.

Further analysis of these systems will give insight into both the coordination structure of the hydrated ions and the effect of pH on these structures.

Additionally, the same methodology will be used to introduce a brucite mineral surface into the simulations and the adsorption process of the ion onto brucite will be studied.

Acknowledgements

We acknowledge the EPSRC for funding of the DISTINCTIVE consortium through grant EP/L014041/1 and the Nuclear Decommissioning Authority, the National Nuclear Laboratory and Sellafield, Ltd, for industrial/financial support. We also thank Jonathan Austin, the industrial supervisors for the project.

Finally, we thank Mike Pacey and Lancaster University for access to their High End Computing HPC facility on which the majority of this research has been performed, as well as the National Service for Computational Chemistry Software (NSCCS) for access to the 'slater' HPC facility.

References

[1] A. Kerridge and N. Kaltsoyannis, "Quantum chemical studies of the hydration of Sr^{2+} in vacuum and aqueous solution.," *Chem. A Eur. J.*, vol. 17, no. 18, pp. 5060–7, Apr. 2011.

[2] E. Makkos, A. Kerridge, and N. Kaltsoyannis, "The importance of second shell effects in the simulation of hydrated Sr $^{2+}$ hydroxide complexes," *Dalt. Trans.*, pp. 11572–11581, 2015.

[3] A. Kerridge and N. Kaltsoyannis, "The coordination of Sr2+ by hydroxide: a density functional theoretical study," *Dalton Trans.*, vol. 40, no. 42, pp. 11066–9, Nov. 2011.

[4] J. Hutter, M. Iannuzzi, F. Schiffmann, and J. VandeVondele, "cp2k: atomistic simulations of condensed matter systems," *Wiley Interdiscip. Rev. Comput. Mol. Sci.*, vol. 4, no. 1, pp. 15–25, Jan. 2014.

[5] M. Ernzerhof and G. E. Scuseria, "Assessment of the Perdew–Burke–Ernzerhof exchange-correlation functional," *J. Chem. Phys.*, vol. 110, no. 11, p. 5029, 1999.

[6] D. Di Tommaso and N. H. de Leeuw, "First Principles Simulations of the Structural and Dynamical Properties of Hydrated Metal Ions Me $^{2+}$ and Solvated Metal Carbonates (Me = Ca, Mg, and Sr)," *Cryst. Growth Des.*, vol. 10, no. 10, pp. 4292–4302, 2010.

[7] T. Tofteberg, A. Öhrn, and G. Karlström, "Combined quantum chemical statistical mechanical simulations of Mg^{2+}, Ca^{2+} and Sr^{2+} in water," *Chem. Phys. Lett.*, vol. 429, no. 4–6, pp. 436–439, Oct. 2006.

[8] C. W. Bock, A. Kaufman, and J. P. Glusker, "Coordination of Water to Magnesium Cations," *Inorg. Chem.*, vol. 33, no. 3, pp. 419–427, 1994.

[9] I. Bakó, J. Hutter, and G. Pálinkás, "Car-Parrinello molecular dynamics simulation of the hydrated calcium ion," *J. Chem. Phys.*, vol. 117, no. 21, pp. 9838–9843, 2002.

[10] F. Jalilehvand, D. Spångberg, P. Lindqvist-Reis, K. Hermansson, I. Persson, and M. Sandström, "Hydration of the calcium ion. An EXAFS, large-angle x-ray scattering, and molecular dynamics simulation study.," *J. Am. Chem. Soc.*, vol. 123, no. 3, pp. 431–441, 2001.

[11] G. Moreau, L. Helm, J. Purans, and E. Merbach, "Structural Investigation of the Aqueous Eu^{2+} Ion:Comparison with Sr^{2+} Using the XAFS Technique," *Transition*, pp. 3034–3043, 2002.

[12] C. W. Bock, G. D. Markham, A. K. Katz, and J. P. Glusker, "The Arrangement of First- and Second-shell Water Molecules Around Metal Ions: Effects of Charge and Size," *Theor. Chem. Acc.*, vol. 115, no. 2–3, pp. 100–112, 2006.

[13] L. Helm and a E. Merbach, "Water exchange on metal ions: experiments and simulations," *Coord. Chem. Rev.*, vol. 187, pp. 151–181, 1999.

[14] T. S. Hofer, H. T. Tran, C. F. Schwenk, and B. M. Rode, "Characterization of dynamics and reactivities of solvated ions by ab initio simulations.," *J. Comput. Chem.*, vol. 25, no. 2, pp. 211–7, 2004.

[15] M. Adrian-Scotto, G. Mallet, and D. Vasilescu, "Hydration of Mg++: a quantum DFT and ab initio HF study," *J. Mol. Struct. THEOCHEM*, vol. 728, no. 1–3, pp. 231–242, Sep. 2005.

[16] G. D. Markham, J. P. Glusker, and C. W. Bock, "The Arrangement of First- and Second-Sphere Water Molecules in Divalent Magnesium Complexes: Results from Molecular Orbital and Density Functional Theory and from Structural Crystallography," *J. Phys. Chem. B*, vol. 106, no. 19, pp. 5118–5134, May 2002.

[17] M. M. Probst, T. Radnai, and K. Heinzinger, "Molecular Dynamics and X-ray Investigation of an Aqueous $CaCl_2$ Solution," *J Phys Chem*, vol. 89, no. 5, pp. 753–759, 1985.

[18] G. Licheri, "X-ray diffraction study of the average solute species in $CaCl_2$ aqueous solutions," *J. Chem. Phys.*, vol. 64, no. 6, p. 2437, 1976.

[19] T. M. Seward, C. M. B. Henderson, J. M. Charnock, and T. Driesner, "An EXAFS study of solvation and ion pairing in aqueous strontium solutions to 300°C," *Geochim. Cosmochim. Acta*, vol. 63, no. 16, pp. 2409–2418, 1999.

[20] I. Persson, M. Sandstrom, H. Yokoyama, and M. Chaudhry, "Structure of the Solvated Stronitum and Barium Ions in Aqueous, Dimethyl Sulfoxide and Pyridine Solution, and Crystal Structure of Strontium and Barium Hydroxide Octahydrate," *Z. Naturforsch*, vol. 50a, pp. 21–37, 1995.

[21] D. Harris, "Hydration of Sr^{2+} in hydrothermal solutions from ab initio molecular dynamics," *J.Phys.Chem.B*, vol. 107, pp. 9056–9058, 2003.

Theme 3 – Silo Ponds and Legacy Wastes
DISTINCTIVE 2nd Annual Meeting
Bristol, UK
19th – 20th April 2016

Developing the use of an Acoustic Backscatter system (ABS) to measure the concentration of nuclear simulants under varying degrees of flocculation

A.S.Tonge[1], S. Freear[2], J. Peakall[3], T.N. Hunter[1]

*Correspondence: pm11a2t@leeds.ac.uk

[1] *School of Chemical and Process Engineering (University of Leeds, LS2 9JT, UK)*
[2] *School of Electronic and Electrical Engineering (University of Leeds, LS2 9JT, UK)*
[3] *School of Earth and Environment (University of Leeds, LS2 9JT, UK)*

Abstract

It is proposed here that further research efforts should be made in order to develop the use of acoustic backscatter to measure concentration in flocculated systems. The use of acoustics is generally widespread in marine, food and water treatment industries and has great potential in applications where access to process fluid presents a chemical or radiological hazard. Despite the fact that there have been many developments made recently by various authors to better understand how acoustic models can be developed to further to broaden their applications to measuring particle size and concentration in flocculated or otherwise cohesive systems there is not a robust model relating flocculated particle structure to its acoustic backscatter properties.

Introduction

Acoustical equipment is used routinely to study sediment transport in coastal and estuarine environments as well as for measuring the flow of currents and their profiles. Sediment transport is calculated from the suspended sediment concentration which can be estimated from the intensity of the backscattered signal [1] [2]. This method of concentration measurement, however, relies on taking a large number of samples in order to determine an empirical relationship between concentration and the backscattered signal intensity which could prove to be both difficult and costly in applications where chemical or Radiological hazards make access to process fluid dangerous or completely impossible. This method also fails to describe the level of flocculation present within the system which can be very important information for both sedimentological and for industrial applications such mineral settling and water treatment operations where settling rates are critical in the design and operation of process equipment [3] [4].

Recent Developments

When attempting to fit experimental values of the particle species backscatter coefficient (k_s) (one of two parameters that define the acoustic properties of a particulate system) to those predicted by the Elastic Sphere and Fluid Sphere models it was found that, although the ES and FS models bounded their data it was not in the way that was first hypothesized as they expected that the experimental data would move from fitting the ES better at smaller sizes and the FS as the flocs grew larger, less dense and incorporated more water [4]. This was not the case however and even applying a distributed mass model to account for floc density change gave results that suggested an alternative model is required [5].

Further to this, Vincent and MacDonald [5] proposed their “flocculi model” when they found that data from a forward-scattering light device (LISST-100) gave particle sizes three times smaller than that of a camera for flocculated particles and inversion of the ABS data gave particle sizes similar to that seen by the LISST it was proposed, as this phenomenon had been seen previously by Graham [6] with an incredibly high resolution holocamera and other authors [7] [8] , that both the light and ultrasound were interacting, not with the whole structure of the floc, but with flocculi [5]. The small, tightly-bound structures that comprise it. Although the correlation coefficient was typically only 0.44-0.49 when correlating the ABS size data with the LISST-100 If this model can be confirmed, in particular within equipment that does not suffer from the bias toward measuring smaller particles more often and is more in-situ, then samples from flocculated systems would not need to have the structure of the macro flocs preserved during transport making samples more reliable in terms of their acoustic properties even if they have undergone some small amount of shear. [5].

The dual frequency method is a concentration inversion method whereby, if k_s, k_t (the transducer constant), ζ (particle attenuation coefficient) and α_w (the attenuation coefficient) are known the concentration at any point in the system can be calculated so long as the backscatter and attenuation coefficients have been found by taking measurements at the desired two frequencies in a homogeneous vessel [9]. This paper describes the modification of a stirred, 80 cm high settling column to include a conical base, a peristaltic pump for fluid recirculation and a Focussed Beam Reflectance Measurement probe for in-situ size measurement of flocs. This was done in order to more reliably characterise flocculated particle size of common nuclear simulants while reducing shear conditions in the tank but still maintaining a homogeneous solution and to determine the shear conditions at which floc breakdown occurs.

Methodology Details

Materials

Three materials were used, Calcite (Calcium Carbonate) and glass beads (Honite-16). Their details are shown in the table below.

Table 1 Details of Materials used in new calibration tank

Material	Supplier	Particle Size (µm)
Calcite (Omyacarb)	Omya	2
Honite-16	Guyson	53 - 106

FBRM Data

Using a Lasentec Probe, Focussed Beam Reflectance Measurement size data was collected in both a 85cm high, 30 cm diameter impeller agitated (at 400 RPM), Perspex tank and a 1L glass beaker for calcite (a common nuclear simulant) and glass particles (Honite-16) as they are known to give a good acoustic response at 1% w/w concentration in water. This was then compared to data taken for the materials in a Mastersizer in order to ensure that the size measured was correct.

Tank Reconstruction

Following the first set of results taken in the Perspex tank it was then modified to include the use of a peristaltic pump to recirculate liquid at a rate of 33 ml/s from the tank outlet at the bottom of the tank back to the top as shown in **Error! Reference source not found.Error! Reference source not found.**.

Sample Data

Following the tank modification Honite-16 was used at weight concentrations of 2% and 4% in order to determine whether the conditions in the tank allowed it to remain homogeneous. Using steel rod with five sets of peristaltic tubing (figure 2) attached to a five-headed peristaltic pump five simultaneous samples from the tank were taken at the waterline and at depths of 8.5, 18.5, 28.5 and 38.5 from the waterline which was at a depth of 24 cm from the top of the tank for the glass and for calcite to ensure homogeneity in the tank.

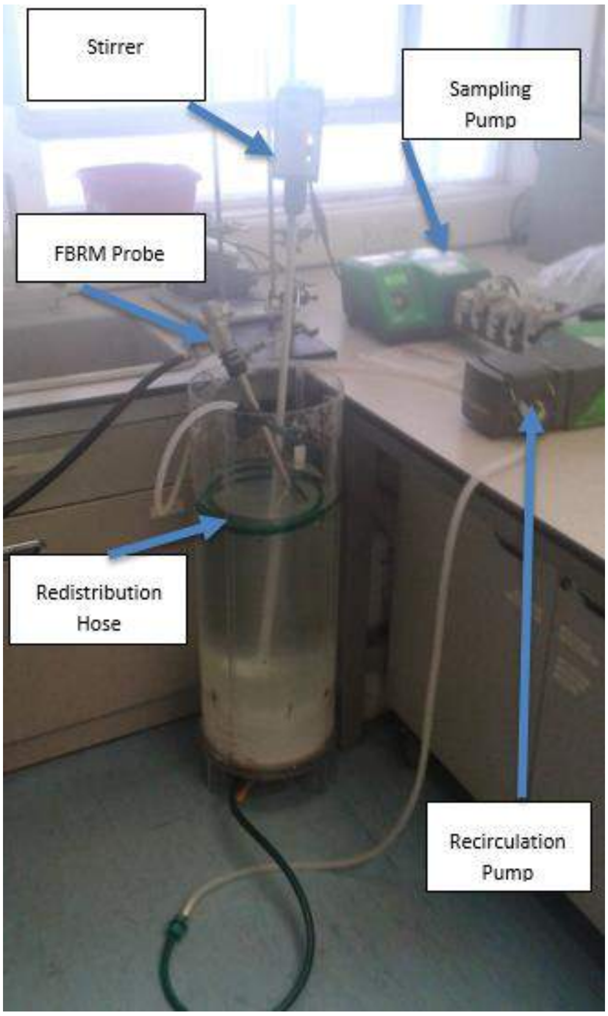

Figure 1 Showing redesigned tank configuration

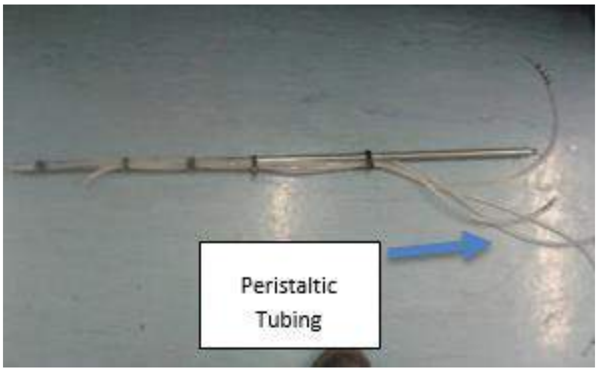

Figure 2 Sampling probe used to take simultaneous samples at various depths in the calibration tank

Results and Discussion

From Figure 2 it can be seen that, despite the large density of the glass particles (2400-2600kg/m^3), it is possible to keep the calibration tank homogeneous in concentration. It was seen, however, that as the recirculation pump outlet was below the waterline the first 10 cm depth in the tank was seen to be of a lower concentration than the rest of the tank and so the sample data for the waterline has not been shown.

Figure 3 Concentration profiles in reconfigured calibration tank for Honite-16 at agitation rate of 400 RPM

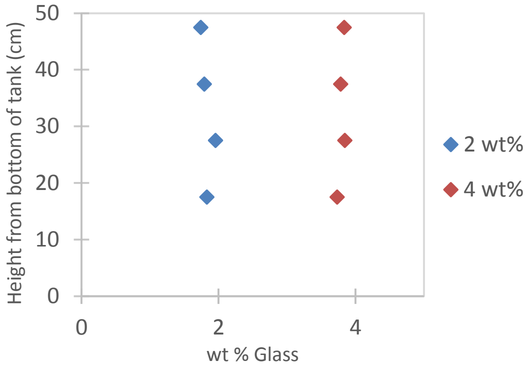

From Figures 4 & 5 it can be seen that the FBRM captured the size data for both calcite and glass well despite the low number of counts attained for the glass particles. This can be attributed to its higher density and therefore lower volume % when compared to the calcite resulting in a lower number of counts.

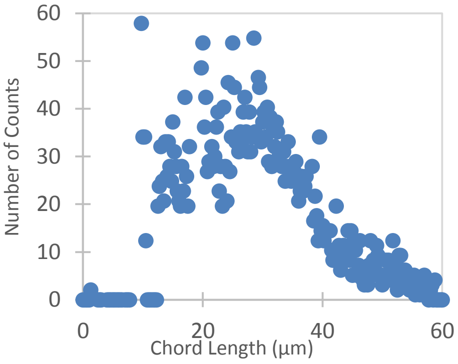

Figure 4 FBRM size data for larger glass particles (large scale)

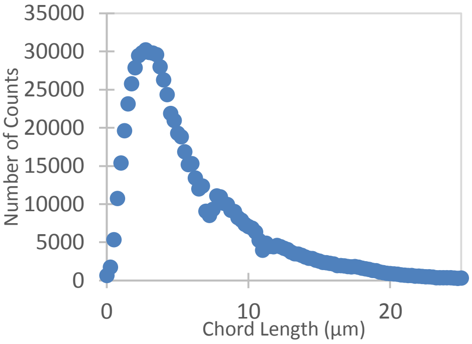

Figure 5 FBRM Size data for Calcite at 1% w/w

Conclusions and Future Work

It can be seen, therefore, that an accurate model for the interaction of flocculated particles with acoustic devices is somewhat lacking but that recent results support the novel concept of the flocculi model which would seem to explain previously anomalous results as well as suggest that sampling need not be done so carefully as the structure of the macro-flocs will not need to be preserved [5]. More laboratory work must be done to confirm this new model utilising more reliable, in-situ techniques to measure size/degree of flocculation accurately and thereby try and find a relationship between the degree of flocculation and the backscatter and attenuation coefficients so that accurate concentration profiles can be produced for the simulant systems and any real-world systems that have similar acoustic properties if taking samples for calibration would prove too costly [10] [3] [11] [5].

A Saturn Digisizer is to be used to determine the size of flocs at different concentrations of simulant and flocculent as it utilises a peristaltic pump to recirculate the flocs rather than the impeller used by the mastersizer. This will ensure that flocs are not broken during measurement and therefore their size can be accurately determined without breaking up their structure. The newly configured calibration tank will therefore be used with the FBRM and a Saturn Digisizer in order to more reliably determine the exact size of flocs produced by calcite and other nuclear simulants at different shear conditions and concentrations of flocculent and simulant material as well as assessing their robustness to shear while also taking acoustic backscatter data simultaneously at multiple levels within the tank. Following this, robust flocs of various sizes can then be produced and acoustically characterised within the redesigned calibration tank and a relationship between floc size/structure and its acoustic backscatter response.

References

[1] K. Deines, “Backscatter estimation using broadband acoustic Doppler current profilers,” in *Proc. Sixth Working Conf. on Current Measurement*, San Diego, CA, 1999.

[2] D. C. Fugate and C. T. Friedrichs, “Determining concentrations and fall velocity of estuarine particle populations using ADV, OBS and LISST,” *Continental Shelf Research, 22,* pp. 1867-1886, 2002.

[3] T. N. Hunter, L. Darlison, J. Peakall and S. Biggs, “Using a multi-frequency acoustic backscatter system as an in situ high concentration dispersion monitor,” *Chemical Engineering Science 80,* pp. 409-418, 2012.

[4] I. Macdonald, C. Vincent, P. Thorne and B. Moate, “Acoustic scattering from a suspension of flocculated sediments,” *Journal of Geophysical Research,* pp. 2581-2594, 2013.

[5] C. Vincent and I. MacDonald, “A flocculi model for the acoustic scattering from flocs,” *Continental Shelf Research 104,* pp. 15-24, 2015.

[6] G. Graham, E. Davies, W. Nimmo-Smith, D. Bowers and K. Braithwaite, “Interpreting LISST-100X measurements of particles with complex shape using digital in-line holography,” *Journal of Geophysical Research: Oceans 117,* p. C05034, 2012.

[7] O. Mikkelsen, P. Hill, T. Milligan and R. Chant, “In situ particle size distributions and volume concentrations from a LISST-100 laser particle sizer and a digital floc camera,” *Continental Shelf Research 25,* pp. 1959-1978, 2005.

[8] P. Hill, J. Newgard, B. Law and T. Milligan, “Flocculation on a muddy intertidal flat in Willapa Bay, Washington, Part II: Observations of suspended particle size in a secondary channel and adjacent flat,” *Continental Shelf Research 60 (Suppl.),* pp. S145-S156, 2013.

[9] H. Rice, M. H. T. Fairweather, B. Mahmoud, S. Biggs and J. Peakall, “Measuring particle concentration in multiphase pipe flow using acoustic backscatter: Generalization of the dual-

frequency inversion method," *Journal of the Acoustical Society of America 136 (1),* pp. 156-169, 2014.

[10] D. Hurther, P. D. Thorne, M. Bricault, U. Lemmin and J.-M. Barnoud, "A multi-frequency Acoustic Concentration and Velocity Profiler (ACVP) for boundary layer measurements of fine-scale flow and sediment transport processes," *Coastal Engineering 58,* pp. 594-605, 2011.

[11] P. Thorne and R. Meral, ""Formulations for the scattering properties of suspended sandy sediments for use in the application of acoustics to sediment transport processes," *Continental Shelf Research 28,* pp. 309-317, 2008.

X-ray tomography insights into gas retention in nuclear legacy waste

M. Johnson*[1], J. Peakall[1], M. Fairweather[1], S.Biggs[2], D. Harbottle[1], T. Hunter[1]

*Correspondence: pm12mcj@leeds.ac.uk

[1] School of Chemical and Process Engineering, University of Leeds, Leeds, LS2 9JT, UK
[2] Faculty of Engineering, Architecture and Information Technology, University of Queensland, Brisbane, Qld 4072, Australia

Abstract

The requirement to evacuate aging legacy facilities at Sellafield represents a multibillion pound challenge and the safety implications of retained hydrogen bubbles must inform the strategy for this legacy waste. This study uses the decomposition of hydrogen peroxide in soft sediments of a magnesium hydroxide test material to replicate behaviour in the magnox swarf storage silos and similar Magnox-era waste, while x-ray tomography is used to gain statistical insights into the retained bubble population. Time dependent x-ray tomograms reveal that bubbles reside only for relatively brief periods of less than an hour in beds of 7 Pa yield stress and that even small bubbles of around 2 mm diameter, with a relatively small buoyancy force, are mobile within the sediment bed. While the larger retained bubbles grow with an increasingly distorted geometry in beds of increased yield stress, the size distribution of bubbles appears largely independent of the bed strength within the 7-234 Pa yield stress range. Each of the beds within this yield strength range have demonstrated the capacity to retain large voidages in the order of 32 %, which would substantially reduce the functional capacity of future waste containers and would reduce the bulk bed density to less than that of a water supernatant, placing submerged beds at risk for rollover events.

Introduction

Decommissioning of the magnox swarf storage silos (MSSS) and first generation magnox storage pond (FGMSP) legacy buildings are priority activities for the Sellafield nuclear decommissioning site [1], accounting for a quarter of its annual budget. Long term underwater storage of magnox clad fuel since the 1960s has allowed the magnesium/aluminum cladding alloy to corrode, with precipitation products consolidating into a legacy of corroded magnox sludge waste [2, 3]. Concerns have arisen regarding the periodic release of significant volumes of gas, formed by a combination of corrosion reactions and by radiolysis of the pond and silo liquors, from these consolidated beds. The economics of evacuating the MSSS to 3 m^3 containers is also greatly influenced by how significantly waste swell due to gas retention reduces the real capacity of these vessels.

Previously, x-ray computed tomography (CT) tests have shown that non-homogeneous gas generation through the sediment enables the bed to segregate into a bulk bed and foam layer, while submerged pathways promote gas transport from the bed and limit the capacity for gas retention [4]. These features have not been observed during recent CT experiments where gas generating reagents are dispersed homogeneously through the bed. The resulting images have demonstrated a well dispersed distribution of bubbles through weak to intermediate strength soft sediments of 7-234 Pa yield stress. Statistical analysis has been performed on the retained bubble population to demonstrate the evolution of bubble size and shape with time and in sediments of different shear yield stress conditions.

Methodology Details

The brucite, $Mg(OH)_2$, test material used in this study is H3 Versamag (Martin Marietta Magnesia Specialties LLC, USA), a fine white precipitated powder with less than 1.2 % oxide impurities and a median particle size of 1.09 µm. Soft sediments are prepared by the addition of water and agitation for 30 minutes using an overhead stirrer. The shear yield stress of these soft sediments has been characterised using the vane method [5] with both a Brookfield DV-II Pro Viscometer and a Bohlin Gemini Rheometer.

X-ray tomography

A 26 ml volume of 35 % w/w hydrogen peroxide (Merck Chemicals, Germany) was injected into a 6.5 l volume of soft sediment and dispersed through the sediment by agitating for 2 minutes using an overhead stirrer. Over the course of 8-12 hrs, the hydrogen peroxide decomposes on contact with the sediment forming bubbles of oxygen:

$$H_2O_2 \rightarrow H_2O + \frac{1}{2}O_2$$

This mixture is pumped using a peristaltic pump to a sideways mounted clear acrylic cylinder of 30 cm diameter and 15 cm length. The vessel is transferred to a Brivo CT385 medical CT scanner (GE Healthcare, UK) at the University of Leeds. Tomograms were captured of a small field of view (FOV) at 0, 1, 2, 4, 6 and 8 hrs and of a larger FOV at 2 and 6 hrs. Additional images of the small FOV were captured at 15 minute intervals in the 7 Pa sediment after it was determined that the residence time of individual bubbles was typically less than an hour. The parameters used for CT imaging for the two FOVs are summarised in Table 1.

Table 1 CT parameters used for two fields of view

	Small FOV	Large FOV
X-ray voltage (kVp)	120	120
X-ray tube current (mA)	79	40
Field of view diameter (mm)	96	250
Field of view depth (mm)	20	140
Pixel dimensions (µm)	250	488
Slice separation (µm)	625	1250

The CT tomograms were post-processed using ImageJ and Matlab to determine a statistical representation of the bubble population. First, the radiodensity distribution was normalised to visualise the slices as a 16-bit greyscale image. The bubbles were then isolated by bi-level thresholding using the Renyi Entropy algorithm [4], such that the bulk sediment would be white and the bubbles black. Finally, adjacent black voxels touching at the corners, edges and faces were interconnected and the individual bubbles numbered using the procedure outlined in Bolte and Cordelieres 2006 [5]. The volume, surface area and centre of mass of each bubble is then logged for analysis.

Results and Discussion

An example of a large FOV x-ray CT slice through a 7 Pa soft sediment is shown in Figure 1. Bubbles are relatively small, no larger than 6 mm in diameter and very spherical. Some areas of slightly more concentrated soft sediment are observed as bright streaks near the edge of the vessel, but the test material is largely homogeneous. The same features were observed in beds of 84 and 234 Pa yield stress.

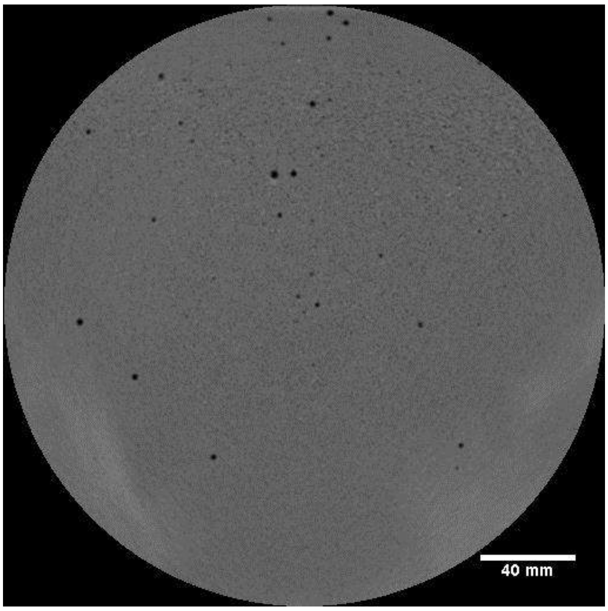

Figure 1 Example slice through a magnesium hydroxide soft sediment of 7 Pa yield stress after 6 hrs gas generation

Post processing of the small FOV tomograms for the 84 Pa sediment generated the transient bubble diameter histograms in Figure 2. From side-on scout images of the entire rig, the bed is observed to swell over the first 4-6 hrs of gas generation, however Figure 2 implies that the the bubble population achieves a relatively steady state size distribution after around an hour of gas generation. The increase in bed voidage observed after the first hour is explained by the increase in the number of bubbles retained in the soft sediment as indicated by the bubble count in the legend of Figure 2.

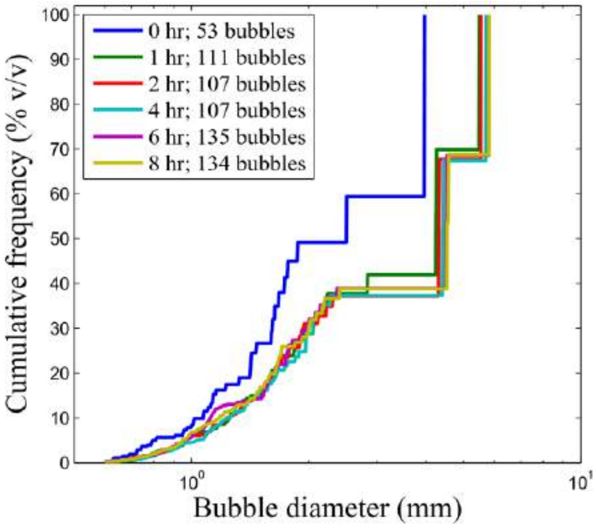

Figure 2 Transient bubble diameter histogram for 84 Pa yield stress soft sediment, captured from the small FOV tomograms

In the same way that two-dimensional tomograms have been stacked and interpolated to produce a three-dimensional representation of the bed, a time sequence of these 2D stacks can be represented as a *hyperstack*. In Figure 3, a hyperstack has been *flattened* such that each different frame, or colour, represents a bubble 15 minutes after the previous frame.

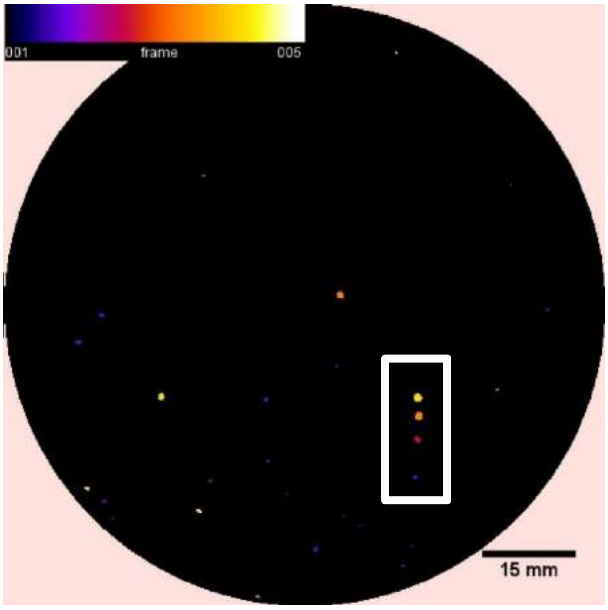

Figure 3 CT slice from a flattened 'hyperstack' of the small FOV showing the growth and upward motion of individual bubbles with time. Each frame/colour is captured at a 15 minute interval.

Most bubbles appear to have a relatively short residence time in the bed as most bubbles cannot be traced between time frames. This implies that bubbles quickly grow to a buoyant volume at which point the bubble is able to *fluidise* the surrounding sediment matrix and escape. Conversely, the region outlined in white shows the same bubble in 4 successive time frames. The bubble grows to a diameter of around 2 mm and over a 45 minute period rises very slowly through the bed at a rate of no more than 25 mm hr^{-1}. Even fairly small bubbles, with minimal buoyant force, appear to be fairly mobile within this low strength bed and reside within the bed over timescales of less than an hour. The fact that Figure 2 shows a steady state size distribution after an hour of gas generation suggests that a mechanism for gas release limits the maximum size to which a bubble can grow to before it is released from the bed.

The mechanism for the release of individual bubbles from low strength soft sediments is believed to be fluidisation [8]. The buoyant force, F_b, of a bubble increases with its volume as shown in equation 1:

$$F_b = \frac{\pi}{6}(\rho_s - \rho_b) g d_b^3 \qquad 1$$

We assume that the buoyant force of the bubble is resisted by the strength of the sediment, which we characterise using the shear yield stress. This critical force, F_c, to restrain a bubble is given by the product of the yield stress, τ, and the bubble cross sectional area:

$$F_c = k d_b^2 \tau \qquad 2$$

where k is a material dependent proportionality constant. If the ratio of these forces exceeds unity than the bubble will be sufficiently buoyant to fluidise the bed. This implies that the critical diameter to which a bubble must grow to escape the bed by fluidisation is proportional to the yield stress.

$$d_{b,crit} \propto \frac{\tau}{(\rho_s - \rho_b)} \qquad 3$$

Consequently, if we increase the shear yield stress of the bed 33-fold from 7 to 234 Pa, substantially larger bubbles should be observed in the higher strength sediment, if the bubble size distribution is limited by fluidisation. This is at odds with Figure 4, which shows three bubble size distributions, obtained from the large FOV tomograms, in beds of different yield stress. The bubble size distribution appears almost identical in beds of 7-234 Pa yield stress and the largest bubble diameter observed in any of the beds is an 8.5 mm diameter bubble in the 84 Pa bed. The maximum voidage also appears independent of yield stress, at around 32 % in each instance. The analysis will be extended into beds of greater yield stress to see if this trend continues, but fluidisation does not explain how these 6-9 mm bubbles are equally able to escape beds of 7-234 Pa yield stress.

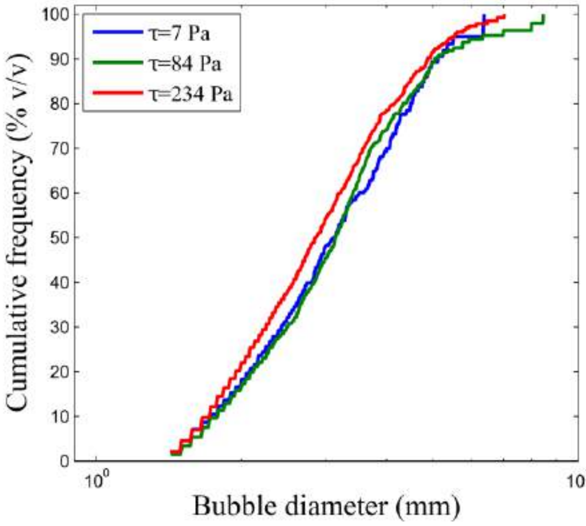

Figure 4 Bubble diameter histograms for the large FOV in soft sediments of 7-234 Pa yield stress

The bubble shape is represented here by the bubbles' corrected sphericity, Ψ. This is the bubble sphericity normalised by that of a cube, since the sphericity of a digitised sphere made of voxels cannot exceed the sphericity of a cube.

$$\Psi = \frac{\pi^{\frac{1}{3}}(6V)^{\frac{2}{3}}}{A}\left(\frac{6}{\pi}\right)^{\frac{1}{3}} \qquad 4$$

where V and A are the volume and surface area of the bubble respectively. Figure 5 thereby shows that the bubbles become less spherical with increased bed strength. This is consistent with observations that beds of greater yield stress also demonstrate an increasingly anisotropic stress distribution [9]. Consequently, the growing bubble displaces the sediment network in the direction that the bed is weakest and so larger bubbles will be more deformed in beds of anisotropic yield stress. As this analysis is extended into beds of greater solids concentration, it is expected that this trend continues until tensile cracks and channels appear in sediments of greater than 800 Pa yield stress, where the capacity for gas retention is reduced.

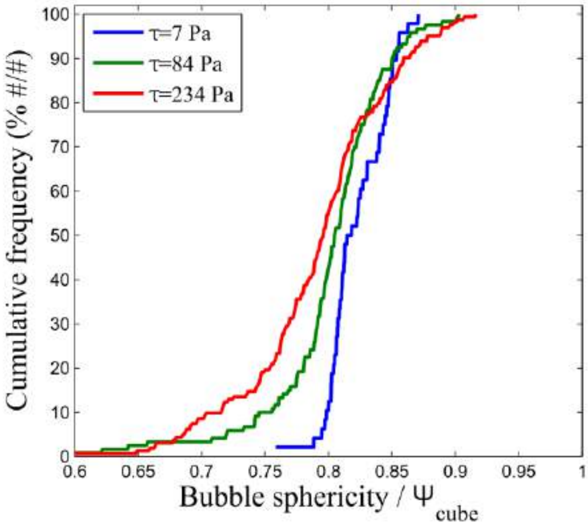

Figure 3 Bubble sphericity histogram for the large FOV in soft sediments of 7-234 Pa yield stress

Conclusions and Future Work

Magnesium hydroxide beds of 7-234 Pa yield stress have all demonstrated the capacity to retain large voidages of gas, occupying up to around 32 % of the ultimate bed volume. This has significant economic and safety implications for new buildings and containers due to receive legacy waste from aging facilities at Sellafield. X-ray tomography has highlighted several features of the retained bubble population under different yield stress conditions:

- The bubble population quickly achieves a steady state size distribution long before the maximum void fraction is reached
- The bubble population is limited to diameters of less than 9 mm and this size distribution appears to be independent of yield stress within the 7-234 Pa yield stress range
- Short time interval tomograms reveal that individual bubbles are mobile within the bed and have short residence times of typically less than an hour
- The largest bubbles grow with reduced sphericity with increasing bed yield stress due to increased anisotropy of stress through higher strength sediments

Acknowledgements

The authors wish to thank the Engineering & Physical Sciences Research Council (EPSRC), the National Decommissioning Authority (NDA) and Sellafield Ltd. for sponsoring this research. Thanks are also given to Geoff Randall and Martyn Barnes for their support, to Samuel Allshorn and Carlos Grattoni for their x-ray tomography expertise and to Tony Windross for engineering the test rigs used in this study.

References

[1] G. McCracken and M. Eilbeck. (2005) Clean up progress on high hazard facilities at Sellafield: magnox swarf storage silos. Proc. ANS Topical Meeting on Decommissioning, Decontamination, and Reutilization, 161–167

[2] R. Burrows, S. Harris and N.P.C. Stevens. (2005) Corrosion electrochemistry of fuel element materials in pond storage conditions. Chemical Engineering Research and Design, 83 (7A): 887– 892

[3] C.R. Gregson, D.T. Goddard, M.J. Sarsfield, and R.J. Taylor. (2011) Combined electron microscopy and vibrational spectroscopy study of corroded magnox sludge from a legacy spent nuclear fuel storage pond. Journal of Nuclear Materials, 412 (1) 145–156

[4] M. Johnson, J. Peakall, M. Fairweather, S. Biggs, D. Harbottle and T. Hunter (2016) Gas Retention and Release from Nuclear Legacy Waste. In proceedings of Waste Management, March 2016, Phoenix, Arizona

[5] N.Q. Dzuy, and D. Boger (1985) Direct yield stress measurement with the vane method. Journal of Rheology, 29 335-347

[6] J.N. Kapur, P.K. Sahoo and A.K. Wong (1985). A new method for gray-level picture thresholding using the entropy of the histogram. Computer vision, graphics, and image processing, 29 (3) 273-285

[7] S. Bolte and F.P. Cordelieres (2006). A guided tour into subcellular colocalization analysis in light microscopy. Journal of microscopy, 224 (3) 213-232

[8] G. Terrones and P. Gauglitz (2002) Vessel-spanning bubble formation in K-basin sludge stored in large-diameter containers. Tech. rep., Pacific Northwest National Laboratory

[9] B. Boudreau (2012). The physics of bubbles in surficial, soft, cohesive sediments. Marine and Petroleum Geology, 38 1–18

Modelling Sludge Mobilisation and Transport

D.O. Njobuenwu*[1], and M. Fairweather[1]

*Correspondence: D.O.Njobuenwu@leeds.ac.uk

[1] *School of Chemical and Process Engineering, University of Leeds, Leeds, LS2 9JT UK*

Abstract

Particle agglomeration can occur during some stages of the decommissioning process (retrieval and transport) of UK legacy nuclear waste, resulting in unwanted effects such as the formation of deposits and plugging of transfer and process pipes. This project, therefore, studies particle-particle interactions to understand particle agglomeration and break-up in turbulent flow using nuclear waste simulant properties.

Introduction

High particle concentrations with volume fractions over a tenth of a percent result in particle-particle collisions becoming an important physical mechanism [1], although only a fraction of the collisions leads to agglomeration, known as the collision efficiency or agglomeration rate. Agglomerates can further associate to form larger structures called flocs. In a reverse process, agglomerates can also be broken-up into smaller particles due to turbulent shear. In physical space, the agglomeration and break-up processes occur concurrently, hence, the rate of formation of agglomerates is then controlled by the balance between agglomeration and break-up.

In nuclear waste sludge processes, where high mass loadings are desirable to minimise waste volumes, agglomeration processes are undesirable. Although the agglomerate density, which includes the interstitial liquid, is less than the primary particle density, agglomerates usually settle faster than primary particles [2]. Agglomeration, therefore, enhances particle deposition leading to bed formation, pipe blockage, surface erosion and alteration in the designed fluid dynamics of any process. During decommissioning of UK legacy nuclear waste and those of any nuclear waste in general, in a temporal storage, the wastes will be retrieved and transported to a supplemental treatment facility for pre-treatment and immobilization before eventually ending up in a permanent storage.

The need to understand agglomeration and break-up processes and design effective waste treatment processes drives this research to determine the probability of fouling, bed formation and pipe blockage due to agglomerated particles.

Methodology

In this section, the deterministic approach adopted for the two-phase simulations in the large eddy simulation (LES) context is presented. An Eulerian description of the continuous phase is employed and coupled with a Lagrangian approach for the dispersed phase. The two phases are coupled through the inclusion of the forces exerted on the particles by the continuous phase and vice-versa.

The BOFFIN-LES code was used to solve the LES equations. The flow was characterised by its shear Reynolds number, $Re_\tau = u_\tau h / \nu$, based on the shear velocity, u_τ, the channel half height, h, and the kinematic viscosity, ν = 10^{-6} m^2 s^{-1}, with the density $\rho = 10^3$ kg m^{-3} and discretised using grid nodes of 129×129×129 in the wall normal, spanwise and streamwise directions, respectively.

The characteristic dimensions of the dispersed phase are presumed small compared to the length scales of the smallest resolved turbulent motions, enabling the particles to be viewed as point sources with respect to the continuous phase. Since the LES solution provides only the resolved values of the carrier phase properties at the particle position, hence, the influences of unresolved SGS velocity fluctuations of the carrier phase on the particle accelerations are introduced through a stochastic Markov model, [3].

An Adams 4th-order predictor-corrector method is used for the particle equation of motion (Eq.1) integration in a Lagrangian particle tracking (LPT) code, with a trilinear interpolation scheme employed for the fluid dynamic properties at the particle position.

$$\begin{aligned}\frac{\mathrm{d}\mathbf{v}}{\mathrm{d}t} &= \frac{(\overline{\mathbf{u}}-\mathbf{v})}{\tau_p} f(Re_p) \\ &+ C_{SL}\frac{3}{4}\frac{\rho}{\rho_p}\left[(\overline{\mathbf{u}}-\mathbf{v})\times\boldsymbol{\omega}\right] \\ &+ \frac{\rho}{\rho_p}\frac{\mathrm{D}\overline{\mathbf{u}}}{\mathrm{D}t} \\ &+ \frac{1}{2}\frac{\rho}{\rho_p}\left(\frac{\mathrm{D}\overline{\mathbf{u}}}{\mathrm{D}t}-\frac{\mathrm{d}\mathbf{v}}{\mathrm{d}t}\right) \\ &+ \mathbf{X}_{\mathbf{sgs}}\end{aligned} \tag{1}$$

where a boldfaced letter denotes a matrix-vector and the terms in the RHS of Eq. **Error! Reference source not found.** are respectively contributions from the drag, shear lift, pressure-gradient, added mass and SGS velocity fluctuations terms. The particle properties are denoted by the subscript *p*, and fluid properties are either given without subscript (for readability) or by the subscript *f* (where it enhances clarity). $\overline{\mathbf{u}}$ and $\boldsymbol{\omega}=0.5(\nabla\times\overline{\mathbf{u}})$ are known resolved fluid velocity and vorticity interpolated at particle position. The term $f(Re_p)$ is the non-linear Schiller and Newman's correction due to the particle finite Reynolds number, Re_p, expressed as $f(Re_p)=1.0+0.15Re_p^{0.687}$. The instantaneous particle Reynolds number is defined $Re_p = |\overline{\mathbf{u}}-\mathbf{v}|d_p/\nu$, where d_p is the particle diameter. $\tau_p=\Phi_p d_p^2/(18\nu)$ is the particle relaxation time and when normalised by the viscous time-scale, $\tau_f=\nu/u_\tau^2$, gives the particle Stokes number, $\tau_p^+=\tau_p/\tau_f$, which is then used to characterise the particle response time, with $\Phi_p=\rho_p/\rho$ being the particle to fluid density ratio.

The dispersed phase is dense so that particle-particle collisions, agglomeration and break-up of agglomerates are all accounted for, leading to a four-way coupled simulation. For particle-particle interactions, the deterministic hard sphere frictionless collision model [4, 5] is used subject to the following assumptions: particles and agglomerates are modelled as spheres; interaction between particles is due to binary collisions; only van der Waals' forces are responsible for post-collision adhesion; only small deformations of particles are allowed post-collision; agglomeration is based on the pre-collision energy momentum balance and van der Waals' interactions [6, 7]; and agglomerate break-up is due to hydrodynamic shear stresses caused by fluid deformations [8].

Results and Discussion

Recent results will be shown at the meeting.

Conclusions and Future Work

LES and LPT are used to simulate particle agglomeration and break-up events, together with a deterministic treatment of inter-particle collisions and particle feedback effects on the fluid phase. Agglomeration is based on the pre-collision energy momentum balance, restitution coefficient and van der Waals' interactions, while agglomerate break-up occurs instantaneously subject to a hydrodynamic stress exceeding a critical value dictated by the properties of the agglomerates modelled using their fractal dimension. These models have been developed using turbulent channel flow. The models will be applied to pipe flows, which are relevant to nuclear waste processing operations.

References

[1]. Elghobashi, S. On predicting particle-laden turbulent flows. *Appl Sci Res.* 1994, **52**(4), 309-329.

[2]. MacLean, G.T. *The settling and compaction of nuclear waste slurries.* Fluor Daniel Northwest, Richland, Washington. , 1999.

[3]. Bini, M. and Jones, W.P. Large-eddy simulation of particle-laden turbulent flows. *J Fluid Mech.* 2008, **614**, 207-252.

[4]. Sundaram, S. and Collins, L.R. Numerical considerations in simulating a turbulent suspension of finite-volume particles. *J Comput Phys.* 1996, **124**(2), 337-350.

[5]. Rani, S.L. ,Winkler, C.M. and Vanka, S.P. A new algorithm for computing binary collisions in dispersed two-phase flows. *Numer Heat Tr B-Fund.* 2004, **45**(1), 99-107.

[6]. Breuer, M. and Almohammed, N. Modeling and simulation of particle agglomeration in turbulent flows using a hard-sphere model with deterministic collision detection and enhanced structure models. *Int J Multiphase Flow.* 2015, **73**(0), 171-206.

[7]. Njobuenwu, D.O. and Fairweather, M. Deterministic modelling of particle agglomeration in turbulent flow. In: *Eighth International Symposium on Turbulence, Heat and Mass Transfer*: Begell House Inc., 2015, pp.587-590.

[8]. Babler, M.U. ,Biferale, L. ,Brandt, L. ,Feudel, U. ,Guseva, K. ,Lanotte, A.S. ,Marchioli, C. ,Picano, F. ,Sardina, G. ,Soldati, A. and Toschi, F. Numerical simulations of aggregate breakup in bounded and unbounded turbulent flows. *J Fluid Mech.* 2015, **766**, 104-128.

Theme 3 – Silo Ponds and Legacy Wastes
DISTINCTIVE 2nd Annual Meeting
Bristol, UK
19th – 20th April 2016

In-line rheometry and flow characterisation of dense slurries in pipe flow using acoustic methods

H.P. Rice*[1], D. Harbottle[1], T.N. Hunter[1], J. Peakall[2] and M. Fairweather[1]

*Correspondence: h.p.rice@leeds.ac.uk

[1] School of Chemical and Process Engineering (University of Leeds, Leeds LS2 9JT, UK)
[2] School of Earth and Environment (University of Leeds, Leeds LS2 9JT, UK)

Abstract

The UK's civil nuclear waste inventory is large, diverse and requires processing and disposal but characterisation of nuclear waste slurries during storage, resuspension and hydraulic transport is made difficult by poor accessibility, radioactivity and chemical hazards. The aim of this study is to develop a suite of safe, accurate, versatile and cost-effective acoustic methods for rapid monitoring and characterisation of high-concentration nuclear waste-analogue slurries, based on existing expertise at the University of Leeds. Results from and proposals for several acoustic methods are described – in-line pipe rheometry, time-domain velocimetry, multi-frequency particle concentration measurement, bed depth and critical deposition velocity determination. A new flow loop laboratory has been commissioned in which these methods will be combined with pumped sampling to investigate horizontal and vertical flow of suspensions of relevance to nuclear waste decommissioning and disposal.

Introduction

The sludges, slurries and suspensions that comprise a proportion of the UK's nuclear waste inventory have a wide range of properties – in terms of particle size, density, concentration, chemistry and radioactivity – and so the methods that are used to characterise them must be versatile and simple to deploy. Following on from expertise developed at the University of Leeds, a number of acoustic methods are proposed or in use for nuclear waste characterisation and flow measurement in a new flow laboratory (Figure 1). Two of these methods (in-line rheometry [1] and critical deposition velocity measurement [2]) are described in detail below, while several others (particle concentration measurement [3], time-domain velocimetry [4] and pumped sampling) are excluded for brevity.

Figure 1 Pipe flow loop at University of Leeds.

Methodology Details

In-line rheometry

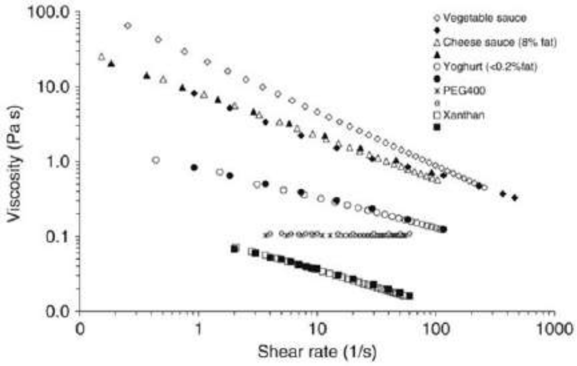

Figure 2 In-line pipe rheometry for various substances compared to conventional off-line results [1].

The viscosity, η, of a fluid can be measured in tube or pipe flow as a function of radial distance from the centreline, r, as follows:

$$\eta(r) = \frac{\tau(r)}{\dot{\gamma}(r)},$$

where $\tau(r)$ and $\dot{\gamma}(r)$ are the local shear stress and shear rate, respectively, and are defined below:

$$\tau(r) = \frac{\Delta P r}{2L},$$

$$\dot{\gamma}(r) = \frac{\mathrm{d}U(r)}{\mathrm{d}r},$$

where ΔP is the pressure drop over a measurement distance L, and U is the local mean axial flow velocity. This method has been shown to give accurate results when compared with conventional off-line viscometry, as shown in Figure 2 [1].

This method can be used in situ and non-intrusively, and avoids the need for potentially costly and dangerous off-line measurement of viscosity.

Bed depth and critical deposition velocity determination

A method for bed depth and critical deposition velocity measurement developed at the University of Leeds [2] has been applied to nuclear-analogue suspensions, with a view to providing predictive capabilities to the nuclear industry and to expand the database of materials and volume fractions for which data exists.

Test materials

Following discussions with industry partners, three nuclear-analogue test materials are being investigated at volume fractions up to 10%: calcium carbonate, magnesium hydroxide and barium sulphate.

Results and Discussion

The following results will be presented:

1. Pipe rheometry results using a Doppler velocimetry/pressure-drop method (Figure 1) will be presented for a number of test materials: water, xanthan gum and glycerol for method validation and the three test materials given above. Results will be compared to conventional, off-line viscometry measurements.

2. Measurements of the critical deposition velocity for the test materials given above will be presented over the full range of volume fractions.

3. The effect of acoustic attenuation on the results, and the implications and consequences for deployment on nuclear sites, will be discussed in detail.

4. In addition, more details and images of the new flow loop laboratory will be presented, along with suggestions for future exploitation.

Conclusions and Future Work

The new flow loop laboratory allows for thorough characterisation of suspensions and slurries with arbitrary concentrations and physical properties with the acoustic methods discussed above, in horizontal and vertical configurations over a range of flow diameters. In addition, laser-based particle image velocimetry (PIV) capabilities are being commissioned for high-resolution, near-wall measurements in the same pipe-flow regimes.

Acknowledgements

The authors thank Bob Harris and Peter Dawson for their advice and technical assistance.

References

[1] Wiklund J (2007), Chem. Eng. Sci. 62 (16) 4277-4293.

[2] Rice HP, Fairweather M, Peakall J, Hunter TN, Mahmoud B and Biggs SR (2015), Chem. Eng. Sci. 126 759-770.

[3] Rice HP, Fairweather M, Hunter TN, Mahmoud B, Biggs SR and Peakall J (2014), J. Acoust. Soc. Am. 136 (1) 156-169.

[4] Jacobson SA, Denbigh PN and Naudé DEH (1985), Ultrasonics 23 (3) 128-132.

Quartz Crystal Microbalance for *In-situ* Rheology Measurements

J.A. Botha*[1], T.N. Hunter[1], S. Biggs[1,2], G.A. Mackay[3], R. Cowley[5], S.E. Woodbury[4], and D.Harbottle[1]

*Correspondence: pm10jab@leeds.ac.uk
[1]*School of Chemical and Process Engineering, University of Leeds, UK;*
[2]*The University of Queensland, Brisbane, Qld 4072, Australia*
[3]*NNL Workington Laboratory, Cumbria, UK;*
[4]*NNL Central Laboratory, Sellafield, Cumbria, UK*
[5]*Sellafield Analytical Services, Cumbria, UK*

Abstract

Sellafield is currently entering a phase of post-operational clean out where the remediation of the site is anticipated to cost £35 bn over the next 100 years. A substantial portion of this cost is associated with the clean-up, transfer and safe storage of legacy particulate wastes encountered in ponds, silos, highly active storage tanks and other large tanks on site. In order to develop suitable strategies for the transport and removal of these particulate suspensions, the rheology of the sludge should be accurately determined. The current work demonstrates the applicability of a quartz crystal microbalance (QCM) to measure sludge rheology; specifically its shear yield stress. The device is simple to operate with no mechanical parts near the test material, is small and portable which allows for deployment into limited access areas and provides the user with in-situ rheological information on the test sample which eliminates the need for operator sampling. The measurement principle of the QCM relates to the changes in resonance frequency and motional resistance of a piezo-electric gold-coated quartz sensor as it is submerged into the desired test material. The air-to-sample frequency and resistance shifts are shown to correlate well with the shear yield stress of a suspension as measured by conventional vane viscometry. An increase in the suspension yield stress relates to a more positive frequency and resistance shift, where this correlation have been confirmed for a range of particle suspensions.

Introduction

Sellafield is currently the largest nuclear site in Europe and globally contains one of the largest inventories of untreated waste. Effective treatment and clean-up of these waste inventories is therefore a significant challenge to the UK's nuclear decommissioning program where costs to turn the site into a greenfield site are estimated to be £53 bn over the next 100 years. A significant portion of these costs relate to the recovery and transport of legacy waste sludge to interim storage facilities. The First Generation Magnox Storage Pond (FGMSP) contains approximately 14,000 m^3 of contaminated water and approximately 1,200 – 1,500 m^3 of complex radioactive sludge formed by the corrosion of Magnox fuel rods due to lengthy storage times in water and organic material and dust entering the open air pond [1, 2].

In order to best design suitable sludge handling processes, the rheological properties of the sludge must be characterised. Sampling is potentially hazardous and is a costly undertaking, and sampling of the sludge introduces history effects where the rheology of the sample changes due to pre-shearing of the sample. A technology that could therefore determine the rheological properties of the sludge *in situ* is an attractive alternative, especially if the new technology could be deployed at a number of locations around a pond or at another facility.

The current research investigates the use of a quartz crystal microbalance (QCM) to measure sludge rheology. The devices are small (sensor area typically less than 1 inch in diameter), portable and contain no electrical parts near the sensor, making their application to measure the rheological properties of complex fluids and sludge across a nuclear facility highly desirable.

The device is traditionally described as being an ultra-sensitive mass balance that have been widely applied in other scientific disciplines to measure the adsorption/desorption of surface active species (surfactants, polymers, biological molecules) at the sensor surface [3-7]. The QCM has also been used in liquid environments where changes in the bulk properties of the nonadsorbing fluid will result in characteristic shifts in the vibrational frequency and motional resistance across the quartz resonator [8, 9]. The objective is to expand the usability of the QCM to include yield stress suspensions, where previous results to the work have been demonstrated at the Waste Management 2016 Symposia [10].

Methodology Details

The particle suspension was prepared by pouring Milli-Q water (resistivity = 18.2 MΩ cm) to a known mass of sample powder to form a suspension of the desired solids concentration. The suspension was mixed using a metal spatula for at least 5 min until the suspension resembled a smooth paste. For pH tests, 10 mM NaCl was added as a background electrolyte and the suspension beaker was covered with parafilm and was left overnight to reach equilibrium before further pH adjustments and measurements occurred.

The particle systems considered were as follows:

- Versamag A (high MgO content $MgOH_2$, Rohm and Haas) – concentration tests, aging tests
- Versamag B (low MgO content $MgOH_2$, Martin Marietta) – concentration tests, aging tests
- Titanium dioxide (ANX Type-N anatase grade, Degussa) – concentration tests, pH tests

Vane viscometry: The suspension shear yield stress was measured using a Brookfield DV II+ Viscometer. A four blade vane (H 43.33 mm; D 21.67 mm) was gently lowered into the particle suspension and rotated at 1 rpm. The resistance to vane rotation is measured as an increase in the torque. At the yield stress the torque passes through a maximum as the suspension begins to flow. To avoid any wall effects the vane-to-cylinder radii ratio was equal to 1:3.5. The sample beaker was clamped to avoid any rotation of the sample when measuring high yield stress suspensions. The yield stress (τ_y) can be calculated by Equation 4 [11]. The yield stress was measured for a suspension at different known solids concentrations.

$$T(max) = \frac{\pi D^3}{2}\left(\frac{H}{D} + \frac{1}{6}\right)\tau_y \qquad \text{(Eq. 4)}$$

Where $T(max)$ = maximum torque, D = vane diameter, H = vane height and τ_y = shear yield stress of the test material.

Quartz crystal microbalance: A 5 MHz AT-cut gold-coated quartz sensor (d = 25.4 mm) was cleaned by sonicating in 2 vol.% Decon-90 solution for 5 min and rinsed thoroughly with Milli-Q water and subsequently ethanol. The sensor was rinsed with Milli-Q water before being dried using nitrogen. The sensor was loaded into a Stanford Research Systems (SRS) QCM 200. The sensor was allowed to stabilize in air for 30 min. A stable sensor resonance was considered when both the frequency and resistance responses are less than 5 Hz/hr and 0.5 Ohm/hr, respectively. The suspension was prepared as previously outlined. The sensor probe was then submerged into the test material and rotated horizontally at an angle of 90° to ensure good contact. Due to the dampening effect the oscillator compensation was adjusted to provide stable oscillation. The sensor was left for approximately 30 min until a new stable response for both the frequency and resistance had been achieved and the values were recorded. The experiment was repeated for each new suspension solids concentration that is to be investigated.

Versamag aging: A Versamag suspension was prepared to a concentration of 22 vol% using the methodology previously outlined. A layer of mineral oil (approx. 20 mL) was gently poured over the surface of the suspension to avoid evaporation. The beaker was then covered using parafilm and was left for the required amount of time. The suspension yield stress then obtained using the methodology previously outlined using separate batches of the suspension. For the QCM frequency and resistance data, the QCM was prepared as previously outlined, however the probe was submerged into a fresh batch of Versamag and the suspension was left in a water bath that was being maintained at 30°C using a hot plate. The suspension was then covered with mineral oil with the probe inserted and was left to collect data in-situ over 70 hrs.

Titanium dioxide pH tests: A 16.2 vol% titanium dioxide suspension was prepared using the methodology previously outlined. The pH of the suspension was altered using NaOH, and for a different batch HCl was used. After each adjustment the suspension was well mixed for 5 min, the beaker was covered with parafilm, then left for 30 min to reach equilibrium. The shear yield stress and QCM frequency and resistance shift data was then obtained by following the methodology previously outlined.

Results and Discussion

Particle concentration: Figure 1 (A) shows the QCM frequency shift and yield stress changes as a function of solids concentration for Versamag A. An increase in the yield stress of the suspension correlates to a more positive frequency shift as well as a more positive resistance shift as can be seen from figure 1 (B). The overall linear trend between the frequency shift, resistance shift and the yield stress of the Versamag suspension begins to break down at higher yield stresses however (Figure 1 (B)) where a similar behaviour has been observed for titanium dioxide and Versamag B (Figure 1 (C)).

The break in the linear trend may be due to a ‘slip effect’ occurring at the sensor – suspension interface; a high yield stress suspension will have network links between the individual particles that are overall too strong to be moved by the vibrating sensor. In order to extend the usability of the QCM to include higher suspension yield stresses, the roughness of the crystal should be modified to provide edges to help maintain hold onto the suspension as the crystal vibrates.

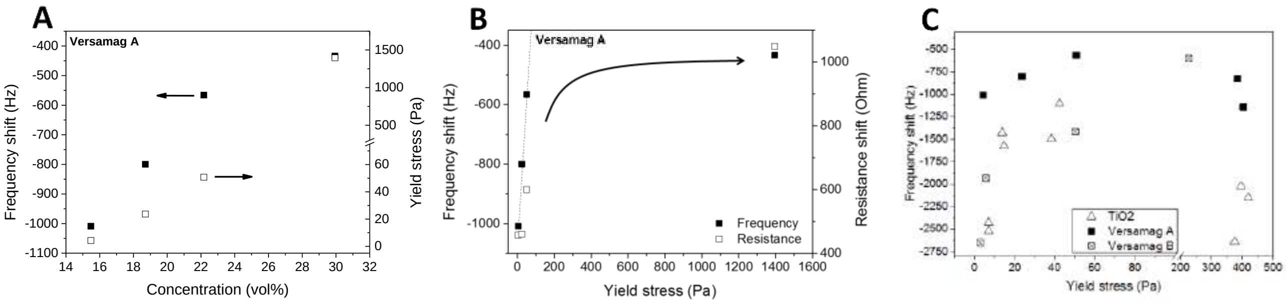

Figure 1 Comparison between the quartz crystal microbalance frequency and resistance shift response to the shear yield stress for Versamag A, Versamag B and titanium dioxide (line in figure 1 B is to guide the eye).

Versamag aging: Figure 2 (A) shows the time dependent shear yield stress and QCM frequency shift data for Versamag A and B. The shear yield stress of the Versamag A increases significantly more than the Versamag B over a 70 hr period (~300 Pa and ~75 Pa respectively). This is followed by a QCM frequency response that closely resembles that of the yield stress data where the frequency shift of Versamag A is significantly more positive than the Versamag B after a 70 hour period.

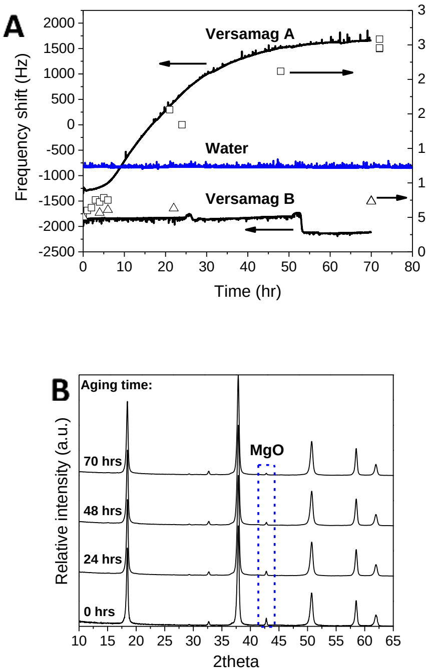

Figure 2 (A) comparison between the shear yield stress and QCM frequency response of Versamag A and B as a function of aging time. and (B) XRD pattern showing the reduction in the MgO content of Versamag A as a function of aging time.

A background test was performed on the QCM where it was submerged in Millipore water over a 70 hr period, and no significant change was observed in its response. The changes shown are therefore purely a result of the changes in the properties of the suspension. Figure 2 (B) shows an XRD analysis of the Versamag A at different points in time during its aging process. The MgO peaks decrease in height with increasing aging time suggesting that the MgO within the Versamag is converting into $Mg(OH)_2$ over time, where it re-precipitates out between neighbouring particle clusters and bind them together, forming larger clusters which will then have a higher yield stress [12, 13]. Since the Versamag B is of a much lower MgO content (approx. 0.2 wt% as opposed to 2.6 wt% for Versamag A), less of the MgO converts into $Mg(OH)_2$ resulting in a smaller increase in its shear yield stress and a more negative frequency shift.

Titanium dioxide pH: Figure 3 (A) shows a comparison between the shear yield stress and the QCM frequency shift of 16.2 vol% titanium dioxide in 10 mM NaCl electrolyte. The QCM frequency response appears to follow the shear yield stress of the suspension at low pH ranges (pH 4 – 6.5). At higher pH values beyond the maximum yield stress of the suspension, this relationship breaks down where the frequency response remains relatively unchanged as the pH of the suspension is increased further. The titanium dioxide – gold interaction could therefore be repulsive at pH values of beyond 6 - 6.5 to 10, resulting in the suspension being unable to completely come into contact with the crystal surface. Using the Hogg, Healy and Fuersten relationship [14], the total interaction potential between the gold and the titanium dioxide particles can be determined by using zeta potential data for both systems from literature [15, 16]. The total interaction potential of a titanium dioxide – gold system in water of a 10 mM background electrolyte solution is shown in figure 3 (B). As the pH of the suspension increases the total interaction potential becomes more positive overall. A positive interaction potential implies that the titanium dioxide – gold interaction system will gain energy which is thermodynamically unfavourable. The curves shown become positive at around a pH of 6, which is at the same point where the QCM frequency response no longer change significantly with increasing pH. The surface on the QCM sensor should therefore be modified in order to change this interaction to a more positive one overall for the given pH range in order to ensure that the crystal will remain in contact with the suspension for the entire pH range.

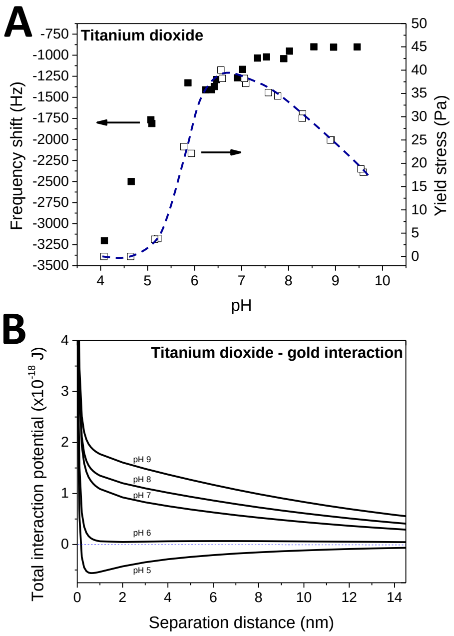

Figure 3 (A) comparison between the QCM shear yield stress and its frequency shift at a pH range of 4 – 10 and (B) the HHF interaction potential between titanium dioxide and a gold surface (line in figure 3 B is to guide the eye).

Conclusions and Future Work

The QCM frequency and resistance response to measure sludge rheology has been demonstrated for a number of different systems. Improvements to the technique can be made by improving the contact mechanics between the crystal surface and the particulate suspension. This will allow for accurate rheological measurements for high yield stress suspensions and suspensions at a range of different pH values. QCM crystals are to be coated with a titanium-oxide layer using a sol-gel process in order to remove the effects of a changing interaction potential with varying pH. The QCM response for this coated crystal in titanium dioxide will then be examined. The crystal roughness will also be improved and quantified using atomic force microscopy measurements and will be used in higher yield stress suspensions in order to extend the usability of the QCM to include higher yield stress suspensions.

Acknowledgements

The authors gratefully acknowledge the financial support from the Engineering Physical Sciences and Research Council (EPSRC) for the iCase award sponsored by the National Nuclear Laboratory (NNL) and Sellafield Ltd.

References

1. Gregson, C.R., et al., *Combined electron microscopy and vibrational spectroscopy study of corroded Magnox sludge from a legacy spent nuclear fuel storage pond.* Journal of Nuclear Materials, 2011. **412**(1): p. 145-156.
2. Sellafield Ltd. *Sellafield making strides in clean-up*. 2015 [cited 2015 30 July]; Available from: http://www.sellafieldsites.com/press/sellafield-making-strides-in-clean-up/.
3. O'Sullivan, C.K. and G.G. Guilbault, *Commercial quartz crystal microbalances - theory and applications.* Biosensors & Bioelectronics, 1999. **14**(8-9): p. 663-670.
4. Keller, C.A. and B. Kasemo, *Surface specific kinetics of lipid vesicle adsorption measured with a quartz crystal microbalance.* Biophysical Journal, 1998. **75**(3): p. 1397-1402.
5. Hook, F., et al., *Variations in coupled water, viscoelastic properties, and film thickness of a Mefp-1 protein film during adsorption and cross-linking: A quartz crystal microbalance with dissipation monitoring, ellipsometry, and surface plasmon resonance study.* Analytical Chemistry, 2001. **73**(24): p. 5796-5804.
6. Caruso, F., et al., *Quartz-Crystal Microbalance and Surface-Plasmon Resonance Study of Surfactant Adsorption onto Gold and Chromium-Oxide Surfaces.* Langmuir, 1995. **11**(5): p. 1546-1552.
7. Marx, K.A., *Quartz crystal microbalance: A useful tool for studying thin polymer films and complex biomolecular systems at the solution-surface interface.* Biomacromolecules, 2003. **4**(5): p. 1099-1120.
8. Kanazawa, K.K. and J.G. Gordon, *Frequency of a Quartz Microbalance in Contact with Liquid.* Analytical Chemistry, 1985. **57**(8): p. 1770-1771.
9. Martin, S.J., V.E. Granstaff, and G.C. Frye, *Characterization of a Quartz Crystal Microbalance with Simultaneous Mass and Liquid Loading.* Analytical Chemistry, 1991. **63**(20): p. 2272-2281.
10. J.A. Botha, W.D., T.N. Hunter, S. Biggs, G.A. Mackay, R. Cowley, S.E. Woodbury and D. Harbottle, *A Novel Techynology for Complex Rheological Measurements.* Waste Management 2016 Symposia, 2016.
11. Dzuy, N.Q. and D.V. Boger, *Direct Yield Stress Measurement with the Vane Method.* Journal of Rheology, 1985. **29**(3): p. 335-347.
12. Mullin, J.W., et al., *Aging of Precipitated Magnesium-Hydroxide.* Industrial & Engineering Chemistry Research, 1989. **28**(11): p. 1725-1730.
13. Gursky, J.A., et al., *Particle-particle interactions between layered double hydroxide nanoparticles.* Journal of the American Chemical Society, 2006. **128**(26): p. 8376-8377.
14. Hogg, R., T.W. Healy, and Fuersten.Dw, *Mutual Coagulation of Colloidal Dispersions.* Transactions of the Faraday Society, 1966. **62**(522P): p. 1638-&.
15. Giesbers, M., J.M. Kleijn, and M.A.C. Stuart, *The electrical double layer on gold probed by electrokinetic and surface force measurements.* Journal of Colloid and Interface Science, 2002. **248**(1): p. 88-95.
16. Paul, N., et al., *Synthesis of nuclear waste simulants by reaction precipitation: Formation of caesium phosphomolybdate, zirconium molybdate and morphology modification with citratomolybdate complex.* Polyhedron, 2015. **89**: p. 129-141.

Cake formation in enhanced shear microfiltration

K. Schou*, M.Dragosavac, R.G. Holdich[1]

*Correspondence: K.Schou@Lboro.ac.uk

[1] Affiliation (Loughborough University, Epinal Way, Loughborough LE11 3TU, United Kingdom, UK)

Abstract

This project investigates enhancing the flux rate in microfiltration through directed membrane surface shear. This is achieved by reducing the filter cake formed by oscillating the filters either vertically or azimuthally. Control of the filter cake build-up enables a higher flux rate, while maintaining the required particle retention.

Introduction

Microfiltration is used in many industries, including in the treatment of nuclear effluent. Currently cross flow filters are employed to filter suspensions. In order to receive reasonable flux across the membrane the cross flow filtration requires constant recirculation of the suspension. By replacing the recirculating pump with directed shear at the membrane surface it may be possible to reduce energy usage and increase flux [1][2], [3][4]

The application of shear enhancement on filtration has been reported to increase flux as high as 18x the pseudo steady state filtration amount [2].A significant amount of research has already been done in this field, [5], [6]. There are industrially available units (V-SEP)[6][7].

This enhancement in pseudo steady state flux is very large, prompting interest in the usage of shear enhanced filtration. In the papers currently reviewed though there is no mention of the reduction in particle retention.

The purpose of this project is to determine the specific mechanism behind the flux increase, to study the controlled shear at the surface of a filtering membrane and a theoretical understanding of a compact but efficient filtering system.

The goal is to replace the current cross flow filtration methods, which require constant recycling of the suspension in order to receive reasonable fluxes, with a more efficient and compact filtration method.

Cake formation is essentially an irreversible process, where applying additional shear will prevent additional cake formation, but not remove the cake which has formed. [8]

Key research questions

The following are the main questions which this project aims to answer.

- Is it the effect of localised shear which creates the increase in flux? If so then how shear is applied is irrelevant
- What are the specific advantages of oscillating or pulsed flow?
- Does the application of the shear (azimuthal/axial) matter?
- How can the filters be scaled up?
- How do filter coatings effect filtration
- What are the potential problems of using this technology?
- What is the effect of frequency and amplitude on flux?
- How easy would a filter be to clean?
- Does the localised shear damage the suspension, creating a more difficult to filter suspension?

Methodology

Experimental Setup

A 1% w/w Calcium carbonate suspension (calcite) was drawn through a filter while the filter was oscillated either axially (vertical) or azimuthally (rotational) for 1 hour. The frequency and amplitude were controlled. The flowrate (from change in mass), trans-membrane pressure (TMP) and absorbance (for particle retention) were logged. The filter cake that had formed was measured optically (photo & image analysis) and was sampled for concentration (dry and wet cake weight) and particle size distribution (Malvern master-sizer).

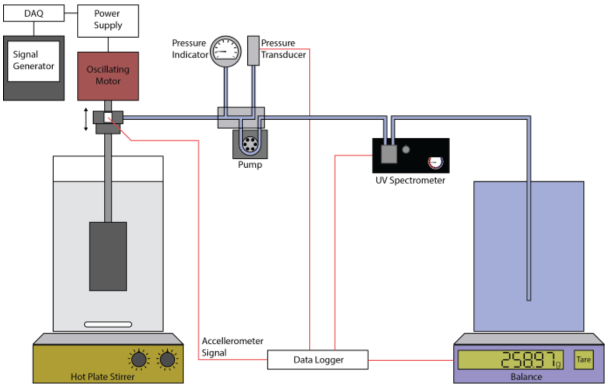

Figure 1, Simple experimental setup

The Suspension

The suspension under test is a 1% w/w Calcium carbonate (chalk) suspension. It is calcite (a cubic structure) which has an average sauter mean diameter (d_{32}) of 2.74μm.

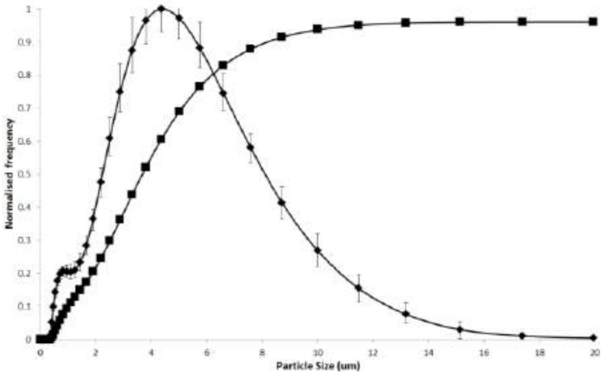

Figure 2, Particle size distribution of the bulk suspension D_{32} is 2.74 μm

The filter cake which formed had consistently a concentration of 37% by volume, (dry/wet cake weighing method) regardless of shear applied. At this concentration the viscosity is 607 mPa.s (tested by concentric cylinder rheometer), bulk viscosity of the suspension can be taken to be 1 mPa.s .

Calcium carbonate was used a suspension medium due to its particle size range, inherent safety, availability & ease of cleaning the filter.

Results and Discussion

Filter cake thickness

The thickness of the cake formed was measured by taking a photograph and measuring on the image. The thickness is heavily effected by the shear applied

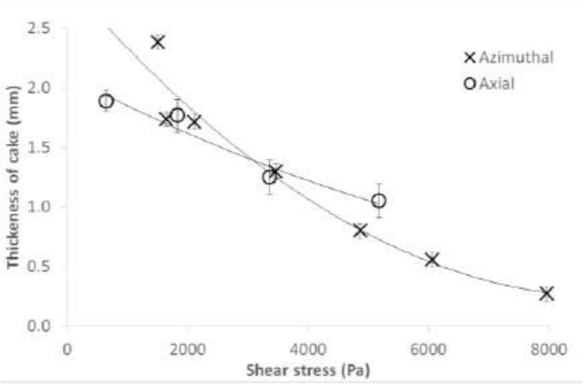

Figure 3, Thickness of the cake formed under shear

As the resistance of the filter is heavily dependent on the resistance due to cake, the reduction of filter cake is a significant finding.

$$R = R_m + R_c$$

$$R_m = Constant$$

$$R_c = \frac{L}{k}$$

Where L is the cake thickness, and k is constant of the material. By controlling the filter cake thickness, we are able to directly control the resistance of the filter. It may be tempting to try and remove the cake entirely with shear, however the cake is important for effective particle retention. Therefore it is ideal to control the filter cake to a very thin layer. The power requirements in order to reduce the formation of the cake get larger as the cake gets thinner, so there are diminishing returns as the cake gets thinner.

Permeability

Under greater shear the permeability is reduced. This is likely due to the removal of larger particles due to drag effects caused by the shear. This leaves smaller particles as the filter cake, which pack tighter, decreasing the permeability. (See Figure 5)

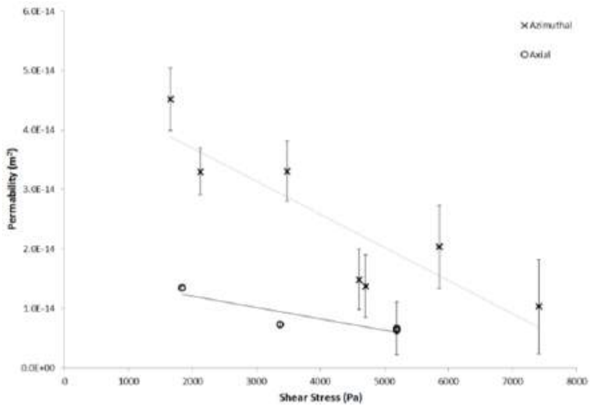

Figure 4, Permeability under different shear rates.

This effect on permeability may impact the reduction in cake resistance, which in turn provides diminishing returns.

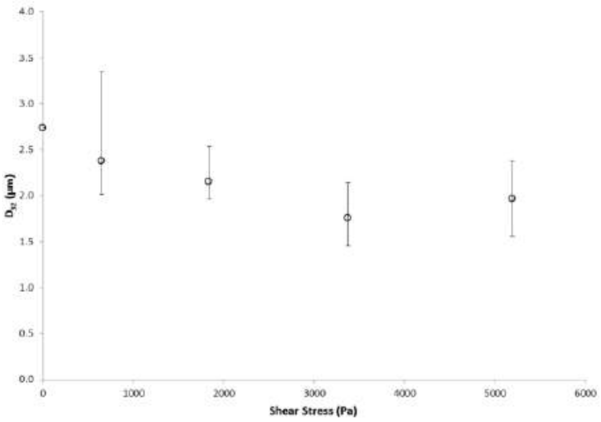

Figure 5, D_{32} of filter cake (range bars are of triplicates)

A slight trend towards lower diameters of particles found in the filter cake as the shear stress increases. A small change in the D_{32} can make a very large difference in the permeability.

Cake formation and striations

Figure 6, Filter cake formed with increasing shear left to right

With the filters above, shear increasing left to right show how the filter cake thickness differs with the applied shear. Additionally there is an effect of striations being formed on the filters under shear, which can be seen from the images. These striations have not yet been investigated, the significance of these are currently unknown.

Conclusions and future work

Applying shear to the surface of the filter has shown to reduce the cake formation (but not removal of the cake when a pressure gradient is present). This reduces the resistance to flow and therefore an increase in flux across the filter.

The reduction in the cake formation appears to effect the composition of the cake. This appears to be different for azimuthal and axial oscillations, the cause of this is currently being investigated.

The current testing has been done with calcium carbonate. Future testing with ferric flocc (used in the EARP) and magnesium hydroxide (used in SixEP) compared to what has been found with calcium carbonate, will have a more direct impact on industry applications.

How the enhanced shear at the membrane surface effects floccs and other shear sensitive materials also needs to be investigated.

Oscillating flow will also be investigated, ideally using solid state devices.

Acknowledgements

I would like to thank the project sponsor Sellafield ltd through the DISTINCTIVE consortium and Loughborough University for making this project possible.

References

[1] M. Y. Jaffrin, “Dynamic shear-enhanced membrane filtration: A review of rotating disks, rotating membranes and vibrating systems,” *J. Memb. Sci.*, vol. 324, no. 1–2, pp. 7–25, Oct. 2008.

[2] F. Zamani, J. W. Chew, E. Akhondi, W. B. Krantz, and A. G. Fane, “Unsteady-state shear strategies to enhance mass-transfer for the implementation of ultrapermeable membranes

in reverse osmosis: A review," *Desalination*, vol. 356, pp. 328–348, Jan. 2015.

[3] H. G. Gomaa, S. Rao, and a. M. Al-Taweel, "Intensification of membrane microfiltration using oscillatory motion," *Sep. Purif. Technol.*, vol. 78, no. 3, pp. 336–344, Apr. 2011.

[4] T. Li, A. W.-K. Law, M. Cetin, and a. G. Fane, "Fouling control of submerged hollow fibre membranes by vibrations," *J. Memb. Sci.*, vol. 427, pp. 230–239, Jan. 2013.

[5] S. C. Low, H. H. Juan, and L. K. Siong, "A combined VSEP and membrane bioreactor system," *Desalination*, vol. 183, no. 1–3, pp. 353–362, Nov. 2005.

[6] M. D. Petala and A. I. Zouboulis, "Vibratory shear enhanced processing membrane filtration applied for the removal of natural organic matter from surface waters," vol. 269, pp. 1–14, 2006.

[7] M. Y. Jaffrin, L.-H. Ding, O. Akoum, and A. Brou, "A hydrodynamic comparison between rotating disk and vibratory dynamic filtration systems," *J. Memb. Sci.*, vol. 242, no. 1–2, pp. 155–167, Oct. 2004.

[8] a. Ould-Dris, M. Y. Jaffrin, D. Si-Hassen, and Y. Neggaz, "Analysis of cake build-up and removal in cross-flow microfiltration of CaCO3 suspensions under varying conditions," *J. Memb. Sci.*, vol. 175, no. 2, pp. 267–283, 2000.

In Situ Monitoring of the Legacy Ponds and Silos at Sellafield

O.S. Ayoola*[1], B. Lennox[1], S. Watson[1] and G.X. Randall[2]

*Correspondence: olusola.ayoola@postgrad.manchester.ac.uk

[1] *The University of Manchester, Dalton Cumbrian Facility, Cumbria, United Kingdom*
[2] *Sellafield Ltd, Sellafield, United Kingdom*

Abstract

The aim of this research is to identify experimental factors that influence the quality of results from sludge sampling and characterisation campaigns, to evaluate their contributions to data uncertainties and to seek ways to optimise the protocol through the use of an in-situ core sampler and analyser. The research involves the use of relevant statistical tools to analyse the results obtained from simulation and laboratory tests. By ensuring high quality in the data obtained from sludge sampling and characterisation campaigns, the quality of decisions taken in the design of sludge transportation and processing systems is further enhanced. The research looks into the measurement of particle size distribution (PSD) as an indicator of the physical properties of sludge.

In this report, the experimental factors considered were the sampling intensity, as represented by the number of samples collected, the sampler device used and the sampling strategy adopted. Other important factors considered were the degree of homogeneity of sludge spatial distribution in the ponds and the method of spatial extrapolation used to predict measured physical properties on non-sampled areas of the sludge bed. Maps showing the confidence limits associated with the resulting spatial extrapolations were also produced.

A useful statistical tool for analysing the influence of different experimental factors on variability of results is the F-statistics. The magnitude of a factor's F-statistics is an indication of the significance of such a factor to variability. From early results obtained from 2D sampling simulations, it was observed that the sampling intensity factor had an F-statistics of about 80,000. This was followed by the sampling strategy factor with an F-Statistics of about 1000. Unexpectedly, the choice of sampler device, which is thought to be an equally significant factor, had an F-statistics of 0. This has led further investigations using a 3D sampling simulation. Analytical factors will also be investigated using the principle of laser diffraction. Another work in progress is the design of a bench-top experiment to investigate the use of an in-situ sampler and analyser for remote characterisation.

Introduction

There are a number of factors that contribute to the reliability of any sampling data and subsequent measurement results. These factors may include; the actual number and spread of samples taken [1], the sampler device used [2] and the method of sample handling adopted [3] [4]. While records of previous sludge sampling and analysis campaigns conducted at Sellafield may be available, there is a need to scientifically evaluate the actual degree of confidence and certainty associated with such measurements. Hence, the contribution of sampling and analysis experimental factors to overall confidence must be well understood. Also, depending on the degree of uncertainty associated with previous records, it may become necessary to device optimisation techniques towards improving such confidence and repeatability of results in future campaigns.

Particle size distribution (PSD) data is critical for the design of appropriate transportation facilities for the various classes of sludge present in the pond [5] and generally in other fields such as water treatment, product quality and performance especially in the production of detergents, food and drugs. In studying the flow-ability and compactness of detergent powders, Hart, 2015 [6] found that there is a significant relationship between the particle size distribution of the powdered detergent and the compactness and tensile strength of detergent tablets formed as well as the flow-ability of the detergent. This assertion is also supported by a study on food processing [7] and another study on drug performance [8] and is also established by Leyva and Mullarney, 2009 [9] wherein the PSD data was used in modelling the flow performance of pharmaceutical powder.

SPATIAL UNCERTAINTY:

The ability to collect representative sludge samples from a given population remains an industrial challenge, but when dealing with an underwater environment, with the likelihood of radiation hazards such as that in Figure 1 which shows a bed of radioactive sludge at the bottom of a long term storage pool NPP A-1 in Jaslovske Bohunice [10], the challenge becomes even more. Factors like; adequacy of the number of samples collected, otherwise represented by the sampling intensity, the strategy for selecting the sampled positions and monitoring of the sampler's location, accessibility to sampled positions, the type of sampler device used, the method of sample handling and the spatial extrapolation method all contribute to the variability, uncertainties and the level of confidence of results on sample representation and consequentially, spatial mapping of PSD.

Figure 1 Radioactive sludge at the bottom of a long-term storage [10]

Analytical Uncertainty:

Studies have shown that in the use of laser diffraction technique for PSD analysis, the optical parameters of the particulate sample and that of the dispersion medium, being vital ingredients for the computational algorithm, affect to a large extent the final result obtained. The refractive index and absorption coefficient have been identified as two of such parameters [11] [12] [4] [3] [13] [14]. While this is understandably a challenge for unknown samples and heterogeneous samples, interestingly, the situation is not any better in the case of known homogenous samples either such as particulate samples produced in the manufacturing industries. This is because there are different approaches to obtaining such parameters with each giving different values. While some studies have recommended specific optimal parameters as generic settings that have proven to reduce variability, there are concerns about the validity and applicability of any one parametric setting in ensuring valid results for all cases [13].

Methodology Details

To evaluate the effect and interactions of experimental factors as they influence result variability, a statistical tool known as the Analysis of Variance (ANOVA) is commonly used [15]. It involves a test in which deliberate changes in the settings of these experimental factors are made and the corresponding experimental results are analysed. In this study, the result to be analysed is the accuracy observed in the PSD spatial map obtained from the treatment. To do this, the PSD characteristics, described by the associated mean size values or even a class of such PSD characteristics at each unit area in the population is represented on a PSD spatial map. Such observed PSD maps are only obtainable by conducting spatial extrapolation from the data collected at sampled points. If the observed PSD map is compared to the correct PSD map of the sludge bed, a performance rating can be determined. In a soil mapping research, Grinand et al., 2008 [1] adopted the use of an error matrix, also known as the confusion matrix, to obtain observed classification accuracy and kappa index rating for result assessment.

In reality however, performance assessment must be made in the absence of any “actual” map. An approach to qualitatively assessment of performance is therefore the use of a confidence map or variation map as observed. It has been observed [1] that the level of correctness of any prediction made at a non-sampled point on the map is dependent on its distance to the sampled point(s) from which its prediction was made.

Simulation Results and Discussion

Observed Map Accuracy

The sludge bed area modelled and sampled was a 200 m x 100 m sludge bed, an arbitrary case for analysis. It was divided into 20,000 pixels each of 1 m x 1 m representing a likely sample point. By comparing the percentage of pixels whose PSD predictions in non-sampled areas, obtained by spatial extrapolation, correspond to that in the sludge bed model, the map accuracy was calculated. It was generally observed that map accuracies improved with increasing number of samples collected. In the case of 8 samples collection (0.04% sampling intensity), an accuracy of about 19% was observed on the average. Whereas, an increase to 200 samples collected (1% sampling intensity), showed that map accuracy increased by 400%. Subsequent increments in the number of samples as can be seen in Figure 2 saw a rather mild improvement in map accuracy. Although this portrays the significance of the number of samples collected, or sampling intensity factor on map accuracy, it can also be deduced that a 100% sampling intensity may not be necessary to achieve a satisfactory map accuracy level. The sampling intensity that produces optimal map accuracy should be most important, for example, 1% sampling intensity in the case of the sludge bed model studied. This optimal setting however, will largely depend on the heterogeneity of the PSD spatial distribution in the actual population.

Figure 2 also depicts the behaviour of a deterministic approach in the presence or absence of spatial autocorrelation as against the behaviour of a geostatistical method. Unlike the geostatistical method that presents fairly similar map accuracies to sludge beds of both cases, the deterministic approach performed better in the absence of spatial autocorrelation.

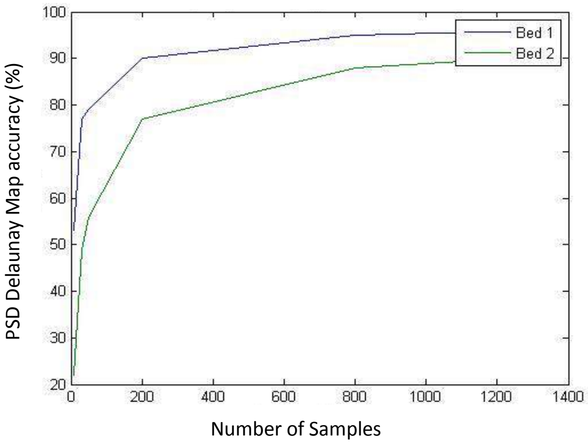

Figure 2 Classification map accuracy obtained using the Delaunay triangular algorithm as number of samples increases in bed 1 and 2

Spatial Distribution Of Confidence Limits And Variance

Figures 3 and 4 show the spread of confidence levels represented by the kriging variance (see Appendix A below for more information) for bed 1 and bed 2 respectively with 8 samples collected. The darker a region, the poorer is the confidence in the PSD predictions obtained from the spatial extrapolation campaign.

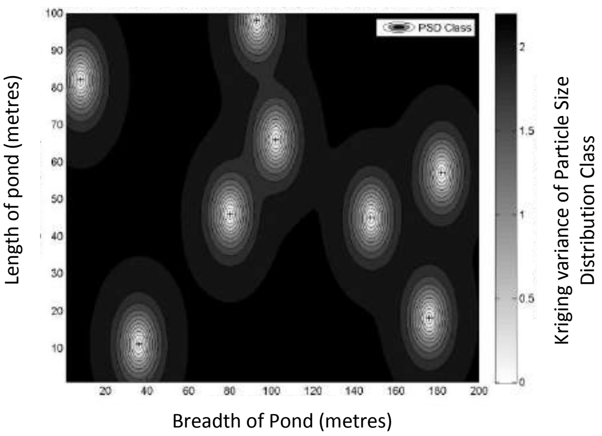

Figure 3 Kriging variance distribution of PSD class sizes for bed 1

Figure 3 shows a better spread of confidence because of the spatial autocorrelation that exists in bed 2. In subsequent investigations, it was observed that with 200 samples collection, the confidence spread improved and was satisfactorily similar for both beds. It can be deduced from this that the spread of confidence improves with sampling intensity; the confidence map provides guidance on areas where further sampling is needed; and with a low sampling intensity, the detection of spatial autocorrelation may result in a better spread of confidence. It must be noted however, that the ability to detect spatial autocorrelation depends on the optimisation of sampling factors.

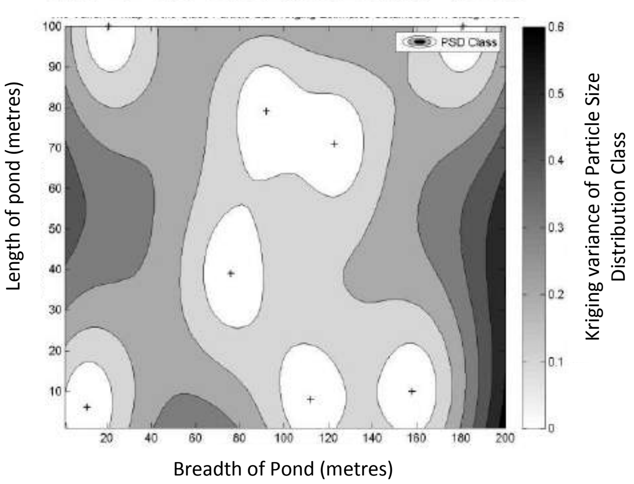

Figure 4 Kriging variance distribution of PSD class sizes for bed 2

Screening And Evaluation Of Sampling Factors

Three major sampling factors were analysed using the 2k factorial ANOVA approach and the results of their F-statistics on bed 1 are as follows;

Number of samples: 84,176.04; Sampling strategy: 996.3; Sampler device used: 0

The magnitude of a factor's F-statistics is an indication of the significance of such a factor to variability. Hence, the number of factor is a vital component of result confidence. Although sampling strategy appears to be satisfactorily significant with regards to bed 1, the result of an ANOVA on bed 2 gives the sampling strategy an F-statistic value of 0.02. Nonetheless, both ANOVA results agree on the insignificance of sampler device used as a component of result variability. Such an unexpected result casts doubts on the validity of the sampler device models regarding the representation of the physical limitations exhibited by a typical sampler on the field. This result needs further investigation.

Conclusions and Future Work

From the above discussions, it can be deduced that the number of samples, preferably represented by the sampling intensity factor, contributes majorly to sampling uncertainties. Also, the sampling strategy factor does significantly contribute to uncertainties.

The method of spatial extrapolation is equally a significant determinant of the accuracy of spatial map predictions for a bed with unknown spatial autocorrelation. It has also been seen that the confidence limit map or variance map as may be the case for kriging, provides insight into areas where further sampling is required to clear out grey areas on the PSD spatial distribution map. Finally, the role of the sampler device used with respect to its physical limitation on penetration depth (as modelled in the simulation exercise) has no significant contribution to variability, this unexpected result, poses a need for more investigation into the practical limitations of samplers used. Expected limitations to be looked into include the bias towards sampling depth penetration, particle size collection and sample retention. Analytical factors will also be investigated using the principle of laser diffraction. Analytical factors will also be investigated using the principle of laser diffraction. Another work in progress is the design of a bench-top experiment to investigate the use of an in-situ sampler and analyser for remote characterisation.

Acknowledgements

The research team would like to acknowledge the funding provided by the Dalton Cumbrian Facility, through the Nuclear Decommissioning Authority and EPSRC - EP/L014041/1.

The kind support from the National Nuclear Laboratory and especially from Dominic Rhodes must also be acknowledged.

References

[1] C. Grinand, D. Arrouays, B. Laroche and M. P. Martin, “Extrapolating Regional Soil Landscapes from an Existing Soil Map: Sampling Intensity, Validation Procedures and Integraton of Spatial Context,” Geoderma, vol. 143, pp. 180-190, 2008.

[2] Central Pollution Control Board, “Manual On Sampling, Analysis and Characterisation of Hazardous Wastes,” Ministry of Environment & Forests, Govt. of India, New Delhi, 2001.

[3] Z. Stojanovic and S. Markovic, “Determination of Particle Size Distribution by Laser Diffraction,” Technics-New Materials, vol. 21, pp. 11-20, 2012.

[4] M. Ryzak, A. Bieganowski and R. Walczak, “Application of Laser Diffraction Method for Determination of Particle Size Distribution of Grey-rown Podzolic Soil,” RES. AGR. ENG., vol. 53, no. 1, pp. 34-38, 2007.

[5] “Technical Report - Sampling,” Sellafield Ltd Technical Directorate.

[6] A. Hart, “Effect of Particle Size on Detergent Powders Flowability and Tabletability,” J Chem Eng Process Technol, vol. 6, no. 1, 2015.

[7] C. Servais, R. Jones and I. Roberts, “The Influence of Particle Size Distribution on the processing of Food,” Journal of Food Engineering, vol. 51, pp. 201-208, 2002.

[8] Z. Sun, N. Ya, R. C. Adams and F. S. Fang, “Particle Size Specifications for Solid Oral Dosage Forms: A Regulatory Perspective,” American Pharmaceutical Review, vol. 13, no. 4, 2010.

[9] N. Leyva and M. P. Mullarney, “Modeling Pharmaceutical Powder- Flow Performance Using Particle - Size Distribution data,” Pharmaceutical Technology, vol. 33, no. 3, 2009.

[10] D Majersky AllDeco, “REMOVAL AND SOLIDIFICATION OF THE HIGH CONTAMINATED,” May 2004.

[11] C. M. Keck, “Cyclosporine nanosuspensions: optimised size characterisation & oral formulations,” Berlin, 2006.

[12] R. G. Knollenberg and R. C. Gallant, “Refractive Index Effects on Particle Size Measurement in Liquid Media by Opticl Extinction,” in Int'l Conf. on Parlicle Detection, Metrology and Control, Arlington, 1990.

[13] A. Sochan, C. Polakowski and G. Lagod, “Impact of Optical Indices on Particle Size Distribution of Activated Sludge Measured by Laser Diffraction Method,” ECOL CHEM ENG, vol. 21, no. 1, pp. 137-145, 2014.

[14] M. Sperazza, J. N. Moore and M. S. Hendrix, “High-Resolution Particle Size Analysis of Naturally Occuring Very Fine-Grained Sediment Through laser Diffractometry,” Journal of Sedimentary Research, vol. 74, no. 5, pp. 736-743, 2004.

[15] J. Gracia-Mesa, F. Delgado-Ramos, M. Munio, E. Hontoria and J. Poyatos, “Comparison of Activated Sludge Technologies by Particle Size Analysis,” Water Air Soil Pollution, vol. 223, pp. 4319-4331, 2012.

Irradiated Sludges

M. O'Leary*[1], C. Johnston[2], G. Tribello[2], J. Kohanoff[2], F. Currell[1]

*Correspondence: moleary05@qub.ac.uk

[1] *Centre for Plasma Physics (Queen's University Belfast, University Road, Belfast, BT9 1NN , UK)*
[2] *Atomistic Simulation Centre (Queen's University Belfast, University Road, Belfast, BT9 1NN, UK)*

Abstract

This project aims to identify production mechanisms of important radiolytic products, especially gaseous products for example molecular hydrogen gas, from Magnox sludges at Sellafield sites. We will use the Q14 irradiation platform, in Queen's University Belfast, to irradiate sludge mimics, and then take measurements of the type and amount of different end products, like hydrogen gas, produced by irradiation. These results will then be compared to the predictions of simulations made by the Atomistic Simulation Centre, also at Queen's University Belfast.

Introduction

Sellafield site has one of the largest inventories of nuclear legacy waste in Europe. Sludge makes up a large amount of this waste, the Magnox Sludges are the most common form of sludge. Magnox sludge is the corroded nuclear fuel rod cladding from the early Magnox nuclear reactor; the cladding is made from alloy Magnox AL80[1], which is made mostly magnesium. Most of the sludge is in the Magnox Swarf Storage Silos. During the 1974 miner's strike, the Magnox Power plants, importantly Calder Hall located on the Sellafield site, had more fuel cycled, to make up for power lost from the coal burning plants. The buffer ponds at Calder Hall, where the fuel rods were stored before being moved for reprocessing, were overwhelmed by the increase in the amount of fuel used in such a short amount of time. The legacy of this is in the First Generation Storage Pond (seen in figure 1), the sludge in these ponds will soon be moved to the Sellafield Sludge Packaging Plant (SPP1, in Figure 2)[1]. The major safety issue in these sludges is the build up and retention of gases. Two main ways to produce gas are through radiolytic production of gases and through the corrosion of the fuel rod cladding. This project will investigate the ways that irradiating sludges affects gas produced in them.

In order to investigate the gases produced by the effects of irradiation on sludges: we will irradiate sludge mimics, and measure the quantity and types of gases produced. The irradiations will be done using Q14, a new irradiation platform at Queen's University Belfast (Figure 3). At the heart of Q14 is a mechatronic irradiation control apparatus, called MJOLNIR-2 that builds on the previously developed MJOLNIR; which was developed to be used as an end station for hanging drip irradiation experiments at the Diamond Light Source[2]. MJOLNIR-2 includes an integrated broad band x-ray source, with the capability to do vertical and horizontal irradiations of samples. Primary application of Q14 will be in the domain of nano-medicine, irradiating various nano-particle solutions.

Figure 1 First Generation Storage Pond

Figure 2 SPP1, Under Construction

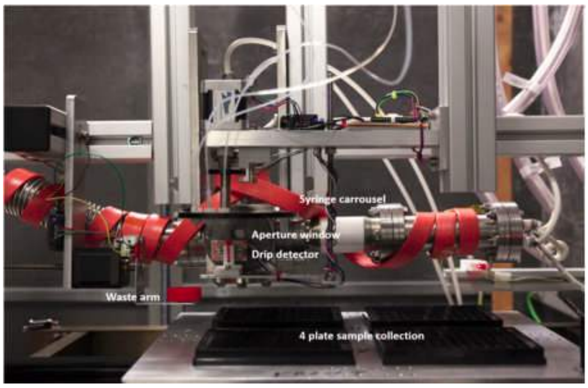

Figure 3 Inside Q14 (MJOLNIR-2)

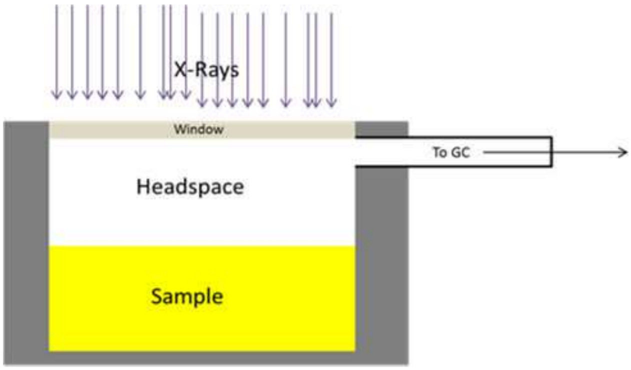

Figure 4 Sample Container Schematic Diagram

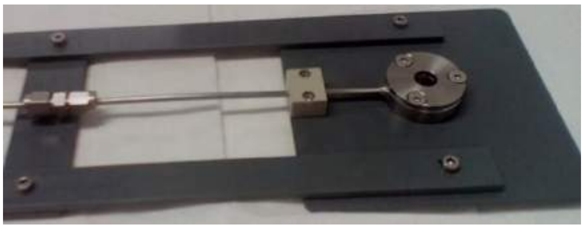

Figure 5 Picture of the Sample Container

Element	Min (% w/w)	Max (% w/w)
Aluminium	0.7	0.9
Beryllium	0.002	0.03
Cadmium	-	0.0002
Calcium	-	0.008
Cerium(1)	-	0.02
Copper	-	0.01
Iron	-	0.006
Lead	-	0.005
Magnesium	base	base
Manganese	-	0.015
Neodymium(1)	-	0.02
Nickel	-	0.005
Silicon	-	0.01
Silver(1)	-	0.01
Thorium(1)+Uranium(1)	-	0.0001
Zinc	-	0.01
Zirconium	-	0.025

Table 1 Composition of Magnox AL80

Methodology Details

The basic methodology, employed in this project, is to: irradiate sludge mimics; then after irradiation to measure the amount of a particular end product produced by irradiating the sample; then these results are compared to the predictions made by simulations, to validate physical reliability of the simulations or to investigate possible radiation induced mechanisms in the sludge.

Initial irradiation will be done on the newly developed Q14 irradiation platform. Q14 consists of MJOLNIR-2, its lead housing and a control station. MJOLNIR-2 has an inbuilt radiation source, an x-ray tube. The x-rays are produced by accelerating electrons at a truncated cylindrical piece copper, onto which pieces of other materials can be placed to produce different x-ray energy spectra. Below and to the side of the target there are beryllium windows, through which the x-rays are emitted.

The samples are held in a sample container made out of stainless steel. The sample container is a cylindrical chamber milled out of stainless steel. The top of the container will have a thin aluminium foil window through which is x-ray transparent, but also keep the container air tight. The side of the sample container will have gas fittings that allow for the removal and sampling of the headspace.

Before the irradiation of sludge mimics can begin the apparatus has to be calibrated, so that the results obtained can be properly interpreted. Chemicals that have well know G values, the amount of a particular end product produced by irradiation for an amount of energy absorbed by the medium, are being used to calibrate the chamber. G value for molecular hydrogen from gamma irradiation is well known for water, across the full range of pH [3]. Sludge mimics that are being used are a mixture of water with Magnesium Hydroxide at the pH of the ponds; then materials of increasing similarity to the sludge in the ponds will be added.

The measurement of the end products involves the use of a variety of methods tailored for each specific end product. For gaseous end products, gas chromatography is used to measure the amount produced. With a thermal conductivity detector (TCD) the concentrations of the different chemicals in a gaseous sample can be measured. By sampling the headspace of the sample container, and then desiccating the headspace sample and then sending the headspace sample through the Gas Chromatograph, the amounts of different gaseous end products can be measured. The Hydrogen gas given of during irradiation can be directly measured by this method; and any gaseous products trapped in the sample can be measured by agitating the sample after taking a headspace sample and then repeating the above method. For aqueous end products, a variety of colorimetric assays in solution are used. Trapping assays are particularly useful in that they remove the particular end product from solution while also producing a noticeable change, acting as a scavenger and an assay.

When, using methods outlined above, the amount of an end product produced is measured; then to get a G-value for the end product one has to know how much energy was absorbed by the sample. Measuring the dose (energy absorbed per unit mass), dosimetry, is important to calculate how much energy was absorbed in the sample. For water many methods of dosimetry have been developed like the Fricke dosimeter, a chemical dosimeter that measures the production of Fe (III) from Fe (II) by irradiation [3]. But it will probable that other methods of dosimetry may have to be developed for sludge mimics, for example applying correction factors to the dose to water derived from Monte Carlo radiation transport simulations.

Discussion and Future Work

Comparison of the results to the predictions of the simulations will help to calibrate those simulations. The mechanisms can be further investigation using scavengers to remove certain intermediary species from solution; thus cutting off certain pathways that were predicted produce a particular end product, then by comparing the yield of that end product with and without the scavenger it will be possible to establish potential pathways for gas production, here using trapping assays will be useful because the amount of the intermediary species produced can also be measured.

Since Q14 was not designed to host experiments with long irradiations that may be necessary later in the project, and may not be capable of the high dose rates that will be needed to get a suitable stimulant of the sludge environment. Then for these longer irradiations and higher dose rates, we are considering the development of a new dedicated radiation source, for this project, will probably be necessary. A design that uses an x-ray source that can perform irradiations in from many angles on a sample is being designed. Work has started on the development of a prototype of this irradiator.

Conclusions

This document outlines the proposed shape of this project over the next few years. The project will mainly look into the possible mechanisms for the production of gaseous end products from the irradiation of sludges, in particular the Magnox sludges. This will be done through the measurement of yields of a variety of end products produced in sludge mimics when they are irradiated; then comparing these results to the predictions of simulations.

Acknowledgements

Thanks to the Mechanical workshop for their help in the construction of our experimental apparatus. Also thanks to Martyn Barnes, of Sellafield Ltd, and Robin Orr, of NNL, our industrial supervisors. Thanks to Hannah Watson for the photo of Q14.

References

[1] http://www.sellafieldsites.com

[2] C Polin et al. Rev. Sci. Instrum. 86 035106 (2015)

[3] JWT Spinks, RW Woods, An Introduction to Radiation Chemistry, John Wiley and Sons, New York, 1990

Determination of Hydrogen Production from Legacy Fuel Storage Pond Sludges through Molecular Modelling

Conrad Johnston*[1], Gareth Tribello[1], Jorge Kohanoff[1], and Martyn Barnes[2]

*Correspondence: cjohnston859@qub.ac.uk

[1] Atomistic Simulation Centre, Queen's University Belfast, Belfast, BT7 1NN, UK
[2] Sellafield Ltd, Birchwood Park Avenue, Warrington Cheshire WA3 6GR, UK

Abstract

The First Generation Magnox Storage Pond (FGMSP) represents one of the highest priority targets for risk reduction at the Sellafield Site. This legacy pond has accumulated a deep layer of sludge over many years, formed primarily from corroding Magnox alloy, but also from windblown debris and decaying organic matter. This sludge is of complex and uncertain composition. Additionally it contains dissolved fission products where cladding has failed and split, or even fragments of spent fuel where cladding has corroded entirely. The production of methane and hydrogen gas complicates the future handling and disposal of this sludge. The focus of the modelling project will be on the radiolytic route to hydrogen production through the study of a water-brucite-hydrocarbon system. By studying a simple model system we will develop an understanding of the underlying chemical reactions. Simulations will be carried out using both classical and quantum, ab initio mechanical molecular dynamics.

Introduction

The sludges found in the First Generation Magnox Storage Pond are essentially the mineral brucite ($Mg(OH)_2$), formed as a corrosion product by reaction of the magnesium in the Magnox alloy with water over many years. The sludge also includes a complex cocktail of contaminants in the form of dissolved fission products and fragments of spent fuel from fuel elements where corrosion has led to cladding failure. Hydrogen gas is formed by the reaction of water with magnesium, by radiolysis of water, and speculatively by a thermal or a catalytic route. Reliable estimates for hydrogen generation are required to underpin the safety case and design for future sludge disposal. Presently, most of the hydrogen produced in the FGMSP can be attributed to the reaction of the magnesium-based Magnox alloy with water, with the radiolysis of water suspected to be a minor secondary route arising due to the high radiation flux from fission products dispersed throughout the sludge. Screening of the sludge as it is transferred to Sludge Packing Plant 1 will remove large solids, effectively removing the corrosion route for hydrogen production and leaving only the radiolysis route, and a postulated catalytic route.

This research will attempt to give quantitative estimates for hydrogen production through the use of multi-scale atomistic modelling. Colleagues will also be irradiating corroded Magnox sludge samples using a new in-house x-ray platform.

Methodology Details

The basis of the modelling project will be the study of a water-brucite-hydrocarbon system. By studying a simple model system we will develop an understanding of the underlying chemical reactions. Simulations will be carried out using both classical and quantum mechanical molecular dynamics using the CP2K package. To date, a brucite bulk system has been modelled. Later, we will increase the complexity by including water and hydrocarbon species to better represent Magnox sludge. Initial work was undertaken to benchmark the ab initio methods and approximations that would be utilised. The model brucite solid system was prepared and relaxed, and replicating the method of Smyth and Kohanoff[1], the effect of incident irradiation was established by vertically attaching an electron to the system. Later, in a similar way, an electron was removed to create an electron hole. The additional electron and the electron hole are representative of electronic defects that arise as a consequence of the low energy secondary electrons that occur in material following a radiation event. The electronic structure of these systems was examined to observe where the excess electron or electron hole localised. The systems were then further relaxed with these defects. Finite temperature ab initio molecular dynamics will be carried out with the bulk model and the two types of electronic defect.

To better explore the feasible chemical reactions, metadynamics simulations will be used to sample the free energy surface of the bulk system. This will help to identify reaction coordinates in an unbiased way. The effect of electronic defects on the energy barriers for these candidate reactions will then be estimated.

Later work will examine the effect of the interaction of water with the surface of the brucite, again looking at electron localisation and free energy barriers to bond breaking. The effect of the surface on hydroxyl radical formation and stability is suspected to be important and so later studies will introduce these radicals with their conjugate hydrogen radicals. Other products known to form from bulk water irradiation will need to be examined, such as hydrated electrons, hydronium ions and oxygen radicals.[2,3,4] A catalytic route may exist for hydrogen production. It is hoped that suspect metal ions can be identified and the system modified to test the effects of these contaminants when they are embedded in the surface in contact with water.[5]

We will examine the rates for different decomposition pathways and will build up a library of likely chemical processes. We can use this information to examine the long term behavior of larger scale systems by inserting this information into a kinetic Monte Carlo program. More complex systems can be studied by examining how these basic processes are perturbed when metallic surfaces are present.

Discussion

The problem of accounting for hydrogen generation in the absence of a corrosion pathway is complicated by the many routes that may contribute to the process. These processes need to be de-coupled from each other and considered independently.

Direct thermal decomposition of water only occurs at elevated temperatures, in the region of 2000 K+[6] , which are infeasible in sludge. However, in the presence of a metallic surface where adsorption can occur, the barriers to water dissociation are reduced through a catalytic process. The low-temperature water-gas shift reaction is an interesting example of a reaction involving the catalysed dissociation of water molecules[5]. In the reversible reaction scheme, CO oxidised by an oxygen atom, generated from the dissociation of water, forms CO_2 and H_2. As the reaction is exothermic, it is favoured at low temperatures, typically around 150 °C. The kinetics at lower temperatures (sub 100 °C) would be interesting to examine. It is conceivable that some of the metals that catalyse this process would be present in the sludge as contaminants through the decay of fission products from the spent Magnox fuel.

Modelling of temperatures in hotspots around fission product contaminants to be evaluated in the sludge could be performed, indicating if temperatures were high enough for a direct catalytic mechanism to occur.

If one considers a purely radiolytic route to hydrogen production, some surface effect still is likely to play a role. The production of hydrogen from plutonium dioxide surfaces can be considered a related problem. Sims, Webb, Brown, Morris and Taylor found that a recombination route reduced radiolysis yields of hydrogen from water adsorbed in monolayers closest to a plutonium dioxide surface, even below what would be expected from bulk water radiolysis[3] An opposite result is reported for oxides of cesium and zirconium, where greatly elevated yields for monolayers nearest the surface were observed.[7] It is clear that adsorbed water behaves vary differently than bulk water under radiolysis and needs close investigation.

The radiochemistry of water is a rich and complex subject. Many different reactions compete simultaneously, involving a range of species, including atoms, ions and radicals of H, H_2O, O_2, OH, H_2O_2 and aqueous electrons. Ershov and Gordeev identified 32 such reactions for their kinetic model.[4] The interactions between these species and a brucite surface will be a subject of particular interest over the course of this work.

Conclusions and Future Work

The problem of hydrogen generation from corroded Magnox sludges is a rich subject with many factors affecting the underlying processes. These processes need to be identified at the most fundamental level before their interactions within the system can be explored.

Acknowledgments

The authors thank the EPSRC for providing this studentship for this project. Thanks goes to the DISTINCTIVE for providing a stimulating network for discussion, and to Sellafield Ltd. and National Nuclear Laboratory for their support and technical advice.

References

[1] Smyth, M., Kohanoff, J., 2012. Excess electron interactions with solvated DNA nucleotides: Strand breaks possible at room temperature. Journal of the American Chemical Society 134, 9122–9125.

[2] Hart, E.J., 1970. The hydrated electron / (by) Edwin J. Hart, Michael Anbar. Wiley-Interscience, Chichester

[3] Sims, H.E., Webb, K.J., Brown, J., Morris, D., Taylor, R.J., 2013. Hydrogen yields from water on the surface of plutonium dioxide. Journal of Nuclear Materials 437, 359–364.

[4] Ershov, B.G., Gordeev, A.V., 2008. A model for radiolysis of water and aqueous solutions of H2, H2O2 and O2. Radiation Physics and Chemistry 77, 928–935.

[5] Phatak, A.A., Delgass, W.N., Ribeiro, F.H., Schneider, W.F., 2009. Density Functional Theory Comparison of Water Dissociation Steps on Cu, Au, Ni, Pd, and Pt. J. Phys. Chem. C 113, 7269–7276.

[6] Ohya, H., Yatabe, M., Aihara, M., Negishi, Y., Takeuchi, T., 2002. Feasibility of hydrogen production above 2500 K by direct thermal decomposition reaction in membrane reactor using solar energy. International Journal of Hydrogen Energy 27, 369–376.

[7] LaVerne, J.A., Tandon, L., 2002. H2 production in the radiolysis of water on CeO2 and ZrO2. Journal of Physical Chemistry B 106, 380–386. doi:10.1021/jp013098s

Investigation of the thermal treatment of waste plutonium contaminated materials (PCM)

L.Boast* [1], R.J.Hand[1], and N.C.Hyatt[1]

*Correspondence: LBOAST1@sheffield.ac.uk

[1] *Immobilisation Science Laboratory, Department of Materials Science and Engineering, the University of Sheffield*

Abstract

Key drivers for the application of thermal treatment processes include the reduced volume, improved passive safety, and superior long term stability, of the vitrified wasteform products. These advantages have led to a renewed interest in thermally treating various UK ILW streams. To support the increased investment in thermal treatment technologies a fundamental understanding of the processes and the impact of waste inventory needs to be established. The research described in this report aims to provide the evidence necessary to support a major investment in thermal treatment of plutonium contaminated materials. The report describes the use of laboratory scale waste simulants to develop an understanding of the waste and matrix interactions during thermal treatment of PCM waste. The report includes the thermal treatment process, characterisation and long term performance of the vitrified product.

Introduction

PCM waste is a subcategory of intermediate level waste, which is generated as a result of the handling of plutonium during nuclear fuel processing and other related activities. The amount of PCM waste in the UK is estimated to be over 31,000m³, with 70% of PCM waste stored at the Sellafield site [1]. The PCM waste, which can incorporate masonry, metal, organic or a mixture of each, are double bagged in heat sealed PVC linings before being stored in 200 L mild steel drums. The heterogeneous nature of the waste material presents a considerable materials science and engineering challenge for PCM waste immobilisation. A process is already in place at the Sellafield site for the treatment of some categories of PCM waste, centred on the Waste Treatment Centre (WTC). The general method of the WTC is compression of the 200 L drums containing the PCM waste, and the resulting crushed drums are grouted in cement and stored within 500 L steel storage containers [2]. There are however concerns regarding the reliability of the supercompaction and subsequent grouting process to deliver a consistent wasteform suitable for long-term storage and eventual disposal [3].

Thermal treatment is the main alternative technology available for the treatment of PCM waste. Key drivers for the application of thermal treatment processes include the reduced volume, improved passive safety, and superior long term stability, of the vitrified wasteform products. Proof of concept studies by the University of Sheffield, have demonstrated PCM compatibility with currently available thermal treatment technology platforms [4]. In this study [4] the authors successfully vitrified simulant PCM waste using ground granulated blast furnace slag (GGBS) which enabled a mixed slag/metal wasteform for high metal waste feeds. However, GGBS has a wide range of applications, combined with low levels of production in the steel industry, means that GGBS is a poor economic choice for the application of nuclear waste vitrification.

The study described in this report uses the same process and wasteform considerations, from the previous study [4] but with the use of recycled soda lime silica (SLS) glass cullet as the glass forming additive. Providing SLS glass cullet meets the required process and wasteform specifications for a vitrified wasteform, SLS will be more advantageous as a choice of additive based upon its unlimited availability. The project will determine the effectiveness of using SLS glass cullet as a glass forming additive.

More specifically the aims of the project are to develop an understanding of waste / matrix interactions during thermal treatment of PCM wastes. The project will contribute to accelerating the acquisition of knowledge and experience required to support NDA in deploying thermal technologies as a national asset for ILW treatment.

Methodology Details

Using Ce as a Pu surrogate laboratory scale experiments using simulant PCM drum mock ups, as shown in figure 1-4, have been performed. The PCM mock up drums include PVC waste, metal waste, mixed waste and masonry waste ensuring a complete understanding of the various wastes streams expected from the PCM waste drums found at the Sellafield site.

Experimental Procedures

The compositions of the four PCM waste simulants are given in table 1.

Waste Type (wt %)	PVC Waste	Metal Waste	Masonry Waste	Mixed Waste
Mild Steel	44.44	20.00	30.00	30.00
PVC	55.56	10.00	10.00	10.00
Metal items	0	70.00	0	15.00
Masonry	0	0	60.00	40.00
Glass	0	0	0	5.00
Total	100.00	100.00	100.00	100.00

Table 1: Representative PCM waste simulants.

Fig1: PVC waste Simulant

Fig2: Metal waste simulant

Fig3: Masonry waste simulant

Fig4: Mixed waste simulant

Fig5: Simulant waste with addition of glass frit at 1:1 wt ratio

The upper estimated PuO_2 content of PCM wastes is the molar equivalent of 0.207 wt% CeO_2 [5]. All melts were doped with 1.043 wt% CeO_2 as a PuO_2 surrogate to allow for conservatism and to ensure detection during analytical studies post processing. Based upon the need for an oxidising material for waste streams with a higher metal proportion to aid vitrification, a recycled glass frit (soda-lime-silica) was selected as an additive at a ratio of 1:1 (waste to additive) for all waste streams. Crucibles shown in figure 5, containing simulant waste and additive were heated overnight at 2 ˚C min to 1100˚ C; crucibles were subsequently transferred to a gas-fired furnace, which had been preheated to 1100°C, then ramped to 1450°C over a period of 90 min. The crucibles were held at 1450˚C for 4 hours before being removed to cool in air to room temperature. It should be noted from figure 5 that a graphite clay crucible was required for the higher weight percentage metal waste feed. This was due to the corrosive nature of the molten metal with alumina crucibles.

Results and Discussion

Melting behaviour showed no violent reactions between the waste simulant and glass additive. As expected a substantial metallic fraction resulted for the vitrified metal type, as shown in figure 6(b).

Fig6: Showing vitrified simulant PCM drum mock ups (a) PVC waste, (b) metal waste, (c) masonry waste, and (d) mixed waste

Wt %	PVC	Masonry	Metal	Mix
SiO_2	37.93	54.85	69.87	54.23
MgO	0.86	0.86	1.17	0.93
Al_2O_3	16.51	11.70	7.6	9.29
CaO	5.46	7.07	7.43	6.9
Na_2O	6.02	6.81	7.72	6.53
Fe_2O_3	30.38	17.65	0.82	18.13
CeO_2	0.42	0.33	0.60	0.43
Other	2.2	1.25	3.98	3.08
Sum	99.31	99.53	98.59	99.09

Table 2 Composition of wasteform (wt%) components via XRF

XRF determined composition of major elements in the glass waste form is shown in table 2. PuO_2 (CeO_2 surrogate) from the PCM is physically and chemically immobilised in the resulting materials, i.e. no residual PuO_2 (CeO_2) remains after processing. All of the analysis indicated that Ce was incorporated into the oxide phase in all samples. It is known that Pu is more thermodynamically favourable to partition within the slag phase; therefore it may be possible to treat the resultant metallic waste as LLW if sufficient separation of the two phases can be achieved.

The overriding difference in slag fraction composition is the Fe_2O_3 content of the final oxide fraction of the wasteform which can be attributed to the type of crucible used and the resulting redox conditions on the melt. EDS analysis determined no measurable retention of Cl within the slag fraction of the wasteforms. It was therefore concluded that all Cl present in the organic waste was volatilised by the high temperature.

Masonry Waste

XRF and SEM/EDS studies demonstrated the glass wasteform to be composed of a $CaO–Fe_2O_3–Al_2O_3–SiO_2$ glass. XRD studies evidenced an amorphous structure with no undissolved material within the glass matrix.

PVC Waste

The XRD pattern of the vitrified PVC waste stream, Figure 7, showed reflections corresponding to spinel phase $Mg(Fe,Al)_2O_4$ (Magnesioferrite). Diffuse scattering corresponding to the presence of an amorphous component in the form of $CaO-Al_2O_3-SiO_2-Fe_2O_3$ glass. The SEM/EDS image in figure 8 show the dendritic crystal structure corresponding to the identified spinel phase.

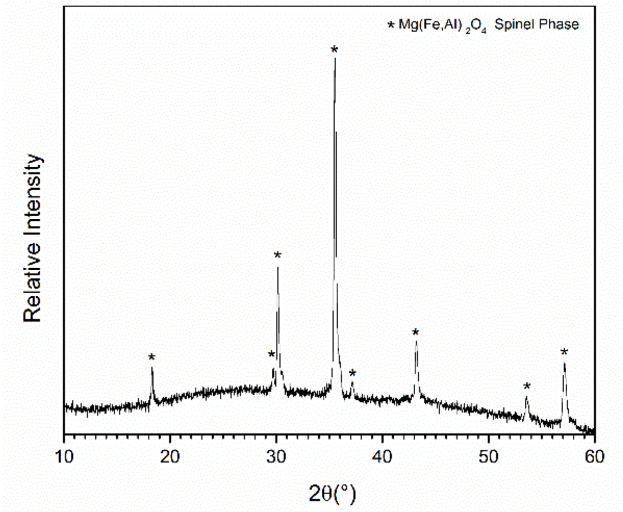

Fig7: X-ray powder diffraction pattern showing identified reflections corresponding $Mg(Fe,Al)_2O_4$ spinel phase, together with diffuse scattering corresponding to the presence of an amorphous component, in the slag produced by vitrification of PVC waste type.

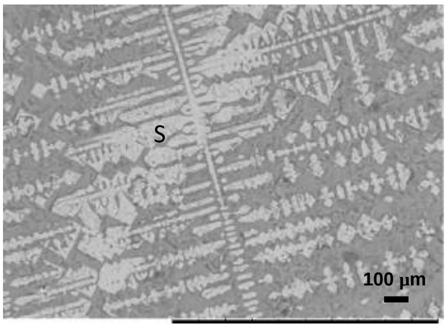

Fig8: BSE image showing microstructure of slag produced by vitrification of PVC waste type. S corresponds to identified spinel phase

Metal Waste

The XRD pattern of the vitrified metal waste stream showed diffuse scattering corresponding to an amorphous component in the form of $CaO-Al_2O_3-SiO_2-Fe_2O_3$ glass. SEM / EDX analysis showed graphite inclusions were present from the corrosion of the crucible.

Mixed Waste

The XRD pattern of vitrified mixed waste stream, Figure 9, showed identified reflections corresponding to crystalline $Ca(Si,Al)_2O_6$ - diopside, and $(Cr,Fe,Al)_2O_4$ - spinel phases. Diffuse scattering corresponding to the presence of an amorphous component in the form of $CaO–Fe_2O_3–Al_2O_3–SiO_2$ glass was also observed. SEM / EDX analysis showed a dendritic structure (spinel phase) and diopside crystal phase within the glass.

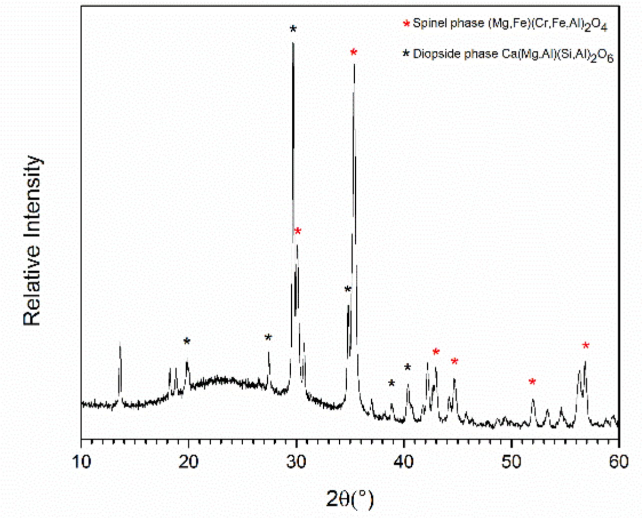

Fig9: X-ray powder diffraction pattern showing identified reflections corresponding $(Mg,Fe)(Cr,Fe,Al)_2O_4$ spinel phase (Red Stars) phases and $Ca(Si,Al)_2O_6$ diopside (black stars), together with diffuse scattering corresponding to the presence of an amorphous component, in the slag produced by vitrification of mix waste type.

Conclusions

CeO_2 as a PuO_2 surrogate from PCM wastes is physically and chemically immobilised in the vitrified SLS products, i.e. no residual CeO_2 remains after processing. All of the analysis indicated that Ce was incorporated into the oxide phase in all samples. The investigation has demonstrated a strong case for vitrifying PCM waste based upon analytical studies showing a high quality glass produced for waste immobilisation with a substantial volume reduction resulting in lower disposal costs.

Further Work

Long term Durability tests

The project has also developed an understanding of the vitrified waste product in terms of stability with respect to generic ILW disposal concepts, through accelerated dissolution experiments. Figure 10 shows the controlled atmosphere experiment designed during the project.

Fig 10: Controlled nitrogen atmospheric chamber to avoid carbonation of samples and ensure high PH conditions to simulate the GDF environment.

PCT test of the vitrified waste types described in the project will be performed for the next 12 months. PCT is used to evaluate the chemical durability of a glass waste form by measuring the concentrations of the chemical elements released to a test solution, in this experiment the solution is a saturated $Ca(OH)_2$ solution to simulate the conditions expected within a GDF. Initial results from the first 48 days of testing show that the materials produced in this investigation are broadly comparable, in terms of durability, to other simulant UK ILW glass products considered potentially suitable for geological disposal. Therefore the project has provided strong evidence that the glass wasteforms meet the defined waste acceptance criteria (WAC).

Ce XANES analysis

Using the light source at Brookhaven National Lab, X-ray absorption spectroscopy has been used to investigate the elemental speciation of Ce within the slag samples. Ce^{3+} was determined as the bulk speciation, which is comparable to the known speciation of Pu^{3+} in silicate glasses at high temperatures. The upper analysed Ce_2O_3 concentration in the slag is well below the solubility limits of Pu_2O_3 in borosilicate glasses. This provides strong evidence the glass developed here would incorporate Pu at the concentration expected from the PCM waste.

Future Work

The author has recently started a PhD industrial secondment with Kurion inc. who has teamed with the UK's National Nuclear Laboratory (NNL) to install a GeoMelt In-Container Vitrification (ICV) system in the Central Lab at Sellafield. The tasks during the three months are to provide operational support and qualify as a Kurion Geomelt operator and support commissioning of the system. The work will also result in the development of glass formulations for a number of melt trials, and to provide a plan for future research utilising the GeoMelt system. The work undertaken on the placement will be used as part of the student's thesis.

Acknowledgements

This work was funded in part by EPSRC under grant EP/L014041/1 - Decommissioning, immobilisation and storage solutions for nuclear waste inventories (DISTINCTIVE). Use of the National Synchrotron Light Source, Brookhaven National Laboratory, was supported by the U.S. Department of Energy, Office of Science, Office of Basic Energy Sciences, under Contract No. DE-AC02-98CH10886. This work was performed in the MIDAS Facility at The University of Sheffield, which was established with support from the Department for Energy and Climate Change. LB is grateful to NDA for provision of an iCASE studentship. NCH is grateful to the Royal Academy of Engineering and the Nuclear Decommissioning Authority for funding.

References

[1] "Treatment of Plutonium Contaminated Materials at Sellafield", Stakeholder Consultation Briefing Note - http://sellafieldsites.com/wp-content/uploads/2012/08/PCM-brochure-low-res.pdf

[2] "Plutonium Contaminated Materials (PCM) – A review of the status at Sellafield, Dounreay, Harwell and Aldermaston"- http://www.hse.gov.uk/aboutus/meetings/iacs/nusac/131005/p15.pdf

[3] "The management of higher activity radioactive waste on nuclear licensed sites" Scottish Environment Protection Agency to nuclear licensees – Nov (2011)

[4] "Thermal treatment of simulant plutonium contaminated materials from the Sellafield site by vitrification in a blast furnace slag" Hyatt N.C., Schwarz R.R., Bingham P.A – (2004) Journal of Nuclear Materials

[5] "Treatment of PCM at Sellafield: BPEO Sellafield" – M.Egan, A. Paulley, G.Towler – 2008 <http://www.sellafieldsites.com/wp-content/uploads/2012/08/PCM-BPEO-Study-QRS-1372A-1-Version-2_0.pdf>.

Theme 3 – Silo Ponds and Legacy Wastes
DISTINCTIVE 2nd Annual Meeting
Bristol, UK
19th – 20th April 2016

A quantum chemical study: Sr^{2+} ion adsorption on the brucite (0001) surface

E. Makkos*[1], A. Kerridge[2], and N. Kaltsoyannis*[3]

*Correspondence: eszter.makkos.13@ucl.ac.uk
nikolas.kaltsoyannis@manchester.ac.uk

[1] *Department of Chemistry (University College London, London, WC1H 0AJ, UK)*
[2] *Department of Chemistry (Lancaster University, Bailrigg, Lancaster LA1 4YB, UK)*
[3] *School of Chemistry (The University of Manchester, Manchester, M13 9PL, UK)*

Abstract

A quantum chemical model of the brucite (0001) surface is developed using the periodic electrostatic embedded cluster method (PEECM) and used to investigate the adsorption of Sr^{2+} hydroxide and hydrate complexes on the surface. The PEECM model is compared to another well established method, periodic density functional theory (periodic DFT), by calculating Sr^{2+} dihydroxide complexes adsorbed on the bare brucite surface. Relative energies between the different complexes are found to be very similar with the different approaches. Explicit water molecules, whose geometries are based on previous molecular dynamic studies, are introduced above the brucite surface with the PEECM model, allowing the interaction of the Sr^{2+} ion with the hydrated surface to be investigated. Several possible complexes are identified with different Sr-surface distances.

Introduction

In the first generation of British civil nuclear power reactors a Mg-Al based alloy, called Magnox, was used as a fuel cladding. The waste was generated in the 1950s onwards and is stored in legacy storage ponds around the UK, such as the one in Sellafield. The ponds are filled with water to act as a radioactivity shield and as a cooling medium and are open to the air. Their content is heterogeneous in nature. The aqueous phase contains a range of soluble radioisotopes, from which the biggest contributors to activity are ^{137}Cs and ^{90}Sr. In addition there is a significant amount of sludge present in the ponds, consisting of a mixture of solid materials from fuel and cladding corrosion (e.g. uranium metal, brucite, Magnox).[1]

The decommissioning of the legacy ponds is an ongoing process, but is time-consuming and costly, with significant uncertainties in the program. The main issue is the uncertain volume and chemical composition of the waste, e.g. the liquid effluent feed to the planned removal process (Site Ion eXchange Plant, SIXEP) which is sensitive to active and inactive cation concentration.[2] There is only limited access to real samples and monitoring the condition in-situ is difficult due to the radiation hazard posed by the ponds. Chemical models can play a crucial role in understanding the conditions in the ponds and in the improvement of the treatment process. Modelling can help to better understand the plant behaviour and predict feed composition may significantly reduce the costs.

We use quantum chemical techniques based on density functional theory (DFT) to gain a better understanding of the conditions in the ponds by studying the interaction of fission-generated strontium, as one of the most abundant radioactive ions in the ponds, with the (0001) surface of brucite, which is the main corrosion product of the Magnox cladding. For this particular problem we employ the periodic electrostatic embedded cluster method (PEECM) which allows us to describe isolated adsorption sites on surfaces. More importantly, it is uniquely capable of dealing with charged systems and introducing higher quality basis sets in the calculations, if necessary, is relatively straightforward. [3]

Computational Details

PEECM model

All calculations were performed with version 6.6 of the TURBOMOLE program using resolution-of-the-identity DFT. Results were visualised with the MOLDRAW chemical graphical software. The TPSS exchange-correlation functional, which employs the meta-generalised gradient approximation (meta-GGA), was used because it was shown to be good for describing Sr^{2+} complexes in previous studies.[4] The brucite surface was considered as a slab containing 1 or 2 layers of $Mg(OH)_2$ and modelled using the PEECM. In this approach, a finite sized cluster of brucite was treated quantum chemically and embedded in a 2D infinite array of point charges (PCs) (aperiodic in the z direction). The cluster was formed from a 6x6 unit cell ($Mg_{36}(OH)_{72}$) per layer of brucite. Experimental cell parameters, obtained via neutron diffraction measurements by Catti *et al.* [5], were used to define both the initial geometry for the quantum mechanical (QM) cluster and the positions of the PCs in the infinite two dimensional array: the *a* and *b* lattice parameters of the hexagonal unit cell were 3.15 Å, and the interlayer distance *c* was 4.77 Å. The following natural charges were used for the periodic PCs: Mg = +1.78, O = -1.33 and H = +0.44 a.u.

Due to the large size of the QM cluster, the def2-SVP basis sets of polarised double-ζ quality were used for all atoms represented in the surface cluster (Mg, O, H). Partial optimisations, in which the boundary atoms of the cluster were held fixed and the inner part allowed to fully relax (see Figure 1), were carried out in the gas phase with the m4 integration grid and the default convergence criteria: SCF energy: 10^{-6}, structural energy: 10^{-6} and energy gradient: 10^{-3}.

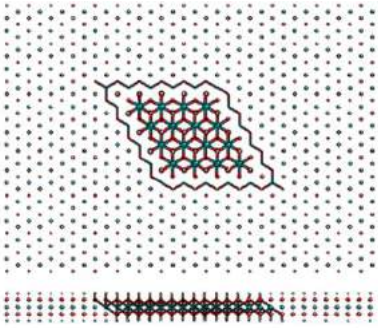

Figure 1 Illustration of the top and side view of the single layer PEECM model. The point charges are represented as balls around the QM cluster, the fixed boundary atoms as wires and the inner part of the cluster as balls and sticks. (Mg=green, O=red, H=grey)

Periodic DFT model

We chose the CRYSTAL14 code to model the brucite (0001) surface with periodic DFT, since this program allows us to use atom-centred basis sets, which are used in TURBOMOLE. We used the PBE exchange-correlation functional with this method as it is one of the most commonly accepted GGA functionals in solid state chemistry. Polarised triple-ζ basis sets derived specifically for solid state calculations were used for the surface atoms. In the case of the Sr atom, a lower quality basis set was used for geometry optimisations, whilst single point energies were calculated using doubly polarised triple-ζ basis sets for the valence electrons with the multi-electron fit quasi-pseudopotential on the core 1s-3d orbitals. We created a series of $Mg(OH)_2$ slabs with different supercell sizes and with 1, 2 and 3 layers of brucite and optimised the internal coordinates for each using a shrinking factor of 4 along with the convergence criteria: SCF energy: 10^{-7} and structural energy: 10^{-7}. We used the 0D 'MOLECULE' option of CRYSTAL14 for the single point energies of the solvated $Sr(OH)_2$ complexes. To make comparison between the two different methods possible, we used the PBE functional with the same computational parameters for the PEECM calculations. Although def2-SVP basis sets were used for the geometry optimisation, single point energies were obtained after geometry optimisation with the above defined CRYSTAL14 basis functions.

Results and Discussion

A comparison study: adsorption of $Sr(OH)_2+4H_2O_4$ on brucite

By comparing the adsorption energies of $Sr(OH)_2$ complexes onto brucite calculated with the two different methods, we aim to show that the embedded cluster model, which we developed with the TURBOMOLE code, gives similar adsorption energies for neutral systems as a well-established periodic DFT code (CRYSTAL14). The initial structure of the $Sr(OH)_2+4H_2O$ complex is based on the most stable Sr^{2+} dihydroxide coordination with two solvation shells from our previous study[6]. We searched for the most stable structure by generating three more initial geometries via random rotation of the original molecule and optimised their geometry on the brucite surface, represented by a single layer 5x5 supercell slab in CRYSTAL (see Figure 2).

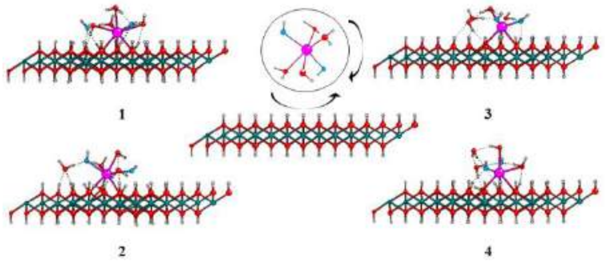

Figure 2 Middle: The ball and stick representation of the 5x5 supercell and the original $Sr(OH)_2$ complex with its complete 1st coordination shell. Side: 1,2,3,4 are the optimised structures of the adsorbed complexes. (Mg=green, O=red, H=grey, Sr=magenta, O in the coordinated OH- groups=blue)

These optimised geometries were used as starting structures in TURBOMOLE, where they were reoptimised with the PEECM model, placing each complex at the same position on the QM cluster. We compared the final geometries of the complexes and calculated the adsorption energies, shown in Table 1, with the following equation:

$$E_{ads} = E_{complex} - \left(E_{brucite} + E_{Sr(OH)_2+4H_2O}\right) \quad (1)$$

$E_{complex}$ is the SCF energy of the adsorbed complex and the surface, while $E_{brucite}$ is the energy of the bare brucite surface, and $E_{Sr(OH)_2+4H_2O}$ is the single point energy of the solvated complex.

E_{ads} (kJ/mol)

method		PEECM	Periodic DFT	
structure	**CN**	***E***	***E***	**E_{diff} (%)**
1	8	-422.7	-431.7	2.1
2	7	-393.8	-402.3	2.1
3	6	-437.2	-444.4	1.6
4	6	-401.1	-416.1	3.6

Table 1 Adsorption energies (E_{ads}) of four $Sr(OH)_2$+$4H_2O$ complexes calculated with PEECM and Periodic DFT. E_{diff} is the percentage energy difference between the two methods. CN=coordination number

Δ E_{ads} (kJ/mol)

	PEECM			Periodic DFT
structure	**single**	**+PC layer**	**double**	**single**
1	14.5	14.2	14.9	12.7
2	43.4	49.0	47.8	42.1
3	0.0	0.0	0.0	0.0
4	36.1	34.0	36.2	28.2

Table 2 Relative adsorption energies (Δ E_{ads}), calculated by comparing the results of structures 1, 2 and 4 to the adsorption energy of the most stable structure (3). Energies are calculated with the two different methods and three different surface representations for the PEECM: 1 layer of brucite (single), 2 layers with an extra PC layer under the cluster (+PC layer) and with a second cluster (double).

Based on the results in Table 1, there is excellent agreement between the adsorption energies obtained from the two methods: the energy difference is between 1.6 and 3.6% in each case. Structure **3** is predicted to be the most stable and the relative adsorption energies, shown in Table 2, are calculated by comparing the energies of the other structures to this one. The differences between the calculated relative energies with periodic DFT and the PEECM model for the single layer surface representation are less than 2 kJ/mol, except structure **4**, where the geometry of the optimised complexes slightly differs between the two methods. Although we calculated the basis set superposition error for the adsorption energies in TURBOMOLE, only slight differences were found, since this type of error is largely cancelled out in the definition of the relative adsorption energy.

When we consider a two layered slab in PEECM either via an extra PC layer (+PC layer) or a second 6x6 cluster (double) underneath the first, the relative adsorption energies are very similar to the single layer results(see Table 2). Furthermore, according to the preliminary results of a cell size study in CRYSTAL, changing the surface cell size has negligible effect on the adsorption energies and including a second layer in the slab causes similarly small (~5 kJ/mol) energy differences, as in the case of the PEECM results. This study suggests that including a 2nd layer in the surface model has only a small effect on the relatively weak adsorption of the hydrated complexes, and the size of the quantum chemically treated cluster is sufficient for the studied systems.

Hydration of the brucite surface

Since the actual sludge is an aqueous environment, our ultimate goal is to study the absorption behaviour of the Sr^{2+} ion on the brucite surface in the presence of water. To introduce a water monolayer in the PEECM model, we used two starting geometries (A and C in Figure 3) derived from molecular dynamics studies of Sakuma *et al.*[7] 36 explicit water molecules were placed above the surface and the point charge region was extended with water equivalents. The water molecules at the QM cluster boundaries were fixed and the remaining molecules were free to relax. Similar structures were made using 2 water layers, shown in Figure 4 with water structure A.

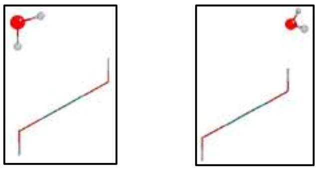

A **C**

Figure 3 A and C positions of water molecules above brucite. In A, the hydrogen of the water molecule is coordinated to the surface oxygen in the down-facing OH group, while in the C coordination there is a hydrogen-bond between the oxygen of the water molecule and the hydrogen of the up-facing OH group.

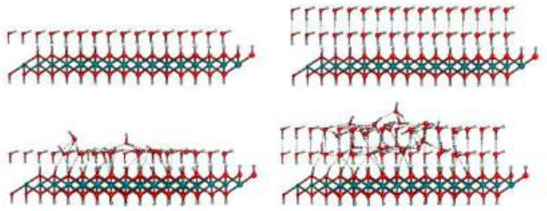

Figure 4 Ball and stick representation of initial (top) and optimised (bottom) geometries of one (left) or two (right) layers of explicit water molecules above the brucite surface in A coordination. (Mg=green, O=red, H=grey)

Adsorption of Sr^{2+} ion on a hydrated brucite surface

We are currently studying the adsorption of the Sr^{2+} ion by using the hydrated surface representations described above and introducing one Sr^{2+} into the systems. To describe the Sr – surface interactions as realistically as possible, we created a theoretical reaction, in which we compared the energy of the adsorbed Sr^{2+} ion with the energy of a solvated one in the bulk solution, i.e. we looked at the propensity of the Sr^{2+} ion to coordinate with the surface rather than remaining in the aqueous phase.We used our previous results regarding the solvated complexes[6] to be able to calculate the energy of this theoretical reaction:

$$E_{ads} = \left(E_{complex} + E_{W24}\right) - \left(E_{hydrated\ layer} + E_{W24_{Sr}}\right) \quad (2)$$

$E_{complex}$ is the SCF energy of the adsorbed complex with the hydrated surface, while E_{W24} is the energy of a 24 water molecule cluster representing the bulk water phase. $E_{hydrated\,layer}$ is the energy of the hydrated brucite surface without the Sr^{2+} ion and $E_{W24_{Sr}}$ is the energy of the solvated Sr^{2+} hydrate complex incorporating its 1st and 2nd solvation shells. Applying equation 2 to Sr^{2+} complexes adsorbed to a surface hydrated with one layer of water resulted in adsorption energies with a magnitude of 100-200 kJ/mol (see Table 3). All systems with one water layer contain a Sr^{2+} ion directly coordinated to three OH groups of the brucite surface. Furthermore, in the case of the two structures derived from the C hydration model, one surface OH group was protonated by a water molecule, resulting in an additional OH group in the water monolayer directly coordinating to the ion. Presumably this extra OH group is responsible for the ~180 kJ/mol energy difference between these structures and the first one.

Hydration model	CN	Structure	E_{ads} (kJ/mol)	$d_{surf\text{-}Sr}$ (Å)
1 water layer				
A	7	$[Sr(OH)_3]^{-}+4H_2O$	-100.9	3.153
C	6	$[Sr(OH)_4]^{2-}+2H_2O$	-284.2	2.709
C	7	$[Sr(OH)_4]^{2-}+3H_2O$	-272.4	2.785
2 water layers				
A	6	$Sr(OH)_2+4H_2O$	-37.2	3.681
A	6	$Sr^{2+}+6H_2O$	-236.5	
C	7	$[Sr(OH)_1]^{+}+6H_2O$	-461.2	4.265

Table 3 Structural properties (CN=coordination number, dsurf=Sr-surface distance) of the optimised Sr^{2+} complexes on a brucite surface with 1 and 2 layers of water along with corresponding adsorption energies calculated using equation 2.

With two layers of water molecules above the surface, we found that the Sr^{2+} ion is more likely to move away from the surface and coordinate with the first monolayer of water rather than directly with the surface. Among the results, which are shown in the second half of Table 3, only the first structure, $Sr(OH)_2+4H_2O$, is directly coordinated to the brucite surface, and it has a significantly smaller adsorption energy than the other structures. In the third system an extra OH^- ion appears due to the protonation of a surface OH group, as described above, which presumably leads to the higher E_{ads} energy.

Although this investigation is still ongoing, these results are compatible with the previously described three possible coordination regimes of Sr^{2+} ion: the inner shell, i.e. direct coordination with Sr-surface distances less than 4 Å, the outer shell (4 < d < 6 Å) where the complex is coordinated to a monolayer of water on the surface, and the uncoordinated regime with d>6 Å.[8]

Conclusions and Future Work

In the first part of this contribution, through a comparison with periodic DFT, we demonstrated that the PEECM model we developed sufficiently reflects the qualities of the brucite surface to be able to describe the surface complexation of Sr^{2+} dihydroxide. We then introduced our hydrated surface model and moved on to the adsorption of the Sr^{2+} ion with this more realistic surface representation. Although this is an ongoing investigation, we found two distinguishable coordination regimes based on the Sr-surface distance and, so far, we have found that the outer shell coordination is more favourable. Furthermore, in the most stable cases, protonation of a surface OH group was predicted which is a phenomena which needs to be studied in more details. We are also investigating systems containing solvated OH^- ions in the water layers and the adsorption of other ions, such as Cs^+.

Acknowledgements

The authors are grateful to the Nuclear Decommissioning Authority and UCL for financial support for a PhD studentship to EM. AK thanks the EPSRC for the award of a career acceleration fellowship (grant EP/J002208/1). The authors would like to acknowledge the use of the ARCHER UK National Supercomputing Service (http://www.archer.ac.uk) and the EPSRC UK National Service for Computational Chemistry Software (NSCCS) at Imperial College London in carrying out this work, besides the computing resources of UCL via the Research Computing "Legion" cluster (Legion@UCL) and associated services. They are also grateful to Dr Jonathan Austin from the National Nuclear Laboratory for helpful discussions.

References

[1] R. Gregson, D. T. Goddard, M. J. Sarsfield and R. J. Taylor*, J. Nucl. Mater.*, **412** (2011) 145

[2] S. Owens, M. Higgins-Bos, M. Bankhead, J. Austin, *NNL Science*, **3** (2015) 4

[3] A. M. Burow, M. Sierka, J. Döbler and J. Sauer, *J. Chem. Phys.*, **130** (2009) 174710

[4] A. Kerridge and N. Kaltsoyannis, *Chem. Eur. J.* **17**, (2011) 5060

[5] M. Catti, G. Ferraris, S. Hull and A. Pavese, *Phys. Chem. Min.*, **22** (1995) 200

[6] E. Makkos, A. Kerridge, N. Kaltsoyannis, *Dalton Trans.* **44** (2015) 11572

[7] H. Sakuma, T. Tsuchiya, K. Kawamura, and K. Otsuki, *Mol. Simulations*, **30**, (2004) 861

[8] A. Kerridge and N. Kaltsoyannis, Proceedings of the DIAMOND 2010 Conference, (2011)

Theme 4 – Structural Integrity
DISTINCTIVE 2nd Annual Meeting
Bristol, UK
19th – 20th April 2016

3D semantic SLAM/Reconstruction in industrial environment

Cheng Zhao(Henry)*[1], Rustam[1], and Ales[1]

*Correspondence: cxz514@cs.bham.ac.uk

[1] *University of Birmingham (Department of Computer Science,*
Edgbaston, Birmingham, West Midlands, UK, B15 2TT)

Abstract

In order to facilitate planning and execution of remote handing during the object manipulation of robot arm in industrial environment, every object should be 3D reconstruction and 3D pose tracking in real-time. This research summary proposes a dense semantic 3D reconstruction approach. It also made some preliminary tests in office environment because our nuclear industrial dataset is still under way. Using Kinect like camera, the RGB and depth images can be obtained. Objects and scene can be 3D reconstructed as point clouds in real-time based graph optimization. At the same time, each voxel of point cloud can be labeled to different classes like wall, ground, pipe, metal, robot and etc. based on Randomized Decision Forest classification and 3D Conditional Random Field refinement. Finally, all the recognized objects can be convert to CAD models in order to 3D pose tracking and object manipulation.

Introduction

In robotic arm manipulation of Nuclear Industrial, facilitating planning and execution of remote handing is a big challenge. The advanced computational vision techniques can perform to recognize object in 3D point cloud from laser scanner or depth camera, built CAD model for those objects and track 3D poses of moving objects. In order to achieve this, 3D semantic real time reconstruction or SLAM (Simultaneous localization and mapping) is necessary. It means that the industrial objects and scene can be reconstructed as 3D point clouds in real-time, and meanwhile every voxel of point cloud will be labeled to different classes like wall, ground, pipe, metal, robot and etc. After that, all the recognized objects can be convert to CAD models using some emerging algorithm.

My work mainly includes two modules: 3D SLAM module and semantic labeling module. The RGB and depth images can be obtained from Xtion or Kinect sensor. Using RGB and depth information, 3D reconstruction can be performed based on graph optimization. Meanwhile, a classic machine learning method like randomized decision forest or deep learning is used for the 2D images labeling. Then the result will be refined using dense conditional random field. Each 3D point cloud can be assigned a class label, giving a dense semantic reconstruction. Finally, the recognized object can be converted to CAD model, which make 3D pose to be tracked easily.

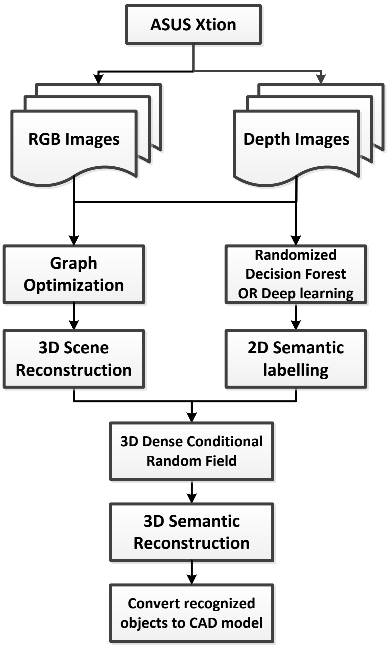

Figure 1 The workflow of the system

Methodology Details

3D SLAM

The concept of Simultaneous Localization and Mapping (SLAM) was firstly proposed by Smith in 1986. The first completed SLAM implementation was done by Annee in 1991. With 30 years progress, with the contributions from so many genius researchers, SLAM had already obtained many significant breakthroughs. The basic theory of SLAM mainly have two branches: Filter and Bundle Adjustment(BA).

1) 1985-2015 Filter

1990, EKF SLAM[1]

2002, FastSLAM[2]

2002, SFIT SLAM[3]

2005, Rao-Blackwellised Particle Filter[4]

2003, Monocular SLAM[5]

2008, EKF SLAM in O(n)[6]

2) 2000-2015 Bundle Adjustment

2000, Bundle adjustment[7]

2006, Graph optimization[8]

2007, PTAM[9]

2008, FrameSLAM[10]

2009, Adaptive relative bundle adjustment[11]

2014, RGB-D SLAM[12]

3) Compare Filter and BA

2012, Visual slam: Why filter?[13]

4) Newest popular SLAM algorithm

2014 LSD SLAM[14]

2015 ORB SLAM[15]

2011 Kinect Fusion[16]

2012 KinLnuous[17]

2014 Dense planner SLAM[18]

2013 SLAM++[19]

2015 Dense semantic SLAM[20]

In our system, graph optimization is used for 3D reconstruction. The 3D reconstruction map of graph-based is a graph consisting of nodes and edges, as shown in equation (1)(2)(3).

$$\mathrm{G}=\{\mathrm{V}，\mathrm{E}\}\ (1)$$

$$V_i = [x, y, z, q_x, q_y, q_z, q_z] = T_i = \begin{bmatrix} R_{3\times3} & t_{3\times1} \\ O_{1\times3} & 1 \end{bmatrix} (2)$$

$$E_{i,j} = T_{i,j} = \begin{bmatrix} R_{3\times3} & t_{3\times1} \\ O_{1\times3} & 1 \end{bmatrix}_{i,j} (3)$$

The nodes contain the visual odometry poses, RGB and depth images of each location. In addition, they also save visual words which are used for loop closure detection. The edges are mode of neighbors and loop closures, which save the geometrical transformation between nodes. When the odometry transformation between the current and previous nodes is generated, the neighbor edges are added to the graph. When a loop closure detection is found between the current node and one of the previous maps, the loop closure edges are added to the graph. After the construction of graph, the graph optimization is performed which calculates the most likely configuration that best satisfies the constraints of edges.

Suppose $x = (x_1,\ x_2 \ldots x_n)^T$ is a vector of parameters which represent the configuration of nodes. $w_{i,j}$ and $\Omega_{i,j}$ represent the mean and the information matrix of the observation of node i and j respectively. For the state x, $f_{ij}(x)$ is the function which can calculate the observation of the current state. The residual $r_{i,j}$ can be calculated via equation (4).

$$r_{i,j}(x) = w_{i,j} - f_{i,j}(x)\ (4)$$

The amount of error introduced by constraints which are calculated by real or visual odometry, weighed by its information, can be obtained via equation (5).

$$d_{i,j}(x)^2 = r_{i,j}(x)^T \Omega_{i,j} r_{i,j}(x)\ (5)$$

Assuming all the constraints to be independent, the overall error can be calculated through equation (6).

$$D^2(x) = \sum_{(i,j)\in\emptyset} d_{i,j}(x)^2 = \sum_{(i,j)\in\emptyset} r_{i,j}(x)^T \Omega_{i,j} r_{i,j}(x)\ (6)$$

where $d_{i,j}(x)^2$ is residual of the edge which connects node i and j in graph ϕ . So the key of graph-based SLAM is to find a state x^* that minimizes the overall error.

$$x^* = \operatorname*{argmin}_x \sum_{(i,j)\in\phi} r_{i,j}(x)^T \Omega_{i,j} r_{i,j}(x)\ (7)$$

Compactly, it is rewritten in equation (8)

$$x^* = \operatorname*{argmin}_x \sum_{(i,j)\in\phi} ||r_{i,j}(x)||^2_{\sum i,j})\ (8)$$

where $\sum_{i,j} = \Omega_{i,j}^{-1}$ is the corresponding covariance matrix of the information matrix. This is a typical Bundle Adjustment (BA) problem. The main optimized iteration strategies contain Gauss-Neton (GN) and Levenberg Marquardt (LM). In this report, the G2O[12][21] framework is used in our work. This approach performs a minimization of non-linear error function that can be represented as a graph. G2O can minimize the error in a graph in which vertices are parameterized by transformation and edges represent constraints between vertices with associated covariance matrices. It maximizes the likelihood of the vertex parameters subject to the constraints using stochastic gradient descent.

Semantic labelling

There are several 3D semantic segmentation approaches for both outdoor and indoor scenes.

Outdoor:[22][23][24]

Indoor:[25][26][27][28]

For the visual features extraction, the most popular feature are shown below:

Color Histogram

Color Moment

Histogram of Gradients(HOG)[29]

Fast Point Feature Histograms(FPFH)[30]

Point-Pair Feature(PPF)[31]

Dominant Orientation Templates(DOT)[32]

For the classification of 2D/3D pixel or voxel, the most useful method are shown below:

Randomized Decision Forest[33]

Hough Forests[34]

3D Conditional Random Field[35]

Multi-scale Convolutional Neural Network[36]

This part work is still under way. Our solution now is that: RGBD images are classified using the randomized decision forest. Then those labeled RGBD images can be combined together based on the graph optimization visual odometry. Finally, the result is refined using 3D dense Conditional Random Field. But in the future, we will turn to CNN model for the voxel classification to increase the accuracy and decrease the time of classification.

Results and Discussion

Many 3D SLAM/Reconstruction tests are performed only in the office environment, because of the dataset of Nuclear industrial environment is still under way. We will make tests as soon as possible when the nuclear dataset is built. The office data form TUM dataset[37] and Birmingham STRANDS dataset[38] are used now. In the Frantend of 3D SLAM, different features like SIFT[39], SURF[40], ORB[41] and BRIEF[42] are tested for feature detection and loop detection. The ICP[43] and RANSAC[44] are tested for motion estimation. In the Backend of 3D SLAM, different graph optimizations algorithms like TORO[45], GTSAM[46] and G2O[21] are tested.

The qualitative result of 3D SLAM in office environment is shown in Figure 2. It is built using SIFT + RANSAC + TORO. The evaluated camera trajectory from RGBD SLAM is shown in Figure 3. The TUM dataset also provide ground truth trajectory from VICON system. The ground truth of office is shown in Figure 4.

We can not evaluate the 3D reconstruction directly. But it is reasonable to assume that the error in the 3D map will be directly related to the error of the camera trajectory. According to [47], there are two mainly error: relative pose error (RPE) and absolute trajectory error(ATE) for the evaluation of the visual odometry drift and the global pose deviation. The RPE considers both translational and rotational errors, while the ATE only considers the translational errors. So, the RPE is always slightly larger than the ATE.

Figure 2 The 3D reconstruction of office environment

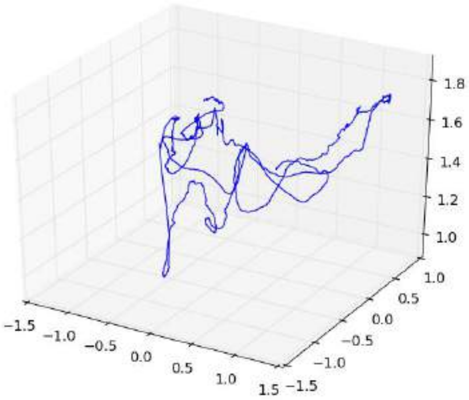

Figure 3 The evaluated trajectory from RGBD SLAM in office environment

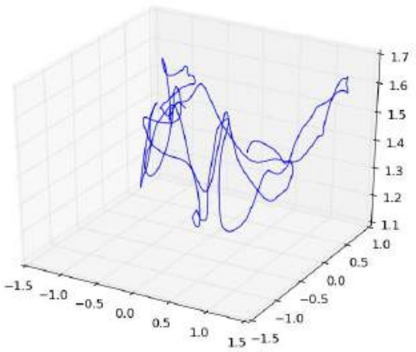

Figure 4 The ground truth trajectory from VICON in office environment

The RPE of the office environment is show in Figure 5 and the RPE with time plot of the office environment is show in Figure 6. The ATE of the office environment is shown in Figure 7 and the ATE plot of the office environment is show in Figure 8.

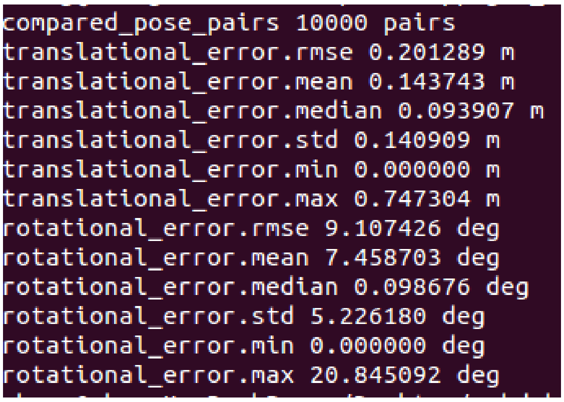

```
compared_pose_pairs 10000 pairs
translational_error.rmse 0.201289 m
translational_error.mean 0.143743 m
translational_error.median 0.093907 m
translational_error.std 0.140909 m
translational_error.min 0.000000 m
translational_error.max 0.747304 m
rotational_error.rmse 9.107426 deg
rotational_error.mean 7.458703 deg
rotational_error.median 0.098676 deg
rotational_error.std 5.226180 deg
rotational_error.min 0.000000 deg
rotational_error.max 20.845092 deg
```

Figure 5 The RPE of the office environment

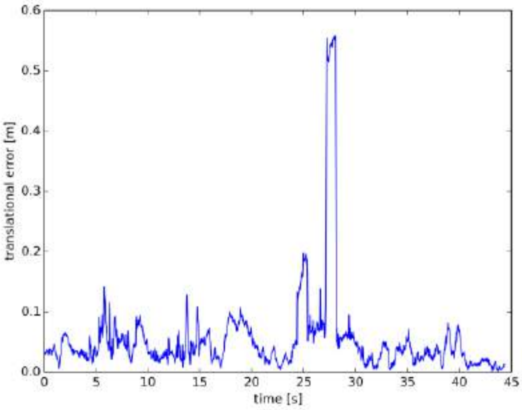

Figure 6 The RPE with time plot of the office environment

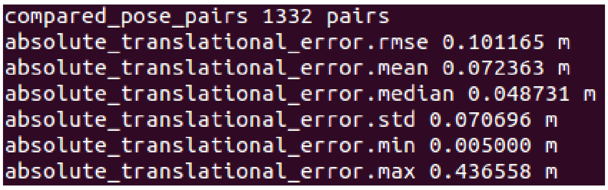

```
compared_pose_pairs 1332 pairs
absolute_translational_error.rmse 0.101165 m
absolute_translational_error.mean 0.072363 m
absolute_translational_error.median 0.048731 m
absolute_translational_error.std 0.070696 m
absolute_translational_error.min 0.005000 m
absolute_translational_error.max 0.436558 m
```

Figure 7 The ATE of the office environment

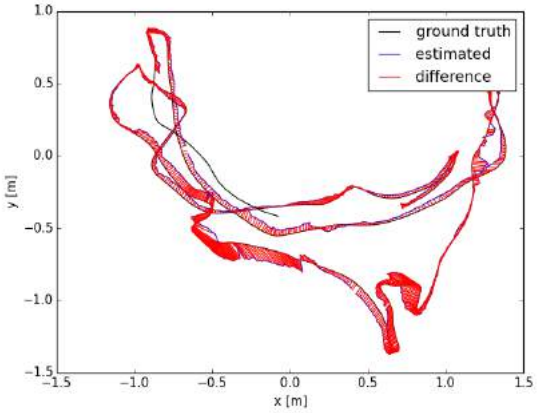

Figure 8 The ATE plot of the office environment

Using Randomized Decision Forest and refined by 3D Conditional Random Field[48], each voxel in the 3D reconstruction can be assigned a class label. Figure 9 shows the original 3D office reconstruction and the Figure 10 shows the labeled 3D office reconstruction. Each voxel is labeled by different color, like red is table, green is table, brown is cupboard and etc. All the objects can be recognized in this office. Then the millions of point clouds belong to the object can be converted to a whole CAD model which is used for 3D pose tracking and object manipulation.

Figure 9 The original 3D reconstruction of an office includes table, chair, cupboard, wall and ground.

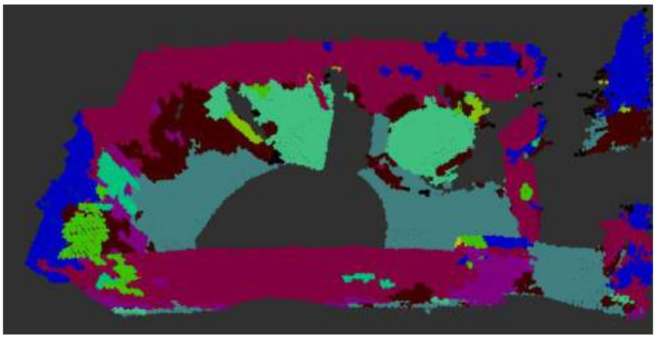

Figure 10 The labeled 3D reconstruction of an office. The table, chair, cupboard, wall and ground are labeled using different color.

Conclusions and Future Work

The next step work will mainly focus on two areas:

1. Build a nuclear environment dataset and perform 3D dense semantic reconstruction tests using this dataset. This dataset will include metal, wood, pipe and many nuclear objects. With the help from Dr. Jeff, many 3D CAD models of real Sellafield nuclear plants will be provided very soon.
2. The CNN model will be used for 2/3D object labelling to increase the accuracy and decrease the labelling time.

Acknowledgements

Many thanks for the help from Dr. Ales, Dr. Rustam, Dr. Jeff and Dr. Lars. Many thanks for the funding support from Nuclear Industry.

References

[1] R. Smith, M. Self, and P. Cheeseman, “Estimating Uncertain Spatial Relationships in Robotics,” in *Autonomous Robot Vehicles*, New York, NY: Springer New York, 1990, pp. 167–193.

[2] M. Montemerlo, S. Thrun, D. Koller, and B. Wegbreit, “FastSLAM: A factored solution to the simultaneous localization and mapping problem,” in *Proc. of 8th National Conference on Artificial Intelligence/14th Conference on Innovative Applications of Artificial Intelligence*, 2002, vol. 68, no. 2, pp. 593–598.

[3] J. Little, “Mobile robot localization and mapping with uncertainty using scale invariant visual landmarks.,” vol. 21, no. 8, pp. 735–758, 2002.

[4] G. Grisetti, C. Stachniss, and W. Burgard, “Improving Grid-based SLAM with Rao-Blackwellized Particle Filters by Adaptive Proposals and Selective Resampling,” in *IEEE International Conference on Robotics and Automation*, 2005, no. April, pp. 2432–2437.

[5] Davison, “Real-time simultaneous localisation and mapping with a single camera,” in *Proceedings Ninth IEEE International Conference on Computer Vision*, 2003, vol. 2, pp. 1403–1410 vol.2.

[6] L. M. Paz, J. D. Tardos, and J. Neira, “Divide and Conquer: EKF SLAM in O(n),” *IEEE Trans. Robot.*, vol. 24, no. 5, pp. 1107–1120, Oct. 2008.

[7] B. Triggs, P. F. McLauchlan, R. I. Hartley, and A. W. Fitzgibbon, “Bundle Adjustment — A Modern Synthesis Vision Algorithms: Theory and Practice,” in *Vision Algorithms: Theory and Practice*, vol. 1883, 2000, pp. 153–177.

[8] S. Thrun, “The Graph SLAM Algorithm with Applications to Large-Scale Mapping of Urban Structures,” *Int. J. Rob. Res.*, vol. 25, no. 5–6, pp. 403–429, 2006.

[9] G. Klein and D. Murray, “Parallel Tracking and Mapping for Small AR Workspaces,” in *2007 6th IEEE and ACM International Symposium on Mixed and Augmented Reality*, 2007, pp. 1–10.

[10] K. Konolige and M. Agrawal, “FrameSLAM: From Bundle Adjustment to Real-Time Visual Mapping,” *IEEE Trans. Robot.*, vol. 24, no. 5, pp. 1066–1077, Oct. 2008.

[11] M. Kattenbelt, M. Kwiatkowska, G. Norman, and D. Parker, “Game-Based Probabilistic Predicate Abstraction in PRISM,” *Electron. Notes Theor. Comput. Sci.*, vol. 220, no. 3, pp. 5–21, Dec. 2008.

[12] F. Endres, J. Hess, J. Sturm, D. Cremers, and W. Burgard, “3D Mapping with an {RGB-D} Camera,” *IEEE Trans. Robot.*, 2013.

[13] H. Strasdat, J. M. M. Montiel, and A. J. Davison, “Visual SLAM: Why filter?,” *Image Vis. Comput.*, vol. 30, no. 2, pp. 65–77, 2012.

[14] J. Engel, T. Schöps, and D. Cremers, “LSD-SLAM: Large-Scale Direct Monocular SLAM,” in *Computer Vision–ECCV 2014*, 2014, pp. 834–849.

[15] R. Mur-Artal, J. M. M. Montiel, and J. D. Tardos, “ORB-SLAM: A Versatile and Accurate Monocular SLAM System,” *IEEE Trans. Robot.*, vol. 31, no. 5, pp. 1147–1163, Oct. 2015.

[16] R. a. Newcombe, A. J. Davison, S. Izadi, P. Kohli, O. Hilliges, J. Shotton, D. Molyneaux, S. Hodges, D. Kim, and A. Fitzgibbon, “KinectFusion: Real-time dense surface mapping and tracking,” in *2011 10th IEEE International Symposium on Mixed and Augmented Reality*, 2011, pp. 127–136.

[17] T. Whelan, M. Kaess, and M. Fallon, “Kintinuous: Spatially extended kinectfusion,” *RSS Work. RGB-D Adv. Reason. with Depth Cameras*, p. 7, 2012.

[18] R. F. Salas-Moreno, B. Glocken, P. H. J. Kelly, and A. J. Davison, “Dense Planar SLAM,” in *Proc. of ISMAR*, 2014, pp. 157–164.

[19] R. F. Salas-Moreno, R. a. Newcombe, H. Strasdat, P. H. J. Kelly, and A. J. Davison, “SLAM++: Simultaneous localisation and mapping at the level of objects,” in *Proceedings of the IEEE Computer Society Conference on Computer Vision and Pattern Recognition*, 2013, pp. 1352–1359.

[20] V. Prisacariu, M. Lidegaard, D. Murray, P. Torr, S. Golodetz, and P. Patrick, “Incremental Dense Semantic Stereo Fusion for Large-Scale Semantic Scene Reconstruction,” *Icra*, p. Prisacariu, V. et al., 2015. Incremental Dense Sem, 2015.

[21] R. Kümmerle, G. Grisetti, H. Strasdat, K. Konolige, and W. Burgard, “G2o: A general framework for graph optimization,” in *Proceedings - IEEE International Conference on Robotics and Automation*, 2011, pp. 3607–3613.

[22] G. Floros and B. Leibe, “Joint 2D-3D temporally consistent semantic segmentation of street scenes,” *Proc. IEEE Comput. Soc. Conf. Comput. Vis. Pattern Recognit.*, no. d, pp. 2823–2830, 2012.

[23] R. Paul, D. Rus, P. Newman, and A. Conference, “Parsing Outdoor Scenes from Streamed 3D Laser Data Using Online Clustering and Incremental Belief Updates,” in *Twenty-Sixth AAAI Conference on Artificial Intelligence*.

[24] Hanzhang Hu, D. Munoz, J. A. Bagnell, and M. Hebert, “Efficient 3-D scene analysis from streaming data,” in *2013 IEEE International Conference on Robotics and Automation*, 2013, pp. 2297–2304.

[25] A. Anand, H. S. Koppula, T. Joachims, and A. Saxena, “Contextually Guided Semantic Labeling and Search for 3D Point Clouds,” *Int. J. Rob. Res.*, vol. 32, pp. 19–34, 2013.

[26] A. Nüchter and J. Hertzberg, “Towards semantic maps for mobile robots,” *Rob. Auton. Syst.*, vol. 56, no. 11, pp. 915–926, 2008.

[27] J. P. C. Valentin, S. Sengupta, J. Warrell, A. Shahrokni, and P. H. S. Torr, “Mesh based semantic modelling for indoor and outdoor scenes,” *Proc. IEEE Comput. Soc. Conf. Comput. Vis. Pattern Recognit.*, pp. 2067–2074, 2013.

[28] J. Stückler, N. Biresev, and S. Behnke, “Semantic Mapping Using Object-Class Segmentation of RGB-D Images,” pp. 3005–3010, 2012.

[29] N. Dalal and B. Triggs, “Histograms of Oriented Gradients for Human Detection,” in *2005 IEEE Computer Society Conference on Computer Vision and Pattern Recognition (CVPR’05)*, 2005, vol. 1, pp. 886–893.

[30] R. B. Rusu, N. Blodow, and M. Beetz, “Fast Point Feature Histograms (FPFH) for 3D registration,” *2009 IEEE Int. Conf. Robot. Autom.*, pp. 3212–3217, May 2009.

[31] B. Drost, M. Ulrich, N. Navab, and S. Ilic, “Model globally, match locally: Efficient and robust 3D object recognition,” in *2010 IEEE Computer Society Conference on Computer Vision and Pattern Recognition*, 2010, no. April 2016, pp. 998–1005.

[32] S. Hinterstoisser, S. Ilic, N. Navab, P. Fua, and V. Lepetit, “Dominant Orientation Templates for Real-Time Detection of Texture-Less Objects,” 2010.

[33] V. Lepetit, P. Lagger, and P. Fua, “Randomized Trees for Real-Time Keypoint Recognition,” in *2005 IEEE Computer Society Conference on Computer Vision and Pattern Recognition (CVPR’05)*, vol. 2, pp. 775–781.

[34] J. Gall and V. Lempitsky, “Class-Specific Hough Forests for Object Detection,” in *Decision Forests for Computer Vision and Medical Image Analysis*, London: Springer London, 2013, pp. 143–157.

[35] J. Lafferty, A. McCallum, and F. C. N. Pereira, “Conditional random fields: Probabilistic models for segmenting and labeling sequence

data," *ICML '01 Proc. Eighteenth Int. Conf. Mach. Learn.*, vol. 8, no. June, pp. 282–289, 2001.

[36] C. Couprie, C. Farabet, L. Najman, and Y. LeCun, "Indoor Semantic Segmentation using depth information," *arXiv Prepr. arXiv1301.3572*, pp. 1–8, 2013.

[37] "TUM dataset." [Online]. Available: http://vision.in.tum.de/data/datasets/rgbd-dataset/download#.

[38] "STRANDS dataset." [Online]. Available: http://strands.acin.tuwien.ac.at/.

[39] D. G. Lowe, "Distinctive Image Features from Scale-Invariant Keypoints," *Int. J. Comput. Vis.*, vol. 60, no. 2, pp. 91–110, Nov. 2004.

[40] H. Bay, A. Ess, T. Tuytelaars, and L. Van Gool, "Speeded-Up Robust Features (SURF)," *Comput. Vis. Image Underst.*, vol. 110, no. 3, pp. 346–359, Jun. 2008.

[41] E. Rublee, V. Rabaud, K. Konolige, and G. Bradski, "ORB: An efficient alternative to SIFT or SURF," in *2011 International Conference on Computer Vision*, 2011, pp. 2564–2571.

[42] M. Calonder, V. Lepetit, C. Strecha, and P. Fua, "BRIEF : Binary Robust Independent Elementary Features," *Eur. Conf. Comput. Vis.*, pp. 778–792, 2010.

[43] P. J. Besl and H. D. McKay, "A method for registration of 3-D shapes," *IEEE Trans. Pattern Anal. Mach. Intell.*, vol. 14, no. 2, pp. 239–256, 1992.

[44] M. a. Fischler and R. C. Bolles, "Random sample consensus: a paradigm for model fitting with applications to image analysis and automated cartography," *Commun. ACM*, vol. 24, no. 6, pp. 381–395, Jun. 1981.

[45] G. Grisetti, C. Stachniss, and W. Burgard, "Nonlinear Constraint Network Optimization for Efficient Map Learning," *IEEE Trans. Intell. Transp. Syst.*, vol. 10, no. 3, pp. 428–439, Sep. 2009.

[46] N. Sünderhauf and P. Protzel, "Towards a robust back-end for pose graph SLAM," *Icra*, pp. 1254–1261, 2012.

[47] J. Sturm, N. Engelhard, F. Endres, W. Burgard, and D. Cremers, "A benchmark for the evaluation of RGB-D SLAM systems," in *2012 IEEE/RSJ International Conference on Intelligent Robots and Systems*, 2012, pp. 573–580.

[48] A. Hermans, G. Floros, and B. Leibe, "Dense 3D semantic mapping of indoor scenes from RGB-D images," in *2014 IEEE International Conference on Robotics and Automation (ICRA)*, 2014, pp. 2631–2638.

Theme 4 – Structural Integrity
DISTINCTIVE 2nd Annual Meeting
Bristol, UK
19th – 20th April 2016

Re-Use and Volume Reduction of Scabbled Contaminated Concrete Arising from Nuclear Decommissioning

T. Lord* Dr L. Black

*Correspondence: cn10tl@leeds.ac.uk

Institute for Resilient Infrastructure, University of Leeds

Abstract

Around 50% of the UK's classified nuclear waste is building waste including concrete, cement and rubble. While research has gone into ways to minimise the volume of this waste, little has examined recycling of the materials. This research aims to investigate methods to reduce the burden on present and future storage and disposal facilities through re-use and volume reduction of conditioned contaminated concrete. MSc research has shown possible reactivity within the scabbled material enabling the potential for use as a cementitious replacement material. The overall aim of future PhD research is to investigate the use of scabbled contaminated concrete as a replacement material within nuclear waste encapsulation grouts, or at volume reduction of conditioned waste.

Introduction

As nuclear facilities come to the end of their design life, decommissioning work is carried out such that the sites can be decontaminated and eventually demolished. Within the United Kingdom this includes a number of power production facilities, particularly of the Magnox fleet, as well as Sellafield nuclear reprocessing and storage site.

Arising from the decommissioning are large quantities of building wastes, rubble and soil, accounting for over half of all classified waste [1]. In an effort to reduce the volume of concrete waste, part of the decommissioning process involves scabbling of contaminated concrete; the removal of the outer contaminated layer of concrete (usually the top 2-3cm) from the larger mass through laser or mechanical means, enabling the bulk of the concrete to be disposed of as low level or exempt waste.

The scabbled material produced is a fine granular material with a large particle size distribution, contaminated with a number of radionuclides that are either chemically bound to specific solid phases of the concrete or absorbed into the pore water of the material [2]. As a contaminated material the scabbled concrete is at present treated as a new Intermediate Level Waste (ILW) stream. The purpose of this project is to examine the nature of the scabbled material and examine options for possible re-use or recycling, primarily as a replacement material in existing cementitious encapsulation grouts.

Re-use and recycling of concrete has been taking place for a number of decades, in an attempt to reduce waste and carbon emissions arising from the construction industry [3]. Due to economic reasons however, little research has been conducted into the re-use of concrete fines as they are seen as detrimental to fresh concrete, particularly due to high absorption and the subsequent requirement for increased water content [4], and are produced in insufficient quantities during processing. Within the nuclear industry however, disposal costs of £14,000 per m^3 of ILW mean that the same economic constraints no longer apply [5], and the filler effect produced by an increase in nucleation sites [6], as well as secondary hydration from any newly exposed anhydrous material during scabbling, present options for investigating the re-use of the material.

MSc Research

Initial research focussed around '*investigating the impact of recycled concrete fines on the engineering* *performance of cementitious infill'.* This involved the synthesis of recycled concrete fines, and characterisation of the resultant powder. This was followed by an investigation of the material's reactivity, impact on microstructure, and engineering performance when blended with fresh cement. Quartz was used as an inert reference material against which the performance of the recycled fines could be measured. A 50MPa CEMI mortar was cast, cured in ideal conditions for 28 days and then ground to provide the recycled fines. The quartz reference material was ground to the same particle size distribution of the ground mortar, using a Malvern Mastersizer to investigate PSD, and a gyromill to grind the materials.

Characterisation

Calorimetry, chemical shrinkage, Mastersizer and SEM shape analysis were used to characterise the ground mortar, in terms of particle analysis and reactivity.

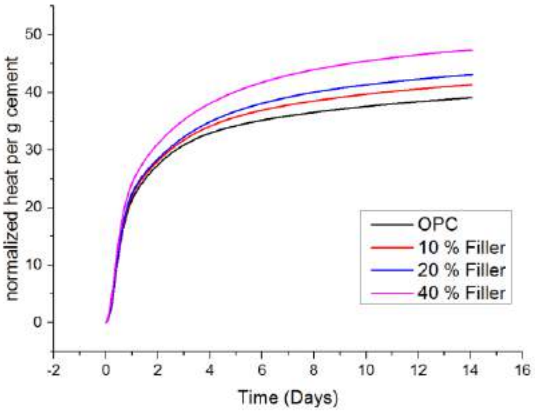

Figure 1 - M1 filler cumulative heat evolution against time, normalized per gram of cement

While chemical shrinkage testing showed little variation in volume change between samples, linked to degree of hydration, calorimetry work showed increased heat of hydration when recycled fines were used within the mix, as seen in figure 1. This clearly shows the filler effect, with increased nucleation sites on the surface of the filler particles enabling more hydration products to be formed [6].

Figure 2 compares the normalised heat per gram of cement of a CEMI reference, a 40% quartz mix and a 40% ground mortar filler replacement. As can be seen, there is a significant increase normalised heat produced when ground mortar is used compared to quartz, suggesting that there is further hydration occurring above and beyond that induced by the filler effect, caused by the presence of additional anhydrous material exposed during the grinding of the mortar.

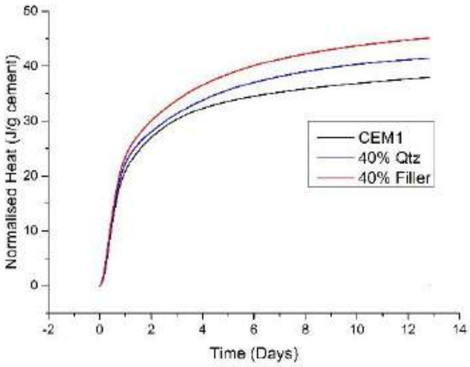

Figure 2 - 40% Quartz Replacement vs 40% Filler Replacement

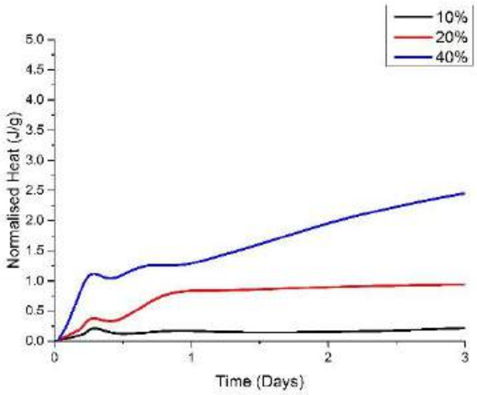

Figure 3 - Hydration of recycled fines component during early stage curing

Figure 3 shows the hydration of the recycled fines component for each replacement level, where the normalised heat of the quartz reference has been subtracted from that of the recycled filler. While compared to a standard CEMI reference the cumulative heat levels aren't high, there are significant peaks to show possible secondary hydration of the recycled material occurring, above that occurring due to the filler effect, as discounted for by the quartz reference mix.

Engineering Performance

Compressive strength testing was used to assess the effect of the recycled fines on the engineering performance of a secondary mortar using the recycled fines, and a quartz reference, as a cementitious replacement material.

Compressive strength testing showed a noticeable increase in strength when recycled concrete is used as a filler as opposed to quartz at 40% replacement, as seem in figure 3, but with both replacements performing significantly worse than the CEMI reference. This significant decrease in compressive strength, with both achieving only approximately 50% of the 28 day strength of the reference mix. This can be attributed to both a decrease in overall cement content leading to reduced strength, as well as increasing the overall water to cement (w/c) ratio, leading to a further decrease in strength [7].

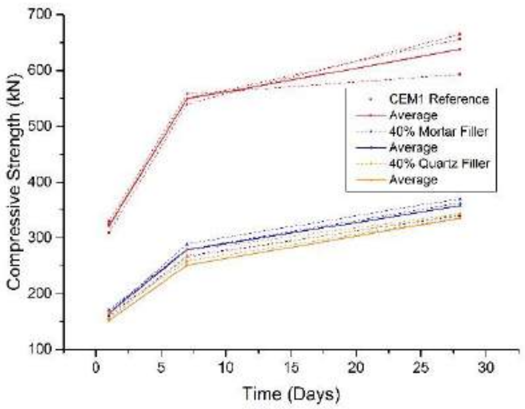

Figure 3 - 1, 7 and 28 day compressive strength comparison

Conclusions

Both compressive strength testing and calorimetry work showed the possible presence of secondary hydration occurring from the use of recycled fines, and so further investigations can be made to examine this effect and its further use in secondary grouts, as a method of reducing the volume of ILW.

Future PhD Research

Following MSc research, the PhD project aims to investigate methods of re-use and volume reduction of scabbled contaminated concrete, with the aim of reducing the volume of ILW sent to long term disposal, in the proposed Geological Disposal Facility (GDF) [8].

This research is in early stages, with 50MPa CEMI and CEMII concrete having been cast, and with curing ongoing at present, before a suitable material can be used for synthesis. Initial research will focus on the re-use of scabbled material within future mortars or grouts for waste disposal, either through harnessing the possible secondary hydration discovered in earlier research, or through incorporating the material within fresh encapsulation grouts, such that the grouts still perform to nuclear specifications, as has been trialled in Japan with some success [9].

Further research will investigate the possibility of volume reduction of the conditioned waste form, to reduce the volume of waste needing disposal in a Geological Disposal Facility (GDF), in an effort to reduce the overall cost of disposal for contaminated concretes. Volume reduction will involve investigation possible activation of the scabbled material, initially through alkali-activation, such that a lower volume of cementitious grout is required to achieve the same performance [10], and so the overall volume of the conditioned waste form can be reduced.

References

1. Nuclear Decomissioning Authority, *2013 UK Radioactive Waste Inventory: Radioactive Waste Composition*. 2014: Moor Row, Cumbria.
2. Bath, A., G. Deissmann, and S. Jefferis. *Radioactive Contamination of Concrete: Uptake and Release of Radionuclides*. in *The 9th International Conference on Radioactive Waste Management and Environmental Remediation*. 2003. Oxford.
3. The Cement Sustainability Initiative, *Recycling Concrete*. 2009, World Business Council for Sustainable Development: Geneva.
4. de Juan, M.S. and P.A. Gutiérrez, *Study on the influence of attached mortar content on the properties of recycled concrete aggregate.* Construction and Building Materials, 2009. **23**(2): p. 872-877.
5. Department of Energy & Climate Change, *Waste Transfer Pricing Methodology for the Disposal of Higher Activity Waste from Nuclear Power Stations*. 2011, Department of Energy and Climate Change: London.
6. Gutteridge, W.A. and J.A. Dalziel, *Filler Cement: The Effect of the Secondary Component on the Hydration of Portland*

Cement. Cement and Concrete Research, 1990. **20**: p. 778-782.
7. Taylor, H.F.W., *Cement Chemistry*. 2 ed. 1997, London: Thomas Telford.
8. Department of Energy & Climate Change, *Implementing Geological Disposal*. 2014, Department of Energy & Climate Change,: London.
9. Ishikura, T., et al., *Utilization of Crushed Radioactive Concrete for Mortar to Fill Waste Container Void Space.* Journal of Nuclear Science and Technology, 2004. **41**(7): p. 741-750.
10. Shi, C., P.V. Krivenko, and D.M. Roy, *Alkali-Activated Cements and Concretes*. 2006, Abingdon, Oxfordshire: Taylor & Francis.

Theme 4 - Structural Integrity
DISTINCTIVE 2nd Annual Meeting
Bristol, UK
19th – 20th April 2016

Atomistic Simulation of Cement-Based Materials for Nuclear Waste Disposal

R. Kavanagh*[1], C. Johnston[1], J. Kohanoff[1], G. Tribello[1], and A. Saúl[2]

*Correspondence: rkavanagh04@qub.ac.uk

[1] Atomistic Simulation Centre, Queen's University Belfast, University Road, Belfast BT9 1NN, UK
[2] Aix-Marseille University, CINaM-CNRS UMR 7325 Campus de Luminy, 13288 Marseille cedex 9, France

Abstract

The *ab initio* simulation of cement-based materials is a vital task in understanding the processes that will occur in the storage of nuclear wastes in preparation for geological disposal in the future. As cement is an amorphous material whose composition is hotly debated, the problem is as complex as it is important. Initial work building on prior work done by collaborators has shown that while calcium-silicate-hydrate materials are unlikely to be strongly affected by the loss of electrons induced by γ-irradiation. The water contained within the cement is likely to undergo reaction and produce a rich cocktail of molecular species, in particular hydroxyl radicals which may produce hydrogen gas, causing expansion and cracking, or contribute to the Pozzolanic reaction which produces a gel-like layer that compromises the mechanical strength of cements. As such, knowledge of the properties of irradiated cement are necessary for the understanding and safe storage of nuclear wasteforms.

Introduction

Cements and grouts consisting of ordinary Portland cement (OPC) and blast furnace slag (BFS) are considered among the most important materials for the long term disposal of intermediate and low-level nuclear wastes in the UK due to their good mechanical and thermal properties and high tolerance for a wide variety of waste types, leading to ease of use.[1] The UK employs an iterative process, slowly improving the quality of cements to provide the requirements for a given application, as complimentary properties are essential in the storage of both short and long-lived wastes.

Cement-based storage in the UK focuses on intermediate-level wastes (ILW) such as brucite ($Mg(OH)_2$) and plutonium contaminated materials (PCM), which are assorted waste items generated in the processing and handling of plutonium. These wastes are stored in a cement matrix encased in a steel container, and the presence of radionuclides such as uranium dioxide (UO_2), plutonium and their associated decay daughters results in a massive range of particles that can interact and affect the properties of cements. Throughout their lifetime as a storage matrix, cements are exposed to ionizing radiation and may undergo detrimental changes that compromise the storage medium. Other such issues to consider include the irradiation of the water contained in cement and substitutions of atoms in the cement structure by radioactive fission products of uranium and plutonium, which may affect the structural properties of the cement matrix.[2] As such, fundamental understanding of the effects of radiation on cements is essential in improving the quality of storage materials.

This work aims to provide an insight into the effects of radiation on an atomic scale in the hopes of providing a fundamental outlook on the properties of cement under irradiation.

Methodology Details

The models employed in this project were the same used by Dezerald et. al.[2]. These were obtained using a combinatorial optimization technique by Abdolhosseini Qomi et. al.[3] to realistically build the calcium-silicate-hydrate (CSH) phases of cement.[4] This original model was produced via a force-field method and eventually adapted to the CP2K open source electronic structure code and used in this work.[5] Initial work consisted of re-optimization of the neutral unit cell using ab intitio density functional theory (DFT). The calculation was performed using the Quickstep[6] algorithm utilizing the Gaussian and Plane Wave (GPW) method[7] with molecularly optimized Gaussian atom-centered basis sets were used[8] in conjunction to the Perdew-Burke-Ernzerhof (PBE) functional.[9]

The cell is a triclinic structure with cell vectors A, B and C equal to 13.244, 18.183 and 23.869 Å respectively. The angles α, β and γ are equal to 90.08, 92.59 and

86.62° and the unit cell is periodic. The system consists of a layered hybrid of tobermorite[10] with 14 Å interlayer spacing and jennite.[11] The structure, figure 1, is shown below and contains 44 Si, 72 Ca, 235 O and 150 H atoms.

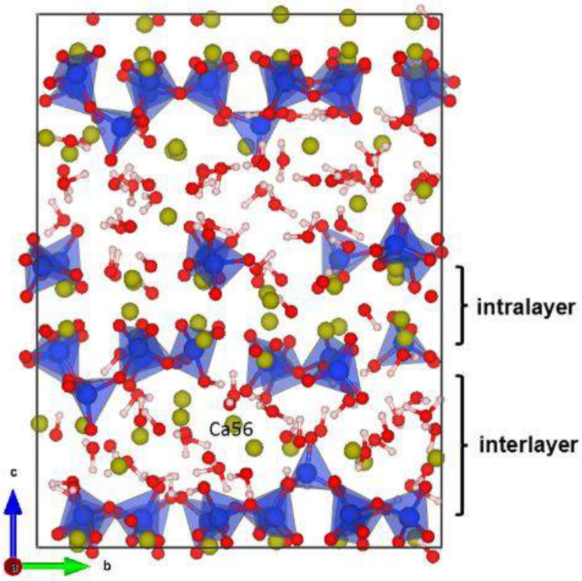

Figure 1 The schematic representation of the C-S-H structure. Hydrogen is shown in white, oxygen in red, silicon in blue and calcium in yellow. The corner-sharing SiO^{4-}_4 tetrahedra forming the silica chains are shown. Reproduced from Dezerald et. al.[2]

Following the CP2K re-optimization, the charge of the system was adjusted to +1 to simulate an electron-hole induced by γ-irradiation. This charge was compensated with a uniform negative background of charge -1. Further single-point energy and geometry optimization calculations were performed using the Minnesota M06-2X global hybrid Hartree-Fock functional with 54% Hartree-Fock exchange to increase the accuracy of the calculations performed on the system. The M06-2X functional was chosen due to its versatility and wide use in the quantum chemistry community. M06-2X is a member of the M06 functional family, which is known for its excellent performance in main-group thermochemistry and kinetics.[12]

Results and Discussion

Simulation of the electron-hole using the PBE functional and subsequent visualisation of the spin density has shown that there are particular oxygen-containing species that preferentially lose an electron (Figure 2). A significant portion of the spin density is located on OH and H_2O moieties scattered throughout the cell, with a smaller portion located on the Si-O tetrahedral oxygen atoms. This suggests that the electronegative, electron rich oxygen atoms spread throughout have the most available electron density to be "knocked" out by γ-irradiation. Electron density is more likely to be situated closer to the oxygen atoms in the more polar O-H species than in less polar Si-O systems, suggesting that the radiolysis of water in the cell as well as damage to the $Ca(OH)_2$ hydroxyl species are the main problems to be considered for this specific model. This was highlighted by Mobasher et. al. who stated that the γ-irradiation of an OPC-BFS cement at 20 and 50 °C shows no significant difference in properties other than a slight increase in cracking, which was attributed to an increase in temperature in conjunction to the γ-irradiation.[13]

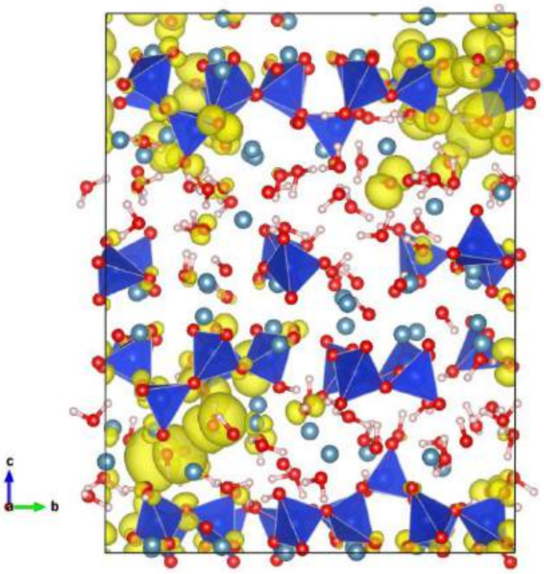

Figure 2 The spin density of the electron hole drawn at an isovalue of 0.0001 e/Å^3 calculated with PBE geometry using the PBE functional. The hydrogen is shown in white, oxygen in red, silicon in dark blue and the calcium in light blue.

Further optimization using the Minnesota functional M06-2X yielded a more localised electron spin density plot wherein the density seems to significantly localise around an OH moiety in the bottom left of the unit cell and to surrounding oxygen species to an extent. Localisation of the electron-hole suggests that the negative spin density, or spin depletion, surrounding the OH species acts as a boundary for the nodal plane. Figure 3 shows the spin density of the electron hole after geometry optimization.

Mulliken population analysis suggests the oxygen atom at the centre of the density possesses a spin moment of close to 1, which is significantly higher than the average spin value of 0.0002 for the oxygen atoms around it. A markedly different charge of -0.33 on the oxygen contrasts the -1.08 average charge of the surrounding atoms. Showing a similar anomalous trend, the H atom bonded to this oxygen possesses a spin moment of -0.03 while other hydrogen atoms in the proximity average to 0.000001.

Hirshfeld analysis was also performed to avoid ambiguities in the Mulliken analysis, which is basis set-dependent. Hirshfeld charges paint a similar picture. The oxygen atom thought to be the location of the hole has a spin moment of 0.834, while other oxygen atoms have virtually no spin with an average of 0.0001. The bound hydrogen acts as the only other significant source of spin at 0.034, meaning that approximately 87% of all spin in the system is localised on the OH species in question. The strong localisation of the electron-hole on this species using M06-2X suggests that PBE can accurately predict the geometry of the electron hole, as supported by Hirshfeld and Mulliken charges.

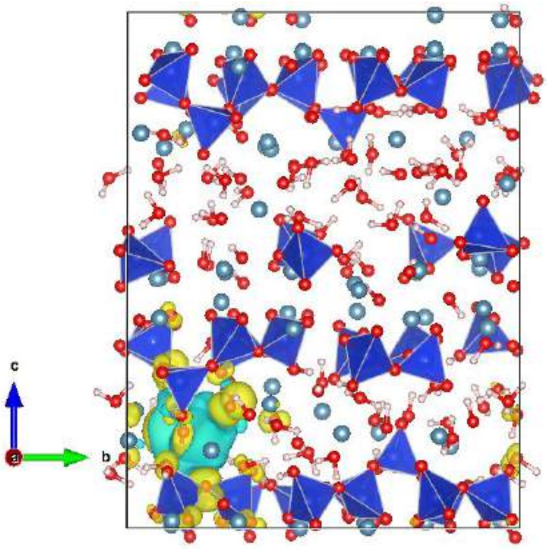

Figure 3 The spin density of the electron-hole drawn at an isovalue of 0.0001 e/Å^3 calculated with PBE geometry using the M06-2X functional. The hydrogen is shown in white, oxygen in red, silicon in dark blue and the calcium in light blue. Yellow density denotes spin-positive regions and blue denotes spin negative.

Analysis of the optimized geometries of the cement unit cell using PBE and M06-2X suggest that the main species susceptible to loss of electrons via γ-irradiation are free H_2O and OH^- species. Removing an electron from OH^- results in the production of a hydroxyl ($OH^\cdot$) radical, which is likely to cause degradation in the cement via the Alkali-Silica Reaction (ASR), or Pozzolanic Reaction, whereby $Ca(OH)_2$ or hydroxyl species react with the silica chains to produce an expansive gel that can cause cracking and eventual failure of the concrete.[14] Also of note is the ability for water in the system to undergo radiolysis and produce a rich range of reactive species such as OH^-, $OH\cdot$, H_3O^+ and H_2O_2 as identified by Ershov et. al.[15],which may react and compromise the wasteform by damaging the CSH phases or producing gases such as H_2 in the pores which can expand and cause cracking.

Conclusions and Future Work

The reactions of cement and the various radiolytic products of water are of particular interest within the nuclear decommissioning context. The results obtained in the present work suggest that while cement is robust to the loss of electrons via γ-irradiation, the effects of water radiolysis may prove significant. Further work addressing the effects of excess electrons in the cement system provides complementary insight into phenomena arising from the irradiation of cement. Currently, the main priority is to expand the cement model. Expansion of the cement model to include aluminates or ferrites such as those found in BFS may provide results of interest, as the enhanced model will be closer to the cements being proposed in the UK for storing nuclear waste. Haber-Weiss-like reactions[16] of H_2O_2 and iron could account for significant production of hydroxyl radicals and subsequent damage or production of hydrogen, and as such should be investigated.

Acknowledgements

The authors would like to thank the Department of Employment and Learning of Northern Ireland for providing this studentship and we are grateful for computational support from the UK national high performance computing service, ARCHER, for which access was obtained via the UKCP consortium and funded by EPSRC grant ref EP/K013564/1.

References

[1] C. Wilding, The performance of cement based systems, Cem. Concr. Res. 22 (**1992**), 299–310

[2] L. Dezerald, J. J. Kohanoff, A. A. Correa, A. Caro, R. J.M. Pellenq, F. J. Ulm, and A. Saul, Cement as a wasteform for nuclear fission products: the case of Sr^{90} and its daughters *Environ. Sci. Technol.*, 49, (**2015**) 13676–13683

[3] M.J. Abdolhosseini Qomi, K.J. Krakowiak, M. Bauchy, K.L. Stewart, R. Shahsavari, D. Jagannathan, D.B. Brommer, A. Baronnet, M.J. Buehler, S.Yip, F.-J Ulm, K.J. Van Vliet and R.J-.M. Pellenq, Combinatorial molecular optimization of cement hydrates, *Nat. Commun.* 5, 4960, (**2014**)

[4] M. J. Abdolhosseini Qomi, M. Bauchy, F.-J. Ulm, and R. J.-M. Pellenq. Anomalous composition-dependent dynamics of nanoconfined water in the interlayer of disordered calcium-silicates, *J. Chem Phys*, 140 (5):054515, (**2014)**

[5] J. Hutter, M. Iannuzzi, F. Schimann, and J. VandeVondele. cp2k: atomistic simulations of condensed matter systems. *Comput. Mol . Sci*, 4, (**2014)**

[6] J. VandeVondele, M. Krack, F. Mohamed, M. Parrinello, T. Chassaing, and J. Hutter. Quickstep: Fast and accurate density functional calculations using a mixed Gaussian and plane waves approach. *Comp. Phys. Commun*, 167 (**2005**)

[7] G. Lippert, J. Hutter, and M. Parrinello. A hybrid Gaussian and plane wave density functional scheme. *Molecular Physics*, 92 (**1997**)

[8] J. VandeVondele and J. Hutter. Gaussian basis sets for accurate calculations on molecular systems in gas and condensed phases. *J. of Chem. Phys.*, 127, (**2007**)

[9] J. P. Perdew, K. Burke, and M. Ernzerhof. Generalized Gradient Approximation Made Simple. *Phys. Rev. Lett.*, 77 (**1996**)

[10] E. Bonaccorsi, S. Merlino, H. Taylor, The crystal structure of Tobermorite 14 Å (Plombierite), a C-S-H phase. *J. Am. Ceram. Soc.* 88 505-512 (**2005**)

[11] E. Bonaccorsi, S. Merlino, H. Taylor, The crystal structure of jennite $Ca_9Si_618(OH)_6$ $8H_2O$ Cem. Concr. Res. 34, 1481-1488 (**2004**)

[12] . Zhao and D. G. Truhlar. *Theor. Chem. Account*, 120(1-3) (**2007**)

[13] N. Mobasher, S.A. Bernal, H. Kinoshita, C.A. Sharrad, J.L. Provis, Gamma irradiation resistance of an early age slag-blended cement matrix for nuclear waste encapsulation *J. Mater. Res.* 9, 1563-1571 (**2015**)

[14]G. Mertens, R. Snellings, K. Van Balen, B. Bicer-Simsir, P. Verlooy, J. Elsen. Pozzolanic reactions of common natural zeolites with lime and parameters affecting their reactivity. *Cem. Concr. Res.* 39 (3) 233–240 (**2009**)

[15] B.G. Ershov, A.V. Gordeev, A model for radiolysis of water and aqueous solutions of H2, H2O2 and O2. *Radiation Physics and Chemistry* 77, 928–935 (**2008**)

[16] J.P. Kehrer, The Haber-Weiss reaction and mechanisms of toxicity Toxicology 149, 43-50 (**2000**)

Theme 4 – Structural Integrity
DISTINCTIVE 2nd Annual Meeting
Bristol, UK
19th – 20th April 2016

Development of Novel, Low Cost Biomineral Permeable Reactive Barriers for Radionuclide Remediation

T.K Mullan*[1], R. Lunn[1], and J.C. Renshaw[1]

*Correspondence: thomas.mullan@strath.ac.uk

[1] Department of Civil & Environmental Engineering, University of Strathclyde, Glasgow, G1 IXJ, UK

Abstract

The microbial production of phosphate minerals has gained attention as a promising mechanism of *in situ* groundwater remediation. To date, most research has focused on the immobilisation of contaminants by the induced precipitation of insoluble contaminant-phosphate minerals (e.g. uranyl phosphates); however, it is also possible to use this technique to manufacture permeable reactive barriers (PRBs) which are then capable of mediating long-term, passive remediation of groundwater flow. This project investigates the use of bacteria and fungi to induce the formation of a phosphate mineral PRB *via* the enzymatic hydrolysis of an organic phosphate substrate (phytate). Attention is given to the factors influencing biomineral formation, composition, and characteristics (e.g. enzyme production and activity, secretion of microbial metabolites, other chemical species present, pH, redox potential) and this knowledge used to promote the manufacture of a biomineral with optimal physicochemical properties for deployment in a PRB (large, reactive surface area with a high capacity for contaminant sorption while remaining hydraulically permeable). Additionally, challenges relating to the scale-up and practical deployment of the process will be considered.

Introduction

Groundwater contamination is a problem that arises at all stages of the nuclear fuel cycle, from mining to plant operation to decommissioning and disposal [1]. Treatment of this contamination is required to prevent further spread into the environment and to avoid the potential for contamination to reach public water supplies. A range of remediation measures exist (e.g. pump and treat), but a particularly attractive option with regards to cost, effectiveness, and low maintenance requirements is the use of permeable reactive barriers (PRBs) [1, 2]. PRBs are a form of passive, *in situ* remediation technology in which a barrier is constructed across the path of groundwater flow; the barrier is constructed from a hydraulically permeable material that allows water to flow through while removing/immobilising contaminants *via* sorption and redox mechanisms [2, 3].

A wide range of materials can be used in PRB construction, for example zerovalent iron or zeolites [2], but within the context of the nuclear industry phosphate minerals (particularly members of the apatite group such as hydroxyapatite [$Ca_5(PO_4)_3OH$]) are considered to be suitable [4]. This is due to their ability to immobilise and incorporate a range of relevant contaminants into their structure [4–8] and stability towards degradation by geochemical processes and ionising radiation [4]. Currently, there is concern over price stability and future supply of geologically-sourced phosphate minerals [4] and the use of biominerals provides a more sustainable option. Phosphate biominerals can be sourced from animal bones [8] or, alternatively, may be produced by microbial processes.

Microorganisms are able to induce phosphate biomineralisation through the action of phosphatase enzymes. These enzymes hydrolyse organic phosphate compounds and release inorganic phosphate into solution, which can then form precipitates with other ions present, for example contaminants in the environment or a supplied source of calcium [6, 9]. The microbial cell may also provide a nucleation point for mineralisation, further supporting the process [9].

Most research to date has focused on using this process to immobilise contaminants directly *via* the formation of insoluble metal phosphates, e.g. [10–14] but it is also possible to use the process to manufacture a biomineral PRB. The use of a ‘priming deposit’ has been identified as necessary for the immobilisation of metals such as Np and Pu, which do not precipitate out of bulk solution as metal phosphates [9], and the formation of a PRB may be a superior option where there is a complex mixture of contaminants at a range of concentrations down to trace levels.

Microbial formation of a PRB may be advantageous from a construction point of view as it should be possible to inject solutions of microorganisms and mineral constituents into the ground, allowing formation to occur *in situ*; this is in contrast to traditional excavation techniques [2] which are more invasive and will produce quantities of excavated soil that will require disposal somehow. It would also be possible to inject soluble phosphates (e.g. K_2HPO_4) but this leads to the high possibility of clogging the injection location; the use of an organic phosphate allows more control over the location of mineralisation [13].

Amorphous calcium phosphate produced by bacterial processes has also been observed to possess superior physicochemical properties to crystalline hydroxyapatite. The produced biomineral showed higher uptake capacities for Sr^{2+}, Co^{2+}, Eu^{3+}, and UO_2^{2+} as compared to a synthetically produced hydroxyapatite, which was attributed to the more amorphous nature of the material, a smaller crystallite size, and a higher specific surface area [6, 15]. Additionally, when compared to synthetic hydroxyapatite and clinoptilolite (a zeolite mineral), the biomineral maintained higher uptake values for Sr^{2+} and Co^{2+} in the presence of competing cations (Na^+, Mg^{2+}, Ca^{2+}) contained in seawater; an important property due to the threat of saline intrusion at sites such as Sellafield and Fukushima [16].

In laboratory scale, proof-of-principle studies, glycerol phosphate compounds have typically been used as an organic phosphate donor molecule. However, the high cost of this compound has been recognised as the main cost-limiting factor in the practical deployment of the technique [9, 17]. An alternative source of phosphate is *myo*-inositol hexakisphosphate (Figure 1), commonly referred to as 'phytic acid' or 'phytate' (in salt form), which is a widespread component of plant tissues [9, 17, 18]. Phytate extracted from plant waste products may be able to provide a readily available and low-cost source of phosphate. Research into phytate degradation has mostly occurred within agricultural sciences [19] and it is only in the past decade that the use of phytate as a substrate for phosphate biomineralisation has been studied [11, 12, 17, 20].

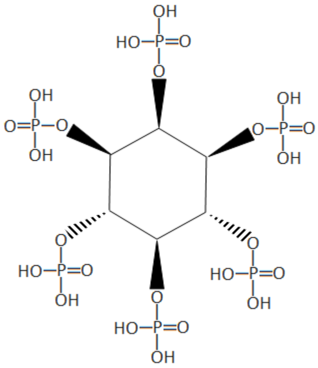

Figure 1 Structure of phytic acid, which mostly occurs in nature as a mixed Mg/K salt [18].

Phosphatase enzymes that hydrolyse phytate are commonly known as 'phytases' and are produced by many microorganisms [19, 21, 22]. Four 'model organisms' have been chosen for use in initial experiments; all are widespread in the environment and have interesting properties that merit further research into their ability to induce phosphate biomineralisation:

1. *Aspergillus niger* (ATCC 201373): A filamentous fungi that has been used commercially for the production of phytase enzymes to enhance animal feed [21]. Recent research has demonstrated the ability of *A. niger* to induce the precipitation of uranyl phosphates (in that case with glycerol 2-phosphate as phosphate source) [10]. However, the species is also known for its high production of organic acids, particularly oxalic and citric acid [23, 24]. These acids may solubilise minerals, leading to the mobilisation of contaminants, or may form complexes with metals at the expense of phosphate precipitation [9, 11, 23, 24]. On the other hand, the presence of citrate in the system during biomineralisation has been shown to improve subsequent metal uptake values [15] while the formation of insoluble oxalates may be able to support contaminant immobilisation [25].
2. *Blastobotrys adeninivorans* (CBS 8335): A species of yeast amongst which phytase activity appears to be a uniform property [26]. *B. adeninivorans* is also able to use phytate as a source of carbon [26] and has been used to induce calcium phosphate precipitation [20].
3. *Bacillus subtilis* subsp. *spizizenii* (ATCC 6633): A gram-positive bacterium. *Bacillus* spp. produce phytase enzymes which display an optimum activity at neutral pH values; this is in contrast to most other phytases which display an acidic pH optimum [21]. The activity of phytase enzymes produced by *Bacillus* spp. is enhanced by the presence of Ca^{2+} ions which bind to the enzyme and increase its stability [22]; the impact this would have on biomineral formation (i.e. would the binding of calcium to enzymes prevent it from taking part in mineral formation?) is currently uncertain.
4. *Escherichia coli* (ATCC 25922): A gram-negative bacterium that has been used commercially for phytase production [21]. *E. coli* has been demonstrated to be capable of inducing phytate-mediated precipitation of hydrogen uranyl phosphate [17].

A range of factors influence the production and activity of phytase enzymes with phosphate concentration and source, C source, presence/absence of O_2, presence of other chemical species, initial pH, and temperature all known to be important [19, 21, 22, 26]. The effect these factors have differs between microbial species and, while an in-depth study of enzyme regulation is beyond the scope of this work, a basic understanding of these processes is required as they will influence mineral precipitation and determine which environments particular microorganisms are best suited to be deployed in.

Outline of initial experiments

Phytate degradation

Initial tests will study the ability of model microorganisms to degrade phytate. Cells will be grown in phosphate-rich and phosphate-depleted media and then extracted and resuspended in solution with phytate. Samples will be extracted and analysed for phytate degradation and free-phosphate released to solution as indicators of phytase activity. Variable parameters will include source of C (e.g. glucose, galactose, phytate), aerobic/anaerobic growth environment, initial pH of phytate solution, presence of chemical species such as Ca^{2+}, temperature, and incubation time.

Analysis

Samples will be extracted from phytate solutions, filter sterilised, and then analysed by anion-exchange chromatography with a sodium carbonate or sodium hydroxide eluent and suppressed conductivity detection. Concentrations of free phosphate ions, oxalate, citrate, and phytate in solution will be measured.

Conclusions and Future Work

Results from the initial experiments detailed above will be able to confirm that the chosen organisms are capable of degrading phytate and provide an idea of the conditions under which optimum phytate degradation occurs. Knowledge regarding the amount of phosphate, oxalate, and citrate released to solution, along with the amount of phytate and phytate hydrolysis products remaining in the system, will then be used to inform biomineralisation experiments. Initially this will be performed in batch solution tests with a focus on precipitating calcium phosphates/hydroxyapatite. The manufacture of other phosphate minerals will also be investigated, with interest given to materials able to incorporate Cs and I, elements that are not easily incorporated into the structure of hydroxyapatite. Produced minerals will be characterised to understand their structure, composition, crystallinity, and specific surface area.

Select biominerals will then be tested in flow-through column experiments. This will involve biomineral formation on a matrix of sand or soil followed by passing through a simulated contaminated groundwater solution. Effluent outflow will be monitored for contaminants passing through the column and leaching of mineral constituents. The impact of biomineralisation on the permeability of the matrix will also be assessed, as the clogging of pores is a major limiting factor in the successful deployment of PRB technology. At the conclusion of these experiments, the columns will be analysed to understand how contaminants have been immobilised by the biomineral and to what extent available sorption sites have been 'consumed'.

In parallel to biomineralisation experiments, work is required to identify a usable source of phytate. Many plant waste products may be useful here (e.g. waste corn, coffee granules, by-products from biodiesel production or fermentation processes) but there is a need to define a cost-effective supply route that provides phytate in sufficient quantities. Additionally, there is a need to develop efficient extraction procedures that can be practically incorporated into a PRB construction process.

Acknowledgements

Funding for this project is provided by Mr. Ian Stalker and the University of Strathclyde Department of Civil & Environmental Engineering.

References

[1] Merkel, B.J., Hoyer, M.: *16 - Remediation of sites contaminated by radionuclides*. In: Radionuclide Behaviour in the Natural Environment (Editors: C. Poinssot and H. Geckeis). Woodhead Publishing, 2012, p. 601–645.

[2] Scherer, M.M. et al.: Chemistry and Microbiology of Permeable Reactive Barriers for In Situ Groundwater Clean up. *Crit. Rev. Environ. Sci. Technol.*, **30** (3), 2000, p. 363–411.

[3] Naidu, R. et al.: *Permeable Reactive Barriers: Cost-Effective and Sustainable Remediation of Groundwater*. In: Permeable Reactive Barrier. CRC Press, 2014, p. 1–24.

[4] Rakovan, J.F., Pasteris, J.D.: A Technological Gem: Materials, Medical, and Environmental Mineralogy of Apatite. *Elements*, **11** (3), 2015, p. 195–200.

[5] Hughes, J.M., Rakovan, J.F.: Structurally Robust, Chemically Diverse: Apatite and Apatite Supergroup Minerals. *Elements*, **11** (3), 2015, p. 165–170.

[6] Handley-Sidhu, S. et al.: Bacterially Produced Calcium Phosphate Nanobiominerals: Sorption Capacity, Site Preferences, and Stability of Captured Radionuclides. *Environ. Sci. Technol.*, **48** (12), 2014, p. 6891–6898.

[7] Murray, F.H. et al.: Immobilization of U-Th-Ra in mine wastes by phosphate mineralization. *Can. Mineral.*, **21** (4), 1983, p. 607–610.

[8] Conca, J.L., Wright, J.: An Apatite II permeable reactive barrier to remediate groundwater containing Zn, Pb and Cd. *Appl. Geochem.*, **21** (12), 2006, p. 2188–2200.

[9] Macaskie, L.E. et al.: *Bacterial precipitation of metal phosphates*. In: Phosphorus in Environmental Technologies: Principles and Applications (Editor: E. Valsami-Jones). IWA Publishing, 2004, p. 549–581.

[10] Liang, X. et al.: Uranium phosphate biomineralization by fungi. *Environ. Microbiol.*, **17** (6), 2015, p. 2064–2075.

[11] Liang, X. et al.: Phosphatase-mediated bioprecipitation of lead by soil fungi. *Environ. Microbiol.*, 2015, p. n/a–n/a.

[12] Liang, X. et al.: Uranium bioprecipitation mediated by yeasts utilizing organic phosphorus substrates. *Appl. Microbiol. Biotechnol.*, 2016, p. 1–11.

[13] Newsome, L. et al.: The biogeochemistry and bioremediation of uranium and other priority radionuclides. *Chem. Geol.*, **363**, 2014, p. 164–184.

[14] Newsome, L. et al.: Uranium Biominerals Precipitated by an Environmental Isolate of Serratia under Anaerobic Conditions. *PLOS ONE*, **10** (7), 2015, p. e0132392.

[15] Handley-Sidhu, S. et al.: Uptake of Sr2+ and Co2+ into Biogenic Hydroxyapatite: Implications for Biomineral Ion Exchange Synthesis. *Environ. Sci. Technol.*, **45** (16), 2011, p. 6985–6990.

[16] Handley-Sidhu, S. et al.: Influence of pH, competing ions, and salinity on the sorption of strontium and cobalt onto biogenic hydroxyapatite. *Sci. Rep.*, **6**, 2016, p. 23361.

[17] Paterson-Beedle, M. et al.: Biorecovery of uranium from aqueous solutions at the expense of phytic acid. *Hydrometallurgy*, **104** (3–4), 2010, p. 524–528.

[18] Shears, S.B., Turner, B.L.: *Nomenclature and terminology of inositol phosphates: clarification and a glossary of terms.* In: Inositol phosphates: linking agriculture and the environment (Editors: B. L. Turner et al.). Wallingford: CABI, 2007, p. 1–6.

[19] Dvořáková, J.: Phytase: Sources, preparation and exploitation. *Folia Microbiol. (Praha)*, **43** (4), 1998, p. 323–338.

[20] Roeselers, G., Van Loosdrecht, M.C.M.: Microbial phytase-induced calcium-phosphate precipitation — a potential soil stabilization method. *Folia Microbiol. (Praha)*, **55** (6), 2010, p. 621–624.

[21] Hill, J.E., Richardson, A.E.: *Isolation and assessment of microorganisms that utilize phytate.* In: Inositol phosphates: linking agriculture and the environment (Editors: B. L. Turner et al.). Wallingford: CABI, 2007, p. 61–77.

[22] Greiner, R.: *Phytate-degrading enzymes: regulation of synthesis in microorganisms and plants.* In: Inositol phosphates: linking agriculture and the environment (Editors: B. L. Turner et al.). Wallingford: CABI, 2007, p. 78–96.

[23] Gharieb, M.M., Gadd, G.M.: Influence of nitrogen source on the solubilization of natural gypsum (CaSO4.2H2O) and the formation of calcium oxalate by different oxalic and citric acid-producing fungi. *Mycol. Res.*, **103** (04), 1999, p. 473–481.

[24] Ceci, A. et al.: Transformation of vanadinite [Pb5(VO4)3Cl] by fungi. *Environ. Microbiol.*, **17** (6), 2015, p. 2018–2034.

[25] Gadd, G.M. et al.: Oxalate production by fungi: significance in geomycology, biodeterioration and bioremediation. *Fungal Biol. Rev.*, **28** (2–3), 2014, p. 36–55.

[26] Sano, K. et al.: Phytase of the yeast Arxula adeninivorans. *Biotechnol. Lett.*, **21** (1), 1999, p. 33–38.

Hydro-mechanical characterisation of colloidal silica grout

C. Wong*[1], M. Pedrotti[1], G. El Mountassir[1], and R. J. Lunn[1]

*christopher.wong@strath.ac.uk

[1] *Department of Civil and Environmental Engineering (University of Strathclyde, Glasgow, UK)*

Abstract

Colloidal silica based grouts are increasingly being considered as a potential grouting technology for the application of subsurface ground barriers, overcoming several limitations of traditional techniques. Colloidal silica grout has an initial low viscosity, small particle size, and is environmentally inert. Colloidal silica grouts are formed of a solution of silica nanoparticles and a salt accelerator such as NaCl. This summary presents results from on-going research at Strathclyde which aims to develop a greater understanding of the hydro-mechanical behaviour of colloidal silica grouts. Laboratory tests were carried out to investigate the stress-strain behaviour of colloidal silica grout samples considering the influence of curing environment, length of curing time, and gel time. A series of one-dimensional oedometer consolidation and direct shear tests were conducted on colloidal silica samples. Additionally, the soil-water retention behaviour of colloidal silica grout was determined.

Introduction

Subsurface migration of contaminants can be a costly and problematic issue. If appropriately managed contaminant risks can be minimised or eliminated. The use of grouts to form a hydraulic ground barrier provides a method of limiting subsurface migration of contaminants. However the use of traditional cement based grouts near surface may not be possible, in particular at sensitive sites, due to ground heave or excavation requirements. Colloidal silica provides an alternative to traditional grouting materials for the formation of in-situ subsurface hydraulic ground barriers.

Colloidal silica has been established as a fluid flow control system over the last two decades within the petroleum industry [1]. Moreover, studies have also considered its potential in various other applications such as for protection against liquefaction [2]. As a potential grout, colloidal silica poses several favourable characteristics: i) initial low viscosity, ii) low permeability after gelling, iii) minimal injection pressure iv) controllable set/gel times from minutes to several days, v) environmental inert nature once formed into a rigid gel state, and vi) its small particle size (when compared with cement grouts) [3]. The characteristics of colloidal silica enable low injection pressures to be used, whilst achieving good penetration of pore space; forming a final grouted soil mass with low permeability [4].

Colloidal silica is a stable aqueous suspension of silica nanoparticles (SiO_2). In alkaline solutions and low electrolyte concentration colloidal silica is stable. Destabilisation of the solution and subsequent gelation can be induced by reducing particle repulsive forces through the addition of an accelerator electrolyte compound such as NaCl.

In order to understand how colloidal silica grouts perform under different mechanical loading conditions, a series of laboratory tests were performed. This paper presents suction measurements and preliminary results from one-dimensional oedometer consolidation testing, and direct shear box testing. The test methods are described in the next section.

Methodology Details

Colloidal silica solution

MasterRoc MP 320 (formerly Meyco MP 320) colloidal silica solution was used in this study. According to BASF product information [5], MP320 has a SiO_2 concentration 40±1%, an average particle size of 0.015μm, and density of 1.3 kg/l. Before mixing with an accelerator at 20°C the solution has a dynamic viscosity of ∼10mPa.s and a pH of 9.5-9.8. For experimental testing, accelerator solutions of NaCl were added at a mixing ratio of 5:1 (colloidal silica to accelerator by volume) was used. All of the test sample mixtures were prepared with a final accelerator (electrolyte) concentration of 0.28M NaCl.

Water retention curve

Due to evaporation or the lowering of the water table, water can be progressively removed from soil pores. The relationship between water content and soil suction (i.e. negative pore water pressure) is known as the water retention curve. The water retention curve can be determined by subjecting a sample to drying and measuring the suction at each stage. In this study total suction of colloidal silica samples was measured using a WP4 Dew Point Potentiameter (Decagon Devices, Inc). The WP4 instrument uses the chilled mirror dew point technique to infer total suction from relative humidity measurements [6].

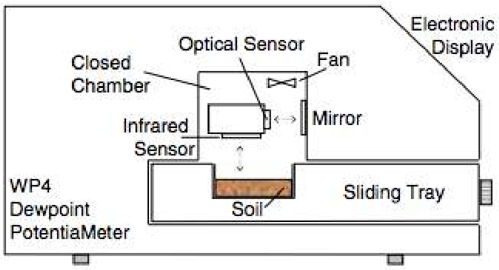

Figure 1 Schematic drawing of a WP4 chilled mirror psychrometer [7]

The suction measurements were carried out on two identical colloidal silica grout specimens with a final electrolyte concentration of 0.28M NaCl. The specimens were prepared and placed into plastic WP4 measuring cups. During the gelling phase (of 1 hr) the mixtures were kept in a 90% relative humidity environment. After gelling, the specimens were left to cure in water for one week (1 week cure). Prior to suction measurement the mass of each specimen was recorded. Following the first WP4 suction measurement, the specimens were left to air dry.

Oedometer Testing

Low permeability materials (e.g. clay soils) do not respond instantaneously to increases in applied vertical stresses, but undergo settlement for a period of time after the load is applied. Compression occurs due to a decrease in the volume of voids as the effective stress increases. The compressibility of soils and low permeability materials can be examined by means of the oedometer test.

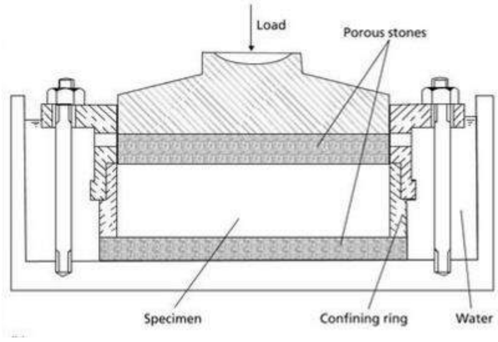

Figure 2 Oedometer loading cell [8]

In the oedometer tests, the colloidal silica grout specimens were enclosed in a metal ring (ensuring one-dimensional compression conditions) and placed between two porous stones (fig. 2). The specimens were then immersed in water. Drainage of specimens occurred only through the porous stones at the top and bottom of the specimen. The vertical displacements were monitored during the consolidation process as successive incremental vertical loads were applied. Specimens were loaded in steps to 1000kPa and unloaded to 1kPa. For each loading step, specimens were left to consolidate over a 24-hour period, with tests lasting 1 week in total. Moisture content measurements were subsequently taken after the final unloading stage of the oedometer test.

Oedometer tests were carried out in order to investigate the influence of curing condition on the grout compression behaviour. Two curing environments were investigated: curing in distilled water and at 90% relative humidity. All specimens were gelled and cured in laboratory temperatures of 20^{o}C. Specimens were gelled under 90% relative humidity. To minimise disturbance, all specimens were prepared within oedometer test rings attached to a plastic base. When specimens achieved the required curing time the plastic base was removed. Subsequently, the test rings were placed directing into the oedometer cell.

Shear strength tests

The shear strength of soils is the maximum resistance that it can offer against shear stress. Direct shear testing is a laboratory test that can be used to determine the shearing behaviour of soils. These parameters are commonly determined within the field of geotechnical engineering, providing necessary information on failure and stability conditions.

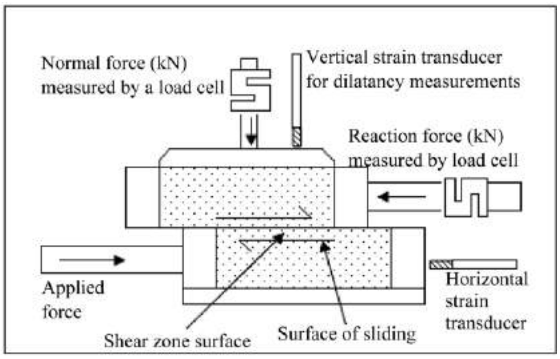

Figure 3 Schematic diagram of the direct shear box test [9]

A schematic of a direct shear box test is shown in figure 3. Specimens are placed within the shear box which consists of two halves (of square cross-section) split horizontally at mid-height. During testing the specimens are subject to a constant vertical load, whilst shear stress is progressively applied by moving the lower half of the shear box, relative to the fixed upper part [8].

A series of direct shear tests were carried out on a sand/gravel mixture grouted with MP320 colloidal silica. All specimens were prepared with the same soil composition of washed building sand (50%), pea gravel (30%), and Scottish beach pebble (20%). Direct shear tests were performed in a large shear box (Wykeham Farrance Shearmatic 300). The initial dimensions of the specimens were: A_0=22500mm^2; L_0=150mm; H_0=140mm. Tests were carried out at normal stresses (σ_N) of 100, 200 and 300 kPa.

Results and Discussion

Soil-water retention curve

Figure 4 shows the soil water retention curve for 0.28M NaCl colloidal silica specimens cured for 1 week in water. Results are compared against test results of kaolin clay from Tarantino [10]. Water is progressively removed from the colloidal silica specimens even at relatively low suctions of several hundred kilopascals. However, the colloidal silica specimens are not fully desaturated until suctions of 100MPa are reached, whereas the kaolin specimen is fully desaturated at 10MPa. The results presented in Figure 4 suggest that, as expected, the colloidal silica grout has a microstructure with smaller pore sizes than the kaolin clay.

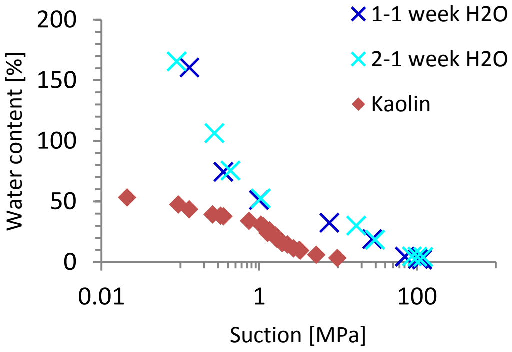

Figure 4 Soil-water retention curve for a 0.28M NaCl colloidal silica 1 week sample cured in water and also results for kaolin clay [10].

Consolidation test results

Figure 5 shows the oedometer tests of two colloidal silica specimens (0.28M NaCl) cured in conditions of distilled water, and relative humidity (RH). Void ratio (volume of voids/volume of solids) is plotted against the effective vertical stress. As the effective stress increases the void ratio decreases as the sample is compressed. The specimen cured in water is the most compressible, exhibiting the greatest change in void ratio (i.e. height change). The specimen cured under RH=90% shows a stiffer initial response on loading which may be attributable to effects of suction developed during the curing duration.

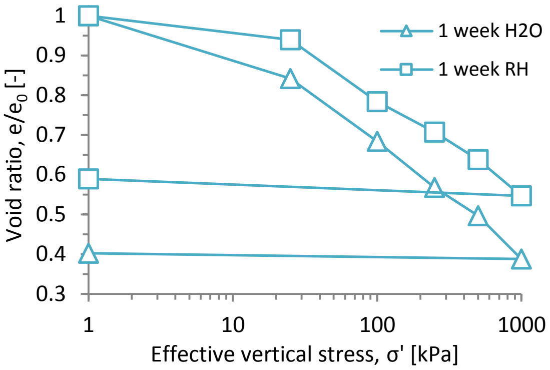

Figure 5 Compression tests with 0.28M NaCl colloidal silica 1 week specimens stored in different curing environments

Figure 6 shows colloidal silica specimens (0.28M NaCl) cured in water for 1 and 2 weeks. Although, the response is very similar between the 1 week and 2 week cured specimens, it appears that the overall compression (change in void ratio) of the specimens is reduced slightly with increasing curing time.

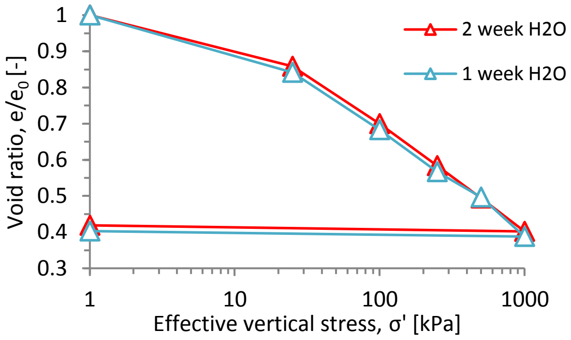

Figure 6 Compression tests with 0.28M NaCl colloidal silica specimens at different curing times

Figure 7 shows the oedometer test results of colloidal silica specimens with different gel times. A gel time of 5.5 hours was controlled by fixing a grout pH of 4 (purple triangle) and a gel time of 1 hr was controlled by fixing a grout pH of 8.7 (blue triangle). Both specimens were cured for 1 week in water prior to testing in the oedometer. The different gel times of the specimens would appear to have a negligible influence on the overall compression within the range of gel times tested.

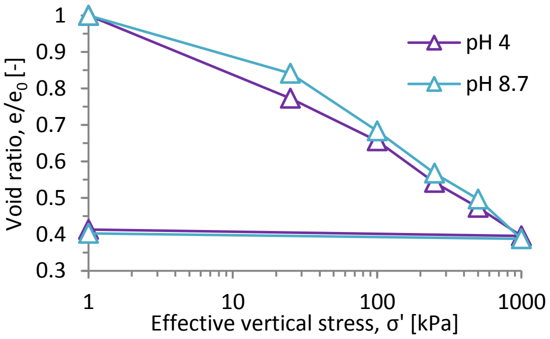

Figure 7 Compression tests of colloidal silica samples at different gel times cured in distilled water.

Direct shear tests

In Figures 8a and b the shearing behaviour for grouted soil specimens cured under distilled water for 7 days and 28 days is compared with that of ungrouted soil specimens, tested under a normal stress of 300kPa.

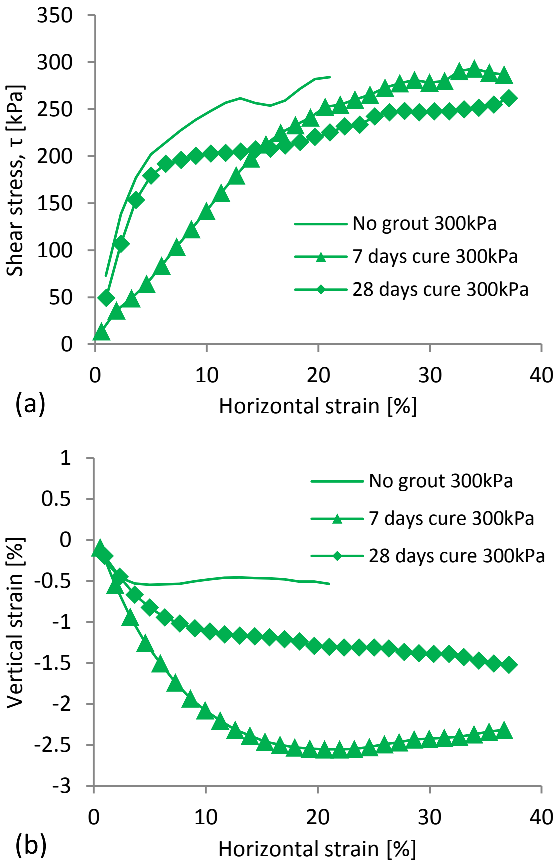

Figure 8 Shearing behaviour of distilled water-cured specimens: (a) Shear stress and (b) vertical strain vs. horizontal strain compared with ungrouted specimens.

The time after curing (i.e. 7 days or 28 days) had little effect on the maximum shear stress reached on shearing. However, the time after curing had a clear influence on the behaviour displayed, the stress-strain response indicates that with increasing curing time the specimens became more brittle, with a tendency to reach higher shear stresses at lower horizontal strains. The vertical strain plots also support this: at 7 days the volume change is contractive and after 28 days it is tending towards more dilatant behaviour. Figures 8a and b highlight that the presence of the colloidal silica grout initially (after 7 days) makes the specimens to some extent more ductile (compared to the ungrouted specimens) and with increasing curing time the specimens tend towards the behaviour of the ungrouted specimens.

Conclusions and Future Work

A series of laboratory tests to explore the influence of curing environment and curing duration on the hydro-mechanical behaviour of colloidal silica grout has been conducted. Comparisons of the soil water retention curve suggest that the microstructure of the colloidal silica may be characterised by smaller pore sizes than kaolin clay. Preliminary results from oedometer tests indicate that increasing the curing duration from 1 week to 2 weeks has a small stiffening effect (reducing overall compression of specimens). Shear test results which compared curing durations of 1 week and 4 weeks appear to show more clearly that a longer curing duration results in a stiffer grout material, which exhibits a more brittle stress-strain response. Future work will include pore size distribution analyses to investigate the influence of curing on the grout microstructure. To further understand the performance of colloidal silica grout under in-situ conditions, further experimental tests will incorporate clay, silt and sand fractions.

Acknowledgements

This work was funded by a UK EPSRC research grant (EP/L0140441/1).

References

[1] J. Jurinak and L. Summers, "Oilfield applications of colloidal silica gel," SPE Production Engineering, vol. 6, no. 4, pp. 406-412, 1991.
[2] P. M. Gallagher, "Passive Site Remediation for Mitigation of Liquefaction Risk," 2000.
[3] M. Noll, C. Bartlett and T. Dochat., "In situ permeability reduction and chemical fixation using colloidal silica," Proceedings of the Sixth National Outdoor Action Conference, 1992.
[4] R. Karol, Chemical Grouting and Soil Stabilization, USA: Marcel Dekker Inc, 2003.
[5] BASF, MasterRoc MP320, Switzerland, 2014.
[6] A. Tarantino, E. Romero and C. Y-J, Laboratory and Field Testing of Unsaturated Soils, Springer, 2008.
[7] B. R, H. S. M and B. Bailey, "Suction measurements – filter paper and chilled mirror psychrometer.," Proceedings of the Texas Section American Society of Civil Engineers, 2002.
[8] R. F. Craig, Craig's Soil Mechanics, Spon Press, 2004.
[9] D. Wijeyesekera, A. Meng Siang and A. Yahaya, "Advanced Statistical Analysis for Relationships between Particle Morphology (Size and Shape) and Shear (Static and Dynamic) Characteristics of Sands," International Journal of Geosciences, vol. 4, no. 10, 2013.
[10] A. Tarantino, "A water retention model for deformable soils," Geotechnique, 2009.

Use of Colloidal Silica Grout for Ground Barriers in Decommissioning: A Project Overview

M. Pedrotti*[1], C. Wong[1], G. El Mountassir[1] and R. Lunn[1]

*matteo.pedrotti@strath.ac.uk

[1] *Department of Civil and Environmental Engineering (University of Strathclyde, Glasgow, UK)*

Abstract

Over the last three decades, colloidal silica has been investigated and more recently adopted as a low viscosity grouting technology (e.g. for grouting rock fractures within geological disposal facilities nuclear waste). The potential of colloidal silica as a favourable grouting material exists due to: its initial low viscosity; its low hydraulic conductivity after gelling (of the order of 10^{-7} cm/s); the very low injection pressures required; its controllable set/gel times (from minutes to several days); the fact it is environmentally inert; its small particle size (less than hundreds of nanometres) and its cost-effectiveness. Colloidal silica can be destabilised by the addition of a salt accelerator compound and a change to pH, resulting in a rapid increase in viscosity (i.e. gelation) and formation of a rigid solid gel. This behaviour allows for low injection pressures to be used during the grouting process due to the initial low viscosity; with the resulting gel forming the contaminant ground barrier. This study aims to investigate the use of colloidal silica based grouts for formation of ground barriers at the Sellafield site. Potential applications include pre-treatment of the ground beneath, and surrounding, legacy structures prior to the retrieval of hazardous wastes and the formation of horizontal and vertical barriers surrounding unlined waste disposal trenches. The programme of research includes the successful completion of a large scale laboratory experiment, followed by field trials, to demonstrate the reliable application of colloidal silica for near-surface ground barrier formation. Here we summarise results to-date on colloidal silica gelling behaviour, grout-site interaction, the colloidal silica grout injection process, injection monitoring and the mechanical characterisation of the colloidal silica grout.

Context

Groundwater control at contaminated sites is often controlled via the use of low permeability barriers created using excavation and replacement or grouting techniques. Soil-bentonite slurry trenches are a commonly employed method. They are constructed by excavating a continuous narrow trench under a bentonite slurry that stabilizes the excavation. The trench is backfilled subsequently with a blend of natural soil and bentonite, thereby displacing the slurry [1]. The completed wall acts as a barrier to lateral flow of water and most fluid pollutants. The main issues with the deployment of this technique on a nuclear decommissioning site relate to worker exposure and the challenge of accessing and excavating contaminated soil.

Jet grouting and permeation grouting are two general categories usually suitable for hydraulic barriers. Jet grouting uses high-energy emplacement of cement or chemical grouts whereby the sediment is displaced and mixed with the grouting material. Permeation grouting is the injection of a liquid grout (low viscosity) that fills the natural porosity and then sets or gels to form a solid void-filling material [2].

The most commonly used grouts are cement grouts where Portland cement is the primary component. The particle size distribution of the cement particles controls the ability of the grout to penetrate small pores or openings. For cement grouts, emplacement is often an issue for finely textured regions. Microfine or ultrafine cement grouts incorporate micron-scale solids in the mix. However grout penetration for cement grouts would only be appropriate for coarse sand or gravel layers, with no fine sediments less than about 0.1 mm diameter [2]. Cement grouts are also not suitable for injection near surface due to the potential for ground heave under the necessary high injection pressures.

Chemical grouts are easier to inject than cement grouts because they are stable solutions, they have lower viscosity and can be injected into smaller pore sizes. However, chemical grouts are often expensive, exhibit syneresis and may contain toxic components [3], colloidal silica represents an exception.

Colloidal silica as a grouting material has been successfully adopted as a fluid-flow control system within the petroleum industry since the late 1980s [4]. Consolidated core plugs of fully cured colloidal silica were observed to withstand applied pressure gradients of more than (56 MPa/m) before exhibiting any permeability change. Passive site remediation proposed by Gallagher [5] studied the application of colloidal silica as a non-disruptive mitigation technique to sites susceptible to liquefaction. Desirable characteristics were long injection periods up to 100 days for low concentration solutions of approximately 10 to 20% colloidal silica concentration. Du Pont Chemicals R & D initiated work examining the feasibility of colloidal silica grout as a soil remediation technique through a series of bench-scale laboratory studies. Gelled colloidal silica was seen to prevent leaching of fluids containing metals through permeability reduction. Further, high affinities for the adsorption of metals from solution were seen by the colloidal silica gel itself [6]. Similarly, the stabilization process of chromium contaminated soils using colloidal silica was investigated by Yossapol and Meegoda [7].

In the 90s, Lawrence Berkley National Laboratory and Brookhaven National Laboratory carried out in-situ [8-12] and laboratory [13-15] tests to demonstrate the use of silica colloids for permeation grouting for containment technology.

Researchers at Chalmers University of Technology have investigated the application of colloidal silica grout to minimise water ingress during the construction and operation of a nuclear waste repository in hard rock at great depth. In order to evaluate penetrability, laboratory mechanical tests on colloidal silica [16, 17] and field tests [18, 19] were performed. More recently, colloidal silica has been adopted in the tunnelling and underground construction industry for preventing water ingress, mainly as a secondary injection grout during the pre-injection stage (i.e. injecting in advance of the tunnel face during excavation) (e.g. Butrón, Gustafson [20], Bahadur, Holter [21]).

Project overview

Despite the well-documented success of colloidal silica based grout for hydraulic barrier formation, research has not translated into widespread industrial use. A key factor in this limited commercial uptake is the lack of a predictive model for grout gelling: whilst data are available to underpin design of a grouting campaign in laboratory conditions, little research has been done to underpin applications in natural groundwater systems (Lakatos et al., 2009).

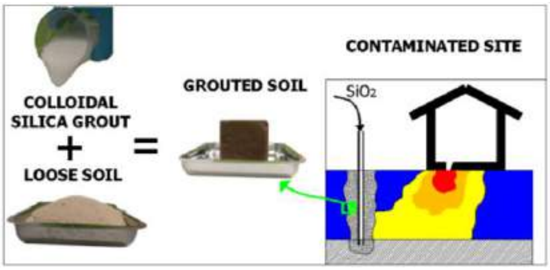

Figure 1. Project overview

The aims of this research project are to (1) develop a predictive understanding of the behaviour of colloidal silica grout in radionuclide contaminated environments and (2) to develop strategies for the formation of horizontal and vertical colloidal silica based hydraulic barriers via near-surface low pressure borehole injection. Particular attention is paid to existing challenges at the Sellafield site, for example, the need to seal the ground beneath leaking waste silos and trenches, without mobilising any radionuclides sorbed onto clays beneath the structure (Figure 1).

Colloidal silica and gelling behaviour

The potential of colloidal silica as a favourable grouting material exists due to: i) its initial low viscosity (close to water), ii) its low hydraulic conductivity after gelling (of the order of 10^{-7} cm/s), iii) the very low injection pressures required, iv) its controllable set/gel times (from minutes to several days), v) the fact it is environmentally inert and vi) its small particle size (less than hundreds of nanometres).

Colloidal silica is a stable aqueous suspension of microscopic silica particles (SiO_2). In alkaline solutions and low electrolyte concentration colloidal silica is stable. Destabilization of the solution and subsequent gelation can be induced by destabilization of the particle repulsive forces through the addition of an accelerator electrolyte compound. This process, shown in Figure 2, results in a rapid viscosity increase after a given period of time (gel time). Gel time has been proven to depend on colloidal particle size, colloidal particle concentration, electrolyte concentration, cation valency, cation atomic mass and temperature (which is not considered here) [22].

Pedrotti et al. [22] describes an electrochemically inferred model that has been developed under the DISTINCTIVE project . This model is able to predict, for the first time, the gelation time and the change in viscosity as a function of pH, electrolyte, silica particle size and silica concentration.

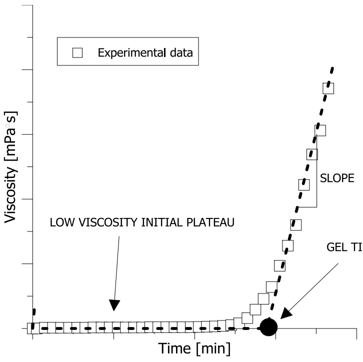

FIgure 2. Gel time

Figure 4 (a) shows an example of the modelled gel time versus the experimental data for variations in solution pH and accelerator concentration. In Figure 3b, viscosity change over time is plotted for a single accelerator concentration of 2M at different pH. In all experiments, the model provides a good prediction of the experimental observations.

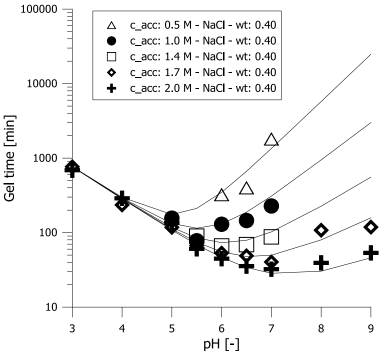

Figure 3. Gel time prediction ([22])

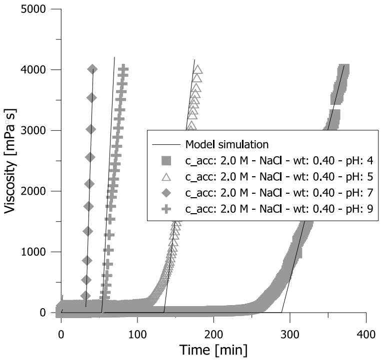

Figure 4. Viscosity prediction ([22])

Accelerator design

The main advantage of the model developed in Pedrotti et al. [22] is the ability to simultaneously account for the presence of many different cation species in the estimation of grout gel time and viscosity. This capability provides a useful tool for the design of grout mixes using colloidal silica that can take account of the situ groundwater conditions, overcoming one of the main challenges to its use in industry.

In Pedrotti et al. [22], purely by way of example, the model is applied to demonstrate design of an appropriate accelerator for colloidal silica grouting at the proposed site for a spent fuel disposal in the Olkiluoto area of Finland [23]. Our calculations show that if the manufacturer recommended grout mix was prepared with in-situ groundwater, which is naturally saline, the gel time would be approximately half that of the same grout mix made with deionised water. By accounting for the cations species already present in the groundwater, however, we show that our model can correct the required accelerator concentration and achieve the desired grout gel time (in this case 55 minutes). We validate our model results using experimental data by preparing a grout mix with artificial groundwater with the same cation composition to that published for the Olkiluoto area [21].

Colloidal silica grout – radionuclide interactions

Since the colloidal silica grout will be injected into contaminated areas (to create hydraulic barriers for nuclear waste disposal), understanding silica-radionuclide interaction is crucial. Firstly, the effect of radionuclides on the colloidal silica grout gel time and on the final hydraulic conductivity should be investigated. Secondly, and perhaps more importantly, the effect of grout injection on subsurface radionuclide mobility, sorption and de-sorption phenomena must be well understood.

Sorption of Sr and Cs has been intensively studied in the last years (among many [24-27]). In general, the sorption of cold Sr and Cs has been studied onto different clays (kaolinite, illite and montmorillonite). Sr and Cs sorption depends on the electrical charge of the clay: hence, different clays result in different amounts of sorbed radionuclides. The electrical charge of clay mineral surfaces is dependent on pH and the concentration of electrolytes in solution, hence, sorption of radionuclides also changes with the pH (the higher the pH the higher the sorption capacity) and the concentration of background electrolytes (the higher the electrolyte concentration the lower the sorption capacity). Previous studies on amorphous silica and colloidal silica have showed silica to have some sorption potential [28, 29].

An experimental campaign is now ongoing to study the de-sorption of Sr and Cs from contaminated clays in the presence of colloidal-silica based grout. The first stage consists of batch experiments to study the desorption from clay minerals of cold isotopes in the presence of water with different background electrolyte concentration (different grout accelerators) and in the presence of colloidal silica in suspension. A second stage is planned to take place at NNL facilities using hot isotopes. The experimental campaign planned to take place at NNL beginning Summer 2016 has been funded via the DISTINCTIVE Active Research Fund.

Design of the injection process

An injection tank (1.5m x 0.4m x 0.2m) has been set up to investigate strategies for grout injection (Figure 5). These experiments will test our capability to accurately predict grout penetration within different soils, using a variety of ground water compositions. Experiments in the injection tank will be designed using the newly developed grout viscosity model coupled with a 3D numerical model of fluid flow in porous media.

Figure 5 Injection tank

The numerical model is being developed with the open source computational fluid dynamics OpenFoam®. As a first stage, the model will simulate a multiphase injection process by implementing a mass balance equation and a generalised form of Darcy's equation. The two fluids will be modelled as incompressible, with an initial assumption of constant viscosity and no electrolyte transport. This model will be validated using tracer tests in the experimental tank. In the second stage, the injected grout will have a time-dependent viscosity resulting in no further movement of the grout once gelled. The ultimate aim is to demonstrate predictive model capability of grout penetration for design of the larger-scale tank and field-scale experiments.

Injection monitoring

Figure 6 ERT setup

A collaboration with Dr Oliver Kuras at BGS has been initiated in order to monitor the movement of grout during injection using the Electrical Resistivity Tomography (ERT) technique.

A preliminary test was conducted by Dr Kuras (BGS) in the laboratories at Strathclyde. A controlled volume of sand was saturated with colloidal silica grout (Figure 6) and results clearly indicated the potential for detecting the presence of the silica grout (illustrated in Figure 7) due to a distinct change in the electrical resistivity.

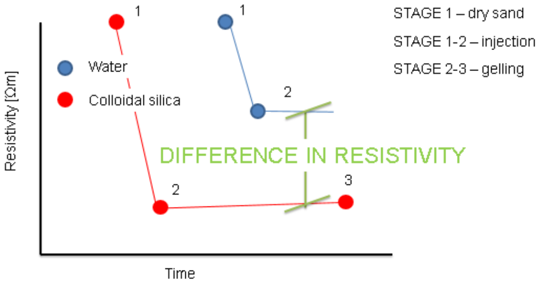

Figure 7 ERT output.

Mechanical characterization

A series of direct shear tests have been carried out on a sand/gravel mixture grouted with colloidal silica. The objective of these tests was to determine the influence of both curing conditions and curing time, on the stress-strain behaviour of the grouted specimens.

Figure 8 Colloidal silica grouted sample of initially loose soil.

The presence of the colloidal silica grout did not change the maximum shear resistance of the material. The shearing resistance remained dominated by that of the natural sand/gravel mixture (i.e. without grout). Tests also showed that the curing environment did not affect the maximum shear resistance nor the mechanical behaviour observed. In terms of shear resistance, these tests are not definitive, since only sand/gravel mixtures have been tested to-date.

The shear tests using the grouted sand/gravel mixtures did demonstrate a significant effect of curing time on the mechanical behaviour of the specimens under increasing shear load. After 7 days of curing, the soil showed contractive behaviour, whilst at 28 days the soil became more brittle, showing some dilation. With increased curing time the stress-strain response tended towards that of the ungrouted specimens.

Conclusions

Small- scale laboratory grouting experiments have been conducted to investigate the behaviour of colloidal silica grout in terms of its gelling behaviour in natural environments, its mechanical properties and its detectability using ERT. A model of colloidal silica gelling has been developed and successfully validated against the experimental data; a publication is now in review. Forthcoming research will focus on conducting and modelling larger-scale laboratory and field tests, and on developing a robust understanding of the interactions between colloidal silica grout and radionuclides within the subsurface.

Acknowledgements

This work was funded by a UK EPSRC research grant (EP/L0140441/1). The authors also thank Nick Atherton for the collaboration.

References

1. Tallard, G., *Slurry trenches for containing hazardous wastes.* Civil Engineering—ASCE, 1984. **54**(2): p. 41-45.
2. Truex, M.J., et al., *Evaluation of In Situ Grouting as a Potential Remediation Method for the Hanford Central Plateau Deep Vadose Zone.* Pacific Northwest National Laboratory, 2011.
3. Gallagher, P.M., S. Spatari, and J. Cucura, *Hybrid life cycle assessment comparison of colloidal silica and cement grouted soil barrier remediation technologies.* Journal of Hazardous Materials, 2013. **250**: p. 421-430.
4. Jurinak, J. and L. Summers, *Oilfield applications of colloidal silica gel.* SPE production engineering, 1991. **6**(04): p. 406-412.
5. Gallagher, P.M., *Passive Site Remediation for Mitigation of Liquefaction Risk*, in *Civil and Environmental Engineering*. 2000, Virginia Polytechnic Institute and State University.
6. Noll, M.R., C.L. Bartlett, and T.M. Dochat. *In situ permeability reduction and chemical fixation using colloidal silica*. in *Proceedings of the Sixth National Outdoor Action Conference*. 1992.
7. Yossapol, N. and J. Meegoda, *Remediation of Heavy Metal Contaminated Soil with Colloidal Silica.* Hazardous and industrial wastes, 2000. **32**: p. 787-798.
8. Persoff, P., et al., *Injectable barriers for waste isolation*. 1995, Lawrence Berkeley Lab., CA (United States).
9. Moridis, G., et al., *A field test of permeation grouting in heterogeneous soils using a new generation of barrier liquids.* Committed To Results: Barriers for Long-Term Isolation. ER, 1995. **95**.
10. Moridis, G., et al. *A field test of a waste containment technology using a new generation of injectable barrier liquids*. 1996.
11. Moridis, G., A. James, and C. Oldenburg, *Development of a design package for a viscous barrier at the Savannah River site*. 1996, Lawrence Berkeley National Lab., CA (United States). Funding organisation: USDOE Office of Environmental Restoration and Waste Management, Washington, DC (United States).
12. Moridis, G.J., S. Finsterle, and J. Heiser, *Evaluation of alternative designs for an injectable barrier at the Brookhaven National Laboratory Site, Long Island, New York.* Water Resources Research, 1999. **35**(10): p. 2937-2953.
13. Hakem, N., et al. *Sorption of cesium and strontium on Savannah River soils impregnated with colloidal silica*. in *International Containment Technology Conference*. 1997. Petersburg:[sn].
14. Manchester, K., et al. *Grout selection and characterization in support of the colloidal*

silica barrier deployment at Brookhaven National Laboratory. in *Proc. 2001 International Contain. and Remed. Technol. Conf. and Exhib., 10-13 June, 2001. Orlando, FL*. 2001.

15. Persoff, P., et al., *Effect of dilution and contaminants on sand grouted with colloidal silica.* Journal of geotechnical and geoenvironmental engineering, 1999. **125**(6): p. 461-469.
16. Axelsson, M., *Mechanical tests on a new non-cementitious grout, silica sol: A laboratory study of the material characteristics.* Tunnelling and underground space technology, 2006. **21**(5): p. 554-560.
17. Butrón, C., M. Axelsson, and G. Gustafson, *Silica sol for rock grouting: Laboratory testing of strength, fracture behaviour and hydraulic conductivity.* Tunnelling and underground space technology, 2009. **24**(6): p. 603-607.
18. Funehag, J. and Å. Fransson, *Sealing narrow fractures with a Newtonian fluid: Model prediction for grouting verified by field study.* Tunnelling and underground space technology, 2006. **21**(5): p. 492-498.
19. Funehag, J. and G. Gustafson, *Design of grouting with silica sol in hard rock–New design criteria tested in the field, Part II.* Tunnelling and underground space technology, 2008. **23**(1): p. 9-17.
20. Butrón, C., et al., *Drip sealing of tunnels in hard rock: A new concept for the design and evaluation of permeation grouting.* Tunnelling and underground space technology, 2010. **25**(2): p. 114-121.
21. Bahadur, A., K. Holter, and A. Pengelly. *Cost-effective pre-injection with rapid hardening microcement and colloidal silica for water ingress reduction and stabilisation of adverse conditions in a headrace tunnel*. in *Underground Space–The 4th Dimension of Metropolises, Three Volume Set+ CD-ROM: Proceedings of the World Tunnel Congress 2007 and 33rd ITA/AITES Annual General Assembly, Prague, May 2007*. 2007. CRC Press.
22. Pedrotti, M.W., C, G. El Mountassir, and R. Lunn, *An analytical model for the control of silica grout penetration in natural groundwater systems.* Tunnel and underground space technology, 2016 (under revision).
23. Ollila, K., *Dissolution of unirradiated UO2 fuel in synthetic groundwater–Final report (1996–1998).* Posiva Report, 1999: p. 99-24.
24. Adeleye, S., P. Clay, and M. Oladipo, *Sorption of caesium, strontium and europium ions on clay minerals.* Journal of materials science, 1994. **29**(4): p. 954-958.
25. Başçetin, E. and G. Atun, *Adsorption behavior of strontium on binary mineral mixtures of Montmorillonite and Kaolinite.* Applied radiation and isotopes, 2006. **64**(8): p. 957-964.
26. Wahlberg, J.S., et al., *Exchange adsorption of strontium on clay minerals*. 1965, US Govt. Print. Off.
27. Wallace, S.H., et al., *Effect of groundwater pH and ionic strength on strontium sorption in aquifer sediments: implications for 90 Sr mobility at contaminated nuclear sites.* Applied Geochemistry, 2012. **27**(8): p. 1482-1491.
28. Sahai, N., et al., *X-ray absorption spectroscopy of strontium (II) coordination: II. Sorption and precipitation at kaolinite, amorphous silica, and goethite surfaces.* Journal of Colloid and Interface Science, 2000. **222**(2): p. 198-212.
29. Lu, N. and C.F. Mason, *Sorption-desorption behavior of strontium-85 onto montmorillonite and silica colloids.* Applied Geochemistry, 2001. **16**(14): p. 1653-1662.